October 2021

DENSITY STATE AND SHEAR BEHAVIOR OF GRANULAR SOILS WITH INFLUENCE OF PARTICLE SIZE DISTRIBUTION

Yibing Deng
University of Massachusetts Amherst

DENSITY STATE AND SHEAR BEHAVIOR OF GRANULAR SOILS WITH INFLUENCE OF PARTICLE SIZE DISTRIBUTION

Yibing Deng

DENSITY STATE AND SHEAR BEHAVIOR OF GRANULAR SOILS WITH INFLUENCE OF PARTICLE SIZE DISTRIBUTION

A Dissertation Presented

by

YIBING DENG

Submitted to the Graduate School of the
University of Massachusetts Amherst in partial fulfillment
of the requirements for the degree of

DOCTOR OF PHILOSOPHY

September 2021

Civil and Environmental Engineering

DENSITY STATE AND SHEAR BEHAVIOR OF GRANULAR SOILS WITH INFLUENCE OF PARTICLE SIZE DISTRIBUTION

A Dissertation Presented

by

YIBING DENG

Approved as to style and content by:

_____
Ching S. Chang, Chair

_____
Guoping Zhang, Member

_____
Byung H. Kim, Member

_____
John E. Tobiason, Department Head
Department of Civil and Environmental Engineering

DEDICATION

To my family

ACKNOWLEDGMENTS

There are many people who helped me along the way on this doctoral journey. I would like to take a moment to thank them.

My foremost and greatest thanks should be given to my advisor Prof. Ching S. Chang for providing the opportunity for me to pursue my doctoral study at Umass Amherst and to develop the research presented in this dissertation. I would like to express my sincere gratitude him for his endless support, guidance, supervision, inspiration, motivation and encouragement through this doctoral journey.

I would also like to thank my committee members: Prof. Guoping Zhang and Prof. Byung H. Kim, for their invaluable suggestions and insightful comments. A particular debt of gratitude is owed to Prof. Guoping Zhang for offering me a chance to work in his research group with supplying half-year living expense.

I gratefully acknowledge the collaboration with Prof. Y. Yilmaz of Gazi University in Turkey who performed drained triaxial tests. I would like to thank to all of the other faculty members in geotechnical engineering group for sharing their expertise and friendship. Great thanks are dedicated to my friends and colleagues met in Umass for their help and friendship.

A heartfelt thank to my wife, my two kids, my parents, parents in law, and my sisters for their love, patience, and support throughout my study in the U.S.

This research was supported by the National Science Foundation (NSF) under the research grant CMMI-1537491 and the research grant CMMI-1917238. The support is greatly acknowledged.

ABSTRACT

DENSITY STATE AND SHEAR BEHAVIOR OF GRANULAR SOILS WITH INFLUENCE OF PARTICLE SIZE DISTRIBUTION

SEPTEMBER 2021

YIBING DENG

B.S., M.S., SHANGHAI MARITIME UNIVERSITY

Ph.D., UNIVERSITY OF MASSACHUSETTS AMHERST

Directed by: Professor Ching S. Chang

Heterogeneous granular soils are ubiquitous in nature and man-made deposits. Heterogeneity of soil is characterized by its particle size distribution (or fines content for gap-graded soils). The particle size distribution of soil is the main factor that affects its mechanical properties. However, in soil mechanics, the influence of particle size distribution on mechanical properties is only considered in an empirical manner. There are few analytical methods that can explicitly account for the effect of particle size distribution. In this study, there are two purposes: 1) to develop a particle packing theory for modeling the effect of particle size distribution on density states of granular soils, including densest, loosest, and critical density states, which are the fundamental properties relating to mechanical behavior of soil, and 2) to study the shear behavior of granular soils with influence of particle size distribution.

The developed particle packing theory is able to predict the density state of multi-sized soils based on their particle morphological characteristics and particle size distribution. The particle packing theory providing an ability to analyze the effect of particle size distribution is important in the understanding of mechanical behavior due to the heterogeneity of soil.

Based on the developed particle packing theory, a framework of modeling the critical state line of granular soils was established by explicitly considering their particle size distribution. Incorporating the evolution of particle size distribution due to particle breakage into the model, this framework can be used for predicting the critical state line of granular material with particle breakage.

A series of drained triaxial compression tests on dense binary silica sand mixtures with 4 different particle size ratios was performed to systematically investigate the effects of fines content and particle size ratio on the drained shear behaviors. It was observed that both fines content and particle size ratio have significant influence on the drained shear behaviors of binary granular soil mixtures. A mechanism was proposed to illustrate the influences of fines content and particle size ratio on the drained shear behavior from the perspective of particle column buckling.

The findings from this research is potentially useful for analyzing geotechnical engineering problems, such as liquefaction of silty sand, landslides of weathered soil, levee failure due to erosion of fine particles, and dam instability due to grain crushing. This study also has potential to be applied in the continuum mechanics for materials of heterogeneous nature.

TABLE OF CONTENTS

Page

LIST OF TABLES

Table Page

LIST OF FIGURES

Figure Page

CHAPTER 1

INTRODUCTION

1.1 Problem Statement

Heterogeneous granular soils are ubiquitous in nature and man-made deposits, which are commonly encountered in dams, fills, fault zones, and landslides. These soils are generally composed of particles with multiple sizes. Heterogeneity of soil is characterized by its particle size distribution (or fines content for gap-graded soils). Experimental investigations have shown that the particle size distribution of granular soil is the main factor that affects its mechanical properties: limiting void ratios, critical state void ratio, initial moduli, compressibility, and strength (e.g., Harehdasht, Karray, Hussien, & Chekired, 2017; Li, Liu, Dano, & Hicher, 2015; Minh & Cheng, 2013; Wichtmann & Triantafyllidis, 2014; Youd, 1973). However, in soil mechanics, the influence of particle size distribution on mechanical properties is only considered in an empirical manner. There are few analytical methods that can explicitly account for the effect of particle size distribution. Understanding the influence of particle size distribution on mechanical properties has great scientific and engineering importance. In fact, particle size distribution constitutes challenging theoretical problems not only in soil mechanics, but also in various fields of physics and chemistry, as first recognized by Kepler and Hilbert (Aste & Weaire, 2008).

Many facets of mechanical properties are related to the void ratio of three density states: densest, loosest, and critical states. Minimum and maximum void ratios correspond to random dense and loose packing states, which are the upper and lower bounds of jammed

state of granular matters. The two limiting void ratios are two important index properties of granular soils, which often used to evaluate the behavior of granular soils through the relative density or the difference between maximum and minimum void ratios (Cubrinovski & Ishihara, 2002; Lade, Liggio, & Yamamuro, 1998; Selig & Ladd, 1973). The critical state has been defined as the state at which the soil continues to deform at constant stress and constant void ratio, which is recognized as being near (or at) the state of jamming transition (Ivsic & Ivsic, 2012). The critical state void ratio is a fundamental property relating to deformation and strength behaviors of soils in soil mechanics (Been & Jefferies, 1985; Imam, Morgenstern, Robertson, & Chan, 2005; Jefferies & Been, 2006; Schofield & Wroth, 1968). It has also been a vital element of constitutive models in the framework of critical state soil mechanics.

Therefore, in order to account for the influence of particle size distribution on the mechanical behavior of granular soil, it is necessary to develop the knowledge for modeling the influence of particle size distribution on the three density states of granular soil, because these density states are the fundamental properties relating to mechanical behavior of granular soil.

1.2 Research Objectives

The main goal of this research is to develop theoretical model that is able to predict the three density states of granular soil with the influence of particle size distribution. The density states include the maximum, minimum and critical state void ratios. The goal in this research can be separated into several specific research objectives as follows:

(1) To develop a statistical model for predicting the minimum and the maximum void ratios of uniform sands based on their particle morphology.

(2) To find the role of particle size distribution in the influence on the maximum, minimum and critical state void ratios of granular soils.

(3) To develop a particle packing theory for predicting the minimum and maximum void ratios of binary and multi-sized soil mixtures.

(4) To develop an analytical model that can be used to determine the critical state line (CSL) of granular materials by explicitly considering their particle size distribution. The developed model should be capable of predicting the influence of gradation on the CSL for: sand-silt mixtures, well graded sands, and granular materials with evolution of gradation due to particle breakage.

(5) To investigate the effects of fines content and particle size ratio on critical state behavior and shear-dilatancy behavior of binary granular soil mixtures.

1.3 Dissertation Outline

This dissertation consists of ten chapters and is formatted as a series of standalone papers. A brief outline of each chapter is given below:

Chapter 2 presents a study of the effect of particle morphology on limiting void ratios of uniform sands. Multi-variable equations, in which the limiting void ratios are functions of both particle size and particle shape, is proposed. This paper has been published in *Engineering Geology* (2018), doi: 10.1016/j.enggeo.2018.02.003.

Chapter 3 presents a study of the role of morphologic indices on the variation of limiting void ratios for uniform sands. New material parameters for sands, morphologic

indices, are introduced to represent the relationship between particle size and shape, and these indices are used to predict the limiting void ratios of sands from particular sites. This paper has been published in *Géotechnique Letters* (2018), doi: 10.1680/jgele.18.00087.

Chapter 4 presents a particle packing model for sand–silt mixtures with the effect of dual-skeleton. This paper has been published in *Granular Matter* (2017), doi: 10.1007/s10035-017-0762-1.

Chapter 5 presents a particle packing model for predicting the minimum and void ratio of multi-sized soil mixtures. This paper has been published in *Journal of Engineering Mechanics* (2017), doi: 10.1061/(ASCE)EM.1943-7889.0001270.

Chapter 6 presents a study of the effects of the packing procedure and particle shape on packing density of binary mixtures. A packing potential index is defined to study the effects. This paper has been published in *Powder Technology* (2020), doi: 10.1016/j.powtec.2020.06.005.

Chapter 7 presents a new formula of inter-granular void ratio of silty sand for the prediction of critical state void ratio of silty sand. The concept of inter-granular void ratio is revisited in view of particle packing theory. This paper has been published in *Géotechnique Letters* (2019), doi: 10.1680/jgele.18.00175.

Chapter 8 presents a model for determining the critical state line (CSL) of granular materials by explicitly considering their particle size distribution. The developed model is capable of predicting the influence of gradation on the CSL for well graded granular materials and for the granular materials with the effect of particle breakage. This paper has been published in *Geoscience Frontier* (2020), doi: 10.1016/j.gsf.2019.06.008.

Chapter 9 presents a study of the effects of fines content and particle size ratio on the drained shear behaviors of binary granular soil mixtures. This paper was submitted to *Géotechnique*.

Chapter 10 presents the conclusions drawn from this research. Recommendations for future research on the density states and strength of multi-sized granular materials are also presented.

CHAPTER 2

LIMITING VOID RATIOS OF UNIFORM SANDS: EFFECT OF PARTICLE MORPHOLOGY[1]

The limiting void ratios (i.e., the minimum and the maximum void ratios) are two important index properties, which are related to the compressibility, shear strength, and permeability of granular soils. Experimental studies have shown that the limiting void ratios are correlated to morphological properties of soil particles (i.e. particle size and particle shape). However, empirical equations available in literature for the limiting void ratios are generally single-variable functions of either particle size, or particle shape. In this study, we propose multi-variable equations, in which the limiting void ratios are functions of both particle size and particle shape. The coupled effects of particle size and particle shape on the limiting void ratios are illustrated. Advantages of the proposed multi-variable equations over the existing single-variable equations are shown by comparing the calculated void ratios with the experimental data on a large number of uniform sand samples. The proposed multi-variable equations can be applied to predict the limiting void ratios of uniform sands encountered in geotechnical engineering projects in order to properly support heavy loads.

[1] This chapter has been published as a standalone paper: Chang, C. S., Deng, Y., & Meidani, M. (2018). A multi-variable equation for relationship between limiting void ratios of uniform sands and morphological characteristics of their particles. *Engineering Geology, 237*, 21–31.

2.1 Introduction

The limiting void ratios (i.e., the minimum and the maximum void ratios) are two important index properties of granular soils, which are correlated to the compressibility, shear strength, and permeability (Selig and Ladd, 1973; Aberg, 1992; Miura et al., 1997; Cubrinovski and Ishihara, 2002; Bandini and Sathiskumar, 2009; Bobei et al., 2009; Peters and Berney, 2010; Belkhatir et al., 2013; Fuggle et al., 2014). Experimental studies have shown that the limiting void ratios are functions of particles morphological characteristics, specifically, the particle size and particle shape (G.-C. Cho, Dodds, & Santamarina, 2006; Miura et al., 1997; Patra, Sivakugan, Das, & Rout, 2010; Rouse, Fannin, & Shuttle, 2008; Rout, 2009; Santamarina & Cho, 2004; Youd, 1973; Zheng & Hryciw, 2016a). These two morphological characteristics, i.e. particle size and particle shape, are dependent on the lithology, transportation history, and deposition environment of the soil. Therefore, the limiting void ratios vary from site to site.

For the two morphological characteristics, particle size is usually measured by a standard sieve analysis. Particle shape, however, has several types of measures, which are roundness, sphericity, aspect ratio, and roughness (Barrett, 1980; Diepenbroek et al., 1992; Hyslip and Vallejo, 1997; Cox and Budhu, 2008; Tafesse et al., 2012; Uday et al., 2013; Okonta, 2015). Roundness measures the sharpness of particles' edges, whereas sphericity and aspect ratio measure the overall shape of the particles. Roughness describes the surface texture of the particles. In geotechnical engineering literature, roundness is the most commonly used parameter to describe the shape of sand particles.

It is important to have a mathematical expression for the relationship between the minimum or maximum void ratio of sands and morphological characteristics of their

particles, because it is a stepping-stone for understanding the relationship between particle morphology and mechanical properties of soils such as shear strength, compressibility, and permeability.

The correlation between particle size and limiting void ratio of granular soil has been investigated in several experimental studies. Miura et al. (1997) examined natural and reconstituted sands, and concluded that the minimum void ratio (e_{min}) and the maximum void ratio (e_{max}) tend to decrease with increase of mean particle size. Cubrinovski and Ishihara (2002) and Bareither et al. (2008) observed the same tendency for clean sands, and for sands with some fines. Rout (2009) and Patra et al. (2010) proposed an empirical equation for the two limiting void ratios as functions of mean particle size D_{50}.

The correlation between particle shape and the limiting void ratio of granular soil has been extensively investigated as well. A number of empirical equations have been proposed by several researchers for the two limiting void ratios as functions of particle roundness (Youd, 1973; Shimobe and Moroto, 1995; Santamarina and Cho, 2004; Cho et al., 2006; Rouse et al., 2008; Zheng and Hryciw, 2016).

Two shortcomings can be identified in the previous studies:

(1) The effect of particle size distribution (PSD) was not separated from the effect of particle morphological characteristics on the limiting void ratio, particularly, in the studies of the correlations between particle size and the limiting void ratio. The samples used were not uniformly graded, sometimes the samples were mixtures of sand and fines.

(2) The coupling effect of particle size and particle shape variation on the limiting void ratios was neglected by only considering a single-variable in the equations.

The empirical equations for the two limiting void ratios are functions of either particle size or particle shape. They were obtained from single-variable regression analysis. However, in general, the limiting void ratios are influenced simultaneously by both particle size and particle shape.

To overcome the first shortcoming, we eliminate the effect of PSD of soil samples by using uniform sand samples. In this study, we generate a database obtained from test results in the literature on very narrowly graded sand samples.

To overcome the second shortcoming, we conduct a multi-variable analysis by considering particle size and particle shape as two separate variables. The limiting void ratio (e_{min} or e_{max}) is considered to be the outcome variable, and the particle size and particle shape are considered to be predictor variables.

In this study, we aim to establish multi-variable equations for the two limiting void ratios as functions of particle size and particle roundness. Using the collected database, the correlations between the predictor variables and the outcome variables are derived to show the relative influence of particle size and particle shape on the two limiting void ratios. Based on the multi-variable analysis, we propose mathematical expressions for the two limiting void ratios (e_{min} and e_{max}) as functions of particle size and particle roundness. The advantage of the proposed equations is demonstrated by comparing the predicted limiting void ratios with those predicted by the existing single-variable equations.

The proposed multi-variable equations can be directly applied to predict the limiting void ratios of uniform sands encountered in geotechnical engineering projects. For soil with a broader range of particle sizes, the equations proposed in this study can be used together with analytical packing models (e.g., Chang, Deng, & Yang, 2017; Chang, Wang,

& Ge, 2015; De Larrard, 1999; Yu & Standish, 1988) for an estimation of the limiting void ratios of multi-sized particle packings.

2.2 Measurement Methods for the Limiting Void Ratios and Morphological Characteristics of Sand Particles

The values of e_{min} and e_{max} can be measured by the commonly used procedures specified in standard tests such as those in American Society for Testing and Materials (ASTM D4253-16, 2016; ASTM D4254-16, 2016), or in Japanese Geotechnical Society (2000). Several other methods are also available in literature to determine the two limiting void ratios (Kolbuszewski, 1948; Mulilis, Arulanandan, Mitchell, Chan, & Seed, 1977; Y. Vaid & Negussey, 1988). These methods may provide slightly different values for the two limiting void ratios (Blaker et al., 2015; Tavenas, Ladd, & La Rochelle, 1973).

Particle size can be expressed as its equivalent spherical diameter obtained from the sieve analysis procedure (ASTM D422-63, 2007). The size of particles between the two adjacent sieves is determined by averaging the opening size of two sieves. It is noted that the measured particle size from sieve analysis is only an approximation, since the particles are not spherical and their sizes are in the range between the sieves intervals (Allen, 1997).

Particle shape can be quantified by several methods. In soil mechanics and engineering geology fields, roundness is the most commonly used measure for quantification of particle shape characteristics. However, there is no institutional standard for its measurement.

Roundness (R), as defined by Wadell (1935), is the ratio of the average radius of curvature of the particle edges to the radius of the maximum inscribed circle:

$$R = \frac{\frac{1}{n}\sum_{i=1}^{n} r_i}{r_{ins}} \tag{2.1}$$

where n is the total number of corners, r_i is the radius of circle fitting the i-th corner, and r_{ins} is the radius of inscribed circle, as shown in Fig. 2.1.

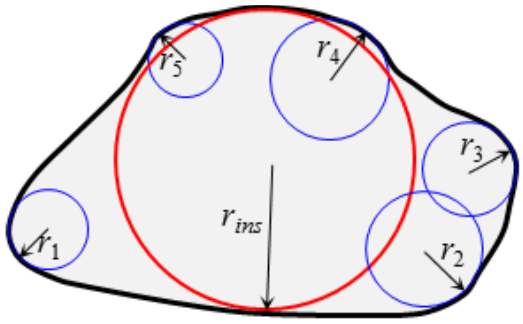

Figure 2.1 Geometric parameters used in the definition of roundness (*R*)

The roundness determined from Eq. (2.1) is not unique because it is obtained based on an arbitrary two-dimensional projected image of the particle, and it is also subjective to the determined size of the circles fitting the corners. Krumbein (1941) and Powers (1953) developed roundness estimation charts consisting of a set of reference particle silhouettes, as shown in Figs. 2.2a and 2.2b. This guide was prepared to facilitate rapid estimation of Wadell's particle roundness through visual comparison. These charts are used in many disciplines including geotechnical engineering, soil science, agriculture, powder engineering, and geology. It is obvious that, similar to particle size, roundness is also an approximate way to describe the shape of particles.

2.3 Database of Particle size, Particle Roundness and Limiting Void Ratios for 26 Types of Uniform Sand

A collection of sand particles can be regarded as uniform sand when its coefficient of uniformity C_u is smaller than 2.5 (Cho et al., 2006; Rouse et al., 2008; Youd, 1973).

Based on this criterion, the data listed in Table 2.1 are for 26 types of uniform sands collected from different locations around the world (Youd, 1973; Edil et al., 1975; Norris, 1977; Cho et al., 2006; Rouse et al., 2008). We also include our own measurements for the Plymouth beach sand, Massachusetts. For the sands listed in Table 2.1, the range of mean particle size is from 0.096 mm to 3.082 mm. The range of particle roundness is from 0.17 to 1. The range of C_u is from 1.1 to 2.4. Fig. 2.3 shows the ranges of D_{50}, R and C_u for the sand samples listed in Table 2.1.

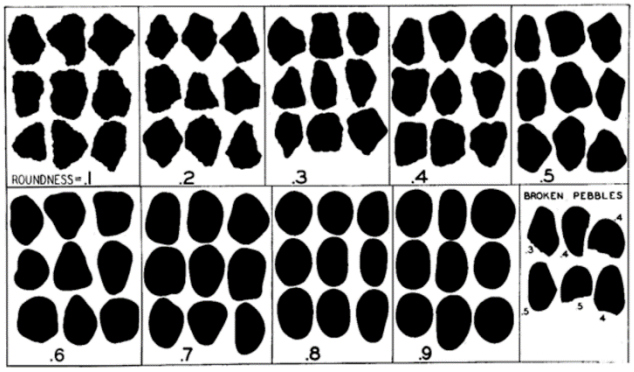

(a) Krumbein's roundness visual chart

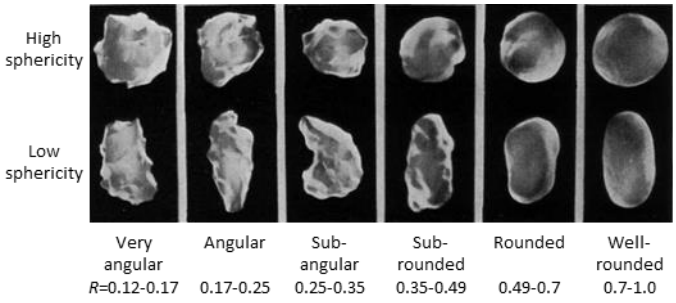

(b) Powers' roundness visual chart

Figure 2.2 Visual comparison charts for roundness: (a) Krumbein (1941); (b) Powers (1953)

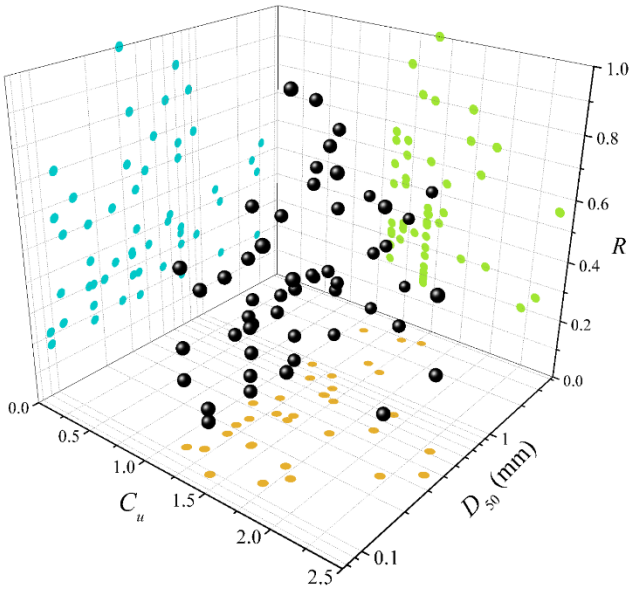

Figure 2.3 The ranges of C_u , D_{50}, and R for the sands selected in this study (Table 2.1)

Table 2.1 Morphological characteristics and the limiting void ratios of selected uniform sands

Sand type	e_{max}	e_{min}	C_u	D_{50}	R	S	Reference	Test method
Crushed basalt	1.42	0.803	1.4	0.096	0.17	-	Youd (1973)	e_{max}: repeated straining in simple shear e_{min}: ASTM D 2049-69
	1.35	0.747	1.4	0.177	0.18	-		
	1.32	0.692	1.4	0.354	0.19	-		
	1.26	0.705	1.4	0.707	0.19	-		
	1.26	0.722	1.4	1.414	0.20	-		
	1.19	0.7	1.4	2.828	0.20	-		
Del Monte White sand	1.203	0.636	1.4	0.096	0.21	-		
	1.082	0.55	1.4	0.177	0.23	-		
	0.971	0.503	1.4	0.354	0.27	-		
Lapis Lustre	0.754	0.46	1.4	2.828	0.44	-		
Monterey sand	0.799	0.458	1.4	0.707	0.34	-		
	0.772	0.469	1.4	1.414	0.39	-		
Ottawa sand	0.83	0.46	1.4	0.177	0.38	-		
	0.772	0.407	1.4	0.354	0.42	-		
	0.704	0.408	1.4	0.707	0.60	-		
Franklin Falls sand	1.08	0.62	1.2	0.714	0.36	0.82	Edil et al. (1975)	e_{max}: the procedure suggested by Kolbuszewski (1948) e_{min}: vibratory densification technique
	1.09	0.63	1.2	0.421	0.35	0.81		
	1.1	0.64	1.2	0.252	0.34	0.81		
Ottawa sand	0.77	0.46	1.2	0.714	0.65	0.87		
	0.82	0.48	1.2	0.421	0.60	0.85		
	0.89	0.53	1.2	0.252	0.52	0.84		
	0.92	0.54	1.2	0.178	0.50	0.83		
	0.92	0.54	1.2	0.126	0.50	0.82		

Table 2.1 (*continued*)

Sand type	e_{max}	e_{min}	C_u	D_{50}	R	S	Reference	Test method
Diagenetic sand	0.723	0.471	1.1	0.922	0.67	0.85	Norris (1977)	e_{min}: ASTM D 2049-69 e_{max}: the procedure suggested by Kolbuszewski (1948)
	0.733	0.486	1.1	0.324	0.64	0.85		
	0.799	0.539	1.1	0.115	0.56	0.83		
Felton Beach sand	0.82	0.54	1.1	2.571	0.49	0.83		
	0.884	0.563	1.1	0.922	0.31	0.82		
	1.002	0.654	1.1	0.324	0.27	0.81		
	1.36	0.856	1.1	0.115	0.22	0.76		
Monterey Coastal dune sand	0.892	0.596	1.1	0.324	0.35	0.8		
	1.012	0.68	1.1	0.115	0.32	0.76		
3P3-Crushed sand	0.95	-	2.2	0.27	0.2	0.7	Cho et al. (2006)	e_{min}: ASTM D1557 e_{max}: ASTM D4254
9C1-crushed sand	0.91	-	2.3	0.52	0.25	0.7		
ASTM 20/30 sand	0.69	-	1.4	0.6	0.8	0.9		
ASTM graded	0.82	0.5	1.7	0.35	0.8	0.9		
Blasting sand	1.025	0.698	1.9	0.71	0.3	0.55		
Glass beads	0.72	0.542	1.4	0.32	1	1		
Jekyll Island sand	1.04	-	1.7	0.17	0.3	0.85		
Margart river sand	0.87	-	1.9	0.49	0.7	0.7		
Nevada sand	0.85	0.57	1.8	0.15	0.6	0.85		
Ottawa F-110	0.848	0.535	1.7	0.12	0.7	0.7		
Ottawa #20/30	0.742	0.502	1.2	0.72	0.9	0.9		
Ponte Vedra sand	1.07	-	1.4	0.18	0.3	0.85		
sandboil sand	0.79	0.51	2.4	0.36	0.55	0.7		
Ticino sand	0.99	0.574	1.5	0.58	0.4	0.8		
Badger sand	0.69	0.49	1.3	0.87	0.81	0.77	Rouse et al. (2008)	e_{min}: ASTM D4253 e_{max}: ASTM D4254
Plymouth Beach sand	0.661	0.42	1.54	3.082	0.54	-	Current study	
	0.693	0.481	1.53	1.304	0.44	-		
	0.72	0.492	1.41	0.601	0.42	-		
	0.902	0.622	1.3	0.326	0.34	-		
	0.97	0.65	1.18	0.212	0.3	-		

Note: C_u = coefficient of uniformity, D_{50} = mean particle size (mm), R = roundness, S = sphericity.

2.4 The Existing Single-variable Equations for Relationship between the Limiting Void Ratios and Particle Size

Rout (2009) and Patra et al. (2010) proposed an empirical equation for relationship between the limiting void ratios and the mean particle size (D_{50}) in the following form:

$$e_{\lim} = b(D_{50})^{\lambda} \tag{2.2}$$

where $e_{\lim}$ is the limiting void ratio (either e_{min} or e_{max}), and b and λ are the model parameters, which take different values for the cases of minimum and maximum void ratios.

Patra et al. (2010) obtained the values of b and λ from test results on uniform and non-uniform sands from 10 rivers in India. The coefficient of uniformity of these sand samples ranges from 1.42 to 9.83. Based on these samples, they determined the following equations for the limiting void ratios:

$$e_{\min} = 0.33(D_{50})^{-0.49};\ e_{\max} = 0.60(D_{50})^{-0.30} \tag{2.3}$$

Fig. 2.4 shows the predicted limiting void ratios by these two equations compared with the test results used by Patra et al. (2010). The coefficient of determination $R^2 = 0.76$ for $e_{\max}$, and $R^2 = 0.85$ for $e_{\min}$.

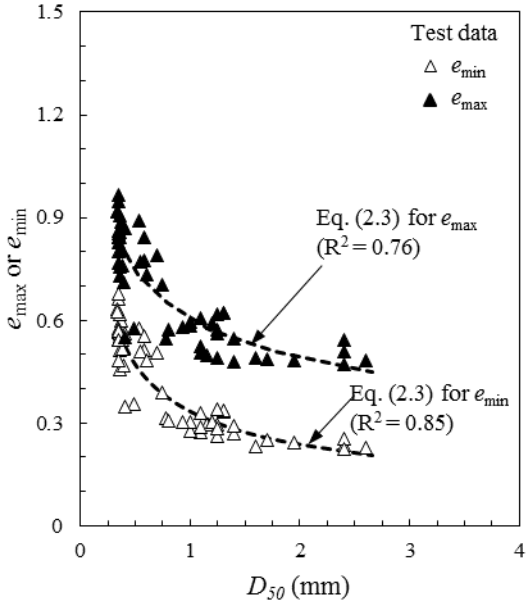

Figure 2.4 Predicted limiting void ratios (dashed lines) versus mean particle size, compared with the measured values on samples with uncontrolled particle gradation (test data from Patra *et al.*, 2010)

In order to filter out the effect of gradation on the limiting void ratios, we use the test data from uniform sands (Table 2.1) and determine a new set of parameters for Eq. (2.2) through the best-fit process. The new values of b and λ are determined and shown in the following equations:

$$e_{\min} = 0.50(D_{50})^{-0.11};\ e_{\max} = 0.79(D_{50})^{-0.13} \quad (2.4)$$

Fig. 2.5 shows the newly predicted limiting void ratios with solid lines using Eq. (2.4). Eq. (2.3) is also used to predict the limiting void ratios for the selected uniform sands and the results are shown with dashed lines. The test data from Table 2.1 are shown by symbols.

It is obvious from Fig. 2.5 that both solid and dashed lines are in poor agreement with the data from Table 2.1. The use of a larger database of uniform sand samples can evaluate the applicability of an empirical equation more accurately. Therefore, Eq. (2.2) proposed by Patra et al. (2010) is shown to not be a suitable predictive equation for the limiting void ratios.

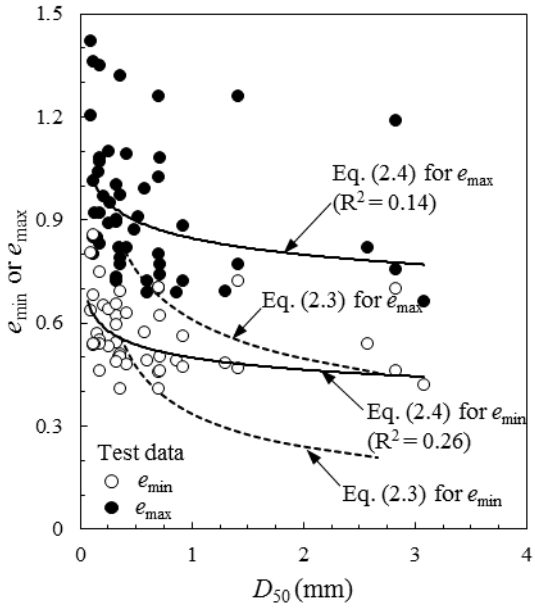

Figure 2.5 Predicted limiting void ratios (solid and dashed lines) versus mean particle size, compared with the measured values from uniform sand samples, listed in Table 2.1

2.5 The Existing Single-variable Equations for Relationship between the Limiting Void Ratios and Particle Roundness

Several researchers have sought to correlate the particle roundness to the limiting void ratios and proposed empirical equations. For example, Shimobe and Moroto (1995) proposed an equation based on the tests results in their database, in which, most samples are uniform sand, but a few samples are mixture of sand and glass beads, which are not uniformly graded. The proposed equation is for maximum void ratio as a function of particle roundness *R:*

$$e_{\max} = 0.64(R)^{-0.354} \tag{2.5}$$

Santamarina and Cho (2004) proposed a hyperbolic equation for relationship between particle roundess *R* and the limiting void ratios, using the test data from Youd (1973), which included eight samples from natural and crushed unform sands. The proposed two equations are as follows:

$$e_{\min} = 0.359 + 0.082(R)^{-1}; e_{\max} = 0.554 + 0.154(R)^{-1} \tag{2.6}$$

Cho et al. (2006) proposed a simple linear equation for relationship between particle roundess *R* and the limiting void ratios, using 19 samples for $e_{\max}$ and 16 samples for $e_{\min}$ from natural and crushed uniform sands. The derived equations are as follows:

$$e_{\min} = 0.80 - 0.34R \;\; ; \qquad e_{\max} = 1.30 - 0.62R \tag{2.7}$$

Rouse et al. (2008) used the same hyperbolic equation proposed by Santamarina and Cho (2004), but the database they used were larger than that used by Santamarina and Cho (2004). In addition to the test data from Youd (1973), their database includes additional samples of sand, glass beads, and gravel. It is comprised of 66 samples for $e_{\max}$ and 46 samples for $e_{\min}$. All samples are uniformly graded. The derived equations are:

$$e_{\min} = 0.433 + 0.051(R)^{-1}; \quad e_{\max} = 0.615 + 0.107(R)^{-1} \qquad (2.8)$$

Fig. 2.6 shows the prediction from Eqs. (2.5) to (2.8) in dashed lines. The prediction results are compared with the test data shown by symbols. The predictions are in good agreement with the measured void ratios.

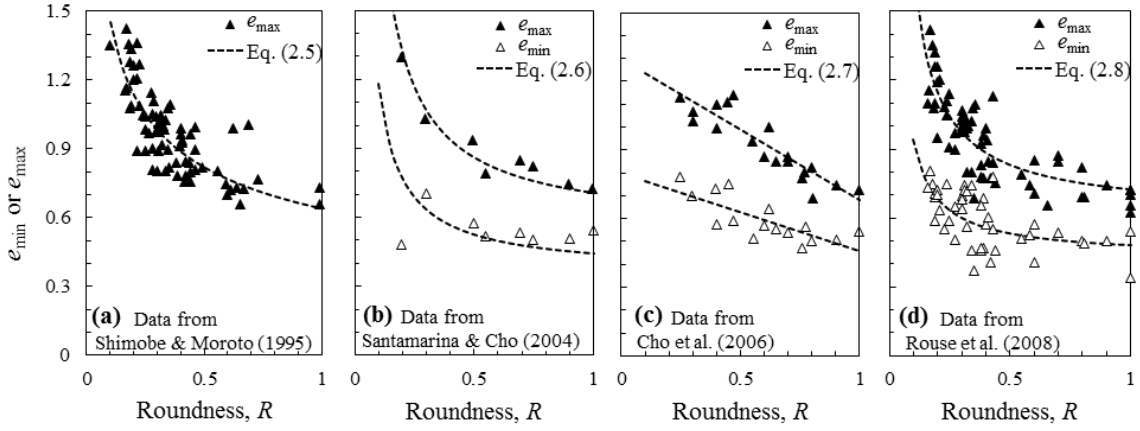

Figure 2.6 Predicted limiting void ratios versus particle roundness from four different empirical equations. Test data from Shimobe and Moroto (1995), Santamarina and Cho (2004), Cho et al. (2006), and Rouse et al. (2008)

We use the data in Table 2.1 to determine new sets of coefficients for Eqs. (2.5) to (2.8) through best-fit process. The following new coefficients are determined.

Using the equation proposed by Shimobe and Moroto (1995) in Eq. (2.5), the following equations are determined:

$$e_{\min} = 0.43(R)^{-0.28} \quad ; e_{\max} = 0.65(R)^{-0.36} \qquad (2.9)$$

Using the equations proposed by Santamarina and Cho (2004) and Rouse et al. (2008) in Eqs. (2.6) and (2.8), the following equations are determined:

$$e_{\min} = 0.39 + 0.06(R)^{-1} \; ; e_{\max} = 0.56 + 0.13(R)^{-1} \qquad (2.10)$$

The linear equation by Cho et al. (2006) in Eq. (2.7) takes new coefficients as follows:

$$e_{\min} = 0.71 - 0.33R \ ; \qquad e_{\max} = 1.24 - 0.71R \qquad (2.11)$$

Eqs. (2.9) to (2.11) are plotted in Fig. 2.7 with solid lines. For comparison, the test data from Table 2.1 are shown by symbols and Eqs. (2.5) to (2.8) are plotted with dashed lines. The deviation between the solid lines and dash lines are due to the difference in the selected databases. The discrepancy is larger for Eq. (2.7) proposed by Cho et al (2006), whereas the discrepancies for the other three equations are relatively small. Comparing the coefficients of determination R^2 shows that predictions by Eq. (2.10) have the best agreement with the measured void ratios.

Fig. 2.7 shows that the single-variable equations with roundness as a predictive variable are suitable to predict void ratio from a larger database, whereas Fig. 2.5 showed that the single-variable equations with particle size as a predictive variable are not suitable.

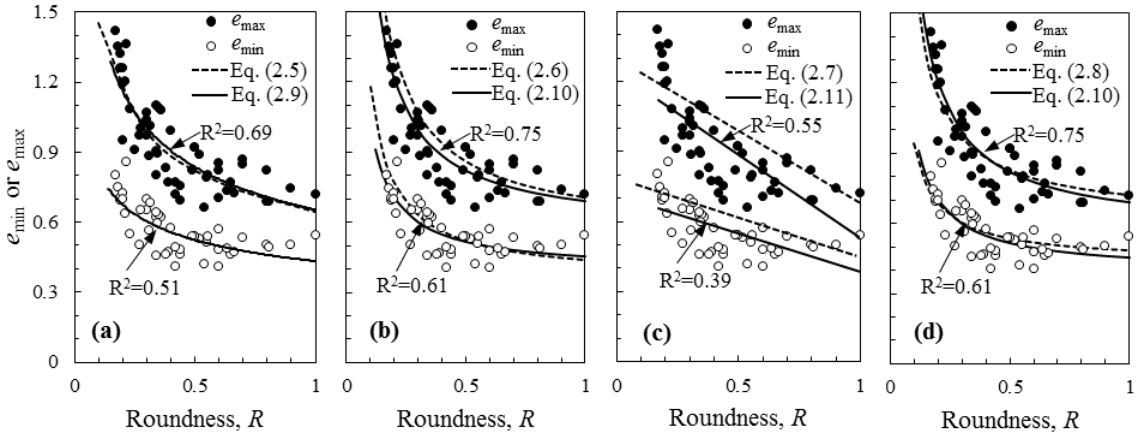

Figure 2.7 Limiting void ratios versus particle roundness predicted by new equations, compared with the measured void ratios of uniform sands, listed in Table 2.1. (The R^2 in each figure corresponds to the two solid lines)

2.6 Proposed Multi-variable Equation for the Limiting Void Ratio as a Function of Particle Roundness and Particle Size

In this section, we construct a multi-variable equation in which the limiting void ratio (e_{min} or e_{max}) is the outcome variable, and mean particle size (D_{50}) and roundness (R) are two predictor variables. To check the plausibility of considering the limiting void ratio as the outcome variable, we perform multi-variable analysis on the data in Table 2.1 and consider (e_{min}, R, D_{50}) and (e_{max}, R, D_{50}) as two sets of three-random variables.

In statistics, covariance is a measure of the joint variability of two random variables, which indicate the strength of dependency between the two random variables. We investigate the dependencies between any two of the three random variables, i.e. between (e_{lim}, R), (e_{lim}, D_{50}) and (R, D_{50}), by studying the covariance between these two random variables.

The covariance matrix Γ of a three-random-variable set (**x**, **y**, **z**) is defined as:

$$\Gamma = \begin{bmatrix} Cov(\mathbf{x},\mathbf{x}) & Cov(\mathbf{x},\mathbf{y}) & Cov(\mathbf{x},\mathbf{z}) \\ Cov(\mathbf{y},\mathbf{x}) & Cov(\mathbf{y},\mathbf{y}) & Cov(\mathbf{y},\mathbf{z}) \\ Cov(\mathbf{z},\mathbf{x}) & Cov(\mathbf{z},\mathbf{y}) & Cov(\mathbf{z},\mathbf{z}) \end{bmatrix} \tag{2.12}$$

This matrix provides the covariance between any two of the three random variables. The covariance $Cov(\mathbf{x},\mathbf{y})$ between random variables **x** and **y** is defined by:

$$cov(\mathbf{x},\mathbf{y}) = \frac{\sum_{i=1}^{n}(x_i - \bar{x})(y_i - \bar{y})}{n-1} \tag{2.13}$$

where $\bar{x}$ and $\bar{y}$ are the average of **x** and **y** variables, respectively. n is the sample size. Note that the covariance matrix is symmetric with respect to its main diagonal; i.e., Cov (**x**, **y**) = Cov (**y**, **x**), Cov (**x**, **z**) = Cov (**z**, **x**), and Cov (**y**, **z**) = Cov (**z**, **y**).

The covariance matrices, Γ_{min} of the variable set (e_{min}, R, D_{50}) and Γ_{max} of the variable set (e_{max}, R, D_{50}), are computed using Eqs. (2.12) and (2.13) for the data listed in Table 1. The variables **x**, **y**, and **z** are assigned to the limiting void ratio, particle roundness R, and mean particle size D_{50}, respectively. The calculated covariance matrices are:

$$\Gamma_{min} = \begin{bmatrix} 0.0112 & -0.013 & -0.017 \\ -0.013 & 0.0409 & 0.0004 \\ -0.017 & 0.0004 & 0.5701 \end{bmatrix}; \quad \Gamma_{max} = \begin{bmatrix} 0.0393 & -0.03 & -0.032 \\ -0.03 & 0.0425 & 0.004 \\ -0.032 & 0.004 & 0.5158 \end{bmatrix} \tag{2.14}$$

In both matrices, the covariance between the limiting void ratio and roundness or mean particle size is negative, indicating an increase of limiting void ratios with a decrease of particle roundness or mean particle size. The magnitude of the covariance indicates the strength of dependency between the two variables. However, this value is not easy to interpret. Therefore, it is common to use the correlation coefficient (i.e. the normalized version of covariance), which ranges from 0 to 1, where 0 indicates complete independency, and 1 indicates complete dependency between the two variables.

The correlation coefficient $\rho(\mathbf{x}, \mathbf{y})$ of any two random variables can be calculated as:

$$\rho(\mathbf{x}, \mathbf{y}) = \frac{Cov(\mathbf{x},\mathbf{y})}{\sigma(\mathbf{x})\sigma(\mathbf{y})} \tag{2.15}$$

where $\sigma(\mathbf{x})$ and $\sigma(\mathbf{y})$ are the standard deviations of variables **x** and **y**, respectively.

The correlation matrix Ω of the three-variable set (**x**, **y**, **z**) is defined as:

$$\Omega = \begin{bmatrix} \rho(\mathbf{x},\mathbf{x}) & \rho(\mathbf{x},\mathbf{y}) & \rho(\mathbf{x},\mathbf{z}) \\ \rho(\mathbf{y},\mathbf{x}) & \rho(\mathbf{y},\mathbf{y}) & \rho(\mathbf{y},\mathbf{z}) \\ \rho(\mathbf{z},\mathbf{x}) & \rho(\mathbf{z},\mathbf{y}) & \rho(\mathbf{z},\mathbf{z}) \end{bmatrix} \tag{2.16}$$

The correlation matrices Ω_{min} and Ω_{max} are calculated using Eqs. (2.15) and (2.16) for the data listed in Table 2.1, based on the covariance matrices Γ_{min} and Γ_{max}. The variables **x**, **y**, and **z** are assigned to the limiting void ratio, particle roundness R, and mean particle size D_{50}, respectively. The calculated correlation matrices are:

$$\Omega_{min} = \begin{bmatrix} 1 & -0.626 & -0.213 \\ -0.626 & 1 & 0.003 \\ -0.213 & 0.003 & 1 \end{bmatrix}; \quad \Omega_{max} = \begin{bmatrix} 1 & -0.742 & -0.227 \\ -0.742 & 1 & 0.027 \\ -0.227 & 0.027 & 1 \end{bmatrix} \quad (2.17)$$

where Ω_{min} and Ω_{max} are the correlation matrices of the set (e_{min}, R, D_{50}) and the set (e_{max}, R, D_{50}), respectively.

In both matrices, the correlation coefficients between the limiting void ratio and particle roundness or between the limiting void ratio and particle size are negative, indicating an increase of the limiting void ratios with a decrease of particle roundness or mean particle size. The magnitude of the correlation coefficient indicates the degree of correlation between two random variables. For the minimum void ratio, the magnitude of correlation coefficient between R and e_{min} is 0.626, which is stronger than that between D_{50} and e_{min} , which is 0.213. Similarly, the magnitude of correlation coefficient between e_{max} and R is 0.742, while it is 0.227 between e_{max} and D_{50}. Therefore, the correlation between R and the limiting void ratios is stronger than that between D_{50} and the limiting void ratios.

The magnitude of the correlation coefficient between R and D_{50} is 0.003 in the correlation matrix for minimum void ratio Ω_{min} and is 0.027 in the correlation matrix for maximum void ratio Ω_{max}. These small values indicate that particle roundness and particle size have very weak correlation. Therefore, R and D_{50} can be considered as two

independent variables. This independency was also supported by Das (2007), who found that there is no correlation between R and D_{50} for sands from six different sources.

Since the variables, R and D_{50}, are correlated with the limiting void ratio, but uncorrelated with each other, the limiting void ratio can be considered as the outcome variable and R and D_{50} can be considered as two independent predictive variables. We propose a multi-variable equation that expresses the limiting void ratio (e_{max} or e_{min}) as a function of the two variables R and D_{50}. The proposed two-variable equation is as follows:

$$e_{\lim} = c_{\lim} \cdot R^{\alpha_{\lim}} \cdot D^{\beta_{\lim}} \tag{2.18}$$

where R and D are both dimensionless. The normalized particle size D is defined as $D = D_{50}/D_{ref}$, with D_{ref} = 1mm. The magnitude of D and D_{50} are identical. The subscript *lim* represents that the variable is associated with either $e_{\min}$ or $e_{\max}$. The coefficient $c_{\lim}$ is a dimensionless constant, which is equal to the limiting void ratio of 1 mm sized sphere packing (i.e. R = 1 and D_{50} = 1). The constants $\alpha_{\lim}$ and $\beta_{\lim}$ are two model parameters that replicate the effects of R and D_{50} on the limiting void ratio. The three constants $c_{\lim}$, $\alpha_{\lim}$ and $\beta_{\lim}$ take different values for the two different cases of $e_{\min}$ or $e_{\max}$.

The constants of Eq. (2.18), $\alpha_{\lim}$, $\beta_{\lim}$, and $c_{\lim}$ are determined for the limiting void ratio ($e_{\min}$ or $e_{\max}$) by a multi-variable regression analysis, using the experimental data listed in Table 2.1. The equations are as follows:

$$e_{\min} = 0.413 \cdot R^{-0.291} \cdot D^{-0.043} \tag{2.19}$$

$$e_{\max} = 0.619 \cdot R^{-0.372} \cdot D^{-0.048} \tag{2.20}$$

Eqs. (2.19) and (2.20) are plotted as two curved surfaces in a three-dimensional (D, R, e_{lim}) space as shown in Fig. 2.8. The coefficient of multiple determination R^2 is 0.62 for $e_{\min}$ and 0.76 for $e_{\max}$.

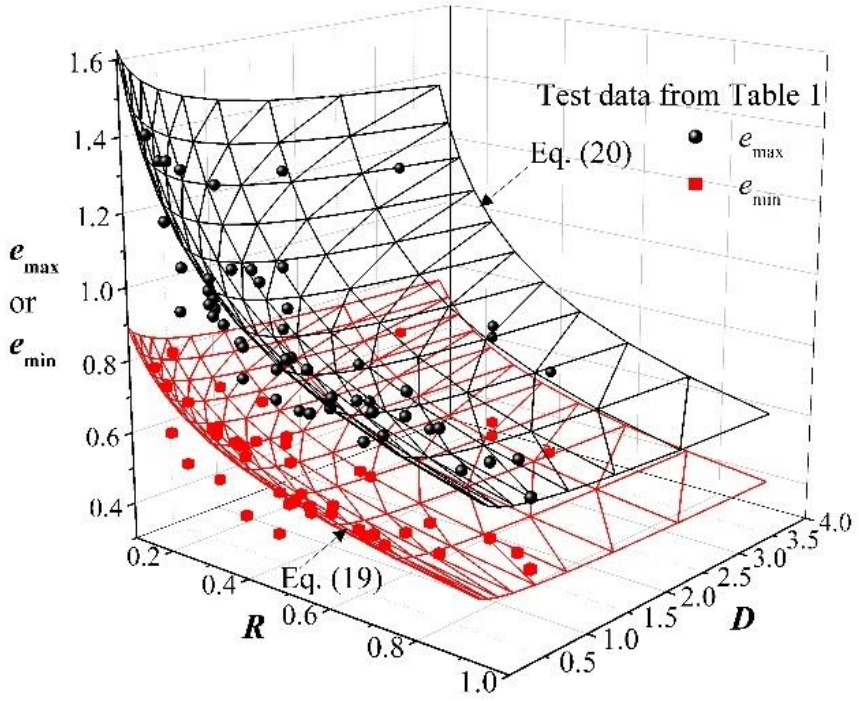

Figure 2.8 Three-dimensional representation of Eq. (2.19) for $e_{\max}$ and Eq. (2.20) for $e_{\min}$ in linear space

Eq. (2.18) can be linearized by taking logarithm of both sides of the equation:

$$\log e_{\text{lim}} = \alpha_{\text{lim}} \log R + \beta_{\text{lim}} \log D + \log c_{\text{lim}} \tag{2.21}$$

Thus, Eqs. (2.19) and (2.20) can be expressed as follows:

$$\log e_{\min} = -0.291 \log R - 0.043 \log D + \log 0.413 \tag{2.22}$$

$$\log e_{\max} = -0.372 \log R - 0.048 \log D + \log 0.619 \tag{2.23}$$

Eqs. (2.22) and (2.23) are identical to Eqs. (2.19) and (2.20), although they are expressed in different forms. Eqs. (2.22) and (2.23) are plotted in a three-dimensional logarithmic space (log D, log R, log e) in Fig. 2.9.

In Eqs. (2.22) and (2.23), the magnitude of $\alpha_{\lim}$, associated with R, is much larger than the magnitude of $\beta_{\lim}$, associated with D (i.e., 0.291 > 0.043 and 0.372 > 0.048). This indicates that particle roundness (R) has more influence than particle size (D) on the value of limiting void ratio.

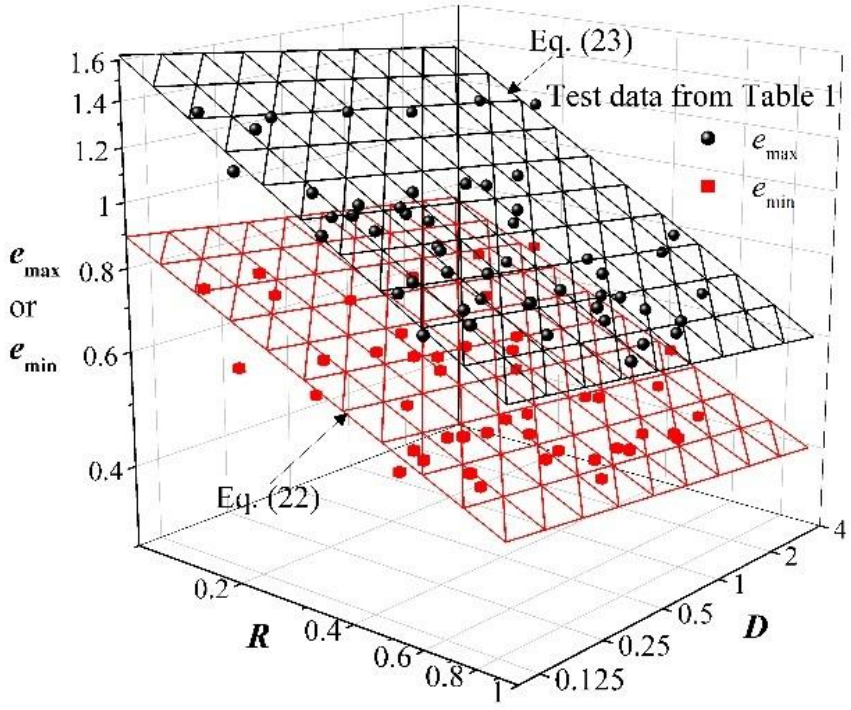

Figure 2.9 Three-dimensional representation of Eq. (2.22) and Eq. (2.23) in logarithmic space.

To depict the the coupled effects of particle roundness and particle size on limiting void ratios, the two planes in the three-dimensional space calculated from Eqs. (2.22) and (2.23) are projected onto the plane of limiting void ratios versus D. The contour lines for various values of roundness R are plotted for e_{min} and e_{max} in Fig. 2.10(a) and 2.10(b), respectively. The corresponding experimental data (from Table 2.1) are shown by symbols. It can be seen from these two graphs that the limiting void ratios decrease with an increase

of particle size, regardless of the particle roundness. For a given particle size, the limiting void ratios decrease with the increase of particle roundness.

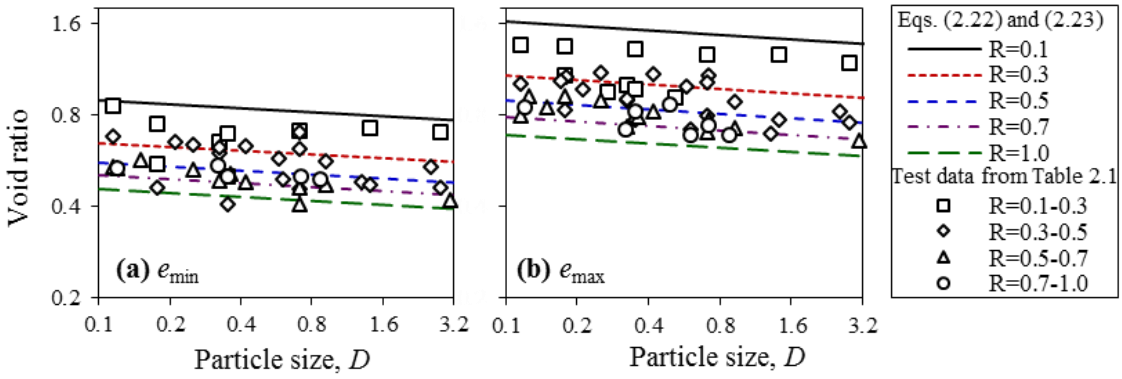

Figure 2.10 Projection of Eqs. (2.22) and (2.23) on the 2-D plane of limiting void ratios versus mean particle size

Similarly, the two three-dimensional planes shown in Fig. 2.8 are projected onto the plane of limiting void ratios versus R, with the contour lines for various values of D shown in Fig. 2.11(a) and 2.11(b). The experimental data from Table 2.1 are shown with symbols. It can be seen from these graphs that the limiting void ratios decrease with an increase of roundness. For a given particle roundness, the limiting void ratios decrease with the increase of particle size. The width of the particle size variation band in Fig. 2.11 is much smaller than the particle roundness variation band in Fig. 2.10. This indicates that the limiting void ratios are strongly correlated with particle roundness, whereas they are weakly correlated with particle size.

2.7 Comparison between the Proposed Multi-variable and the Existing Single-Variable Equations

The following examples illustrate the advantage of the proposed multi-variable equation over the single-variable equations.

2.7.1 Compared to the Single-variable Equation with Particle Size as the Predictive Variable

First, we compare the performance of the proposed multi-variable equation with Eq. (2.4) that uses particle size as the single predictive variable. It has been shown in Fig. 2.5 that Eq. (2.4) is in poor agreement with the measured data and is not a suitable predictive equation. Conversely, the proposed multi-variable equation is a suitable predictive equation based on its high value of R^2, which is 0.62 for $e_{\min}$ and 0.76 for $e_{\max}$ as shown in Fig. 2.8. A comparison of the measured and predicted results between the proposed multi-variable equation and the single-variable equation for angular sand is shown in Fig. 2.12. The two dashed lines for $e_{\min}$ and $e_{\max}$ are computed from the single-variable equation (Eq. (2.4)). The predicted values from the multi-variable equations (Eqs. (2.19) and (2.20)) are shown with cross symbols. The two zones for $e_{\min}$ and $e_{\max}$ between the solid lines are computed from the multi-variable equations (Eqs. (2.19) and (2.20)) for particle roundness of R = 0.17 and 0.20. The multi-variable equations are in better agreement with the test results compared to the single-variable equation.

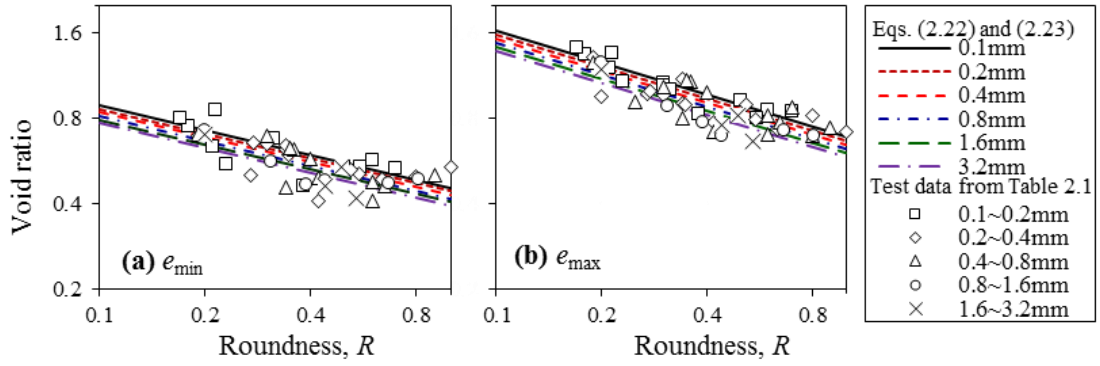

Figure 2.11 Projection of Eqs. (2.22) and (2.23) on the 2-D plane of limiting void ratios versus particle roundness

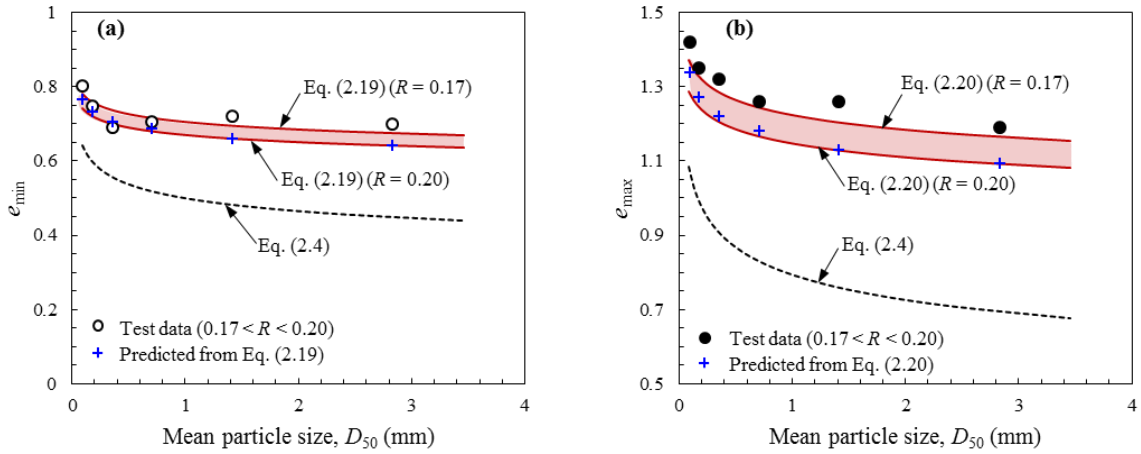

Figure 2.12 Comparison of the performance of the proposed multi-variable Equations (2.19) and (2.20), with the results from single-variable Equation (2.4) for samples with particle roundness (*R*) ranging from 0.17 to 0.20 (Test data selected from Table 2.1)

2.7.2 Compared to the Single-variable Equation with Particle Roundness as the Predictive Variable

Among the three single-variable equations, which take particle roundness as a predictive variable (Eqs. (2.9), (2.10), and (2.11)), Eq. (2.10) has the highest value of R^2, as shown in Fig. 2.7. Here, we compare the performance of the multi-variable equations

(Eqs. (2.19) and (2.20)) with the single-variable equation (Eq.(2.10)). It is noted that R^2 alone cannot be used as a meaningful comparison of models with different numbers of independent variables (Richard, 1994). For a meaningful comparison between the two models, we use the Mean Absolute Percentage Error (MAPE).

For the comparison, two groups of samples are selected from Table 2.1 based on their mean particle size: (a) small particle size samples with D_{50} ranging from 0.075 to 0.15 mm, and (b) large particle size samples with D_{50} ranging from 1.0 to 3.5 mm.

The predictions of $e_{\min}$ using the single-variable equation Eq. (2.10) are shown by the dashed lines in Fig. 2.13a and 2.13b. The test data are shown with symbols. It can be seen in Fig. 2.13a that Eq. (2.10) overpredicts the test results for samples with large particles, whereas Eq. (2.10) underpredicts the test results for samples with small particles (Fig. 2.13b).

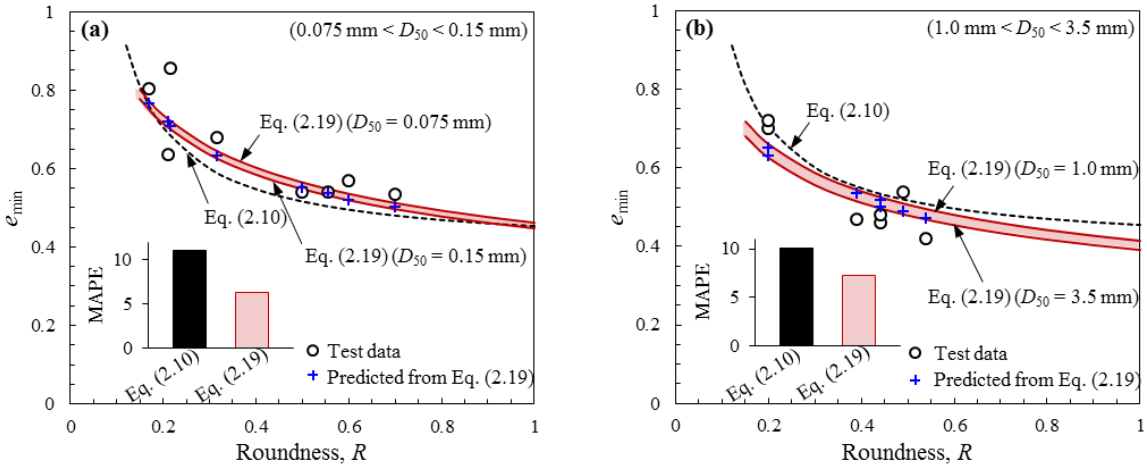

Figure 2.13 Comparison of the predicted and measured minimum void ratios between the multi-variable equation (Eqs. (2.19)) and the single-variable equation (Eq. (2.10)): (a) for samples of small particle sizes, and (b) for samples of large particle sizes (Test data from Table 2.1)

The proposed multi-variable equation, Eq. (2.19), can predict minimum void ratio based on particle roundness for various values of mean particle size. The predicted values from Eq. (2.19) are shown with cross symbols. The two solid lines in Fig. 13a are predicted based on mean particle sizes of 0.075 mm and 0.15 mm. The shaded zone between the two solid lines represents the predicted range for small particle size samples. In Fig. 2.13b, the shaded zone between the two solid lines for 1.0 mm and 3.5 mm represents the range of predicted values for large particle size samples. The predictions from the multi-variable equation tend to fit the experimental data better than predictions from the single-variable equation (Eq. (2.10)). The mean absolute percentage error (MAPE) between predictions and measurments are also shown for each relationship in Fig. 2.13.

The predictions of $e_{\max}$ using the single-variable equation (Eq. (2.10)) are shown by the dashed lines in Fig. 2.14a and 2.14b. The predicted values from Eq. (2.20) are shown with cross symbols. The test data for these two groups of sand samples are shown with symbols. It can be seen from Fig. 2.14a and Fig. 2.14b that Eq. (2.10) underpredicts the test results for samples with small particles, while it overpredicts the test results for samples with large particles.

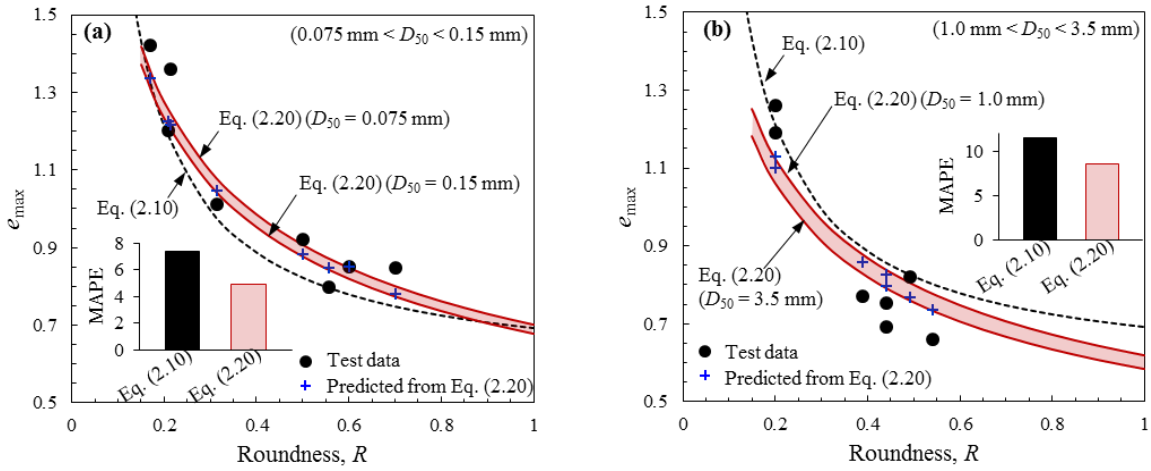

Figure 2.14 Comparison of the predicted maximum void ratio from multi-variable equation (Eq. (2.20)) and single-variable equation (Eq. (2.10)): (a) for samples with small particles, and (b) for samples with large particles (Test data selected from Table 2.1)

Fig. 2.14a shows the predicted range of maximum void ratio for samples with small particles. Fig. 2.14b shows the same range for samples with large particles. The prediction from the multi-variable equation tends to fit the experimental data better than the single-variable equation. The mean absolute percentage error (MAPE) from predictions are also shown for each equation in Fig. 2.14.

From the comparisons of the mean absolute percentage error (MAPE) in all cases shown in Fig. 2.13 and Fig. 2.14, the percentage error is 7.4% to 11.5% for single-variable equations and 4.9% to 8.5% for multi-variable equations. In terms of void ratio, the difference between the two models is in the range of 0.03 to 0.08. This corresponds to approximately 5% to 20% improvement in the prediction of relative density when using the proposed multi-variable equations, which leads to a notable difference in the estimated strength and compressibility of soils (U.S. Navy, 1982).

It is noted that the proposed multi-variable equations can only be used to predict the limiting void ratios of uniform sands. Although the granular soil encountered in geotechnical engineering are more likely to be widely graded, it is not uncommon to encounter uniform sand, for example, the clean sand deposit in the Northern Lower-Peninsula region of Michigan in the United States (Muszynski, 2006). The limiting void ratios predicted by the multi-variable equations are useful in the design of compaction specifications for a natural sand or for an imported backfill of a retaining structure in order to properly support heavy loads. The predicted limiting void ratios can also be used in the recently developed models to estimate the compressibility of sands (Meidani, Chang, & Deng, 2017).

Obviously, the proposed equations cannot be applied directly to the soil with a broader range of particle sizes. However, as indicated in many analytical packing models, the limiting void ratio of a multi-sized packing can be derived from the limiting void ratios of mono-sized packings (Chang et al., 2015; Chang et al., 2017; De Larrard, 1999; Dewar, 1999; Furnas, 1931; Goltermann, Johansen, & Palbøl, 1997; Kwan, Chan, & Wong, 2013; Powers, 1968; Stovall, de Larrard, & Buil, 1986; Westman & Hugill, 1930; Yu & Standish, 1988). In general, a multi-sized packing is treated as a mixture of 10-12 size classes of particles. The limiting void ratio of a mono-sized packing for each size class particles is required as input data for the analytical packing models in order to predict the limiting void ratio of the multi-sized particle packing. Therefore, the multi-variable equation developed in this study can serve as an aid to provide the input data for the analytical packing models and obtain an estimation of the limiting void ratios of multi-sized particle packings.

2.8 Conclusions

Experimental data have shown that morphological characteristics of sand particles (i.e. particle size and particle roundness) affect the minimum and maximum void ratios of uniform sands. In this paper, we proposed two multi-variable equations to predict minimum and maximum void ratios of uniform sands from their particle size and particle shape.

The statistical analysis on this dataset showed that the correlation between particle roundness and the limiting void ratios of uniform sands is relatively strong (correlation coefficient is 0.62 to 0.75). The correlation between particle size and the limiting void ratios of uniform sands is, however, weak (correlation coefficient is 0.21 to 0.23). There is nearly no correlation between particle size and particle roundness for uniform sands selected in this study (correlation coefficient is less than 0.03). Therefore, particle size and particle roundness were considered as two independent predictive variables, and the limiting void ratios were considered as the dependent outcome variables.

The multi-variable statistical analysis showed that the relationship between the limiting void ratios and the two morphological characteristics of sand particles are two parallel planes in a three-dimensional logarithmic space made of particle size, particle roundness and limiting void ratio.

The comparison between the experimental results and predicted values showed:

(1) The single-variable equation with particle size as a predictive variable is not suitable for application. The multi-variable equation is a suitable predictive equation.

(2) The single-variable equation with particle roundness as a predictive variable was in reasonable agreement with the measured data. However, it over-predicted the

limiting void ratios for samples with large particles, but under-predicted the limiting void ratios for samples with small particles. The prediction error of the proposed multi-variable equation is reduced to about 2/3 of the prediction error of the single-variable equation. In terms of predicted void ratio, the difference between the two models is in the range of 0.03 - 0.07. This corresponds to approximately 5% - 20% in relative density, which leads to a notable difference in the estimated strength and compressibility of sands.

The proposed multi-variable equations can be directly used to predict the limiting void ratios of uniform sands encountered in geotechnical engineering projects. The predicted limiting void ratios are useful in the design of compaction specifications in order to properly support heavy loads. The multi-variable equation developed in this study can be used together with an analytical packing model (e.g. Chang et al., 2017, 2015; De Larrard, 1999; Yu & Standish, 1988) for a better estimation of the limiting void ratios of multi-sized particle packings.

CHAPTER 3

THE ROLE OF MORPHOLOGIC INDICES ON THE VARIATION OF LIMITING VOID RATIOS FOR UNIFORM SANDS[2]

New material parameters for sands, morphologic indices, are introduced to represent the relationship between particle size (*D*) and shape (*R*), and these indices are used to predict the limiting void ratios of sands from particular sites. In previous regression analyses, we determined a surface in the 3D space made up of three variables: the limiting void ratio, *D* and *R*, where the two variables *D* and *R* are considered to be independent. In this study, however, it has been shown that *D* and *R* have a well-defined relationship for sand samples from the same site, where particles tend to have the same genesis and transport history. Due to the existence of a relationship between *D* and *R*, the function, which best-fit the data in the 3D space, cannot be determined using the commonly used regression method. The orthogonal regression method is adopted to derive equations for the relationships among the three variables: limiting void ratio, *D* and *R*. The derived equations demonstrate the role of morphologic indices on the variation of limiting void ratios for uniform sands.

List of Notation

The following symbols are used in this chapter:

a_1, a_2, a_3, a_4 coefficients to define a 3D-line

[2] This chapter has been published as a standalone paper: Chang, C. S., Meidani, M., & Deng, Y. (2018). Role of morphologic indices on the variation of limiting void ratios for uniform sands. *Géotechnique Letters*, *8*(4), 248–255.

c_1, m_1	particle-shape influence parameters
c_2, m_2	particle-size influence parameters
c_3, m_3	morphologic indices
C_u	coefficient of uniformity
D	particle size
e^{lim}	limiting void ratios
e^{min}, e^{max}	minimum and maximum void ratios
R	particle roundness

3.1 Introduction

The limiting void ratios (e^{lim}), i.e. minimum and maximum void ratios, are fundamental properties of granular soils, which are related to various aspects of mechanical behavior, such as compressibility, shear strength and permeability of granular soils (Aberg, 1992; Bobei et al., 2009; Cubrinovski & Ishihara, 2002; Fuggle et al., 2014; Meidani et al., 2017; Miura et al., 1997; Peters & Berney, 2010; Selig & Ladd, 1973).

The limiting void ratios of granular soils are significantly influenced by gradation, particle size, and particle shape. To eliminate the complex effects of gradation on limiting void ratios, several researchers focused on uniform sands and proposed empirical equations to predict the limiting void ratios from particle size (Cubrinovski & Ishihara, 2002; Miura et al., 1997; Patra et al., 2010; Rout, 2009), or from particle roundness (Russell, 1937; Inman, 1953; Pettijohn & Lundahl, 1943; Balazs & Klein, 1972). It is noted that the main measures for particle shape are sphericity (a measure of sphere similarity), roundness (a measure of how much the corners and edges have been worn away) and surface texture (a

measure of small-scale features) (Barrett, 1980; Diepenbroek et al., 1992). The roundness of a clastic particle, reflecting its abrasion history, is more popularly used in the literature for describing the influence of particle shape on limiting void ratios.

Recently, a multi-variable equation was proposed by Chang et al. (2018), incorporating the coupling effects of particle size and roundness on the limiting void ratio of uniform sands. In this multi-variable equation, the particle size (D) and particle roundness (R) are two independent predictor variables. The independence of D and R was verified based on the poor correlation (0.07), computed from a database of uniform sands collected from sites widely dispersed around the world. Fig. 3.1 shows the lack of correlation between these two variables. The lack of correlation between D and R was also supported by Das (2007) based on his study on sands from different sources.

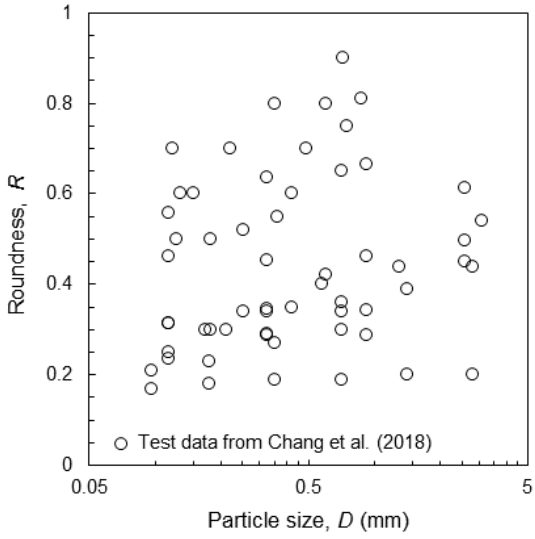

Figure 3.1 Correlation between particle size (*D*) and roundness (*R*) for uniform sands (data from Chang *et al.*, 2018)

However, in the field of sedimentology, many investigators have advocated *D* and *R* are related. From the geological point of view, the value of *R* is dependent on the genesis and the transport history of particles. The original particle roundness (*R*) is referred to as the particle geometry by genesis. During particle transport, the original *R* is modified by various abrasion processes such as attrition, chipping, grinding, wearing and flaking. The intensity of abrasion depends not only on the particle mineralogy but also on the transport history that causes particle-to-particle collisions. Abrasion has a lesser effect on small particles because their mass is so slight that the force of impact against one another is not sufficient enough to produce rounding. On the contrary, abrasion has a greater effect on large particles of greater mass because their force of impact against one another causes sufficient grinding and wearing to produce rounding. This physical phenomenon has been explored by Pettijohn and Lundahl (1943) for beach sand. In nearly every sample of sand examined by them, the coarsest fraction was much better rounded than the smallest size.

Based on the experimental observation for particles having the same genesis and transport history, Pettijohn (1957) stated that "There is a marked correlation between roundness and size. The larger sizes of any given sample are much better rounded than the smaller grades." They found that the relationship can be expressed by $R = mD^n$. The same relationship was observed for the sands of the Mississippi River (Russell and Taylor, 1937), of the St. Peter sandstone (Wadell, 1935), and other sands of various locations (Balazs and Klein, 1972; Inman, 1953; Inman et al., 1966; Ramez and Mosalamy, 1969).

Therefore, from experimental evidences, for the soil samples from the same site, a relationship between *D* and *R* exists because soil particles from the same site are likely to have the same genesis and transport history. The lack of relationship shown in Fig. 1 can

be explained by the fact that soil samples were not separated into specific locations, hence these samples do not have the same genesis and transport history.

In this study, the multi-variable relationship among limiting void ratio, *D* and *R* for sand samples collected from specific sites is investigated. The well-defined relationship between *D* and *R* is first verified and morphologic indices are introduced to represent the relationship between these two variables. Then, multi-variable equations are proposed through regression analysis. The proposed equations are validated by experimental data and the role of morphologic indices on the variation of limiting void ratio is demonstrated.

3.2 Morphologic Indices for Sand Particles

In order to study the relationship among particle size, shape, and limiting void ratios for same-site sands, sand samples from nine different sites are selected. Each sample was sieved into several size fractions. For each of the selected sand samples, the measured e^{min} and e^{max}, and the measured mean values of *D* and *R* of each size fraction are listed in Table 3.1. The mean value of *R* is obtained from *n* particles of each size fraction: *n* is typically greater than 50 as reported in the literature (e.g. Russell and Taylor, 1937; Pettijohn and Lundahl, 1943; Inman, 1953; Ramez and Mosalamy, 1969; Balazs and Klein, 1972; Youd, 1973; Edil et al., 1975; Norris, 1977).

A linear relationship between log *R* and log *D* is adopted and plotted to fit the experimental data for various types of sand as shown in Fig. 3.2. It is noticed that each data point in Fig. 3.2 typically represents the average roundness of at least 50 particles. For example, in the data reported by Pettijohn and Lundahl (1943), each point represents 350

particles as shown in Fig. 3.3. The six data points in Fig. 3.3 actually represent the average of 2100 data points.

Note that, the average coefficient of determination (R^2) for all lines in Fig. 3.2 is high (i.e. 0.96), which indicates a good fit between these lines and data points. However, it may not be considered as a rigorous proof of the linear relationship between log *R* and log *D*, because the average data points for some soils in Fig. 3.2 cover only a limited number of particle sizes (e.g. only three points for Coastal dune sand, Inman et al., 1966). Nevertheless, the linear relationship is adopted because of its simplicity for characterizing the morphology of soil particles.

The linear relationship can be defined by two parameters: the slope m_3 and the intercept c_3, as shown in Fig. 3.2. The slope m_3 is an index reflecting the change of particle roundness due to abrasion history, whereas the intercept c_3 is an index reflecting the particle roundness by genesis. We define these two parameters as morphologic indices of the material.

Table 3.1 Morphological characteristics and limiting void ratios of selected uniform sands

Sand type	e^{max}	e^{min}	C_u	D	R	S	Test method	Reference
Crushed basalt	1.42	0.803	1.4	0.096	0.17	-	e^{max}: repeated straining in simple shear e^{min}: ASTM D2049-69 (ASTM, 1969)	Youd, (1973)
Crushed basalt	1.35	0.747	1.4	0.177	0.18	-		
Crushed basalt	1.32	0.692	1.4	0.354	0.19	-		
Crushed basalt	1.26	0.705	1.4	0.707	0.19	-		
Crushed basalt	1.26	0.722	1.4	1.414	0.2	-		
Crushed basalt	1.19	0.7	1.4	2.828	0.2	-		
Del Monte White sand	1.203	0.636	1.4	0.096	0.21	-		
Del Monte White sand	1.082	0.55	1.4	0.177	0.23	-		
Del Monte White sand	0.971	0.503	1.4	0.354	0.27	-		
Franklin Falls sand	1.08	0.62	1.2	0.714	0.36	0.82	e^{max}: the procedure suggested by Kolbuszewski (1948) e^{min}: vibratory densification technique	Edil et al., (1975)
Franklin Falls sand	1.09	0.63	1.2	0.421	0.35	0.81		
Franklin Falls sand	1.1	0.64	1.2	0.25	0.34	0.81		
Ottawa sand	0.77	0.46	1.2	0.714	0.65	0.87		
Ottawa sand	0.82	0.48	1.2	0.421	0.6	0.85		
Ottawa sand	0.89	0.53	1.2	0.252	0.52	0.84		
Ottawa sand	0.92	0.54	1.2	0.178	0.5	0.83		
Ottawa sand	0.92	0.54	1.2	0.126	0.5	0.82		
Diagenetic sand	0.723	0.471	1.1	0.922	0.665	0.853	e^{min}: ASTM D2049-69 (ASTM, 1969) e^{max}: the procedure suggested by Kolbuszewski (1948)	Norris, (1977)
Diagenetic sand	0.733	0.486	1.1	0.324	0.636	0.845		
Diagenetic sand	0.799	0.539	1.1	0.115	0.556	0.826		
Felton Beach sand	0.82	0.54	1.1	2.571	0.491	0.831		
Felton Beach sand	0.884	0.563	1.1	0.922	0.309	0.82		
Felton Beach sand	1.002	0.654	1.1	0.324	0.274	0.806		
Felton Beach sand	1.36	0.856	1.1	0.115	0.215	0.755		
Bear River sand	0.843	0.544	1.1	2.571	0.451	0.81		
Bear River sand	0.888	0.588	1.1	0.922	0.287	0.806		
Bear River sand	1.26	0.814	1.1	0.115	0.251	0.766		
Ottawa sand	0.72	0.51	1.2	0.75	0.75	0.9	Not Reported	Thomann, (1990)
Ottawa sand	0.84	0.57	1.1	0.22	0.7	0.8		
Ottawa sand	0.9	0.59	1.9	0.13	0.6	0.6		
Plymouth Beach sand	0.661	0.42	1.5	3.082	0.54	-	e^{min}: ASTM D4253-00 (ASTM, 2006a) e^{max}: ASTM D4254-00 (ASTM, 2006b)	Chang et al., (2018)
Plymouth Beach sand	0.693	0.481	1.5	1.304	0.44	-		
Plymouth Beach sand	0.72	0.492	1.4	0.601	0.42	-		
Plymouth Beach sand	0.902	0.622	1.3	0.326	0.34	-		
Plymouth Beach sand	0.7	0.65	1.2	0.212	0.3	-		

3.3 Multi-collinear Regression

In a previous analysis (Chang et al., 2018), the limiting void ratio e^{lim} (either e^{min} or e^{max}) is considered as a function of the other two independent variables *D* and *R*. The function is a surface in the space of (*R*, *D*, e^{lim}) as shown in Fig. 3.4a. The coefficients describing the surface was determined by a multi-variable regression analysis, for a database of uniform sands from various sites. However, when the sand samples are selected from a particular site, the two predictor variables, *D* and *R*, have a well-defined relationship. Consequently, the function of e^{lim} is not a surface, rather it is a line in the (*R*, *D*, e^{lim}) space, as shown in Fig. 3.4b. In this case, the commonly used multi-variable regression analysis does not provide stable solutions. This is called the problem of multi-collinearity in regression analysis. An alternative mathematical method, e.g. the orthogonal regression analysis (Atieg & Watson, 2003), needs to be adopted to determine the regression coefficients.

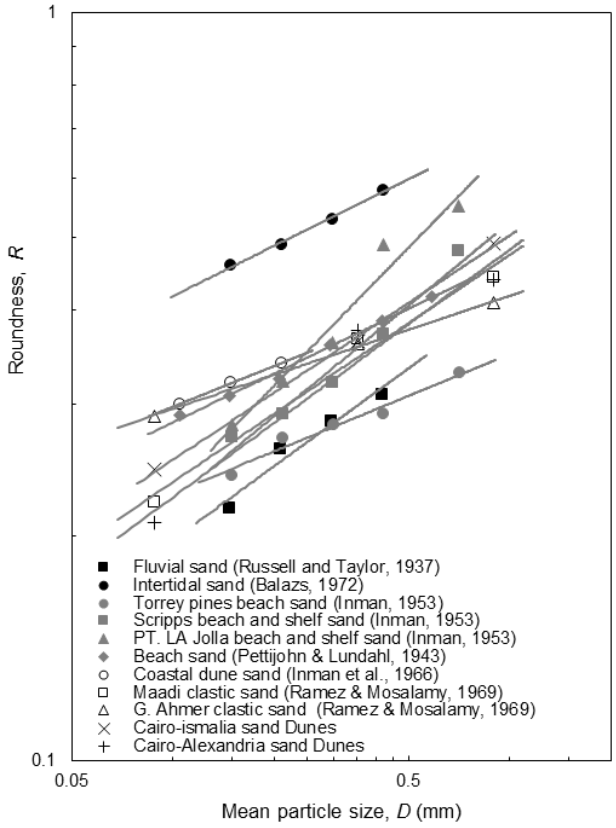

Figure 3.2 Existing relationships between particle size (*D*) and roundness (*R*) for uniform sands with different genesis and/or transportation history

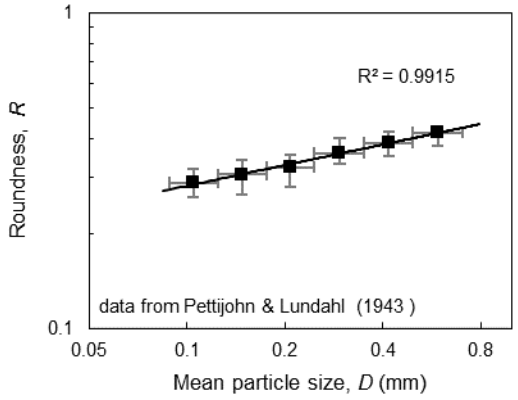

Figure 3.3 Relationship between particle size (*D*) and roundness (*R*) for Beach Sand (data from Pettijohn & Lundahl, 1943)

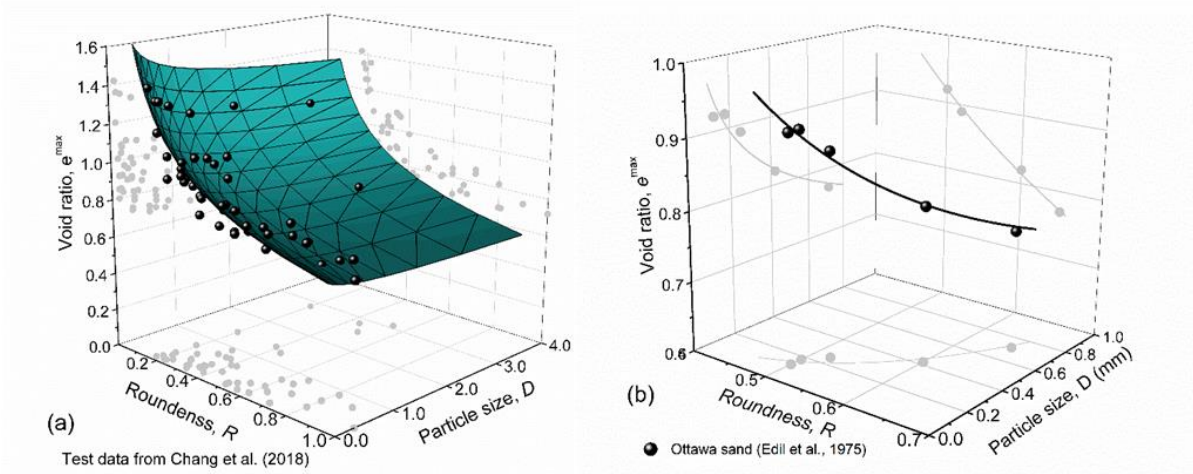

Figure 3.4 Functional relationship in the three-dimensional space (R, D, e^{lim}): (a) a surface function, (b) a line function

Assuming a line in (x, y, z) space passing through a reference point (x_0, y_0, z_0), this line can be expressed by Eq. (3.1) as follows:

$$\frac{x-x_0}{v_x} = \frac{y-y_0}{v_y} = \frac{z-z_0}{v_z} \tag{3.1}$$

Let the reference point $(x_0,\ y_0, z_0)$ has the coordinates $(a_2,\ a_4, 0)$, and let coefficient $a_1 = v_z/v_y$ and coefficient $a_3 = v_z/v_x$. Therefore Eq. (3.1) can be rearranged to give:

$$z = a_1\, a_2 + a_1 y\,; \quad z = a_3\, a_4 + a_3 x \tag{3.2}$$

The 3D-line can be, instead of Eq. (3.1), more conveniently expressed by two separate equations in Eq. (3.2). It requires four constants, a_1, a_2, a_3, a_4, to define the 3D-line. The orthogonal regression method can then be used to determine the four coefficients, a_1, a_2, a_3, a_4, from the test data for sand samples taken from a particular site.

By letting the three axes (x, y, z) be represented by ($\log R$, $\log D$, $\log e^{lim}$), the two separate equations in Eq. (3.2) can then be written as:

$$\log e^{lim} = \log c_1 + m_1 \log R \tag{3.3}$$

$$\log e^{lim} = \log c_2 + m_2 \log D \tag{3.4}$$

These two equations describe the 3D-line in the space of ($\log R$, $\log D$, $\log e^{lim}$). Eq. (3.3) is the projection of the 3D-line on the ($\log R$, $\log e^{lim}$) plane, defined by the particle-shape influence parameters c_1, m_1. Eq. (3.4) is the projection of the 3D-line on the ($\log D$, $\log e^{lim}$) plane, defined by the particle-size influence parameters c_2, m_2. A regression analysis is needed to determine whether the 3D-line is a good model.

The four coefficients, a_1, a_2, a_3, a_4, are obtained from orthogonal regression analysis (Atieg and Watson, 2003) for both e^{min} and e^{max} cases for 9 uniform sands. Using Eq. (3.2), the four influence parameters, c_1, c_2, m_1, m_2, in Eq. (3.3) and Eq. (3.4) can be related to the four coefficients, a_1, a_2, a_3, a_4, by:

$$m_1 = a_1, m_2 = a_3, \log c_1 = a_2 a_1, \log c_2 = a_4 a_3 \tag{3.5}$$

The computed four influence parameters, c_1, c_2, m_1, m_2, are listed in Table 3.2.

The 3-D lines for 9 uniform sands, using the influence parameters listed in Table 3.2, are plotted in the space of ($\log R$, $\log D$, $\log e^{lim}$) in Fig. 3.5. The measured values are plotted by symbols. The average coefficient of determination R^2 is 0.92, indicating the 3D-lines have a good fit to the data points in the space.

The 3D-lines projected on the ($\log R$, $\log e^{lim}$) plane (Fig. 3.6) and the 3D-lines projected on the ($\log D$, $\log e^{lim}$) plane (Fig. 3.7) are compared with measured data for e^{min} and e^{max}.

Table 3.2 Parameters obtained from regression analysis for sands listed in Table 3.1

Soil type	Ref.	Maximum void ratio						Minimum void ratio					
		m_1	c_1	m_2	c_2	m_3	c_3	m_1	c_1	m_2	c_2	m_3	c_3
Crushed basalt	Youd, (1973)	-1.01	0.24	-0.05	1.26	0.05	0.19	-0.68	0.23	-0.03	0.71	0.05	0.19
Del Monte White sand	Youd, (1973)	-0.85	0.32	-0.16	0.82	0.19	0.33	-0.92	0.15	-0.18	0.41	0.19	0.33
Ottawa sand	Edil et al., (1975)	-0.66	0.58	-0.11	0.75	0.17	0.68	-0.62	0.35	-0.10	0.45	0.17	0.68
Franklin Falls sand	Edil et al., (1975)	-0.32	0.78	-0.02	1.07	0.05	0.37	-0.56	0.35	-0.03	0.61	0.05	0.37
Bear River sand	Norris, (1977)	-0.79	0.40	-0.13	0.93	0.17	0.34	-0.78	0.26	-0.13	0.60	0.17	0.34
Diagenetic sand	Norris, (1977)	-0.56	0.57	-0.05	0.71	0.09	0.68	-0.75	0.35	-0.06	0.46	0.09	0.68
Felton Beach sand	Norris, (1977)	-0.63	0.47	-0.16	0.91	0.25	0.36	-0.59	0.32	-0.15	0.59	0.25	0.36
Ottawa sand	Thomann, (1990)	-1.10	0.53	-0.13	0.69	0.12	0.79	-0.73	0.42	-0.08	0.50	0.12	0.79
Plymouth Beach sand	Chang et al., (2018)	-0.71	0.41	-0.15	0.74	0.21	0.43	-0.79	0.25	-0.17	0.50	0.21	0.43

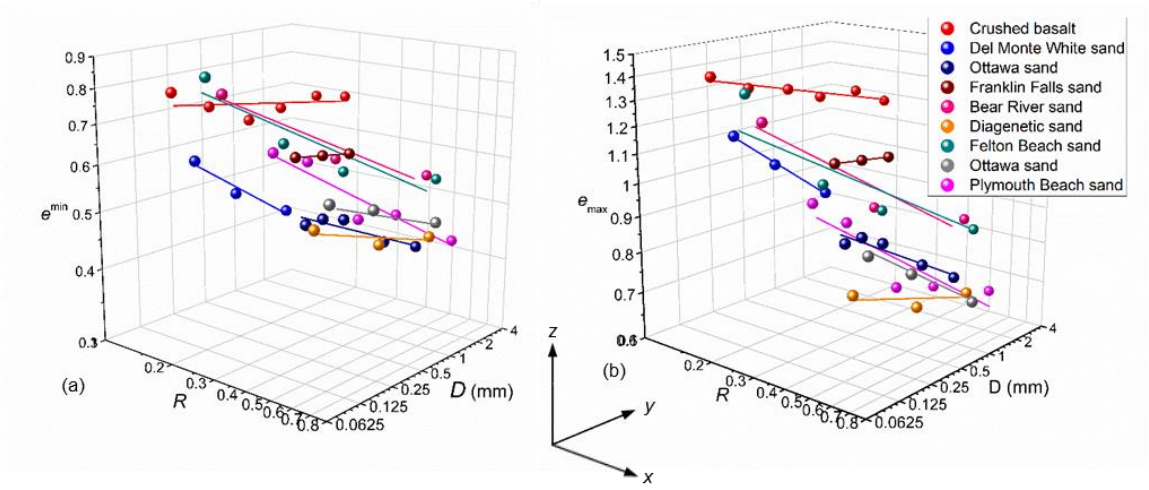

Figure 3.5 Linear correlation among *R*, *D*, and e^{lim} illustrated for 9 different sands in 3-D logarithmic space

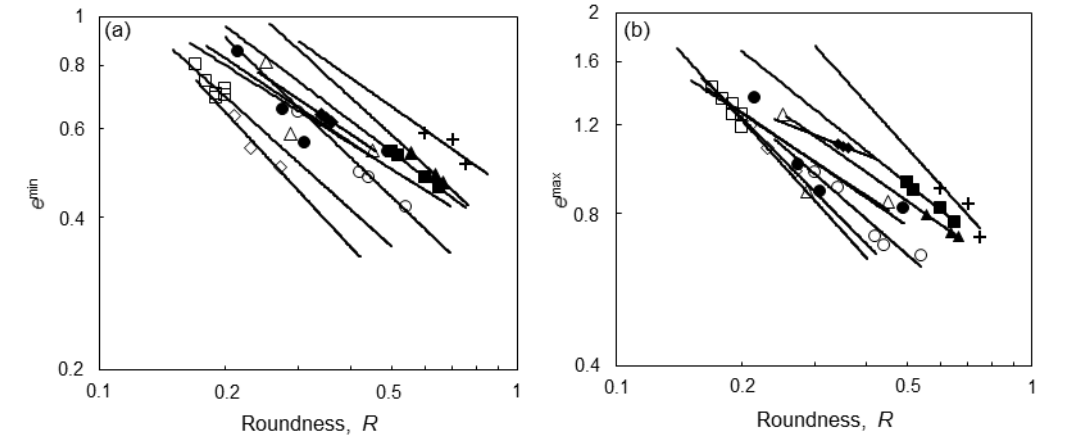

□	Crushed basalt (Youd, 1973)	◇	Del Monte White sand (Youd, 1973)	△	Bear River sand (Norris, 1977)
■	Ottawa sand (Edil et al., 1975)	◆	Franklin Falls sand (Edil et al., 1975)	●	Felton Beach sand (Norris, 1977)
▲	Diagenetic sand (Norris, 1977)	+	Ottawa sand (Thomann, 1990)	○	Polymouth Beach sand (Chang et al., 2018)

Figure 3.6 Correlation between e^{lim} and particle roundness (*R*) in logarithmic space, shown for 9 different sands

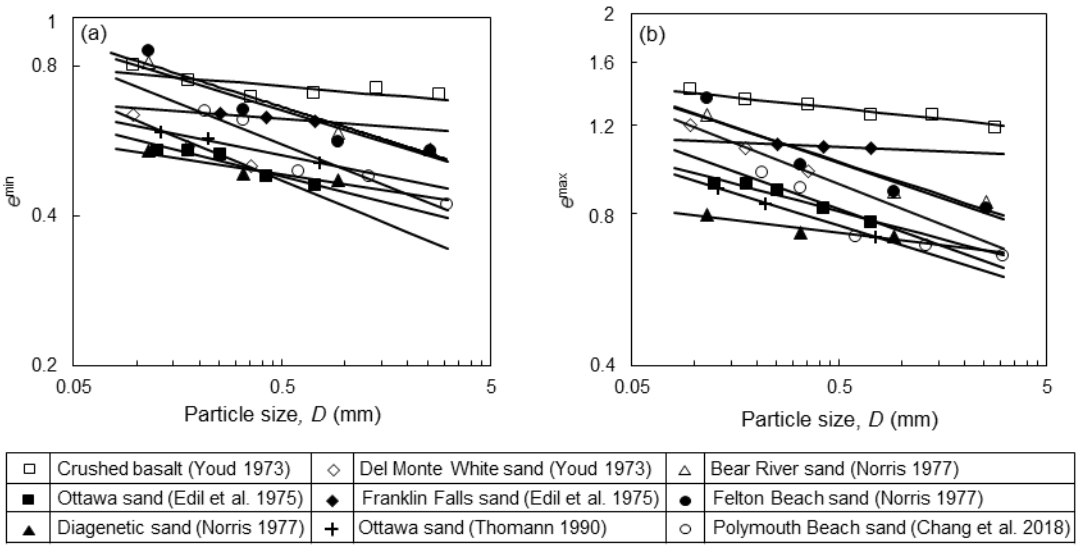

Figure 3.7 Correlation between e^{lim} and particle size (D) in logarithmic space, for 9 different sands

3.4 The Role of Morphologic Indices on Limiting Void Ratios

The characteristics of multi-collinearity (Chatterjee et al., 2000) indicates that the projection of the 3D-line on the third plane, i.e., (log R, log D) plane, should accurately predict the relationship between D and R. The projected line on this plane is given by:

$$\log R = \log c_3 + m_3 \log D \tag{3.6}$$

where the two morphologic indices c_3 and m_3 can be obtained from the four regression coefficients, a_1, a_2, a_3, a_4, by the following equations:

$$m_3 = a_3/a_1,\ log c_3 = (a_3 a_4 - a_1 a_2)/a_1 \tag{3.7}$$

Using Eq. (3.5) and Eq. (3.7), the values of the two indices c_3 and m_3 can be directly related to the four influence parameters, m_1, c_1, m_2, c_2, by:

$$m_3 = m_{2/} m_1;\ c_3 = (c_2/c_1)^{1/m_1} \tag{3.8}$$

These two indices are computed for 9 different sands and listed in Table 3.2. The 3D-lines projection on the (log R, log D) plane are shown in Fig. 3.8, compared with

measured data. The validity of Eq. (3.8) is verified by the good agreement between the computed and measured data.

Using Eq. (3.8), the relationship $m_2 = m_1 m_3$ is obtained. This shows, how and to what degree, the influence parameters of particle size or shape is dependent on the morphologic indices. From the test results in Fig. 3.6. The slopes of lines (i.e. m_1) are nearly parallel for both e^{min} and e^{max}, with a mean value of m_1 = -0.75 and a small deviation. Fig. 3.9a shows a plot of m_3 versus m_1. The typical ranges are from -0.6 to -0.9 for m_1, from 0.05 to 0.23 for m_3, and from -0.03 to -0.17 for m_2. The ratio m_3/m_2 is shown as solid line in Fig. 3.9b.

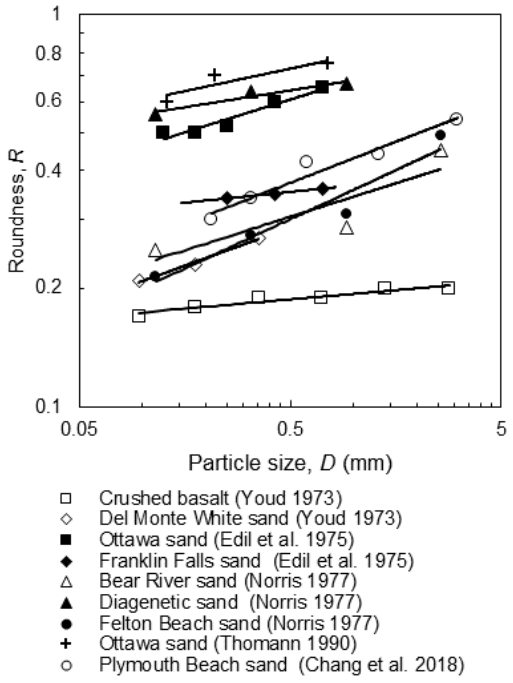

Figure 3.8 Correlation between particle roundness (*R*) and particle diameter (*D*) in logarithmic space, for 9 different sands

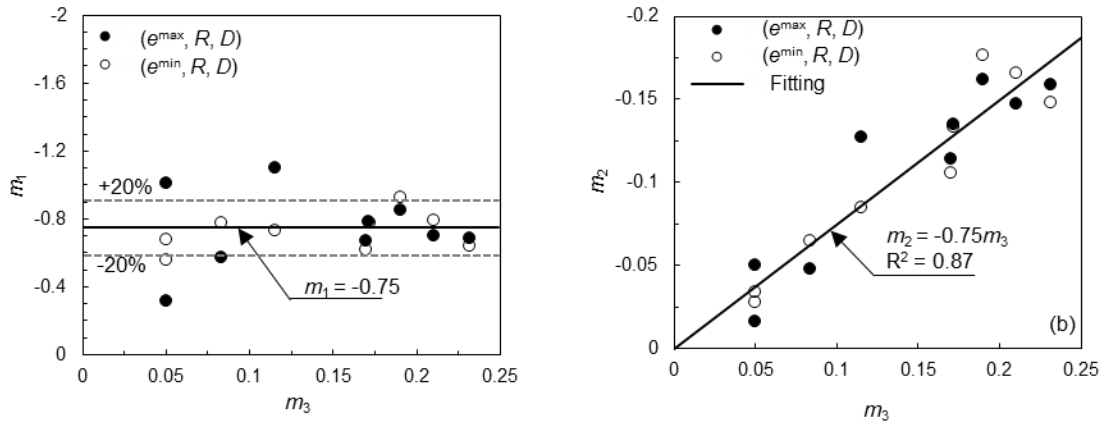

Figure 3.9 (a) The influence parameter m_1 versus the morphologic index m_3, (b) the influence parameter m_2 versus the morphologic index m_3

For the example of e^{min} of Crushed Basalt in Fig. 3.8 and Table 3.2, the slope is flat ($m_3 = 0.05$), which means the particle shape changes negligibly with respect to particle size. This behavior of negligible change in particle shape is similar to the fractal hypothesis reported by Sammis et al. (1987) from their observation of geological fault gouges. Using the first part of Eq. (3.8) with measured m_1= -0.68 and $m_3 = 0.05$, it predicts a small value of m_2 = -0.03, which means e^{min} of a uniformly graded Crushed Basalt changes negligibly with respect to particle size. The predicted value is in good agreement with the tests results by Youd (1973). The change of void ratio with respect to particle size is important in the study of mechanics in granular breakage (Einav, 2007; Gang Li et al., 2015).

For the example of e^{min} of Plymouth Beach Sand in Fig. 3.8 and Table 3.2, the slope is steep with the index $m_3 = -0.21$, which means the particle shape changes significantly with respect to particle size, from large sub-round particles to small angular particles. Using the first part of Eq. (3.8) with measured m_1= -0.79 and $m_3 = -0.21$, it

predicts a large value of $m_2 = -0.17$. This means the e^{min} of a uniformly graded Plymouth Beach Sand changes significantly with particle size.

Using the second part of Eq. (3.8), given $c_3 = 0.19$ and $c_1 = 0.23$ for Crushed Basalt, it predicts $c_2 = 0.71$. Given $c_3 = 0.43$ and $c_1 = 0.25$ for Plymouth Beach Sand, Eq. (3.8) predicts $c_2 = 0.50$. The predicted values are in good agreement with the measured values.

Fig. 3.10a shows a plot of c_3 versus c_2. If $m_1$is approximated to be -0.75 (the mean value), the morphologic index c_3 versus the ratio c_2/c_1 is shown as solid line in Fig. 3.10b, which can be used for approximate estimation. The typical ranges are from 0.2 to 0.8 for c_3, from 0.4 to 1.2 for c_2, and from 0.15 to 0.78 for c_1.

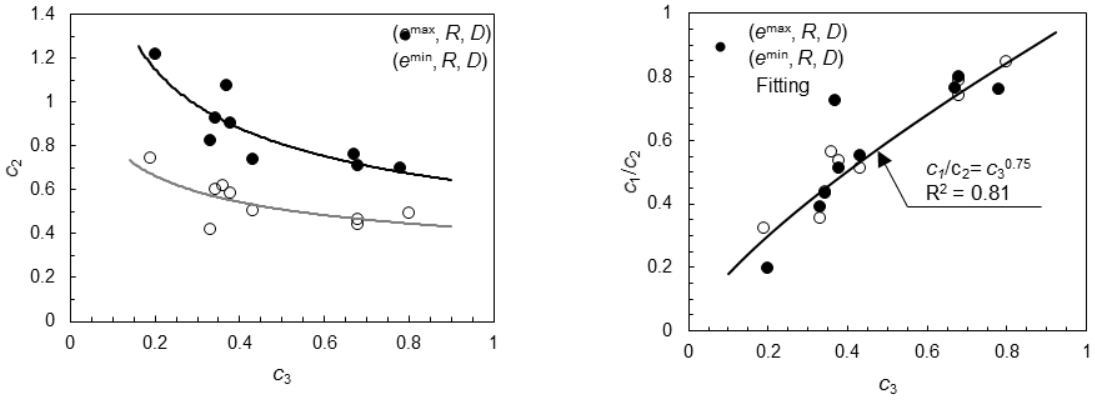

Figure 3.10 (a) The influence parameter c_2 versus the morphologic index c_3, (b) The influence parameter c_1/c_2 versus the morphologic index c_3

The above-mentioned equations are only applicable to predict the limiting void ratio for uniform sands. Although most soils encountered in geotechnical engineering are widely graded, it is not infrequent to encounter deposited clean uniform sands, for example, in the Northern Lower-Peninsula region of Michigan in the United States (Muszynski,

2006). The derived equations in this study are relevant to geotechnical practice dealing with natural deposits of clean sand.

Furthermore, as indicated in many analytical packing models, the limiting void ratio of a multi-sized packing can be derived from the limiting void ratios of mono-sized packings (Chang et al., 2017; De Larrard, 1999; Stovall et al., 1986; Yu & Standish, 1988). Therefore, the derived equations in this study can be used with an analytical packing model to estimate the limiting void ratios of a well-graded soil.

3.5 Conclusions

Orthogonal regression analysis is performed on sand samples from specific sites to find the relationships among the variables of limit void ratio, D and R. The multi-variable equations derived from the regression analysis show that the relationship among the limiting void ratio, D, and R is a straight line in a logarithmic space of the three variables.

The derived equations show that morphologic indices are controlling factors for the variation of limiting void ratios, which is validated by the experimental data for 9 uniform sands. Future work is needed to study the morphologic indices for soils with various genesis and transport history, such as residual soils, sedimentary deposits, river sands, and fractured rockfills.

CHAPTER 4

A PARTICLE PACKING MODEL FOR SAND-SILT MIXTURES WITH THE EFFECT OF DUAL-SKELETON[3]

The study of particle packing models for binary mixtures, is important in the field of granular materials, from both theoretical and practical perspectives. A number of particle packing models have been developed for predicting packing density (or void ratio) of a binary mixture. However, the measured results and the predicted values do not always agree with each other, particularly in the range of fines content between 25%-50%. It is postulated herein that the discrepancies between the measured results and the predicted values are primarily due to the incorrect assumptions used in the existing models. In the existing models, the packing density is determined from one of the following two assumed mechanisms of particle mixing: (1) the mixed packing has a dominant large-particle skeleton and the small particles fill the voids of the large-particle skeleton, or (2) the mixed packing has a dominant small-particle skeleton and the large particles are embedded in the small-particle skeleton. It is obvious that the first assumed mechanism is only applicable for mixtures with low fines content, whereas the second assumed mechanism is only applicable to mixtures with high fines content. Therefore, the predictions from existing models are unsuitable for mixtures with medium fines content, such as a mixture of fines content between 25%-50%. In this study, a 3-D discrete element simulation is carried out to show that, for a mixture of medium fines content, the packing structure has a dual-

[3] This chapter has been published as a standalone paper: Chang, C. S., & Deng, Y. (2017). A particle packing model for sand–silt mixtures with the effect of dual-skeleton. *Granular Matter, 19*(4), 80.

skeleton, which is neither dominated by a large nor small-particle skeleton. Then, we postulate that, in the mixed packing, both mechanisms can take place: filling of small particles and embedment of large particles. The concepts of "dual-skeleton index" and "index size" are proposed to account for the interactive effects of filling and embedment. Based on this postulation, we develop an analytical method, which has the capability of predicting minimum void ratio for sand-silt mixtures with various fines contents. The developed model is then validated by the experimental results obtained from 16 types of sand-silt mixtures.

4.1 Introduction

Packing of particulate materials has been broadly studied for design and manufacturing in many fields, such as mineral, metallurgical, pharmaceutical, and geotechnical industries (Holtz, Kovacs, & Sheahan, 2011; Kelly & Spottiswood, 1982; Muzzio, Shinbrot, & Glasser, 2002; Rhodes, 2008). Two approaches have been adopted for modelling particle packing: (1) computer simulation and (2) analytical method. A brief summary of these two approaches is given below.

With the rapid advances in computer technology, the method of computer simulation has progressed significantly. Computer simulation has been applied by many researchers for studying geometric packing properties of polydisperse granular material (e.g., Dutt and Elliott, 2014; Jalali and Li, 2007; Ogarko and Luding, 2013; Voivret et al., 2007; Yi et al., 2012, etc.) and for studying the effect of polydispersity on the mechanical response of granular material (e.g., Luding, 2004; Shaebani et al., 2012; Wiącek and Molenda, 2014, etc.). Many studies have been devoted specifically to the geometric

properties and the bulk mechanical properties of binary mixtures (e.g., An, 2013; Desmond and Weeks, 2014; Fuggle et al., 2014; Kumar et al., 2016; Martin and Bouvard, 2004; Skrinjar and Larsson, 2004; Ueda et al., 2011, etc.).

The computer simulation results resemble that obtained from experimental tests on particle packing. However, due to the wide range of particle sizes in real granular soil, the size of a large particle can be easily several hundred times larger than that of a small particle. Thus, a soil specimen of ordinary size, which has a wide range of particle sizes, generally involves an enormous number of particles ($>10^9$), which exceeds the capacity of a standard computer. As a consequence, the computer simulation method becomes impracticable to simulate real particle size for soil with wide gradations.

Moreover, as pointed out by Dodds (1980), the results from computer simulations cannot give any insight into the particle packing without the aid of some interpretive model. Therefore, the analytical modeling is useful from the point of view of engineering application, although it may be empirical to some degree.

Development of analytical equations has been pioneered by Westman and Hugill (1930), and Furnas (1931) for the prediction of the packing density of binary mixtures. They have identified two effects due to the mixing of particles: (1) the filling effect, which takes place when small particles are filled into the large-particle skeleton, and (2) the embedment effect, which occurs when large particles are embedded into the small-particle matrix. However, their equations are limited to the extreme case of very large particle size ratio mixtures (i.e. the size of large particles is substantially greater than the size of small particles).

In the sixties, considerable progress has then been made to predict the density of mixtures of two size of spherical particles with smaller particle size ratios. Powers (1968) considered the *loosening effect*: for smaller particle size ratio mixtures, the size of voids among large particles may be smaller than the size of small particles. Thus, when small particles are filled into the large-particle skeleton, the small particles push apart the surrounding large particles and loosen the skeleton. Aïm and Goff (1968), and Toufar et al. (1977), took account of the *wall effect*: for smaller particle size ratio mixtures, when a large particle is embedded into the small-particle skeleton, the voids between large and small particles are greater than that of greater particle size ratio mixtures.

More recently, the more versatile models have been developed by Stovall et al. (1986), Yu and Standish (1988, 1987), Goltermann et al. (1997), De Larrard (F. De Larrard, 1999) and Dewar (1999). They proposed mathematical expressions to take account of both the *loosening effect* and *wall effect* as a function of particle size ratio. In their mathematical expressions, two material parameters are used: a filling effect parameter and an embedment effect parameter. Various mathematical expressions have been proposed based on the particulate material used in various studies.

Goltermann et al. (1997), De Larrard (1999) and Dewar (1999) have applied their model to concrete aggregate mixture. Jones et al. (2002) has compared the three models and found their accuracy and applicable range of particle size ratio vary substantially. The difference between these packing models indicate that each model has limited applications for certain industry material pertaining to the particle geometry and the range of particle sizes of the specific material used. Soils, as a natural deposit, covers a large range of particle sizes and shapes. Thus, the applicability of these models to soil is questionable.

For this purpose, Chang et al. (2015) developed a packing model for sand-silt mixtures. In most of the existing models, the controlling variable is selected to be the packing density (i.e. 1- porosity) or the specific volume (reciprocal of packing density) of the binary mixtures. However, Chang et al. (2015) found that from the experimental results on sand-silt mixtures, void ratio is linearly proportion to fines content. Therefore, void ratio was selected as the controlling variable in their model, instead of packing density or specific volume. This remark was supported by experimental results on sand-silt mixtures (Ching S. Chang et al., 2015).

For most of the existing particle packing models in the literature, a common deficiency in the prediction is observed. Compared to the experimental results, the predictions are generally accurate at low fines content (when the large-particle skeleton is dominant), and at high fines content (when the small-particle skeleton is dominant). However, the accuracy declines when the fines content is between 25%-50%. Often times, the discrepancies between the predicted and measured values are found to be significant and unacceptable.

De Larrard (1999) believed that the particle packing model should be valid if the material is sufficiently compact. Thus, the discrepancy is caused by the fact that the particulate material is not fully compacted. Therefore, he added another parameter, *compaction index*, to consider the effect due to insufficient compaction. Using this parameter, the discrepancy was reduced. From another perspective, Kwan et al. (2013) believed that the discrepancy is caused by neglecting the idea that voids can be changed due to the wedging of small particles between large particles. They developed a model with

one additional parameter, which allows for the *wedging effect*, thus reducing the discrepancy.

From our perspective, we believe that the discrepancy is mainly caused from the basic assumptions used in almost all particle packing models. The basic assumptions are: the filling of small particles into a dominant large-particle skeleton, or the embedment of large particles into a dominant small-particle skeleton. The first assumption is accurate for predictions of mixtures with low fines content (a dominant large-particle skeleton), while the second is accurate for mixtures with high fines content (a dominant small-particle skeleton). However, when the fines content is between 25%-50%, the packing skeleton is in the form of a dual-skeleton, which is neither dominant by large or by small-particle skeletons. Therefore, the assumption is no longer suitable in this range of fines content. In this study, we attempt to modify the theory so that the packing structure of a dual-skeleton can be correctly considered. This approach, unlike the approaches by De Larrard (1999) or by Kwan et al. (2013), does not require additional parameters.

Herein, we consider that the dual-skeleton consists of two sub-skeletons: the large-particle skeleton and the small-particle skeleton. We perform DEM simulation to illustrate the growing/declining nature of the two sub-skeletons as a function of fines content. Then, a *dual-skeleton index* and an *index size* are postulated to represent the state of packing structure. Based on this postulation, we formulated equations for the two assumed mechanisms of particle mixing, filling and embedment, by considering the packing structure of the dual-skeleton. A new model is then developed. The agreement between measured and predicted results are greatly improved for the entire range of fines content

for sand-silt mixtures. The developed model is verified by the experimental results of sand-silt mixtures.

4.2 Dual-skeleton

4.2.1 DEM Results

Densification of granular material has been simulated using discrete element method (DEM) by many investigators (An, 2013; Kumar et al., 2016; Martin & Bouvard, 2004; Skrinjar & Larsson, 2004). In these studies, the densification procedure varies in these DEM simulations. Here, we deal with sand-silt mixtures, thus we use the densification procedure described in ASTM D4253 (2006) for determining the minimum void ratio (maximum density) of granular soil. Following the standard, a cylindrical standard mold (diameter of 152.4 mm, height of 155.2 mm and nominal volume of 2830 $cm^3 \pm 42.45\ cm^3$) is used in the simulations (Fig. 4.1), and the granular packing is densified by a seating load, and then vertical vibration is applied.

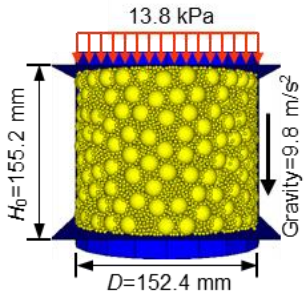

Figure 4.1 Dimension of mold used in DEM simulation

The commercial DEM program PFC3D v5.0 developed by Itasca (Itasca Consulting Group, 2014) is used for the simulation. The basic model parameters used in the DEM simulations are given in Table 1: an aggregate elastic modulus of 30 GPa, a rigid wall stiffness of 3×10^{11} N/m (stiffness of simulation container), an aggregate-to-aggregate

contact friction coefficient $\mu = 0.5$ corresponding to an internal friction angle of 27°, and a solid density of 2660 kg/m^3. These values were found to be appropriate for aggregates (Shen & Yu, 2011) and are used in the present analysis. A simplified Hertz-Mindlin law at contacts is used.

Table 4.1 Parameters used in DEM

Parameter	Value
Young's modulus *E* (GPa)	30
Poisson's ratio	0.3
Friction coefficient	0.5
Normal critical damping ratio	0.03
Particle density (kg/m^3)	2660
Wall stiffness (N/m)	3×10^{11}

The binary mixture consists of particles of two sizes: 15.2 mm and 3.04 mm. Depending on the content of small particles (i.e. fines content), the packing within the mold consists of about 1,000-100,000 particles. Particles of large and small sizes are randomly generated in a space within a cylindrical wall. Then, gravitation is applied to gravitate these particles and create a packed sample in the cylindrical space. The sample is densified by applying a seating load of 13.8 ± 0.1 kPa, and then vertical vibration is applied. The magnitudes of vibration amplitudes and frequencies vary for each packing, which were selected based on the trial procedures outlined in the ASTM D4253 standard (ASTM D4253-00, 2006).

We recognize that different packing algorithms or different values of friction coefficient should influence the packing void ratio. However, the purpose of this DEM simulation is not to investigate the influences of these factors. Rather, the purpose is to illustrate the trend of skeleton change with respect to fines content. Therefore, we only perform the simulations using one set of typical material parameters.

The results of the DEM simulations are plotted in Fig. 4.2, in the form of void ratio e versus fines content f_c of the packing. The void ratio is defined as the ratio of void volume to solid volume of the granular packing. The porosity n is defined as volume fraction of voids. The void ratio e is related to porosity by:

$$e = \frac{n}{1-n} \; ; \qquad n = \frac{e}{1+e} \tag{4.1}$$

For avoiding ambiguity and for distinction, instead of e, the minimum void ratio of the binary mixture is denoted as e^M with a superscript 'M'.

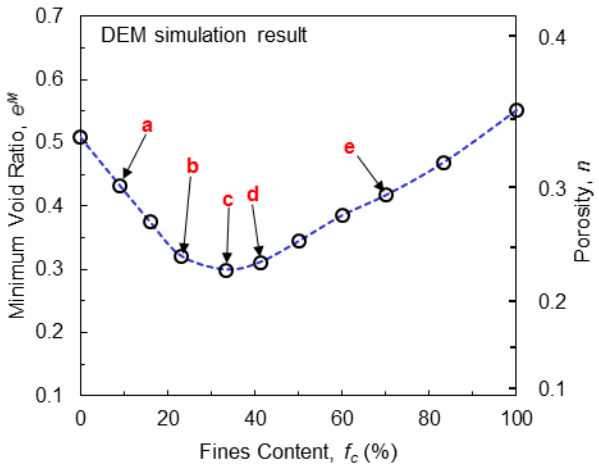

Figure 4.2 DEM simulation results of minimum void ratio vs. fines content

The results of DEM show that the packing structure changes with the fines content. Five different levels of fines contents are marked in Fig. 4.2. The plane sections of the 3-D packing structures corresponding to the 5 different fines contents are schematically shown in Fig. 4.3. At point a of the curve in Fig. 4.2, the large-particle skeleton is dominant. As the fines content increases to point b, the large-particle skeleton begins to decline while the small-particle skeleton starts to grow (Fig. 4.3(b)). At point c, which is the lowest point of the curve (i.e. termed as the threshold fines content), the large-particle and the small-

particle skeletons are about equally dominant (Fig. 4.3(c)). At point d, the small-particle skeleton is slightly bigger than the large-particle skeleton (Fig. 4.3(d)). At point e, the small-particle skeleton becomes dominant (Fig. 4.3(e)). The two distinct structures are obvious for fines content f_c < 10% and for f_c > 70% (Fig. 4.3(a) and Fig. 4.3(e)). Fig. 4.3 shows that the increase of fines content causes the decline of the large-particle skeleton and the growth of the small-particle skeleton. This general trend is consistent with findings in the literature (Thevanayagam, Shenthan, Mohan, & Liang, 2002; Ueda et al., 2011; Wiącek, 2016).

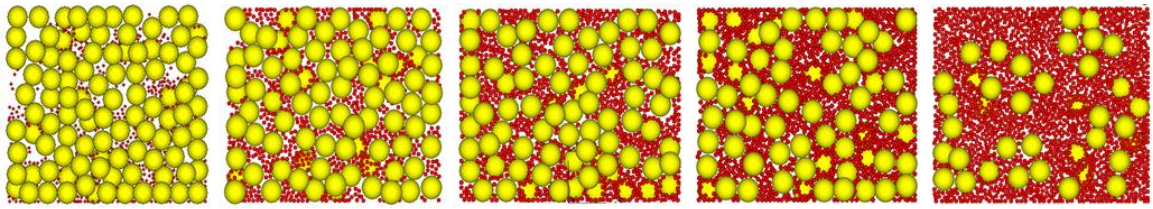

Figure 4.3 The packing structures for a binary mixture with various fines content: (a) f_c = 9.1%; (b) f_c = 23.2%; (c) f_c = 33.3%; (d) f_c = 41.2%; (e) f_c = 66.7%

4.2.2 Small-particle Network, Filled and Wedged Small Particles

For a packing with low fines content, most large particles are connected as a network. At low fines content, the large-particle network occupies most of the space. The presence of small particles is in the form of fillers in the voids among large particles, and in the form of wedged particles between large particles (Fig. 4.4 (a)). In each void among large particles, the fillers are clustered as a particle group. The particle group in a void is not connected to that in another void. With the increase of fines content, small particles begin to push large particles apart and build thicker layers between large particles, which connect the fillers and create the small-particle skeleton (Fig. 4.4(b), 4.4(c)).

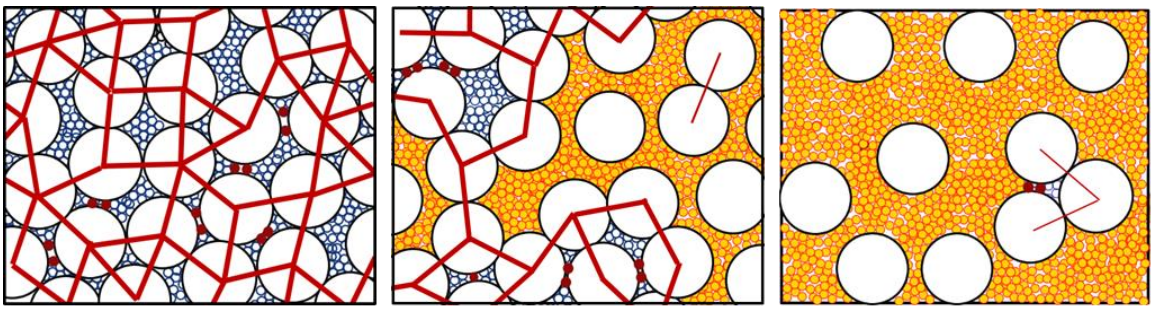

(a) (b) (c)

the thick (red) lines represent the network of large particles; the thin (red) lines represent the embedded clusters of large particles; the solid (red) small disks represent the small particles wedged between two large particles; the shaded (yellow) small disks represent the network of small particles; the hollow (blue) small disks represent the small particle filled into the voids among large particles

Figure 4.4 The schematic transition of large-particle network and small-particle network with increase of fines content: (a) low fines content, (b) transitional fines content and (c) high fines content

The volume fraction of all small particles ϕ_S (also termed fines content f_c) is the summation of the volume fraction of wedged particles ϕ_W, the volume fraction of filled particles ϕ_F, and the volume fraction of small-particle network ϕ_{SNK}, i.e.,

$$\phi_S = \phi_W + \phi_F + \phi_{SNK} \tag{4.2}$$

The small-particle network is defined as the greatest group of small particles connected in the packing, which exceeds 95% of the sample height. The wedged particles are the small particles that satisfy both the following conditions: (1) the small particle does not connect with the small-particle network, and (2) the small particle connects with two or more large particles with non-negligible contact forces. The filled particles are the small particles that satisfy both the following conditions: (1) the small particle does not connect with the small-particle network, and (2) the small particle connects with one or less large particles with negligible contact forces.

Fig. 4.5 shows the volume fractions of ϕ_{SNK}, ϕ_F and ϕ_W versus fines content. At low fines content, most of the small particles are within the voids as fillers, very few small-particles are wedged between large particles, and the large-particle network occupies most of the space. At fines content $\phi_S = 23\%$, the volume fraction ϕ_W = 4% for wedged particles and ϕ_F = 19% for filled particles. Thus, there is no small-particle network (i.e. ϕ_{SNK}= 0, see Eq. (4.2)) indicating that the fillers are isolated particle groups. With the increase of fines content, the fillers start to connect and transform into the small-particle network. Consequently, the amount of fillers decreases while the size of the network increases. The DEM results show that when the fines content increase to about 33%, the network increases to about 10%; the fillers decrease to about 16%; and the wedged particles slightly increase to 7%.

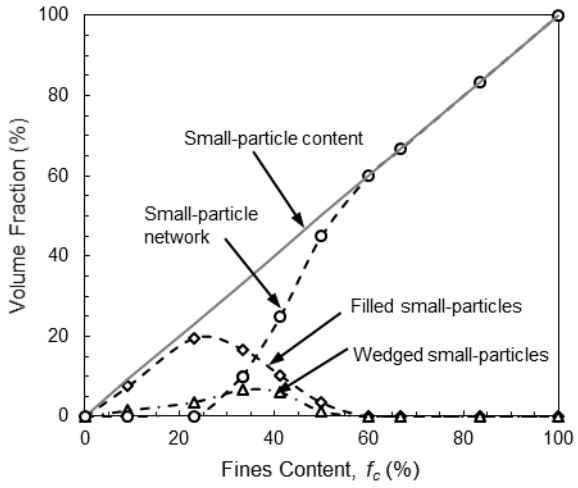

Figure 4.5 Volume fractions of small-particle network, wedged particles, and fill particles

4.2.3 Large-particle Network and Embedded Large Particles

For a packing with high fines content, most small particles are connected as a small-particle network. The presence of large particles is in the form of embedded inclusions in the small particle matrix. In general, the large particles are in three forms: embedded large-particles clusters, embedded single large-particles, and large-particle network (Fig. 4.4). The volume fraction of all large particles ϕ_L is the summation of the volume fraction of embedded large-particle clusters ϕ_{EC}, the volume fraction of embedded single particles ϕ_{ES}, and the volume fraction of large-particle network ϕ_{LNK} , i.e.,

$$\phi_L = \phi_{EC} + \phi_{ES} + \phi_{LNK} \tag{4.3}$$

The large-particle network is defined as the greatest group of large particles connected in the packing, which exceeds 95% of the sample height. An embedded single particle is the large particle that does not connect with any other large particles. An embedded particle-clusters is the large particles that satisfy the following two conditions: (1) the large particle does not connect with the large-particle network, and (2) the large particle connects with one or more other large particles.

Fig. 4.6 shows the variation of ϕ_{LNK}, ϕ_{EC}, ϕ_{ES} with fines content. At low fines content, the value $\phi_{LNK} = \phi_L$ indicates that the large-particle network is fully connected, and there are no embedded inclusions (i.e., $\phi_{EC} = \phi_{ES} = 0$). The volume fraction of network ϕ_{LNK} decreases rapidly between 23%-50% fines content. At fines content is $\phi_L = 50\%$, the large-particle network has broken down into embedded clusters and single particles $\phi_{LNK} = 0$; the volume fraction of embedded particle-clusters $\phi_{EC} = 42\%$ and the volume

fraction of embedded single particles ϕ_{ES} = 8% (see Eq. (4.3)). At 83% fines content, nearly all embedded inclusions are isolated single particles.

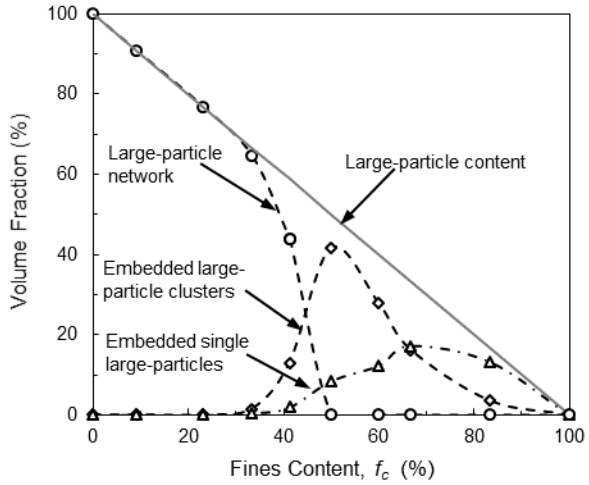

Figure 4.6 Volume fractions of large-particle network, embedded single large particles and embedded large particle-clusters

4.2.4 Growth and Decline of the Two Sub-skeletons

Observed from the DEM analysis, at any given fines content, the skeleton is made up of two sub-skeletons: large-particle and small-particle skeletons, intertwined in the packing. With an increase of fines content, decline of the large-particle network and growth of the small-particle network occur simultaneously, as shown in the previous section.

It is noted that both the large-particle skeleton and small-particle skeleton are only general terms to qualitatively describe the packing structure. Due to the complexity of packing structure, it is not plausible to precisely define the two terms in a quantitative manner. However, the proportion of the two sub-skeletons has a significant influence on the packing density and should be included as a variable in the analytical model for packing density. For this purpose, we define a *dual-skeleton index* ψ of a binary mixture in the following form:

$$\psi = \frac{x - d_2}{d_1 - d_2}; \quad d_1 \geq x \geq d_2 \tag{4.4}$$

where the particle sizes for the large and small particles are denoted by d_1, d_2 respectively. The variable x is termed as *index size*. The *dual-skeleton index* $\psi(x)$ is a function of x, which represents the relative proportion of the two sub-skeletons in the packing. When $x = d_1$, then $\psi(d_1) = 1$, the packing consists of only the large-particle skeleton; the small-particle skeleton is null. When $x = d_2$, then $\psi(d_2) = 0$, the packing consists of only the small-particle skeleton; the large-particle skeleton is null. When $d_1 > x > d_2$, then $1 > \psi(x) > 0$, the packing consists of both the large and the small-particle skeletons (dual-skeleton). The value of $\psi(x)$ is dependent on the relative value of x with respect to d_1 and d_2.

It is noted that x is a function of fines content. Therefore, the *dual-skeleton index* $\psi(x)$ varies with fines content. At a low fines content, $x \approx d_1$ and $\psi(x) \approx 1$, the packing structure is dominant by the large-particle skeleton $\psi(d_1)$. At a high fines content, $x \approx d_2$ and $\psi(x) \approx 0$, the packing structure is dominant by the small-particle skeleton $\psi(d_2)$. In the middle range of fines content, $d_1 > x > d_2$, the packing structure is neither large-particle skeleton dominant nor small-particle skeleton dominant. The packing structure has a dual-skeleton index $\psi(x)$, which is dependent on fines content.

4.3 New Model

4.3.1 Mix Mechanism Using Dual-skeleton Index Size

For a binary mixture comprised of two components of mono-size particles, the large size d_1, and the small size d_2, the solid volumes of each component are denoted by V_{s1} and V_{s2}, respectively. The solid volume fractions of each component are defined as:

$$y_1 = \frac{V_{s1}}{V_{s1} + V_{s2}} \quad ; \quad y_2 = \frac{V_{s2}}{V_{s1} + V_{s2}} \tag{4.5}$$

The solid volume fraction of small particles y_2 is also termed as fines content f_c, and the solid volume of large particles $y_1 = 1 - f_c$.

The minimum void ratio of a mono-size packing containing only component 1 (i.e. large particles) is denoted by e_1 whereas of a mono-size packing containing only component 2 (i.e. small particles) is denoted by e_2. By definition,

$$e_1 = V_{v1} / V_{s1} \quad ; \quad e_2 = V_{v2} / V_{s2} \tag{4.6}$$

where V_{v1} and V_{v2} are the void volumes within the mono-size packing containing only large particles and the mono-size packing containing only small particles, respectively.

The minimum void ratio of the binary mixture is denoted by e^M. The purpose of this proposed model is to estimate the value of e^M based on the set of values d_1, d_2, e_1, e_2, y_1 and y_2.

For a binary mixture, the void ratio can be divided into two terms:

$$e^M = \overline{e}_1 y_1 + \overline{e}_2 y_2 \tag{4.7}$$

where $\overline{e}_1$ and $\overline{e}_2$ are partial void ratios of each component of the binary mixture, respectively. The partial void ratios may be treated as though they represent the void ratios

of the components in the packing. The concept of partial void ratios is similar to the concept of partial specific volume used by Yu and Standish (1988). Assuming that there is no disturbance during particle mixing, the partial void ratios are the same as the void ratios of mono-size packings (i.e., $\bar{e}_1 = e_1$ and $\bar{e}_2 = e_2$). In this special case, the value of e^M according to Eq. (4.7) is equivalent to the Voigt (upper) bound in composite mechanics (Voigt, 1889). In a general case, the partial void ratios are smaller than the void ratios of mono-size packings due to the disturbance during particle mixing.

Chang et al. (2015) considered the effect of particle mixing by using the filling effect parameter $a(r)$ and the embedment effect parameter $b(r)$, and derived the void ratio of the mixture in the following form:

$$e^M = \begin{cases} e_1 y_1 + \left(e_2 - a(r)(1+e_2)\right) y_2 & \text{large - particle skeleton dominant} \\ \left(1-b(r)\right) e_1 y_1 + e_2 y_2 & \text{small - particle skeleton dominant} \end{cases} \tag{4.8}$$

The filling effect parameter $a(r)$ and the embedment effect parameter $b(r)$ are dependent on the particle size ratio $r = d_1/d_2$, which has been proposed by Chang et al. (Ching S. Chang et al., 2015) in the following form:

$$a(r) = \left(1 - \frac{d_2}{d_1}\right)^p; \qquad b(r) = \left(1 - \frac{d_2}{d_1}\right)^s \tag{4.9}$$

It is noted that the model developed by Chang et al. (2015) is limited by the same assumption adopted in most of the existing models for binary mixtures (Furnas, 1931; Kezdi, 1979; François de. Larrard, 1999; Stovall, De Larrard, et al., 1986; A. B. Yu & Standish, 1988, 1991). The assumption accounts only for two scenarios: (1) In the first part of Eq. (4.8), the mixed packing is large-particle skeleton dominant, thus the partial void

ratio $\bar{e}_1$ is assumed to be the same as the void ratio of mono-size packing of large particles ($\bar{e}_1 = e_1$). However, the partial void ratio $\bar{e}_2$ of the small particles as fillers is not the same as that of the mono-size packing of small particles e_2, and (2) In the second part of Eq. (4.8), the mixed packing is small-particle skeleton dominant, thus the partial void ratio $\bar{e}_2$ is assumed to be the same as the void ratio of mono-size packing of small particles ($\bar{e}_2 = e_2$). However, the partial void ratio $\bar{e}_1$ of the large particles as embedded inclusions is not the same as the value of e_1.

In the proposed model, we consider that the mixed packing is neither large-particle skeleton dominant, nor the small-particle skeleton dominant. The mixed packing is regarded as a dual-skeleton represented by $\psi(x)$. Thus, both partial void ratios are not equal to the void ratios of mono-size packings (i.e. $\bar{e}_1 \neq e_1$ and $\bar{e}_2 \neq e_2$). We postulate that both filling and embedment mechanisms occur in the particle mixing. Thus

$$e^M = \bar{e}_1 y_1 + \bar{e}_2 y_2 = \big(1 - b(x)\big) e_1 y_1 + \big(e_2 - a(x)(1 + e_2)\big) y_2 \tag{4.10}$$

Note that $a(r)$ and $b(r)$ are replaced by $a(x)$ and $b(x)$ because, in the present model, the controlling size is taken to be x. By replacing the controlling size from d_1 (for the filling case) or d_2 (for the embedment case) to x, Eq. (4.9) becomes:

$$a(x) = \left(1 - \frac{d_2}{x}\right)^p \quad ; \quad b(x) = \left(1 - \frac{x}{d_1}\right)^s \tag{4.11}$$

The values of *p* and *s* in Eqs. (4.9) and (4.11) are considered to be mainly associated with particle shape. Since particle shapes are not commonly measured in engineering

practice, in this model, the values of p and s are treated as material parameters, which are calibrated from experimentally measured void ratios. This will be discussed in next section.

The variation of $a(x)$ and $b(x)$ are dependent on the particle size ratio d_1/d_2 of the binary mixture. The two curves of $a(x)$ and $b(x)$ are shown in Fig. 4.7 for $d_1/d_2 = 4$, 10 and 30 and $p = s = 1.2$. The range of x is $d_1 \geq x \geq d_2$. The range of both $a(x)$ and $b(x)$ are between 0 and 1.

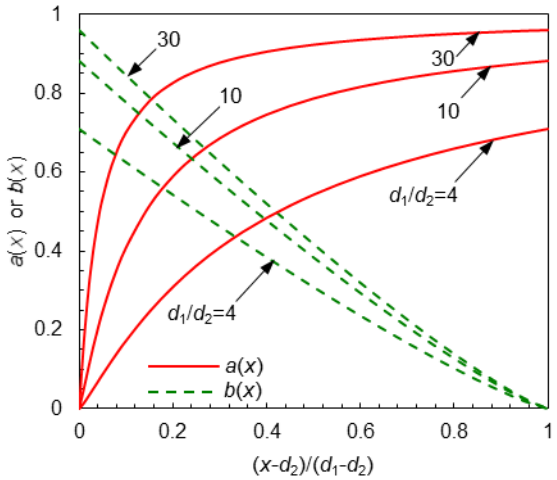

Figure 4.7 Variation of $a(x)$ and $b(x)$ for different particle size ratio calculated from Eq. (4.11)

In the proposed Eq. (4.10), the void ratio of a binary mixture e^M is a function of index size x, which is a continuous variable. Let $x = d_1$, then according to Eq. (4.11), $b(x) = 0$, and Eq. (4.10) becomes:

$$e^M = e_1 y_1 + \left(e_2 - a(x)(1+e_2)\right) y_2 \tag{4.12}$$

This equation is the same as the first part in Eq (4.8). Furthermore, if $d_1 \gg d_2$, according to Eq. (4.11), $a(x) = 1$, which leads to:

$$e^M = (1 - f_c)e_1 - f_c \tag{4.13}$$

This equation shows that the filling of small particles does not alter the total volume of large-particle packing (see Chang et al., 2015). This is also the basis of the theories by Furnas (1931) and Kezdi (1979).

On the other hand, let $x = d_2$, then according to Eq. (4.11), $a(x) = 0$, and Eq. (4.10) becomes:

$$e^M = \big(1 - b(x)\big) e_1 y_1 + e_2 y_2 \tag{4.14}$$

This equation is the same as the second part of Eq (4.8). Furthermore, if $d_1 \gg d_2$, according to Eq. (4.11), $b(x) = 1$, which leads to:

$$e^M = f_c e_2 \tag{4.15}$$

This equation shows that the embedment of large particles does not alter the void volume of small-particle packing (see Chang et al., 2015). This assumption is also the basis of theories by Furnas (1931) and Kezdi (1979).

Combining Eqs. (4.10) and (4.11), the void ratio of a binary mixture e^M can be expressed below as a function of f_c and x:

$$e^M(f_c, x) = e_1(1 - f_c)\left(1 - \left(1 - \frac{x}{d_1}\right)^s\right) + e_2 f_c - \left(1 - \frac{d_2}{x}\right)^p (1 + e_2) f_c \tag{4.16}$$

In this equation, the values of d_1, d_2, e_1, e_2 are known, and the values of p and s are considered as material parameters. However, the index size x is not known priori. It is an undetermined variable that can be determined by satisfying the following optimum condition, shown in Eq. (4.17). Note that the variable x is not an additional material parameter.

$$\frac{\partial e^M(f_c, x)}{\partial x} = 0 \tag{4.17}$$

The italic symbol ∂ in Eq. (4.17) is the operator of partial differentiation. The term on the left side of Eq. (4.17) denotes the partial derivative of e^M with respect to x.

The value of index size, *x,* cannot be arbitrary. The most appropriate index size corresponds to the optimum condition shown in Eq. (4.17). The optimum condition is the one that gives the highest void ratio out of all values of $e^M(x)$. The highest e^M is the easiest outcome to be achieved during mixing because it would consume the least energy. Thus, the value of *x* is determined based on Eq. (4.17).

4.3.2 Determination of Parameters of *p* and *s*

The values of *p* and *s* can be determined directly from the experimental data. Fig. 4.8 shows the experimental results plotted in terms of void ratio versus fines content (e^M vs. f_c). The slope at the left end M_1 can be obtained by taking the partial derivative of e^M in Eq. (4.16) with respect to f_c, and let $f_c = 0$ and $x = d_1$, then:

$$\frac{\partial e^M}{\partial f_c} = e_2 - e_1 - \left(1 - \frac{d_2}{d_1}\right)^p (1 + e_2) = M_1 \tag{4.18}$$

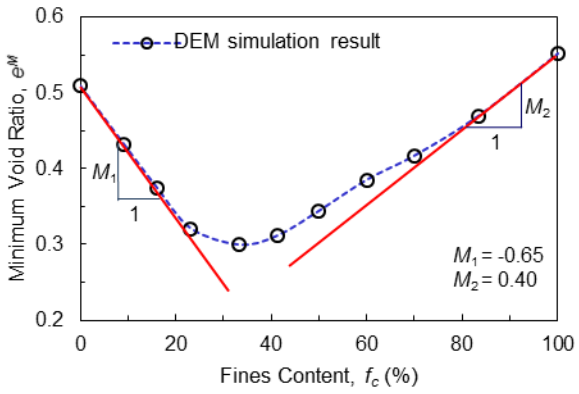

Figure 4.8 Slope M_1 at f_c = 0% and slope M_2 at f_c = 100%

By rearranging Eq. (4.18), the value of p can be related to slope M_1, given by

$$p = \log\left(\frac{e_2 - e_1 - M_1}{1 + e_2}\right) / \log\left(1 - \frac{d_2}{d_1}\right) \tag{4.19}$$

Similarly, the slope at the right end, M_2, can be obtained by taking the derivative of e^M in Eq. (4.16) with respect to f_c, and let $f_c = 1$ and $x = d_2$, then:

$$\frac{\partial e^M}{\partial f_c} = e_2 - e_1 + \left(1 - \frac{d_2}{d_1}\right)^s e_1 = M_2 \tag{4.20}$$

By rearranging Eq. (4.20), the value of s can be related to slope M_2, given by

$$s = \log\left(\frac{M_2 - (e_2 - e_1)}{e_1}\right) / \log\left(1 - \frac{d_2}{d_1}\right) \tag{4.21}$$

From Eqs. (4.19) and (4.21), the values of p and s can be determined from M_1 and M_2, which can be directly obtained from experimental results.

At an extreme condition, when $p = 0$ and $s = 0$, Eq. (4.18) shows that $M_1 = -(1+e_1)$, and Eq. (4.20) shows that $M_2 = e_2$. These two slopes represent the two lower-bound lines in Fig. 4.9.

On the other extreme, when $p = \infty$ and $s = \infty$, Eq. (4.18) shows that $M_1 = e_2 - e_1$, and Eq. (4.20) shows that $M_2 = e_2 - e_1$. These two slopes are identical and represent the upper-bound line in Fig. 4.9.

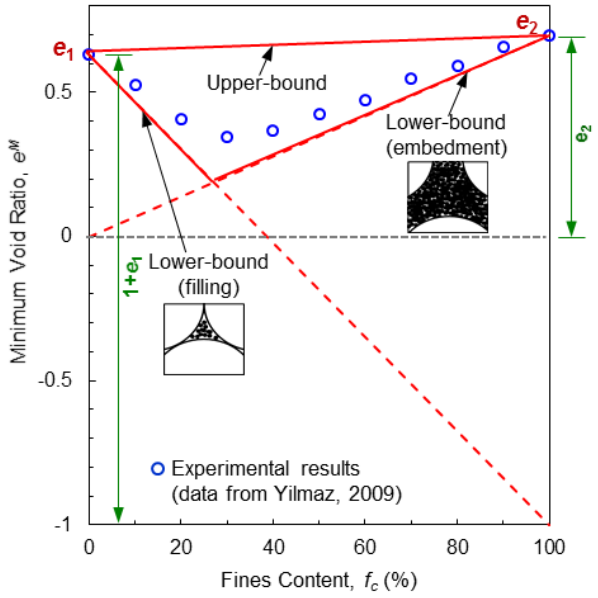

Figure 4.9 The limiting conditions of void ratio vs. fines content (experimental data from Yilmaz (2009))

4.4 Model Feature

4.4.1 Prediction Procedure

The proposed model for predicting the void ratio of a mixture can be summarized in Eqs. (4.16) and (4.17). To illustrate the prediction procedure of this model, experimental results on three types of mixtures are used: Silica sand-silt mixtures (Yilmaz, 2009), Nevada sand-silt mixtures (Lade et al., 1998), and binary mixtures of spheres used in the DEM simulation. Based on the experimental results, the parameters of p and s are determined using Eqs. (4.19) and (4.21). The values of p, s, e_1, e_2, d_1, d_2 for the three mixtures are listed in Table 4.2.

Table 4.2 Parameters for the three mixtures

Mixture	Ref.	d_1(mm)	d_2(mm)	e_1	e_2	p	s
Nevada 50/80-Nevada fines	(Lade et al., 1998)	0.21	0.05	0.581	0.754	3.5	1.6
Silica#16-#18 #50-#80	(Yilmaz, 2009)	1.08	0.26	0.633	0.696	2.2	2
DEM Simulations	-	15.2	3.04	0.509	0.551	3.6	1.6

Eq. (4.16) shows that the void ratio of the mixture is a function of two variables: the fines content and the index size, i.e. $e^M(f_c, x)$. Here, if we treat f_c as a constant, then the values of $e^M(x)$ can be computed. For an example of Nevada sand mixtures, we calculated the values of e^M versus x for six values of fines contents, $f_c = 15, 22, 30, 45, 60$ and 80, then plotted the results in Fig. 4.10(a). The same procedures were repeated for Silica mixtures and DEM spheres mixtures, as shown in Fig. 4.10(b) and 4.10(c).

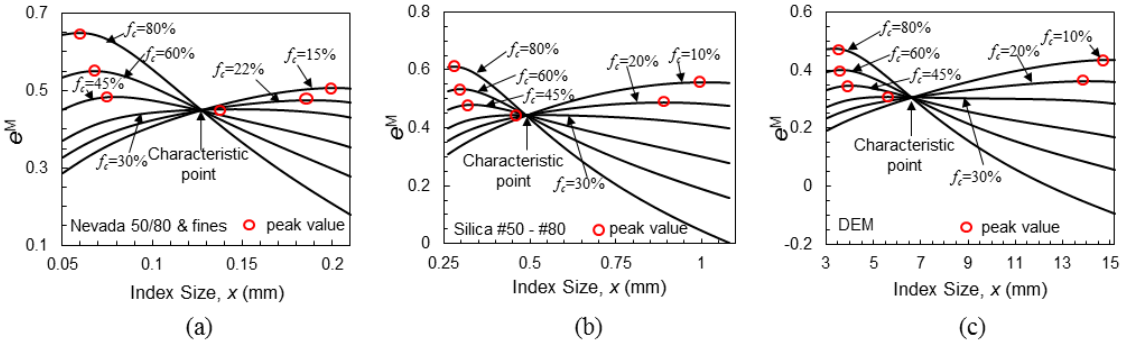

Figure 4.10 Variation of e^M versus x for each fines content calculated from Eq. (4.16): (a) Nevada sand-silt mixtures; (b) Silica sand-silt mixtures and (c) DEM sphere mixtures

For each curve of a given fines content, a peak point is marked by a circle. At the peak point, the optimum condition (zero first derivative) of Eq. (4.17) is satisfied, thus the coordinate of the peak point (e^M, x) is the solution for each corresponding curve. Thus, the solutions for $e^M(f_c)$ and $x(f_c)$ are obtained. The calculated values of e^M are plotted versus

f_c in Fig. 4.11, and compared to the experimental results for Nevada and Silica sand-silt mixtures as well as the DEM sphere mixtures. The comparisons are in good agreement.

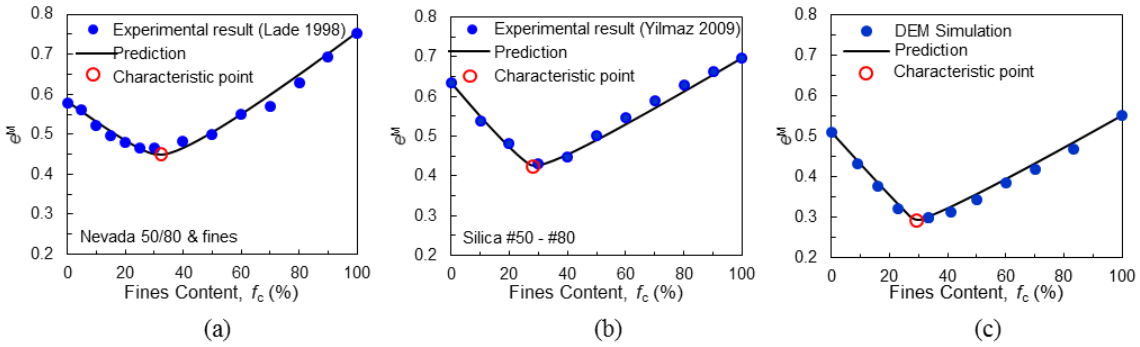

Figure 4.11 Comparisons between predicted and measured results: (a) Nevada sand-silt mixtures; (b) Silica sand-silt mixtures and (c) DEM spheres mixtures

The lowest point of each curve shown in Fig. 4.11 is termed as the characteristic point, marked by a hollow circle. The lowest void ratio corresponding to this point is termed as *characteristic void ratio*. The fines content corresponding to this point is termed as *characteristic fines content*. The concaved curve shape shown in Fig. 4.11 is a distinctive feature, which have been observed in many experimental studies for sand-silt mixtures. The *characteristic fines content* in other studies has been termed threshold fines content (Thevanayagam et al., 2002), transitional fines content (Yang, Lacasse, & Sandven, 2006), and limiting fines content (Polito & Martin, 2001).

The relationship between x and f_c computed from the prediction procedure is plotted in Fig. 4.12 for Nevada sand-silt mixtures, Silica sand-silt mixtures, and DEM sphere mixtures.

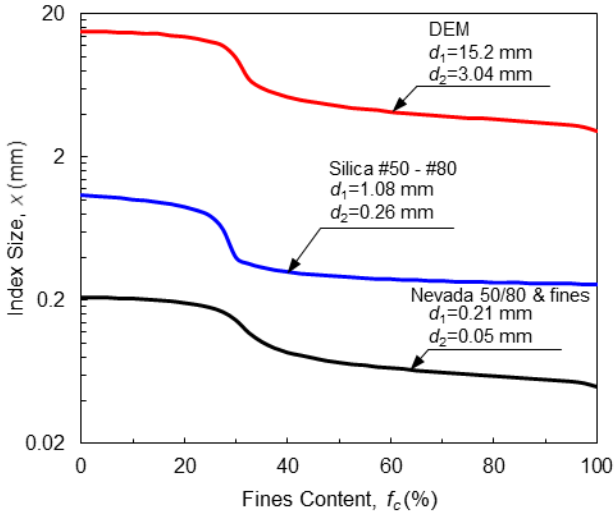

Figure 4.12 The index size x versus fines content f_c

Using Eq. (4.4), the curves in Fig. 4.12 are then converted to the curves of dual-skeleton index ψ versus fines content and plotted in Fig. 4.13. It shows that the dual-skeleton index of Silica sand-silt mixtures decreases at a faster rate than those of Nevada sand-silt mixtures and DEM spheres mixtures. This implies that the large-particle skeleton of Silica sand-silt mixtures declines faster than those of Nevada sand-silt mixtures and DEM sphere mixtures.

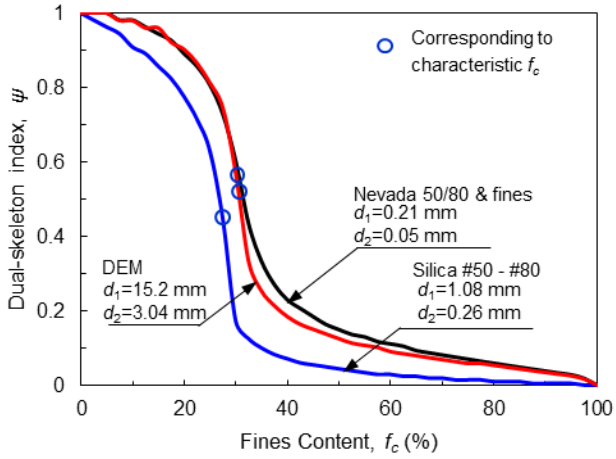

Figure 4.13 Variation of dual-skeleton index ψ versus fines content f_c

These *characteristic fines contents* obtained from Fig. 4.11 are marked as hollow circles on the curves in Fig. 4.13. It shows that, at these fines contents, the corresponding dual-skeleton index are about 0.5, indicating that the packing structures under these fines contents are neither dominant by large-particle skeleton nor dominant by small-particle skeleton.

4.4.2 First Characteristic Equation

After carrying out the partial differentiation, Eq. (4.17) can be explicitly expressed as:

$$e_1(1-f_c)\frac{s}{d_1}\left(1-\frac{x}{d_1}\right)^{s-1}-(1+e_2)f_c\frac{pd_2}{x^2}\left(1-\frac{d_2}{x}\right)^{p-1}=0 \qquad (4.22)$$

Eq. (4.22) is an algebraic equation corresponding to the partial differential equation in Eq. (4.17). Mathematically, this algebraic equation is termed as characteristic equation. Eq. (4.22) provides a relationship between x and f_c, specifically $x = x(f_c)$. It is noted that the solutions obtained this way are identical to the solutions given in Fig. 4.12.

By utilizing the characteristic equation Eq. (4.22), we can simplify the prediction procedure outlined in the last section. We can start the prediction procedure by solving Eq. (4.22) for the solution $x = x(f_c)$. Then simply substitute the solution $x = x(f_c)$ into Eq. (4.16) to solve for the value of $e^M(f_c)$.

4.4.3 Second Characteristic Equation

Since Eq. (4.16) shows that the void ratio of the mixture is a function of two variables: the fines content and the index size (i.e. $e^M(f_c, x)$), there exists two characteristic

equations. In the last section, we discussed the first characteristic equation, which is corresponding to the partial differential equation with respect to x displayed in Eq. (4.17). In this section, we discuss the second characteristic equation, which corresponds to the partial differential equation with respect to f_c shown below:

$$\frac{\partial e^M(f_c, x)}{\partial f_c} = 0 \tag{4.23}$$

The partial derivative of e^M with respect to f_c in Eq. (4.23) mathematically represents the tangential slope of the curve, e^M versus f_c. Viewing the curves in Fig. 4.11, at the point of the lowest value of e^M on each curve, the tangential slope is horizontal (or zero slope). Thus, at this point, Eq. (4.23) is satisfied.

For convenience of carrying out the partial derivative, we express Eq. (4.16) in the following two separate terms:

$$e^M(f_c, x) = \alpha(x) + \beta(x) f_c \tag{4.24}$$

where, $\alpha(x) = e_1 - \left(1 - \frac{x}{d_1}\right)^s e_1$; $\beta(x) = e_2 - e_1 - \left(1 - \frac{d_2}{x}\right)^p (1 + e_2) + \left(1 - \frac{x}{d_1}\right)^s e_1$ (4.25)

Thus, Eq. (4.23) leads to:

$$\frac{\partial e^M(f_c, x)}{\partial f_c} = \beta(x) = 0 \quad \text{or} \quad e_2 - e_1 - \left(1 - \frac{d_2}{x}\right)^p (1 + e_2) + \left(1 - \frac{x}{d_1}\right)^s e_1 = 0 \tag{4.26}$$

The algebraic equation of Eq. (4.26) is the characteristic equation corresponding to the partial differential Eq. (4.23). Eq. (4.26) contains only one unknown variable x. The solution of this equation provides $x = x_c$. We term x_c as the *characteristic index size*. Substituting x_c into Eq. (4.24), $\beta(x_c) = 0$, the void ratio under this condition $e_c^M = e^M(f_c, x_c)$ can be computed by the following form:

$$e_c^M = e^M(f_c, x_c) = e_1 - \left(1 - \frac{x_c}{d_1}\right)^s e_1 \tag{4.27}$$

Two features can be observed from Eq. (4.27):

First, Eq. (4.27) shows that, at $x = x_c$, the void ratio e_c^M is not a function of fines content. Thus, at $x = x_c$, the curves of e^M vs. x with various fines contents pass through the same point in Fig. 4.10.

Second, since x_c corresponding to zero slope in Eq. (4.26), the value of e_c^M represents the lowest values of e^M on the curve shown in Fig. 4.11.

Substituting $x = x_c$ into Eq. (4.22), the corresponding fines content $f_c = f_c^c$ is the *characteristic fines content*.

$$f_c^c = \frac{s}{d_1}\left(1 - \frac{x_c}{d_1}\right)^{s-1} \Big/ \left(\frac{s}{d_1}\left(1 - \frac{x_c}{d_1}\right)^{s-1} + \frac{(1+e_2)pd_2}{e_1 x_c^2}\left(1 - \frac{d_2}{x_c}\right)^{p-1}\right) \tag{4.28}$$

The *characteristic fines contents* calculated from this equation are identical to those obtained from Fig. 4.11 for Nevada sand-silt mixtures, Silica sand-silt mixtures, and DEM sphere mixtures.

4.5 Comparison with Previous Model

In the present model, the dual-skeleton index varies continuously with the fines content. The model by Chang et al. (2015) is a simplified case of the present model. To simplify the present model, we assume that the index size x, instead of being a continuous function of fines content, is a step function of two constants, in which the index size x changes abruptly from d_1 to d_2 as shown in Fig. 4.14(a).

Following Eqs. (4.10) and (4.11),

(1) Let $x = d_1$, the value of $b(x)$ = 0 and $a(x) = a(d_1)$.

(2) Let $x = d_2$, the value of $a(x)$ =0 and $b(x) = b(d_2)$.

Under these two conditions, the present model reduces to the following two specific equations:

$$e^M(d_1) = e_1(1-f)_c + e_2 f_c - \left(1-\frac{d_2}{d_1}\right)^p (1+e_2) f_c \quad \text{for index size } x = d_1, \text{ and} \quad (4.29)$$

$$e^M(d_2) = e_2 f_c + e_1\left(1-\left(1-\frac{d_2}{d_1}\right)^s\right)(1-f_c) \quad \text{for index size } x = d_2. \quad (4.30)$$

For a given fines content f_c, two values are obtained: $e^M(d_1)$, and $e^M(d_2)$. The higher value of the two is the predicted minimum void ratio of the mixture, i.e.,

$$e^M = \text{Max}\left(e^M(d_1),\ e^M(d_2)\right) \quad (4.31)$$

The predicted minimum void ratios for Nevada sand-silt mixtures (Lade et al., 1998) by the simplified model and by the present model are shown in Fig. 4.14(b). In both model predictions, we use the same parameters of p and s for the mixtures, which are estimated from the slopes M_1 and M_2 of the experimental curves. Although the simplified model can capture the trend of experimental results, the measured data is not in agreement with the bi-linear lines, especially in the middle range of fines content as shown in Fig. 4.14(b). The predictions by the present model is non-linear, which is a better fit for the void ratio in the whole range of fines content. The behavior of soil mixtures in the middle range fines content are of more interest to geotechnical engineers because silty sand with this range of fines content are most susceptible to liquefaction damage.

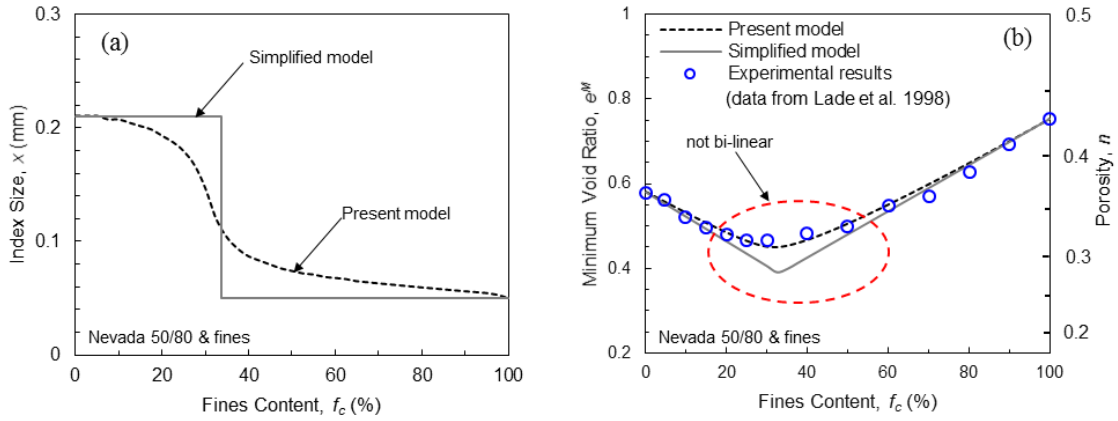

Figure 4.14 Comparison of two methods: (a) the index sizes and (b) the predicted minimum void ratios (experimental data from Lade *et al.* (1998))

4.6 Evaluation of the New Model

Herein, experimental results from 16 soil mixtures (Y. T. Cho, 2014; Fourie & Papageorigou, 2001; Lade et al., 1998; Lade & Yamamuro, 1997; Pitman, Robertson, & Sego, 1994; S. L. Yang, 2004; Yilmaz, 2009) are selected for evaluating the proposed model by comparing the predicted value with the measured results. The basic information for the sand-silt mixtures and the parameters p and s are listed in Table 4.3. The comparison is shown in Fig. 4.15. The average coefficient of determination R^2 for the 16 soil mixtures is 0.96, which indicates a good agreement between the predicted values and measured results.

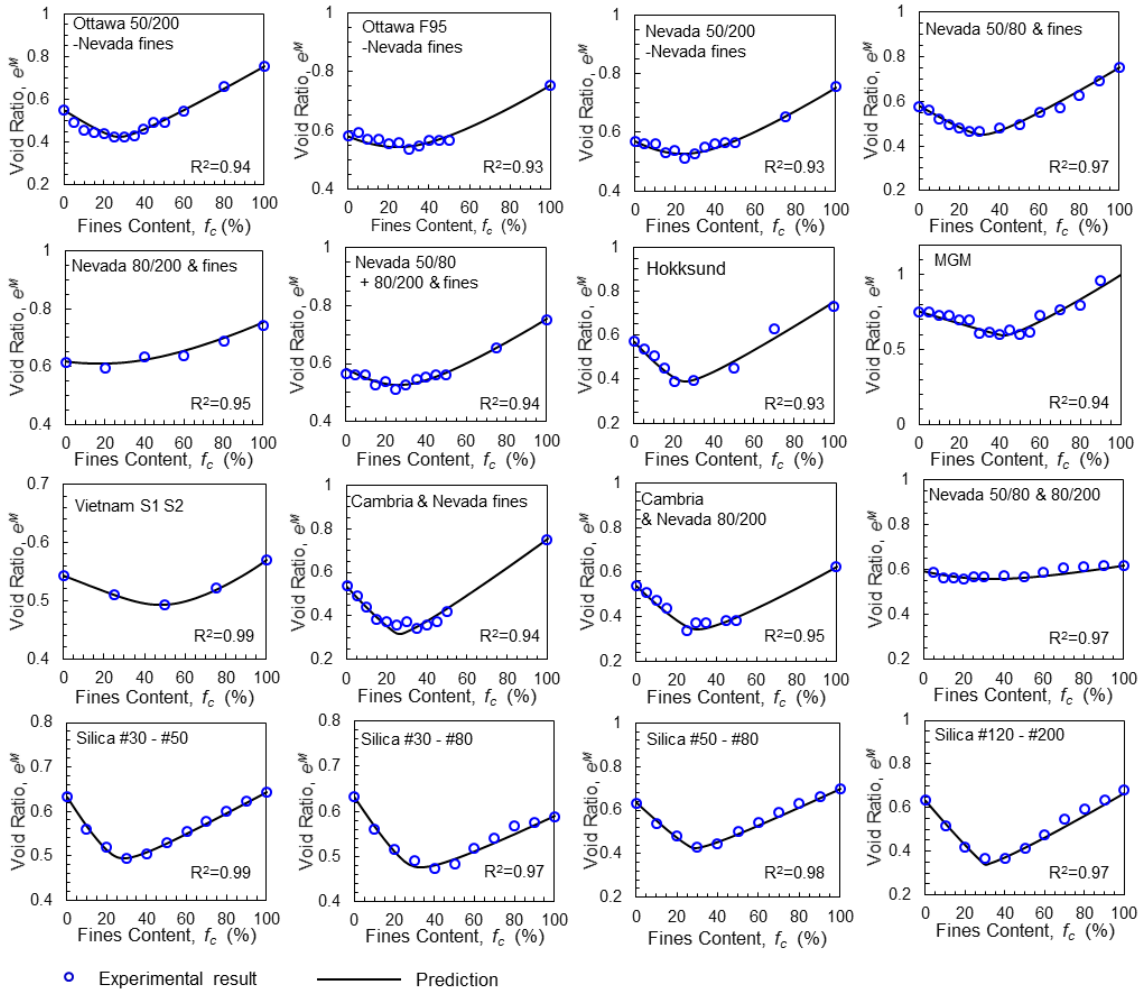

Figure 4.15 Comparison between predicted and measured minimum void ratios for 16 types of sand-silt mixtures (experimental data from Table 4.3)

4.7 Conclusions

DEM shows that the particle packing structure of a binary mixture is a dual-skeleton, which consists of two intertwined skeletons: the large-particle skeleton and the small-particle skeleton. The proportion of the two sub-skeletons depends on the fines content of the packing. In the range of medium fines content, 25%-50%, neither of the sub-skeletons can be considered as dominant. Therefore, the assumption in the existing models that the

mixed packing is either dominated by large-particle skeleton or by small-particle skeleton is not applicable in the middle range of fines content.

The proposed concept of index size is useful to account for the influence of dual-skeleton. Using the index size as a variable of dual-skeleton, the dominant skeleton is no longer limited to be either the large-particle skeleton or the small-particle skeleton. This variable allows both the filling and embedment mixing mechanisms to occur in the same packing, thus the formulations of particle mixing effects are more realistic for the whole range of fines content. This model, overcoming the shortage of previous models, is able to capture the non-linear characteristics of void ratio versus fines content. Evaluation of the model, based on the comparisons between the predicted and measured results for 16 soil mixtures, has demonstrated that the applicability of the model is suitable for natural deposit of sand-silt mixtures.

Table 4.3 List of 16 soil mixtures

Sand/silt Mixture	Ref.	d_1(mm)	d_2(mm)	e_1	e_2	particle shape (coarse)	particle shape (fine)	p	s
Ottawa 50/200-Nevada fines	(Lade & Yamamuro, 1997)	0.2	0.05	0.548	0.754	angular	angular	2.8	1.8
Ottawa F95-Nevada fines		0.16	0.05	0.58	0.754	subround	angular	3.6	2.3
Nevada 50/200-Nevada fines		0.14	0.04	0.57	0.754	subangular	angular	3.5	2.5
Nevada 50/80-Nevada fines	(Lade et al., 1998)	0.21	0.05	0.581	0.754	subangular to angular		3.5	1.6
Nevada 80/200-Nevada fines		0.12	0.05	0.617	0.754	subangular to angular		3.8	2.2
Nevada 50/80 - Nevada80/200+fines		0.17	0.05	0.581	0.754	subangular to angular		3.3	2.3
Hokksund	(Yang, 2004)	0.45	0.04	0.57	0.76	sharp edges, cubical	angular, subangular	3.8	3.8
MGM	(Fourie & Papageorigou, 2001)	0.12	0.01	0.755	1	highly angular to subround	thin and plate-like	13	1.2
Vietnam	(Cho, 2014)	0.37	0.16	0.552	0.583	subangular	subangular	4	1.4
Cambria-Nevada fines	(Lade et al., 1998)	1.5	0.05	0.538	0.754	round	angular	10	3
Cambria-Nevada 80/200		1.5	0.12	0.538	0.624	round	angular	6.5	2.5
Nevada 50/80- Nevada 80/200		0.21	0.12	0.581	0.617	subangular to angular		2.4	1.9
Silica#16-#18 #30-#50	(Yilmaz, 2009)	1.08	0.4	0.633	0.644	subangular	subangular	1.75	2.2
Silica#16-#18 #30-#80		1.08	0.42	0.633	0.59	subangular	subangular	1.9	1.9
Silica#16-#18 #50-#80		1.08	0.26	0.633	0.696	subangular	subangular	2.2	2
Silica#16-#18 #120-#200		1.08	0.1	0.633	0.682	subangular	subangular	4.3	2.2

CHAPTER 5

MODELLING OF MINIMUM VOID RATIO FOR GRANULAR SOIL WITH MULTIPLE SIZES[4]

Minimum void ratio is an important soil property in the practice of geotechnical engineering. It correlates to the volume change tendency, the pore fluid conductivity and the shear strength of the soil. Minimum void ratio for granular soil is highly dependent on its particle size distribution. However, very few analytical models are available for predicting minimum void ratios as a function of particle size distribution. The aim of this paper is to develop a mathematical model that can predict the minimum void ratio for granular soil with arbitrary particle size distribution, based on a more fundamental approach using the concept of dominant particle network. The developed model is evaluated by the simulation results using discrete element method (DEM) and by the experimental results on granular soil with four different gradations to illustrate the applicability of model. The results predicted by the model show very good agreement with the data from DEM simulations and experiments.

List of Notation

The following symbols are used in this chapter:

α, β the coefficients of the relationship between minimum void ratio and particle size;

μ friction coefficient;

[4] This chapter has been published as a standalone paper: Chang, C. S., Deng, Y., & Yang, Z. (2017). Modeling of Minimum Void Ratio for Granular Soil with Effect of Particle Size Distribution. *Journal of Engineering Mechanics*, *143*(9), 04017060.

a_{ij} filling coefficient for j-th component filled into the i-th dominant packing;

b_{ij} embedment coefficient for j-th component embeded into the i-th dominant packing;

C_u uniformity coefficient;

$d_1, d_2 \ldots . d_n$ the particle sizes from coarse to fine for a packing consisting of n-size particles;

$\hat{d}_i , \hat{d}_{i+1}$ the maximum and minimum particle sizes of the i-th division of the gradation curve;

e, e_{min} the void ratio of a packing, the minimum void ratio of a packing;

e_i, e^M the minimum void ratio of a packing that contains particles of single size d_i, the minimum void ratio of a multisize particle packing;

e_i^M the estimated minimum void ratio of a multisize particle packing assuming that the i-th component is the dominant particle size;

$e_{min}^{Mix.i}$, $\hat{e}_{min}^{Mix.i}$ the measured and the predicted values of minimum void ratio for the i-th soil mixture;

G_s specific gravity of the solid particles in the soil;

N_b the total number of particles with centroids located within the spherical domain in DEM;

P_i percent finer by weight corresponding to size $\hat{d}_i$;

p, s coefficients accounting for particle size effect;

S_i the solid phase for i-th component in the packing;

V^a, V^b the increase void phase due to filling and embedment;

V^{ball} the volume occupied by the particles within the spherical domain in DEM;

$V^{overlap}$ the volume of overlaps between particles within the spherical domain in DEM;

$V^{(P)}$ the volume of the particle (P) with centroid within the spherical domain in DEM;

V_i^r the residual void phase of the i-th base packing after filling of small particles;

$(V_s)_i$ the solid volume of the particles of i-th size;

$(V_s)_T$ the total solid volume of the multisize particle packing;

V^{sphere} the total volume of a spherical domain in DEM;

$(V_v)_i$ the void volume of a packing containing particles of single size d_i;

V_v total void volume of mixture;

$y_1, y_2, \ldots . y_n$ the solid volume fractions of each particle sizes;

y_L, y_M, y_S the solid volume fractions of large particles, medium particles and small particles respectively in a ternary packing;

$(\Delta V_v^a)_{ij}$ the increase in void volume of the i-th base packing as a result of j-th particle filling;

$(\Delta V_v^b)_{ij}$ the increase in void volume of the i-th base packing as a result of j-th particle embedment;

δ_e the root of square sum of residuals for $e_{\min}$.

5.1 Introduction

Granular soil consists of soil particles of different sizes. Research on soil mechanics, for several decades, revealed that the particles size distribution of granular soils has significant effects on its mechanical properties (Aberg, 1992; Bobei et al., 2009; Cubrinovski & Ishihara, 2002; Fuggle et al., 2014; Miura et al., 1997; Peters & Berney, 2010; Selig & Ladd, 1973). This is not surprising because particle size distribution greatly influences the configuration of packing structure, which is an important factor governing the mechanical properties of materials. The importance of particle size distribution has also been noted in many branches of industry, such as ceramics processing (Reed, 1995), powder metallurgy (Smith, 2003), and concrete mixes (Powers, 1968).

Studies of packing density as a function of particle size distribution were sparsely published around 1930's. Research interest of high-density packing of ceramics and metal particles received sizable attention around 1954, for the reason of impetus of atomic energy and space research. However, the research works were mainly considering packing of uranium oxide and focusing on the optimum particle size distribution for maximum packing density (McGeary, 1961). More recently, there are studies in concrete mixture and powder mixture (de. Larrard, 1999; Stovall, de Larrard, et al., 1986; Yu & Standish, 1987). These studies usually concern about mixtures with two or three particle sizes.

Soils, as a natural deposit, covers a large range of particle sizes and shapes. The predictive methods for maximum packing density of soil with different sizes of particles are mostly empirically based. The earlier empirical models can be found by Humphres (1957) and by the American Association of State Highway and Transportation Official (AASHTO 1986). These two models were studies by Fragaszy and Sneider (1991) for

improving compaction control of granular fill. More recently, Cubrinovski and Ishihara (2002) examined a large number of test data on silty-sand and presented a set of empirical equations to show the influence of fines content on the magnitude of minimum void ratio.

There are very few analytical models for predicting minimum void ratio (corresponding to maximum packing density). Kezdi (1979) outlined an analytical method to estimate the minimum porosity for sand-silt mixtures. The method is based on the ideal situation that the pore space among sand grains can be effectively filled by silt particles without alternating the packing structure of sand. Thus, the method often overestimates the experimentally measured maximum packing density (Vallejo, 2001). In association with the liquefaction potential of silty-sand, Lade et al. (1998) also proposed an analytical method for predicting the minimum void ratio of silty sand. However, this method is also based on the ideal situation used by Kezdi (1979), thus overestimates the maximum packing density. To avoid this limitation, Chang et al. (2015) have proposed an analytical method for predicting the minimum void ratio for sand-silt mixtures. However, the analytical models mentioned above have been focused on sand-silt mixtures, which are considered as packings comprised of particles with two different sizes. These models cannot be applied to soils with wide range of particle sizes.

Apart from these studies, computer simulation analyses using discrete element method have also been implemented to study the void ratios of particle mixtures (An, 2013; Fuggle et al., 2014). The trend of computer simulation results resembles that obtained from experimental tests. However, the discrete element method cannot handle the case with large size ratio of particles. The commonly used particle size ratio is less than 10. Due to the wide range of particle sizes in real granular soil, the size of a large particle can be easily

several hundred times larger than that of a small particle. Therefore, computer simulation methods are not yet feasible of predicting the minimum void ratio for real soil with wide gradations.

In this chapter, an analytical method is developed to have the capacity of predicting minimum void ratio for mixtures of multisize particles. The developed model is verified by the simulation results of discrete element method (DEM) for a ternary packing, and by the experimental results of real soils with four different particle size distributions.

5.2 Model for Packing with Multiple Particle Sizes

5.2.1 Packing Structure Descriptor

For a packing comprised of n-size particles, the particle sizes from coarse to fine are denoted by $d_1, d_2 \ldots . d_n$. The volume fractions of each particle sizes are denoted by $y_1, y_2 \ldots . y_n$. The minimum void ratio of the multisize particle packing is denoted as e^M, whereas the minimum void ratio for a packing containing particles of single size d_i, is denoted as e_i. Thus for a multisize particle packing, there exist n values of e_i (i.e. $e_1, e_2 \ldots . e_n$), each e_i corresponding to a particle size d_i.

The purpose of this proposed model is to estimate the value of e^M based on the set of values $\{e_1, e_2 \ldots . e_n\}$. Intuitively, the theory of mixtures is the first choice for estimating the void ratio of the mixture. However, it is clearly that the theory of mixtures cannot provide the correct solution because the measured results are significantly below the Reuss bound (lower bound) of the mixture-theory, although the Voigt bound (upper bound) seems to be not violated (Chang et al., 2015). The theory of mixtures is not applicable to soils

because it does not account for the mix mechanism of particles, for instance, the filling of small particles into voids and the embedment of large particles into smaller particles.

In consideration of the mix mechanism, we first select a dominant particle size d_i. The packing containing particles of single size d_i is regarded as the base packing, which is used for building up the multisize particle packing. The mix mechanism is accounted in the process of building up the multisize particle packing. The particles with sizes smaller than the "dominant particle size (i.e d_i.)" are regarded as fillers into the voids of the base packing, whereas the particles with sizes greater than the "dominant particle size" are regarded as inclusions embedded in the base packing, as schematically shown in Fig. 5.1(a). The schematic plot of Fig. 5.1(a) is termed packing descriptor. Because the dominant particle size can be anyone of the n-sizes of particles. Thus, many possible descriptors can be established for the packing. For example, in a 7-size packing mixture, seven possible descriptors can be established. Two out of the seven descriptors are shown as examples in Fig. 5.1(b) and Fig. 5.1(c). For Fig. 5.1(b), d_3 is the dominant particle size. For Fig. 5.1(c), d_4 is the dominant particle size.

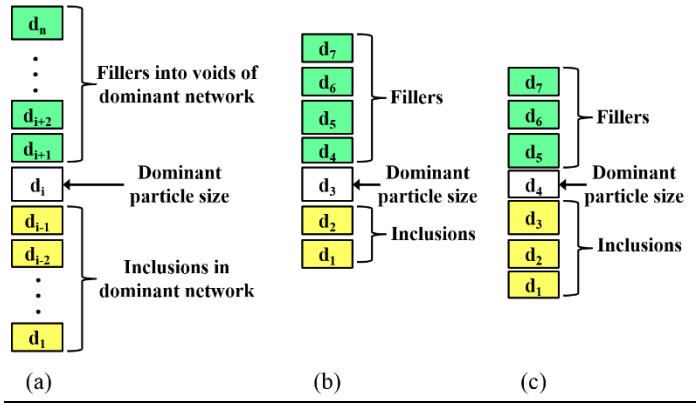

Figure 5.1 (a) Schematic plot for the packing structure descriptor of a multi-size mixture, (b) one example of the descriptor for a 7-size mixture, (c) another example of the descriptor for a 7-size mixture

The descriptor designates the presence of particles as filler or embedment in a packing structure, thus can be regarded as a genetic code of the packing structures. Each descriptor has a connection to the underlying characteristics of a category of packing structures. For a simple case of binary packing, two descriptors can be generated. The typical packing structures corresponding to these two descriptors are shown in Fig. 5.2a. Similarly, for a ternary packing, the typical packing structures and their corresponding descriptors are shown in Fig. 5.2b. In Fig. 5.2a, it is easy to see the contrast of the two packing structures, and identify their descriptors. However, in Fig. 5.2b, it is not as evident to identify the descriptors from packing structures. Obviously, for some cases, especially for a multisize particle packing, the packing structures are very complex and it is not easy to identify their descriptors.

It is noted that a descriptor contains only simple information, which is not meant to have direct association to a complex packing structure. On the contrary, the descriptors are delineated to classify complex packing structures into manageable categories so that the complex problem can be simplified for analysis. In next section, we use the concept of phase-diagrams to categorize packing structures. Furthermore, we describe the connections between descriptors and phase diagrams.

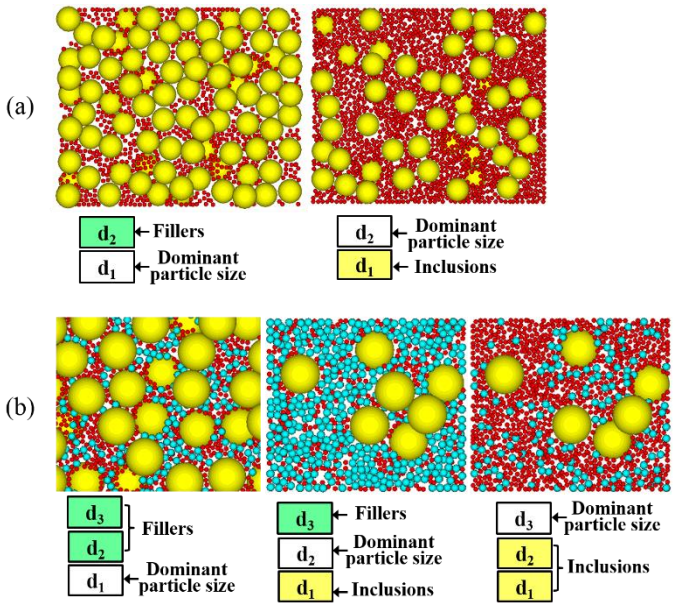

Figure 5.2 Packing structures and descriptors for (a) binary packing and (b) ternary packing

5.2.2 Phase Diagram and Packing Descriptor

The phase-diagram shows the composition of void and solid phases. In what follows, we describe the process of building up a phase-diagram based on a descriptor.

Let d_i be the dominant particle size of a multisize particle mixture, the phase diagram can be presented in Fig. 5.3. Fig.5.3a shows the phase-diagram of the base packing, which yields a void ratio e_i. For building up the phase diagram of the multisize particle packing, particle sizes other than d_i are mixed into the base packing. It is noted that the subscript of d_i has the order from coarse to fine. Thus, the particles smaller than the dominant particle size d_i are denoted as d_j ; $j=i+1,n$. The particles larger than the dominant particle size are denoted as d_i ; $j=1, i-1$. The mechanism of mix includes following:

(1) Filling of particles smaller than d_i into the voids, which causes the following effects:

a. Increase of solid volume: the amount of solid volume increase is the summation of all particles smaller than i-th particle size (i.e. $\sum_{j=i+1}^{n}(V_s)_j$), where $(V_s)_j$ is the solid volume of j-th component.

b. Decrease of void volume due to particles filled into void space: the amount of void volume decrease is the summation of all particles smaller than i-th particle size (i.e., $\sum_{j=i+1}^{n}(V_s)_j$)

c. Increase of void volume due to packing disturbance as a result of filling: the amount of void volume increase is denoted by $\sum_{j=i+1}^{n}(\Delta V_v^a)_{ij}$, where $(\Delta V_v^a)_{ij}$ is the change in void volume due to filling of the j-th component into the i-th dominant packing.

(2) Embedment of particles larger than d_i into the basic packing

a. Increase of solid volume: the amount of solid volume increase is the summation of all particles larger than i-th particle size (i.e., $\sum_{j=1}^{i-1}(V_s)_j$)

b. Increase of void volume due to packing disturbance as a result of embedment: the amount of void volume increase is denoted by $\sum_{j=1}^{i-1}(\Delta V_v^b)_{ij}$, where $(\Delta V_v^b)_{ij}$ is the change in void volume due to embedment of the j-th component into the i-th dominant packing.

Fig. 3b shows the phase-diagram of the limiting case, in which the increase of void volumes described above are zero as a result of filling and embedment process. That gives

$$\sum_{j=i+1}^{n}(\Delta V_v^a)_{ij}=0 \quad ; \quad \sum_{j=1}^{i-1}(\Delta V_v^b)_{ij}=0 \tag{5.1}$$

Thus, the void ratio of the mixture e_i^M (the subscript i refers to the dominant particle size d_i) for the limiting case can be expressed as:

$$e_i^M=\frac{(V_v)_i-\sum_{j=i+1}^{n}(V_s)_j}{(V_s)_i+\sum_{j=1}^{i-1}(V_s)_j+\sum_{j=i+1}^{n}(V_s)_j} \tag{5.2}$$

Note that the denominator of Eq. (5.2) is the total volume of solid $(V_s)_T$. i.e.,

$$(V_s)_T=(V_s)_i+\sum_{j=1}^{i-1}(V_s)_j+\sum_{j=i+1}^{n}(V_s)_j=\sum_{j=1}^{n}(V_s)_j \tag{5.3}$$

Fig. 5.3c shows a general case that the base packing is disturbed during mixing. The increase of void volumes described above are non-zero as a result of filling and embedment process. Thus, based on the phase diagram for a multisize particle packing in Fig. 5.3c, the void ratio of the mixture e_i^M is given by,

$$e_i^M=\frac{(V_v)_i+\sum_{j=1}^{i-1}(\Delta V_v^b)_{ij}+\sum_{j=i+1}^{n}(\Delta V_v^a)_{ij}-\sum_{j=i+1}^{n}(V_s)_j}{(V_s)_i+\sum_{j=1}^{i-1}(V_s)_j+\sum_{j=i+1}^{n}(V_s)_j} \tag{5.4}$$

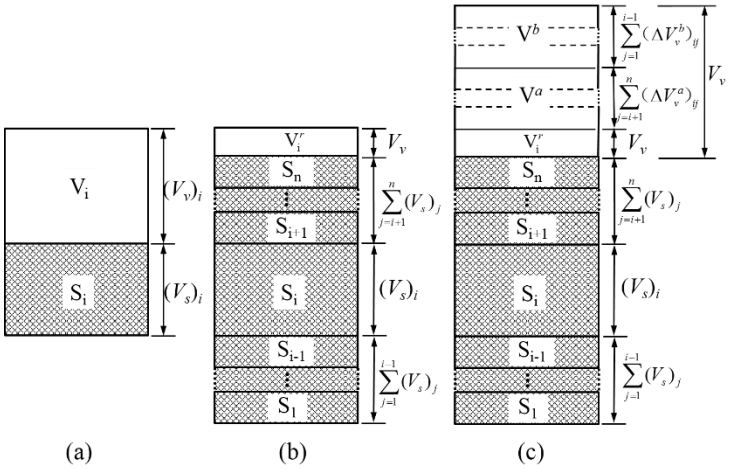

Figure 5.3 Phase diagrams for the packing structure of a multi-size mixture dominant by *i*-th particle size: (a) base packing structure (before the other components are added); (b) mixture (limiting case); (c) mixture (general case)

In this multisize particle packing, the values of $(\Delta V_v^a)_{ij}$ and $(\Delta V_v^b)_{ij}$ are the change in void volumes due to filling and embedment of the j-th component into the i-th base packing. Thus, the values of $(\Delta V_v^a)_{ij}$ and $(\Delta V_v^b)_{ij}$ are proportional to the amount of the solid volume of j-th component $(V_s)_j$. The change in void volumes depend on many other factors, specifically, the geometric properties of particles. For convenience, we express the change of void volumes due to packing disturbance in the following form:

$$(\Delta V_v^a)_{ij} = \big(1 - a_{ij}\big)\big(1 + e_j\big)(V_s)_j \quad (\text{j} > \text{i}) \qquad \text{filling process} \qquad (5.5)$$

$$(\Delta V_v^b)_{ij} = \big(1 - b_{ij}\big)e_j(V_s)_j \qquad (j < i) \qquad \text{embedment process} \qquad (5.6)$$

The value of both coefficients a_{ij} and b_{ij} are between 0 and 1. The parameter a_{ij} is termed filling coefficient. The parameter of b_{ij} is termed embedment coefficient. They are dependent on the geometric properties of particles and need to be calibrated from test results. The condition of $a_{ij} = 1$ and $b_{ij} = 1$ corresponds to the lower bound case, in which the change of void volumes are zero as a result of filling and embedment process.

On the other hand, the condition of $a_{ij} = b_{ij} = 0$ corresponds to the upper bound case, in which the change of void volumes is highest as a result of filling and embedment process. Eqs (5.5) and (5.6) were constructed in such a way that when $a_{ij} = b_{ij} = 0$, the values of $(\Delta V_v^a)_{ij}$ and $(\Delta V_v^b)_{ij}$ substituted into Eq. (5.4), would yield a value of e_1^M equivalent to the Voigt upper bound, as shown in Eq. (5.7).

$$e_i^M = \frac{\sum_{j=1}^{n} e_j (V_s)_j}{\sum_{j=1}^{n} (V_s)_j} = \sum_{j=1}^{n} e_j y_j \tag{5.7}$$

in which, the solid volume fractions are defined as

$$y_j = (V_s)_j / (V_s)_T \tag{5.8}$$

where $(V_s)_T$ is the total solid volume of the multisize particle packing defined in Eq. (5.3).

5.2.3 Equations for Minimum Void Ratio of a Multisize Particle Packing

Substituting Eqs. (5.5) and (5.6) into Eq. (5.4), the void ratio of the mixture can be expressed as

$$e_i^M = \sum_{j=1}^{n} e_j y_j - \sum_{j=1}^{i-1} b_{ij} e_j y_j - \sum_{j=i+1}^{n} a_{ij} (1 + e_j) y_j \tag{5.9}$$

$$e^M = Max \left\{ e_i^M, i = 1, n) \right\} \tag{5.10}$$

It is noted that the void ratio e_i^M in Eq. (5.9) is derived assuming that d_i is the dominant particle size. Since *i* varies from 1 to n, thus n numbers of e_i^M can be computed from Eq. (5.9). Out of the n numbers of e_i^M, only one is the true solution. If the selected "dominant particle size" is not appropriate, then there would either be excess of filler

particles for the available voids in the base packing; or there would be too much inclusions for the available volume of the base packing. Out of the n numbers of e_i^M, the highest e_i^M is the easiest outcome to be achieved during mixing because it consumes the least energy. Thus, the true dominant size is defined as the one that corresponds to the highest void ratio out of the n numbers of e_i^M calculated from Eq. (5.9). It is noted that Dominant particle size does not necessarily mean that the particles of that size have the highest volume fraction of all particle sizes.

The coefficients a_{ij} and b_{ij} are associated to the disturbance of the i-th base packing due to the mix of j-th component. Their values are significantly influenced by the particle sizes of i-th and j-th components, d_i and d_j. The values of a_{ij} and b_{ij} can be expressed in the following form:

$$a_{ij} = \left(1 - \frac{d_j}{d_i}\right)^p \ (for\ j > i) \tag{5.11}$$

$$b_{ij} = \left(1 - \frac{d_i}{d_j}\right)^s \ (for\ j < i) \tag{5.12}$$

Eq. (5.11) is associated to the filling of j-th component particles into i-th base packing, thus $d_j < d_i$ or $0 < d_j/d_i < 1$. On the other hand, Eq. (5.12) is associated to the embedment process, thus $d_j > d_i$ or $0 < d_i/d_j < 1$. The extreme conditions are examined below.

(1) $d_j \ll d_i$: The j-th particle size is very small so that the small particles can be effectively filled into the void space of i-th base packing. Eq. (5.11) gives $a_{ij} = 1$, which is the lower bound case.

(2) $d_j \gg d_i$: The j-th particle size is very large compared to the particles of i-th base packing. Eq. (5.12) gives $b_{ij} = 1$, which is also the lower bound case.

(3) $d_i = d_j$: The j-th particle size is equal to particle size of i-th base packing. Eqs. (5.11) and (5.12) lead to $a_{ij} = b_{ij} = 0$, which represents the upper bound case.

These two equations provide the range of $0 \le a_{ij} \le 1$ and $0 \le b_{ij} \le 1$.

The values of p and s in Eqs. (5.5.11) and (5.12) are influenced by the shape of particles. Since particle shapes are not commonly quantitatively measured in engineering practice, in this model, the values of p and s are treated as material parameters, which are calibrated from measured void ratios from experiments.

5.2.4 Reduced to Binary and Ternary Packing

(1) Binary packing

The derived model for multisize particle packing can be reduced to a simple model for binary packing. For a binary mixture, let y_1 and y_2 be the solid volume fraction for large and small particles respectively. Equations (5.9) – (5.10) lead to the following expressions:

$$e_1^M = e_1 y_1 + e_2 y_2 - a_{12}(1 + e_2) y_2 \quad \text{for dominant particle size} = d_1, \text{ and} \quad (5.13)$$

$$e_2^M = e_1 y_1 + e_2 y_2 - b_{21} e_1 y_1 \quad \text{for dominant particle size} = d_2. \quad (5.14)$$

The higher value is the true void ratio of the mixture, i.e. $e^M = Max\ \{e_1^M,\ e_2^M\}$.

(2) Ternary packing

The derived model can also be reduced for a ternary packing. For a ternary mixture, let y_1 , y_2 and y_3 be the solid volume fraction for large, medium and small particles respectively. Equations (5.9) – (5.10) lead to the following expression:

For dominant particle size = d_1:

$$e_1^M = e_1 y_1 + e_2 y_2 + e_3 y_3 - a_{12}(1+e_2) y_2 - a_{13}(1+e_3) y_3 \tag{5.15}$$

For dominant particle size = d_2:

$$e_2^M = e_1 y_1 + e_2 y_2 + e_3 y_3 - b_{21} e_1 y_1 - a_{23}(1+e_3) y_3 \tag{5.16}$$

For dominant particle size = d_3:

$$e_3^M = e_1 y_1 + e_2 y_2 + e_3 y_3 - b_{31} e_1 y_1 - b_{32} e_2 y_2 \tag{5.17}$$

The higher value is the true void ratio of the mixture, i.e. $e^M = Max\{e_1^M,\ e_2^M, e_3^M\}$.

5.3 Evaluation of the New Model

5.3.1 Evaluation of the New Model Using DEM Simulation

Densification of granular material has been simulated using DEM by many investigators (e.g., An et al., 2009). However, the process of these DEM simulations did not follow the procedure recommended by American Society for Testing and Materials (ASTM) for determining the minimum void ratio. The present DEM simulation process follows the procedures described in ASTM D4253 (ASTM 2006) for minimum void ratio determination; the standard mold (diameter of 152.4mm, height of 155.2mm and nominal volume of 2830 $cm^3 \pm 42.45\ cm^3$) is used in simulation (Fig. 5.4). The packing is densified by applying a seating load (13.8 ± 0.1 kPa), and then vertical vibration is applied.

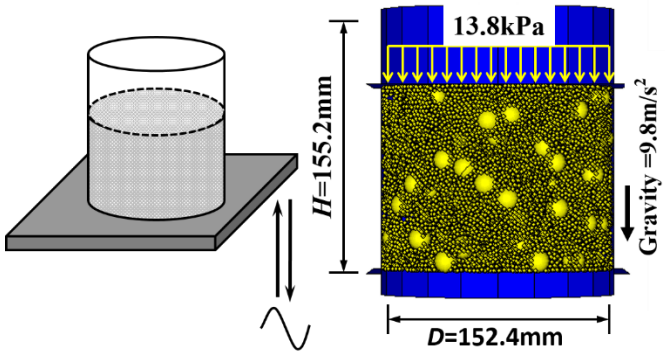

Figure 5.4 The sketch of ASTM procedure for obtaining minimum void ratio in DEM modeling

The basic model parameters used in the DEM simulations are given in Table 5.1. The material parameters were selected mainly based on past successful experience in the literature. An aggregate elastic modulus of 30 GPa, a rigid wall stiffness of 300 GPa (stiffness of simulation container), an aggregate-to-aggregate contact friction coefficient of $\mu = 0.5$ corresponding to an angle of internal friction of 27°, a density of 2660 kg/m3, were found to be appropriate for the particles (Shen & Yu, 2011) and are used in the present paper. A simplified Hertz–Mindlin law at contacts is used.

Table 5.1 Parameters used in DEM

Parameter	Value
Young's modulus *E* (GPa)	30
Poisson's ratio	0.3
Friction coefficient	0.5
Normal critical damping ratio	0.03
Particle density (kg/m^3)	2660
Wall stiffness (GPa)	300

Four particle sizes are considered in the DEM simulation, i.e. 15.2 mm, 5.07 mm, 3.04 mm, and 2.03 mm. Depending on the combination of particle sizes, the packing within the mold consists of about 1,000-300,000 particles. The packing is densified by applying

a seating load of 13.8 ± 0.1 kPa, and then vertical vibration is applied to the table. The values of vibration amplitudes and frequencies vary for each particle packing. The values were selected based on the trail procedures outlined in the ASTM D4253 standard (ASTM 2006). The value used for pure large particle packing is 1.52 mm and 32 Hz, respectively; the value for pure small particle packing is 0.4 mm and 62 Hz, respectively. Typical values are between these ranges.

The results of the DEM simulations are plotted in terms of void ratio e and coordination number C_n of the packing. The void ratio e of the packing are measured within a spherical domain, which are calculated by the following equation:

$$e = \frac{V^{sphere} - V^{ball}}{V^{ball}} \tag{5.18}$$

where V^{sphere} is the total volume of the spherical domain, and V^{ball} is the volume occupied by the particles within the spherical domain. Note that the particles can be overlapped in the discrete element method, thus the volume V^{ball} is computed by:

$$V^{ball} = \sum_{N_b} V^{(P)} - V^{overlap} \tag{5.19}$$

where N_b is the total number of particles with centroids contained within the spherical domain; $V^{(p)}$ is the volume of the p-th particle within the spherical domain; and $V^{overlap}$ is the volume of overlaps between particles within the spherical domain.

Typical examples of computed void ratio are shown in Fig. 5.5. During vibration, fluctuations were observed. As time increases, the sample is continuously densified. After 2 seconds, the void ratio starts to reach the asymptotic level. When the vibration stopped, particles gradually settled down and form a stable packing. Fig. 5.5 indicates that 2.5 seconds duration of vibration is long enough for void ratio to reach the asymptotic level.

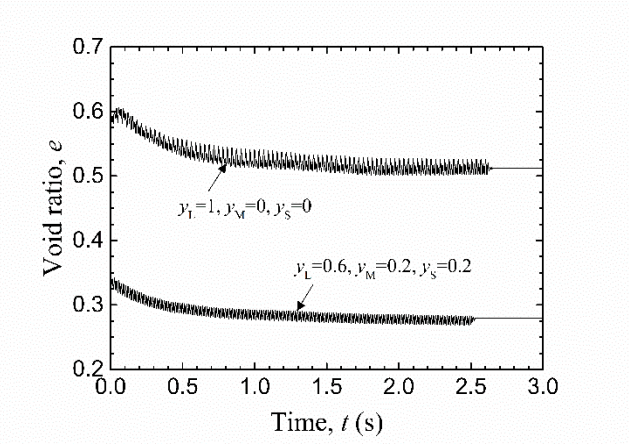

Figure 5.5 Typical results obtained from DEM for void ratio versus time of vibration

DEM simulation was conducted to obtain the minimum void ratios for 7 mixtures of two particle diameters, 15.2 mm and 5.07 mm with various of fines contents, as listed in Table 5.2. DEM simulation was also conduct to obtain the minimum void ratios for 22 mixtures of three particle diameters, 15.2 mm (large particles, L), 3.04 mm (medium particles, M), 2.03 mm (small particles, S) with various of volume fractions y_L, y_M, and y_S, as listed in Table 5.3.

Table 5.2 The minimum void ratios for mixtures of two particle diameters, 15.2 mm and 5.07 mm obtained from DEM simulation and from model prediction

Case	Fines content (%)	DEM simulation e_{min}	Model prediction e_{min}	d_i(dominant) (mm)	$\frac{V^{overlap}}{V^{ball}}$(%)
1	0	0.509	0.509	15.2	0.270
2	12.5	0.450	0.446	15.2	0.215
3	25	0.383	0.382	15.2	0.174
4	30	0.369	0.357	15.2	0.173
5	50	0.409	0.400	5.07	0.178
6	75	0.473	0.460	5.07	0.208
7	100	0.521	0.521	5.07	0.239

The ratio of the overlapped volume to the total particle volume and the minimum void ratios obtained from DEM simulation for these mixtures are also listed in Table 5.2 and Table 5.3, compared with the predicted void ratios calculated using the model proposed in last section. The calculation procedures are described later.

In Table 5.2 and Table 5.3, there are four mono-size packing with particle sizes 15.2 mm, 5.07 mm, 3.04 mm, and 2.03 mm. Their minimum void ratios e_{min} are 0.509, 0.521, 0.551, and 0.551 in DEM simulations. For the packing of large spheres is 0.509 and for the packing of small spheres is 0.551. Since both packings are made of spheres, the void ratios are expected to be same if the packing structures are same. The difference in packing structures may be caused by two factors: (1) the particle size difference, and (2) the difference in total area of inter-particle contact. The particle size difference leads to the differences in the ratios of particle size to mold size, thus causes different degrees of boundary effects. The particle size difference also leads to the differences in particle mass and contact stiffness, which in turn affect the natural frequencies of the two packing systems. The total contact area difference causes the difference in friction loss when particles are under vibration loads to reach the minimum void ratio. These two factors may attribute to the difference in e_{min}.

In Table 5.2, there are 7 binary mixtures. In Table 5.3, there are 10 binary mixtures made of large/medium particle sizes (LM); 5 binary mixtures made of large/small particle sizes (LS); and 5 binary mixtures made of medium/small particle sizes (MS). The minimum void ratios of these binary mixtures obtained from DEM simulations are shown in symbols on Fig. 5.6 with respect to fines content for four different particle size ratios (i.e., 7.5, 5.0,

3.0, 1.5). The fines content for a binary packing is the volume fraction of the smaller particles.

Table 5.3 The minimum void ratios for mixtures of three particle diameters, 15.2 mm (L), 3.04 mm (M), 2.03 mm (S) obtained from DEM simulation and from model prediction

Case	Weight fractions			DEM simulation	Model prediction	d_i (dominant) †	$\frac{V^{overlap}}{V^{ball}}$
	y_L	y_M	y_S	e_{min}	e_{min}		(%)
1	1	0	0	0.509	0.509	d_1	0.270
2	0.90909	0.09091	0	0.442	0.432	d_1	0.211
3	0.76923	0.23077	0	0.317	0.314	d_1	0.116
4	0.66667	0.33333	0	0.299	0.29	d_2	0.148
5	0.58824	0.41176	0	0.311	0.320	d_2	0.134
6	0.5	0.5	0	0.344	0.355	d_2	0.140
7	0.4	0.6	0	0.385	0.394	d_2	0.166
8	0.33333	0.66667	0	0.407	0.420	d_2	0.173
9	0.16667	0.83333	0	0.469	0.486	d_2	0.209
10	0	1	0	0.551	0.551	d_2	0.240
11	0.8333	0	0.1667	0.326	0.335	d_1	0.167
12	0.657	0	0.343	0.26	0.26	d_3	0.104
13	0.44444	0	0.55556	0.345	0.355	d_3	0.128
14	0.22	0	0.78	0.436	0.454	d_3	0.178
15	0	0	1	0.551	0.551	d_3	0.236
16	0	0.75	0.25	0.522	0.526	d_2	0.230
17	0	0.5	0.5	0.521	0.508	d_3	0.226
18	0	0.25	0.75	0.532	0.53	d_3	0.232
19	0.323172	0.348755	0.328073	0.378	0.392	d_2	0.149
20	0.6	0.2	0.2	0.279	0.296	d_2	0.117
21	0.1927	0.6055	0.2018	0.449	0.455	d_2	0.191
22	0.1927	0.2018	0.6055	0.448	0.448	d_3	0.180

†d_1=15.2 mm, d_2=3.04 mm, d_3=2.03 mm

According to the DEM results for binary mixtures of four different size ratios, a set of values of a_{ij} and b_{ij} can be calibrated based on Eqs (5.13) and (5.14). The four set of values of a_{ij} and b_{ij} are shown in symbols on Fig. 5.8, which can be used to determine a

set of values of p and s based on Eqs. (5.11) and (5.12). The values are: $p = 2.51$ and $s = 1.68$.

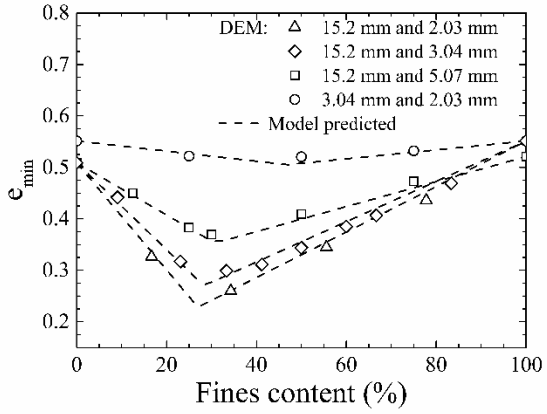

Figure 5.6 The minimum void ratios computed by DEM and by the proposed model for binary mixtures

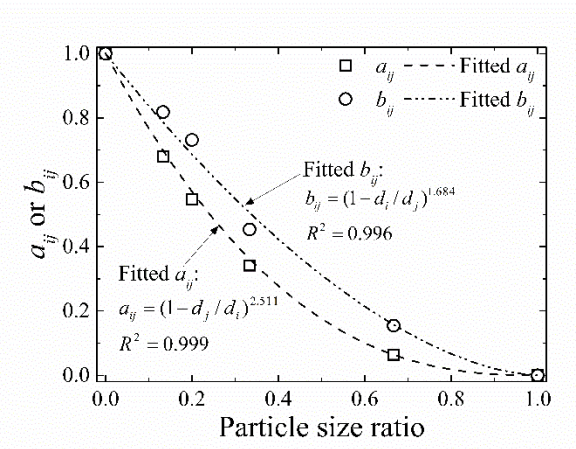

Figure 5.7 The values of *p* and *s* obtained from the results of DEM simulation

After p and s are obtained, the ternary mixtures for any fractions of three components can be predicted. The predicted values of minimum void ratios are plotted in a ternary plot and compared with that from DEM results in Fig. 5.8. The results show very good agreement.

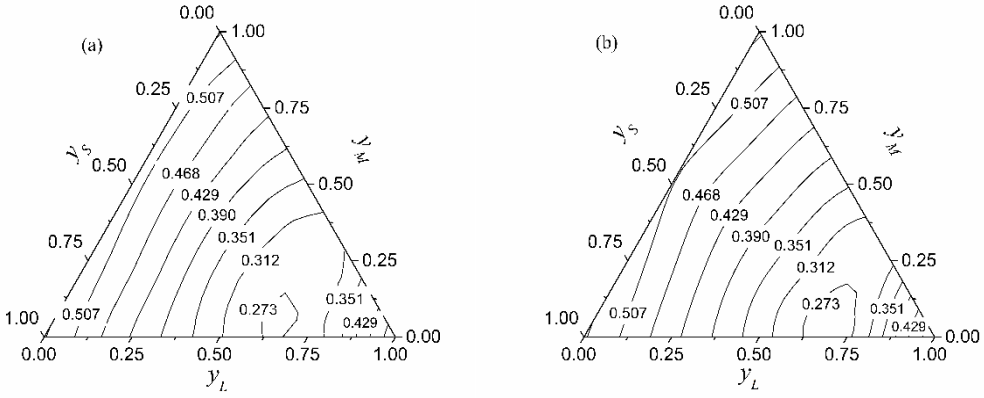

Figure 5.8 Comparison of the minimum void ratios computed by (a) DEM Simulation and (b) the proposed model for the ternary packing

5.3.2 Evaluation of the New Model Using Experimental Results of Real Soil

In this section, the experimental results for sand mixtures were used to evaluate the model. The experimental results were reported by Youd (1973) on crushed basalt (Basalt Rock Quarry, Napa, Calif.) fractioned and combined into 4 proportioned mixes. Fig. 5.9 presents the 4 gradation curves for these four mixes. The specific gravity, particle shape and the coefficient of uniformity (C_u) for the particles of each soil mixture are listed in Table 5.4. Each mixture was compacted to reach the maximum dry density by repeated straining in simple shear procedure. The experimentally measured minimum void ratios corresponding to the maximum dry densities for each mixture are also listed in Table 5.4. Regarding the four mixes, the mean particle size for all four mixes is 0.7mm; and the range of particle size distribution is between $C_u = 1.4 – 8$. According to the Unified Classification System, particle size distribution with $C_u > 4$ is considered to be widely graded. Among the four mixes, two of them are considered to be widely graded.

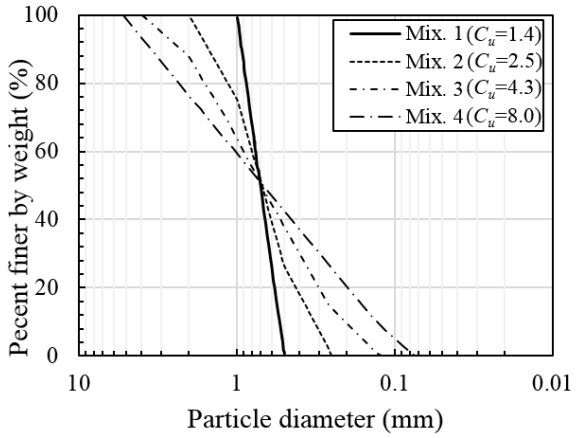

Figure 5.9 Gradation curves of four types of sand mixtures. (Data obtained from Youd, 1973)

Table 5.4 Properties of four different sand mixes. (Data obtained from Youd, 1973)

Mix. No.	G_s	C_u	Roundness	e_{min}
1	2.85	1.4	0.19	0.705
2	2.85	2.5	0.19	0.590
3	2.85	4.3	0.19	0.480
4	2.85	8.0	0.19	0.439

(1) *Discretization*

The soil gradation, as shown in Fig. 5.9, are continuous curves with respect to particle size. Therefore, in order to treat the soil as a multisize particle packing, we need to approximate the soil as an n-component mixture, whereas each component is assumed to be of uniform particle size. Consequently, the gradation curve needs to be discretized by dividing it into n-components. The division process is detailed below (Fig. 5.10). Suppose that the range of particle size is from $\hat{d}_{n+1}$ to $\hat{d}_1$ for a soil mixture. Divided by n divisions, there are $n + 1$ ticks: $\hat{d}_1, \ldots \hat{d}_n, \hat{d}_{n+1}$ (subscript order is from large size to small size). The i-th division has a size range from $\hat{d}_{i+1}$ to $\hat{d}_i$. Using a geometric series for the values of

the tick marks, so that for all divisions, the ratios of $\hat{d}_i / \hat{d}_{i+1}$ are constant. This ratio can be determined from the total range $\hat{d}_1$, $\hat{d}_{n+1}$ and the number of divisions *n*, given by

$$\frac{\hat{d}_i}{\hat{d}_{i+1}} = \left(\frac{\hat{d}_1}{\hat{d}_{n+1}} \right)^{1/n} \qquad (i = 1,2,\ldots n+1) \tag{5.20}$$

Thus, the i-th tick mark $\hat{d}_i$ is related to $\hat{d}_1$, $\hat{d}_{n+1}$ and *n* by

$$\hat{d}_i = \hat{d}_1 \left(\frac{\hat{d}_{n+1}}{\hat{d}_1} \right)^{(i-1)/n} \qquad (i = 1,2,\ldots n+1) \tag{5.21}$$

The particle size d_i for the i-th division is the geometric average of its particle size range.

$$d_i = \sqrt{\hat{d}_i \hat{d}_{i+1}} \tag{5.22}$$

The soil can thus be considered as a mixture consisting of n-component particles with particle size d_i (i = 1 to n). Each component is represented by a division of the gradation curve. The solid volume fraction y_i for each component in the mixture can be calculated from the gradation curve as shown in Fig. 5.10:

$$y_i = P_i - P_{i+1} \tag{5.23}$$

where P_i is the value on the vertical axis of the gradation curve (in percentage) corresponding to size $\hat{d}_i$ on the horizontal axis.

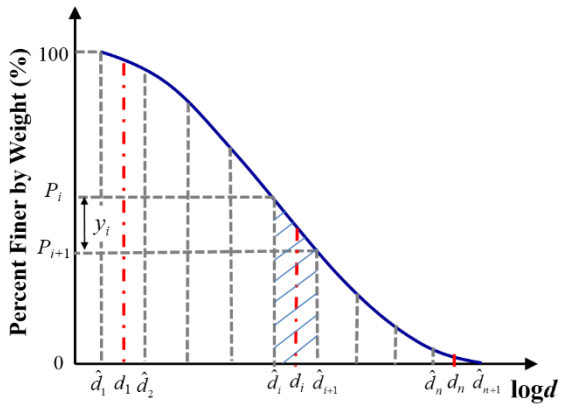

Figure 5.10 The divisions for a gradation curve

(2) *Determination of e_i*

To compute the minimum void ratio for a multisize soil mixture, it requires the information of particle sizes d_i (i = 1, 2…n), volume fractions, y_i (i = 1, 2…n), and the value of minimum void ratios for packings of equal particle size, e_i (i = 1, 2…n). Youd (1973) had measured e_i for six packings with the following mean particle sizes: 0.095 mm, 0.184 mm, 0.373 mm, 0.747 mm, 1.483 mm, and 2.943 mm. All six mixes have the same coefficient of uniformity C_u = 1.4. It is noted that, from a sieving process, it is not possible to achieve a packing consisting of particles with exactly same size. The uniformity C_u = 1.4 represents a packing with very narrow distribution of particle sizes, which can be considered as a packing of equal size particles. The measured minimum void ratios of crushed basalt for the 6 different particle sizes are plotted in Fig. 5.11.

An empirical correlation between minimum void ratio and particle size was proposed by using a power function to fit the experimental results (Rout 2009; Patra et al. 2010).

$$e_i = \alpha d_i^{\beta} \tag{5.24}$$

where α and β are two coefficients. This empirical equation is suitable for many types of soil. Fig. 5.11 shows the comparison of this equation and the experimental data for seven different types of soil with very narrow grain size distributions (C_u = 1.4) for different mean grain sizes. The coefficients of determination R^2 and the best-fitted values of α and β are shown in Table 5.5. For crushed basalt (Youd 1973), α = 0.7016, and β = -0.04. These two values are used in the subsequent analysis.

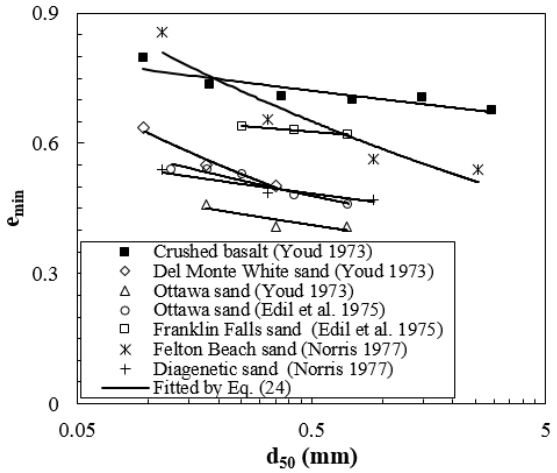

Figure 5.11 The comparison of equation (5.24) and experimental data for seven different types of soil with very narrow grain size distributions

Table 5.5 The coefficient of determination R^2 and the values of α and β in Eq. (5.24) for seven different types of soil with very narrow grain size distributions

Soil type	Reference	C_u	α	β	R^2
Crushed basalt	Youd, (1973)	1.4	0.7016	-0.040	0.804
Del Monte White sand	Youd, (1973)	1.4	0.4130	-0.179	0.970
Ottawa sand	Youd, (1973)	1.4	0.3878	-0.087	0.735
Ottawa sand	Edil et al., (1975)	1.2	0.4458	-0.104	0.916
Franklin Falls sand	Edil et al., (1975)	1.2	0.6136	-0.031	1.000
Felton Beach sand	Norris, (1977)	1.09	0.5872	-0.148	0.902
Diagenetic sand	Norris, (1977)	1.09	0.4629	-0.065	0.911

(3) *Determine the required n-components for mixture*

In order to represent the packing of graded soil by a *n*-component multisize particle packing, the number of n should be large enough to approximate the continuous gradation curve. Here, we investigate the suitable value of n required to represent a soil with a wide range of particle sizes. The predicted value of minimum void ratio is expected to vary with the number of *n* and is expected to be converged as the number of n increases. Thus, we can determine the suitable value of *n* given a level of error tolerance.

The values of *p* and *s* were studies by Chang et al. (2015) for sand-silt mixtures (binary packing). Based on this study, two sets of parameters of *p* and *s* were select as upper and lower bounds to cover all possible range of soil properties. The two sets are: $p = 7$, $s = 6$ and $p = 1.2$, $s = 1.4$ as shown in Fig. 5.12.

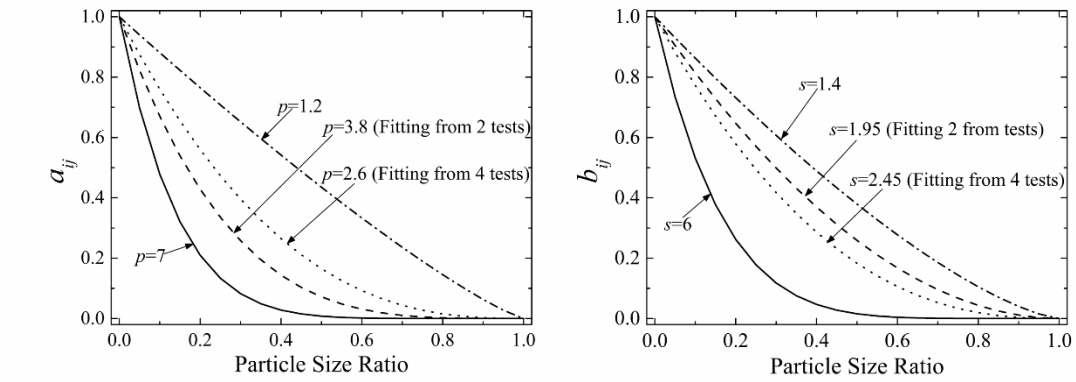

Figure 5.12 The upper and lower bounds of (a) parameter *p* and (b) parameter *s*, compared with that obtained by fitting from test results on crushed basalt

On Fig.5.13 (a), the soil mix 2 ($C_u = 2.5$) was selected, and the analyses of minimum void ratio were repeated by using (n = 2, 3 4, 5, 6), which correspond to the size ratios

$\hat{d}_i / \hat{d}_{i+1}$ = 2.83, 2.0, 1.68, 1.52, 1.41, 1.35. The minimum void ratio predicted using different size ratios $\hat{d}_i / \hat{d}_{i+1}$ were plotted for the two sets of *p* and *s*.

On Fig.5.13 (b), the soil mix 4 (C_u = 8) was selected, and the analyses of minimum void ratio were repeated by using (*n* = 2, 3 4, ..11), which correspond to the size ratios $\hat{d}_i / \hat{d}_{i+1}$ = 8.3, 4.1, 2.9, 2.3, 2.0, 1.8, 1.7, 1.6, 1.53, 1.47. The minimum void ratio predicted using different size ratios $\hat{d}_i / \hat{d}_{i+1}$ were also plotted for the two sets of *p* and *s*.

Clearly, the computation results in Fig. 5.13 show that minimum void ratio is a function of size ratio. The calculated minimum void ratio is converged to an asymptotic value as the value of $\hat{d}_i / \hat{d}_{i+1}$ decreases (i.e., the number of division *n* increases). For the ratio $\hat{d}_i / \hat{d}_{i+1}$ less than 1.8, the calculated minimum void ratio is converged to the asymptotic value, regardless the values of *p* and *s* used in the analysis. Thus, the requirement of size ratio less than 1.8 is adopted in the analysis for discretizing the gradation curves.

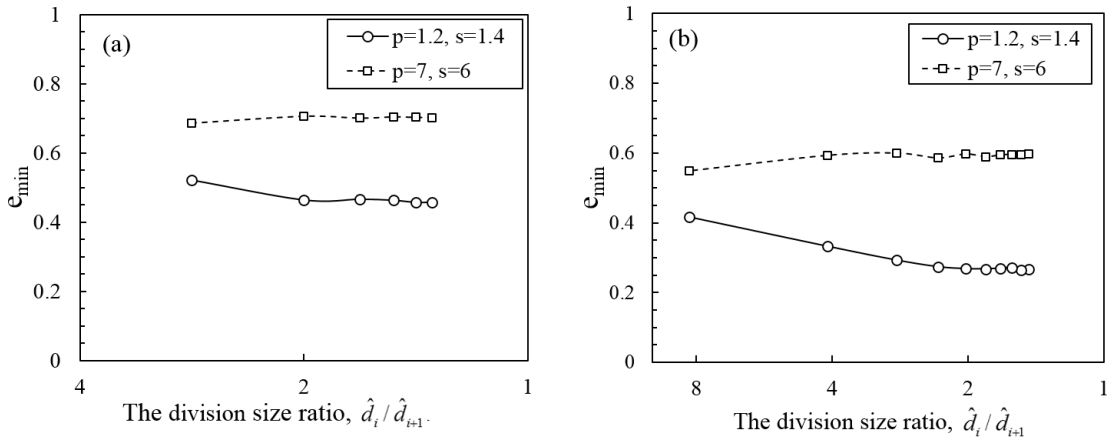

Figure 5.13 Required division size ratio to reach the converge value (a) Mix. 2; and (b) Mix. 4

(4) *Evaluation of the model*

In the following analysis, we use the total number of divisions, n = 2 for the gradation curve of Mix. 1 (C_u = 1.4) shown in Fig. 5.9, which corresponds to a size ratio $\hat{d}_i / \hat{d}_{i+1}$ = 1.42; the total number of divisions n = 4 for the gradation curve of Mix. 2 (C_u = 2.5), which corresponds to a size ratio $\hat{d}_i / \hat{d}_{i+1}$ = 1.68; the total number of divisions n = 6 for the gradation curve of Mix. 3 (C_u = 4.3), which corresponds to a size ratio $\hat{d}_i / \hat{d}_{i+1}$ = 1.8; and the total number of divisions n = 7 for the gradation curve of Mix. 4 (C_u = 8.0), which corresponds to a size ratio $\hat{d}_i / \hat{d}_{i+1}$ = 1.8. These divisions are sufficient small to obtain converged results.

Two data points are enough to determine the two parameters p and s. The parameters p and s were determined by best fitting the measured results of two tests (Mix. 2 and Mix. 4), denoted as $e_{\min}^{Mix.2}$ and $e_{\min}^{Mix.4}$. The predicted values by the model are denoted as $\hat{e}_{\min}^{Mix.2}$ and $\hat{e}_{\min}^{Mix.4}$. The residuals δ_e is defined by the following equation.

$$\delta_e = \sqrt{(e_{\min}^{Mix.2} - \hat{e}_{\min}^{Mix.2})^2 + (e_{\min}^{Mix.4} - \hat{e}_{\min}^{Mix.4})^2} \tag{5.25}$$

The contour of the residuals δ_e is plotted against corresponding parameters of p and s in Fig. 5.14. The optimum values p = 3.8 and s = 1.95 were found when δ_e is the minimum. The contour shows that there are no other local minimum points in the contour plot, thus by using test results for two mixes, the p and s can be uniquely determined.

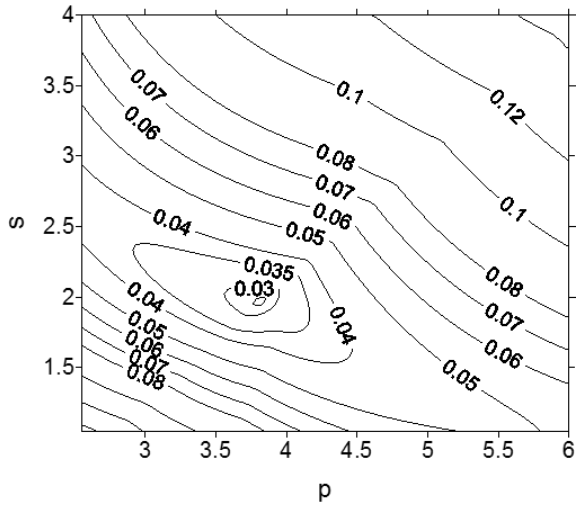

Figure 5.14 Root of squared sum residuals for various values of parameters *p* and *s* (Fitting from two tests)

Then, the determined value of *p* and *s* are used to predict the other two tests, Mix.1 and Mix. 3. The predicted values of minimum void ratios are plotted and compared with the experimental results for the four soil mixtures in Fig. 5.15. The results show very good agreement.

Although the results of two tests are enough for determining the values of *p* and *s*, the parameters of *p* and *s* can also be determined by best fitting all four test results (Mix. 1 to Mix. 4). In this case, the residuals δ_e is defined by the following equation.

$$\delta_e = \sqrt{\sum_{i=1}^{4} (e_{\min}^{Mix.i} - \hat{e}_{\min}^{Mix.i})^2} \tag{5.26}$$

In this case, the optimum values $p = 2.6$ and $s = 2.45$ were found when δ_e was the minimum. Using these values of *p* and *s,* the predicted values of minimum void ratios for all four tests are plotted and compared with the experimental results for mixtures of real soil in Fig. 5.15. The results are slightly better than that of the *p* and *s* values determined from two data points. Comparing the two predictions, the values of *p* and *s* seem to be not

sensitive to the predicted values. The values of p and s (p = 2.6 , s = 2.45 and p = 3.8 and s = 1.95) are also plotted in Fig. 5.12 to be compared with the values of upper and lower bounds.

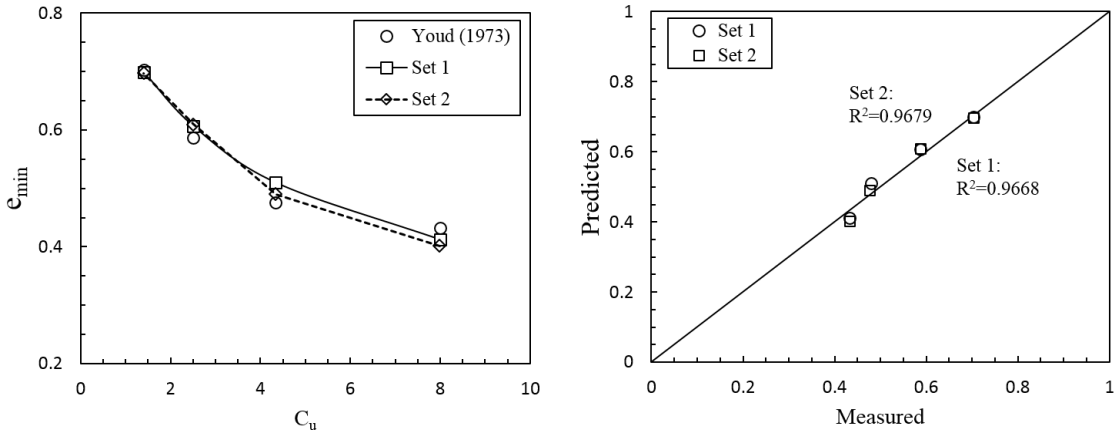

Figure 5.15 The predicted values of minimum void ratios using two different set of *p* and *s* values (Set 1: *p* = 3.8, *s* =1.95 fitting from 2 tests; and Set 2: *p* =2.6, *s* =2.45 fitting from 4 tests), compared with the experimental results for four mixtures of crushed basalt

To predict the value e_{min} of a mixture with arbitrary particle size distribution, one requires the minimum void ratios for packings of equal particle size, e_i ($i = 1,2..n$). The information of e_i of each particle size can be obtained by an empirical equation (Eq. 5.24), in which, the parameters α and β are calibrated by performing at least 2 tests. Due to the amount of experiments required for calibrating the model parameters, this model is not expected to be readily useful in engineering practice for predicting minimum void ratio. However, the proposed model provides an analytical method that explicitly accounts for the effect of particle size distribution on packing density, which is essential for the study of a wide range of geotechnical problems involving the change of particle size distribution, such as the settlement due to particle crushing in rock fill dams or internal erosion in dikes.

5.4 Conclusions

Minimum void ratio for granular soil is highly dependent on its particle size distribution. However, very few analytical models are available for predicting minimum void ratios as a function of particle size distribution. In this paper, a simple descriptor is used to describe the packing structure. This descriptor indicates the order of particle sizes in filling and embedment process, and has a direct link to phase diagram, which allows the determination of minimum void ratio for granular soil with an arbitrary particle size distribution. The developed model was evaluated by DEM simulation results for 3-size particle packing. It is also evaluated by experimental results on real soil with four different gradations to illustrate the applicability of this model. The results predicted by the model show very good agreement with the data from DEM simulation and from experiments.

CHAPTER 6

PACKING POTENTIAL INDEX FOR BINARY MIXTURES OF GRANULAR SOIL[5]

Packing procedure is the mechanical process of forming a packing of soil particles, such as funnel pouring, tamping, rodding, pluviation, compaction, vibration, compression, etc. For a sand-silt mixture, packing procedure and particle shape have significant effects on the density of the binary mixture. However, these two factors have not been considered in most of the existing particle packing density models. Thus, the existing particle packing density models are not applicable to sand-silt mixtures. In this chapter, we aim to study the packing procedure and particle shape effects on density of binary mixtures. We firstly define a packing potential index, which is a measure of volume reduction potential due to mixing of two components of a binary mixture system under a packing procedure. To understand the nature of packing potential index, we compare the packing potential indices of 24 different types of mixtures collected from the literature; the 24 types of mixtures were formed by two different types of packing procedure (i.e., for achieving minimum and maximum void ratios). It is found that the packing potential index is nearly independent of packing procedure but significantly dependent on the compound particle shapes of a mixture. Then, we mathematically link the packing potential index to the particle interaction parameters used in the particle packing density models. And we analyze the data to discuss the effect of packing procedure on the void ratios of sand-silt mixtures. We

[5] This chapter has been published as a standalone paper: Chang, C. S., & Deng, Y. (2020). Packing potential index for binary mixtures of granular soil. *Powder Technology, 372*, 148–160

then propose an approach within the framework of particle packing density model to predict the void ratios of sand-silt mixtures under different packing procedures with the consideration of particle shape effect.

6.1 Introduction

The paper is motivated by problems of silty sand from soil mechanics, in which, the variable of void ratio, instead of packing density, is commonly used. The void ratio e can be related to the packing density ϕ by: $\phi = 1/(1+e)$ or $e = (1/\phi) - 1$.

There are several analytical models to study the void ratios of binary particle mixtures in many branches of industry, such as ceramics processing (Reed, 1995), powder metallurgy (Smith, 2003), and concrete mixes (Powers, 1968). Among these models, the most popular ones are based on the hypothesis of two mechanisms of particle arrangements (Furnas, 1931; Westman & Hugill, 1930): (i) the filling mechanism of the fine particles filling into voids among coarse particles; (ii) the embedment mechanism of coarse particles occupying solid volumes in place of porous bulk volumes of the fine particles. The filling mechanism occurs for mixtures with low fines contents; and the embedment mechanism occurs for mixtures with high fines contents. In these two mechanisms, the models did not consider particle interactions that cause packing disturbance; thus, the models only provide good estimates of lower bound solutions.

These models were then evolved to consider the effect of particle interaction. During filling of fine particles, loosening of the coarse particle network may occur when fine particles are pushed into the voids among coarse particles. On the other hand, during embedment of coarse particles, disrupting the packing of fine particles may occur at the

wall-like boundaries of coarse particles. The packing model introduced by Powers (1968) considers the loosening effect. The packing models developed by Aïm and Goff (1968) and Toufar et al. (1977) account for the wall effect. The packing models developed by Yu et al. (1996), Goltermann et al. (1997), Stovall et al. (1986), De Larrard (1999), Dewar (1999), and Kwan et al. (2013) take into account of both the loosening and wall effects.

The loosening and wall effects have been found to be significantly affected by particle size ratio *r* (i.e., ratio of fine to coarse particle sizes) (McGeary, 1961). Thus, the effects are expressed as particle interaction functions dependent on the particle size ratio. The two parameters (*a* and *b*) in the particle interaction functions were obtained by regression analysis of experimental results on packing densities for mixtures with different size ratios. The interaction parameters and interaction functions derived in the models by Yu et al. (1996), De Larrard (1999), and Kwan et al. (2013) have different forms.

It is obvious that the loosening and wall effects can be affected by other factors of particle morphology, such as particle shape, roundness and surface texture roughness. Among several aspects of morphology, the particle shape has been considered in the model by Yu et al. (1996), however, the particle shape considered was simple idealized nonspherical shape (e.g., cylinders, disks). For most material, the particle morphology is complex and difficult to be measured quantitatively. Hence, from either a theoretical or a practical point of view, the complex particle morphology cannot be considered in the model in a fully satisfied manner. And most currently available models do not consider factors of particle morphology. Because of this limitation in models, the evaluation of several models by Jones (2002) indicated that each of these models is applicable only to a certain type of industrial material. Also indicated by Chang et al. (2015), due to a large span of size and

shape differences, the parameters used in these models are not suitable for sand-silt mixtures.

Furthermore, the complexity involves not only particle morphology, but also the packing procedure (i.e., method of mixing, placement and compaction), by which the binary packing is physically formed. The factor of packing procedure is not addressed in most binary packing models. De Larrard (1999) developed the ‘‘compressible packing model” (CPM) by introducing the compaction index K, which is assumed to be related to the applied compaction effort, thus is dependent on the packing procedure. The value of *K* is an empirical parameter varying from 4 to 9 suggested for pouring, rodding, vibration and compression, and is also varying with grain shape (round & crushed) (De Larrard, 1999). He proposed a method to convert the virtual packing density to the actual packing density through the compaction index. But the CPM is not suitable for geotechnical material such as silty sand (Chang et al., 2015).

In geotechnical engineering, minimum and maximum void ratios (e_{max} and e_{min}), which represent the densest and loosest states of a soil mixture, are widely applied in earthwork design and planning. The packing procedures of achieving e_{max} and e_{min} are very different. Thus, understanding the effect of the packing procedures on the density of mixtures is important in geotechnical engineering.

In this chapter, we aim to study the effects of particle shape and packing procedure on densities of binary mixtures. We firstly define a packing potential index, the value of which is a number between 0 and 1. This index is a measure of void reduction potential due to mixing of two components of a binary mixture under a packing procedure. To study how the packing potential index may vary with the type of mixtures and with the type of

packing procedure, we compare the packing potential indices for 24 systems of soil mixtures collected from the literature; the 24 systems of mixtures were formed under two different types of packing procedure (i.e., for achieving minimum and maximum void ratios).

Then, we mathematically derive the relationship between the packing potential index and the particle interaction parameters, and analyze the data to discuss the effect of packing procedure on void ratio of mixtures. Finally, we discuss an approach, under the framework of particle packing model, for predicting void ratio (e_{max} and e_{min}) of a mixture under different packing procedures with the consideration of particle shape effect.

6.2 Packing Potential Index

Consider a binary packing mixture composed of 2 groups of particles. The particle sizes for the two groups are denoted by d_1 and d_2, respectively (note that $d_1 \geqslant d_2$). The solid volume fractions of the two groups of particles are denoted by y_1 and y_2, respectively (note that $y_1 + y_2 = 1$).

We aim to determine the void ratio e of a binary soil mixture based on the monodisperse void ratios of the two components (e_1 and e_2). Note that the void ratios, e, e_1 and e_2, are measured from three packings formed by the same packing procedure.

The void ratio e of a binary soil mixture is between the upper bound and lower bound void ratios, which can be constructed by the monodisperse void ratios of the two components (e_1 and e_2). The upper bound void ratio, e^U, is hypothesized to be the Voigt average of the monodisperse void ratios, given by

$$e^U = e_1 y_1 + e_2 y_2 \tag{6.1}$$

The upper bound is plotted as line AB in Fig. 6.1, in which the fines content, $f_c = y_2$.

In contrast, the lower bound void ratio, e^L, is derived by assuming that the two groups of particles in the mixture have no interactions (Furnas, 1931; Westman & Hugill, 1930). There are two scenarios: (1) every fine particle exists only in the void space between coarse particles (i.e., in the coarse particle dominant region), which is shown as line AC in Fig. 6.1, or (2) every coarse particle is fully dispersed in the matrix of fine particles (i.e., in the fine particle dominant region), which is shown as line CB in Fig. 6.1. The equations for AC and CB are given respectively by

$$e^L = e_1 y_1 - (1 + e_1) y_2 \; ; \qquad e^L = e_2 y_2 \tag{6.2}$$

The slope of AC is -(1+ e_1) and the slope of CB is e_2 as shown in Fig. 6.1. The line ACB is the lower bound.

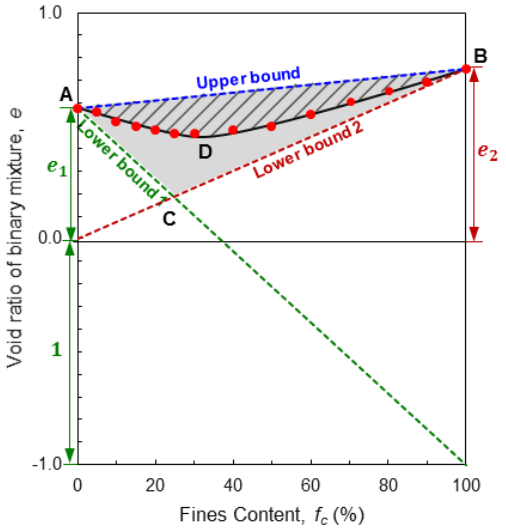

Figure 6.1 Upper and lower bounds of void ratios of a system of mixtures under a packing procedure

For a system of mixtures (i.e., mixtures with the same two components of various combinations), the void ratios of the binary mixtures with various f_c are between the upper and the lower bounds as the curve ADB shown in Fig. 6.1. For convenient, we define a packing potential index Ω as the ratio of area ADB to area ACB, which is a material descriptor for a system of mixtures. This index is a measure of volume reduction potential due to mixing of two components of a binary mixture system under a packing procedure, which is a simple scaler and can be directly obtained from experimental data. Thus, it is convenient to be used for studying the effect of particle shape and packing procedure. The value of packing potential index Ω is between 0 and 1. The higher value of Ω indicates a higher potential of volume reduction of the mixtures.

For the case of $e_1 = e_2$, the monodisperse void ratio is same for both components and is the upper bound. Under the same packing procedure, the binary mixtures, for all fines content, can generally be packed to a denser packing than the monodisperse packing. The packing potential index Ω indicates roughly how much denser the binary mixtures can be effectively achieved compared to the monodisperse packing.

The purpose of a packing density model is to predict the void ratio *e* of a binary mixture based on the values e_1 and e_2 of the monodisperse packings. Thus, it is important to study various factors that affect the packing potential index.

6.3 Factors Affect Packing Potential Index

6.3.1 Effect of Particle Morphology

The packing potential index is significantly affected by particle size ratio *r* (i.e., $r = d_2/d_1$, the particle size of fine particles divided by the particle size of coarse particles)

as indicated in the test results of spherical steel shots by McGeary (1961) and in the test results of spherical glass beads by Kwan et al. (2013), as shown in Fig. 6.2a and Fig 6.2b. Steel shots and glass beads are round particles. The particle size range is from 0.16 mm to 3.14 mm for steel shots, and from 1.43 mm to 15.73 mm for glass beads. The packing potential index is plotted for mixtures with various size ratio in Fig. 6.2c. The size ratio of fine particles to coarse particles ranges from 0.05 to 0.75. For binary mixtures with small size ratios ($d_1 >> d_2$), the packing potential indices are nearly 1, meaning that the mixture is more capable of specific volume reduction and can be packed approaching the lower bound solution. Whereas, for mixtures with large size ratios ($d_1 \approx d_2$), the packing potential indices are nearly zero, and the void ratios of the mixtures can be achieved approaching to the upper bound.

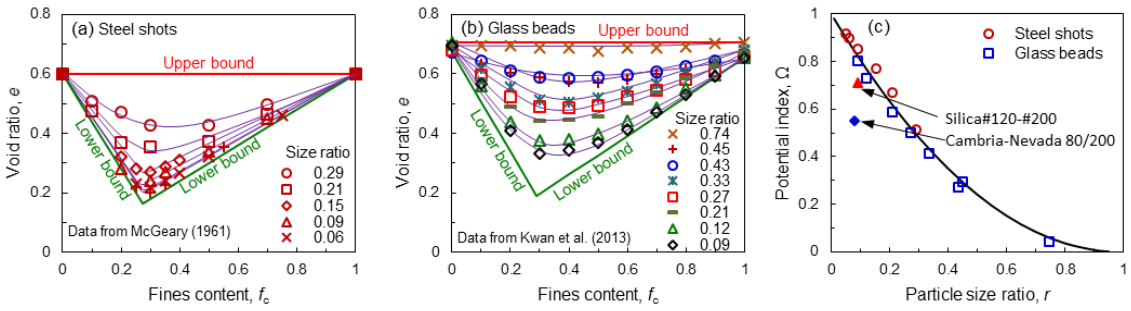

Figure 6.2 (a) Test results for steel shots reported by McGeary (1961), (b) Test results for glass beads reported by Kwan *et al.* (2013), (c) the effect of particle size ratio on packing potential index obtained from test results on steel shots and glass beads

It is noted that, for a binary mixture of steel shots or of glass beads, the mixture is composed of two groups of mono-sized particles. However, for silty-sand, the two groups of particles are not mono-sized. The sand particles are relatively uniform, but the silt particles usually have a wider range of sizes. Thus, the sand-silt mixture is a deviation from

the standard meaning of binary mixtures defined in particle packing models. However, in this study, we have neglected this factor because the grain size distribution of silt is seldom measured in geotechnical practice, and the information on measured void ratios of mono sized silt is not available in the literature. The mean particle size for sand or silt is referred to as the particle size denoted by d_1 or d_2 in this study.

Besides particle size ratio, it is reasonable to expect that particle morphology is also a crucial factor that influences the packing potential index. There are many aspects of particle morphology, which can be generally expressed in terms of elongation ratio (i.e., aspect ratio), roundness, sphericity, angularity and surface roughness (Clayton, Abbireddy, & Schiebel, 2009). At a larger scale, the term ‘‘sphericity” is used to characterize the overall shape of the granular particle by a measure of the degree of conformity of particle shape to that of sphere circumscribing the particle (Alshibli & Alsaleh, 2004). At a smaller scale, the term “roundness” defined by Wadell (1933) is used to describe the degree of sharpness of particle edges/corners. At an even smaller scale, surface roughness (Hettiarachchi & Mampearachchi, 2020) is used to describe the surface texture. There is no consensus on which descriptor is better to characterize the particle morphology, for example of the overall particle shape alone, there are three measures: aspect ratio, sphericity, angularity, etc.

Although digital image analysis and computed tomography techniques have been employed to quantitatively characterize the aggregate morphology (Zheng & Hryciw, 2016b), in general practice, the morphology parameters are often not measured in experiments. In most test results presented in the literature, only qualitative descriptors of particle shapes (such as round, angular, sub-angular, etc.) are provided.

Fig. 6.3 illustrates the measured void ratios and the calculated upper and lower bounds for 3 systems of mixtures under the same packing condition. The compound particle shapes are denoted as coarse particle shape/ fine particle shape for the following 3 systems of mixtures: Steel shots (round/round), Silica sand-silt (subangular/subangular), and Cambria-Nevada sand-silt (round/angular). Note that the particle size ratios for these 3 systems of mixtures are nearly same, but the three packing potential indices are different as shown in Fig. 6.3. The shapes of coarse particles and fine particles are similar for steel shots and silica sand-silt, whereas different for Cambria-Nevada sand-silt. Because of the effect of particle shape the three packing potential indices do not follow the curves of sphere particles previously shown in Fig. 6.2c. Hence, not only the particle shape of a single component but also the compound particle shapes of two components have significant effect on the packing potential index.

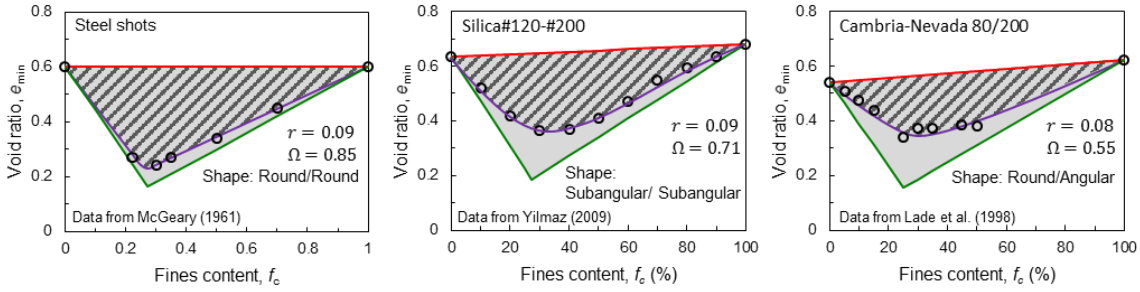

Figure 6.3 The packing potential index for three systems of mixtures

To further investigate the effect of particle shape, 13 sets of spherical particles binary mixtures and 24 sets of sand-silt mixtures from the literature are collected (see Table 6.1) for studying the packing potential index as a function of particle shape in a qualitative way. The compound particle shapes of the 37 systems of mixtures are classified into three groups: round/round (R/R), angular/angular or subangular/subangular (A/A, SA/SA), and

round/ angular or round/subangular (R/A, R/SA). The computed packing potential indices versus particle size ratio are shown in Fig. 6.4 for the three groups of compound particle shapes. Fig. 6.4 shows that the effect of particle shape is significant on the values of packing potential index. As shown in Fig. 6.4, given a particle size ratio, for binary mixtures composed of two similar shape components, the packing potential index Ω of a R/R mixture is greater than that of a A/A or SA/SA mixture. The packing potential index Ω of a mixture composed of two different shape components is usual smaller than that of a mixture composed of two similar shape components.

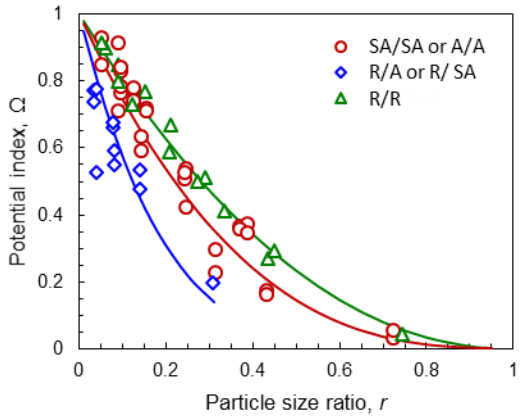

Figure 6.4 The packing potential index versus particle size ratio for mixtures with 3 groups of compound particle shapes.

Table 6.1 List of material properties for 24 sets of binary soil mixtures

Sand/silt Mixture	Ref.	d_1(mm)	d_2(mm)	e_{min}		e_{max}		particle shape (coarse)	particle shape (fine)	p	s
				e_1	e_2	e_1	e_2				
Ottawa 50/200-Nevada fines	Ref[1]	0.2	0.05	0.548	0.754	0. 806	1. 181	angular	angular	2.8	1.8
Ottawa F95-Nevada fines		0.16	0.05	0.58	0.754	0. 868	1. 179	subround	angular	3.6	2.3
Nevada 50/200-Nevada fines		0.14	0.04	0.57	0.754	0. 878	1. 181	subangular	angular	3.5	2.5
Nevada 50/80-Nevada fines	Ref[2]	0.21	0.05	0.581	0.754	0. 855	1. 183	subangular to angular	subangular to angular	3.5	1.6
Nevada 80/200-Nevada fines		0.12	0.05	0.617	0.754	0. 938	1. 169	subangular to angular	subangular to angular	3.8	2.2
Nevada 50/80 - Nevada80/200+fines		0.17	0.05	0.581	0.754	0. 876	1. 180	subangular to angular	subangular to angular	3.3	2.3
Cambria-Nevada fines		1.5	0.05	0.538	0.754	0. 765	1. 176	round	angular	10	3
Cambria-Nevada 50/80		1.5	0.21	0.538	0.581	0.765	0.854	round	subangular	3	3
Cambria-Nevada 80/200		1.5	0.12	0.538	0.624	0. 768	0. 937	round	angular	6.5	2.5
Nevada 50/80- Nevada 80/200		0.21	0.12	0.581	0.617	0. 854	0. 938	subangular to angular	subangular to angular	2.4	1.9
Foundry sand/crushed silica fines	Ref[3]	0.25	0.01	0.608	0.627	0.8	2.1	round to subround	angular	5.5	6
Hokksund	Ref[4]	0.45	0.04	0.57	0.76	0. 949	1. 413	sharp edges, cubical	angular, subangular	3.8	3.8
MGM	Ref[5]	0.12	0.01	0.755	1	1. 247	2. 740	highly angular to subround	thin and plate-like	13	1.2
Vietnam	Ref[6]	0.37	0.16	0.552	0.583	0. 703	0. 755	subangular	subangular	4	1.4
Silica#16-#18 #30-#50	Ref[7]	1.08	0.4	0.633	0.644	0. 970	1. 048	subangular	subangular	1.75	2.2
Silica#16-#18 #30-#80		1.08	0.42	0.633	0.59	0. 970	0. 996	subangular	subangular	1.9	1.9
Silica#16-#18 #50-#80		1.08	0.26	0.633	0.696	0. 970	1. 114	subangular	subangular	2.2	2
Silica#16-#18 #80-#100		1.08	0.17	0.633	0.682	0.97	1.121	subangular	subangular	2.6	1.8
Silica#16-#18 #80-#120		1.08	0.14	0.633	0.697	0.97	1.124	subangular	subangular	2.9	1.8
Silica#16-#18 #80-#200		1.08	0.1	0.633	0.651	0.97	1.084	subangular	subangular	3.1	2.5
Silica#16-#18 #100-#120		1.08	0.14	0.633	0.697	0.97	1.125	subangular	subangular	2.3	2
Silica#16-#18 #100-#200		1.08	0.1	0.633	0.668	0.97	1.084	subangular	subangular	2.7	2
Silica#16-#18 #120-#200		1.08	0.1	0.633	0.682	0.970	1.115	subangular	subangular	4.3	2.2
Silica#16-#18 #200-#400		1.08	0.06	0.633	0.7	0.97	1.091	subangular	subangular	4	2

Note: Ref[1]- (Lade & Yamamuro, 1997); Ref[2]- (Lade et al., 1998); Ref[3]- (Thevanayagam et al., 2002); Ref[4]- (Yang, 2004); Ref[5]- (Fourie & Papageorigou, 2001); Ref[6]- (Cho, 2014); Ref[7]- (Yilmaz, 2009)

6.3.2 Effect of Packing Procedure

In geotechnical engineering, the loosest and densest density states (i.e., maximum and minimum void ratios) of soil are of interest. Several packing procedures have been used for the two limiting void ratios, such as moist tamping, vibratory table, customized sample preparation method, or a combination of these methods. Among these processes, two standards process specifications (ASTM) (ASTM D4253-00, 2006; ASTM D4254-00, 2006) are most commonly used, in which the loosest state (maximum void ratio) is achieved by a process of funnel pouring, in which a funnel is used to pour the dry material into a mould, and slowly turn the mould upside down. Whereas, the densest state is achieved by vibration method with a static weight. It is noted that, before either packing procedure is applied, the particles are thoroughly mixed for all the fractions (AASHTO, 1986).

The three systems of mixtures (in Fig. 6.5) are used to examine the effect of packing procedure. Fig. 6.5a shows the void ratios of mixtures achieved by "minimum void ratio" packing procedure, and Fig. 5b shows the void ratios of mixtures achieved by "maximum void ratio" packing procedures. The two different packing procedures have significant effect not only on the void ratios of monodisperse packings but also on the void ratios of binary mixture packings.

The packing potential indices are different for different systems of mixtures as shown in Fig. 6.5: the packing potential index is high for the silica sand-silt mixture, medium for the Ottawa sand-Nevada silt mixture, and low for the Vietnam mixture. However, it is interesting to observe that for each system of mixtures, the packing potential

index is nearly same between the two different procedures. Thus, the dependence of the packing potential index on the packing procedure may be very weak.

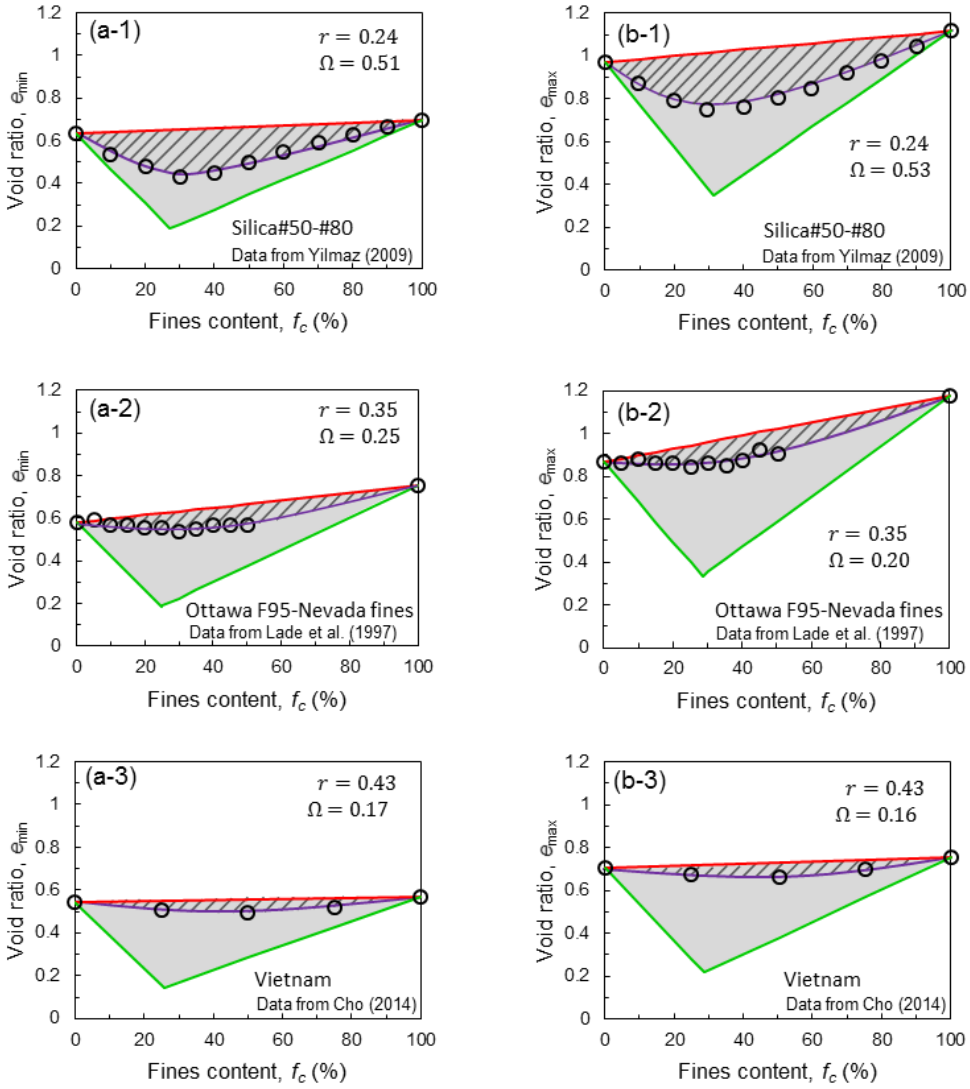

Figure 6.5 (a) The void ratios achieved by "minimum void ratio" packing procedure: (a-1) Silica #50-#80 mixture (a-2) Ottawa F95-Nevada fines mixture (a-3) Vietnam sand-silt mixture; (b) The void ratios achieved by "maximum void ratio" packing procedure: (b-1) Silica #50-#80 mixture (b-2) Ottawa F95-Nevada fines mixture (b-3) Vietnam sand-silt mixture

To further examine the influence of packing procedure on the packing potential index, the 24 systems of mixtures listed in Table 6.1 were analyzed. The packing potential

indices obtained from the "minimum void ratio" packing procedure (Ω_{min}) are plotted in Fig. 6.6 versus the packing potential index obtained from the "maximum void ratio" packing procedure (Ω_{max}). The correlation between the two packing potential indices is very strong with a coefficient of determination $R^2 = 0.91$. Thus, based on the results of the 24 systems of mixtures, packing potential index has a very weak dependence on packing procedure. Consequently, the packing potential index can be treated as a material property, dependent only on the system of mixtures.

It is interesting to note that packing procedure has a significant influence on the packing density, but very small influence on the packing potential index. That means, for a system of mixtures, the upper and lower bound densities are affected by the packing procedure, but the mixture densities relative to the upper and lower bounds are not affected by the packing procedure. This characteristic is helpful for modeling mixture densities due to different packing procedures.

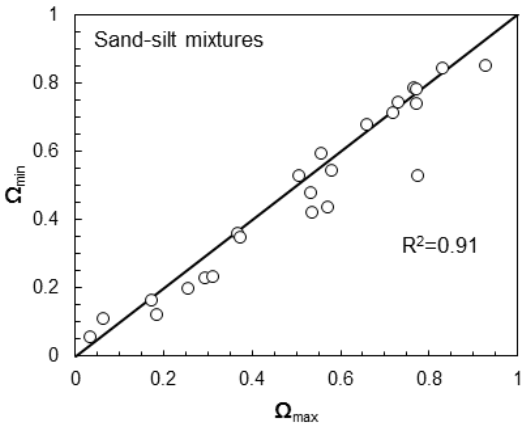

Figure 6.6 The effect of packing procedure on packing potential index for 24 systems of binary soil mixtures

6.4 Role of Packing Potential in Particle Packing Model

Most particle packing density models available in the literature (Kwan et al., 2013; Stovall et al., 1986; Yu et al., 1996) have the similar approach, which is a two-step process: (1) develop upper bound and lower bound void ratios based on the given monodisperse void ratios e_1 and e_2, for packings of coarse and fine particles, and (2) determine the void ratio *e* of the mixture based on the upper and lower bounds, using the particle interaction parameters. Note that the packing potential is a measure that represents the position of the void ratio *e* relative to the upper bound and lower bound. Thus, the packing potential parameters and particle interaction parameters have the same physical meaning and the same purpose. In the following, we aim to find the relationship between the packing potential parameters and the particle interaction parameters.

6.4.1 Linear Particle Packing Model

As defined previously in Fig. 6.1, the packing potential index Ω is a material property for a system of mixtures (i.e., mixtures with the same two components of various combinations). In order to reveal the effect of fines content of each mixture, we define a packing potential parameter ω for a mixture with specific fines content f_c. Fig. 6.7a shows a data point D, which represents a mixture with fines content f_c, the packing potential parameter ω is defined by

$$\omega = (e^U - e)/(e^U - e^L) \tag{6.3}$$

The value of ω represents the position of the void ratio *e* relative to the upper bound and lower bound void ratios (i.e. e^U and e^L). The parameter ω is dependent on e^U and e^L, which are functions of fines content, given in Eqs. (6.1) and (6.2). The area ratio

Ω as shown in Fig. 6.1 can be treated as the average of ω over the all range of fines content f_c.

$$\Omega = \int_0^1 \omega(f_c)\, df_c \tag{6.4}$$

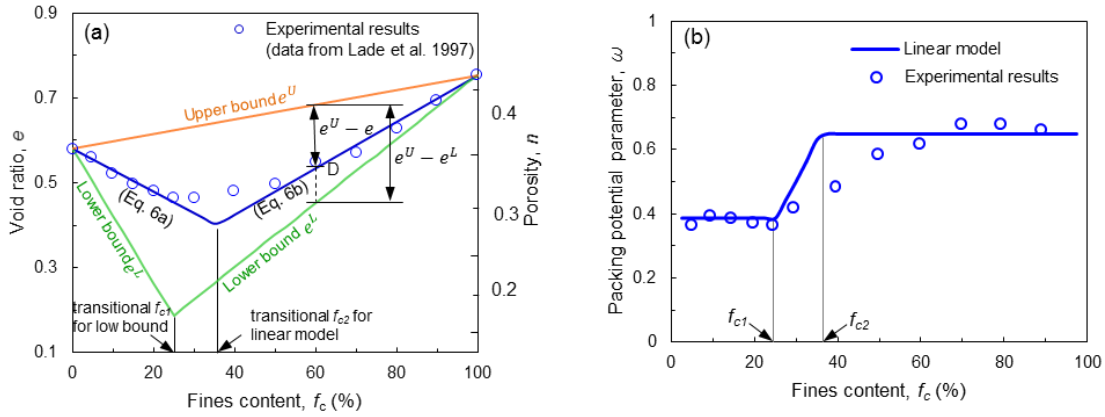

Figure 6.7 (a) Definition of packing potential parameter ω for a given mixture with specific fines content, (b) The packing potential parameter ω as a function of fines content

The void ratio e for the mixture in Eq. (6.3) can be expressed as

$$e = e^U - \omega(e^U - e^L) \tag{6.5a}$$

It is noted that, in Fig. 6.7a, the upper bound is a straight line, but the lower bound has two segments separated by the transitional fines content f_{c1} and the measured test results has two segments separated by the transitional fines content f_{c2}. The coarse particle dominant region can be defined by $f_c < f_{c1}$ and the fine particle dominant region can be defined by $f_c > f_{c2}$. The region in $f_{c1} < f_c < f_{c2}$ is considered as transition zone. Thus, from Eq. (6.1) and Eq. (6.2), the value of $(e^U - e^L)$ is different for the two dominant regions:

$$e^U - e^L = (1 + e_2)y_2 \qquad \text{for } f_c < f_{c1} \tag{6.5b}$$

$$e^U - e^L = e_1 y_1 \qquad \text{for } f_c > f_{c2} \tag{6.5c}$$

The value of ω for a mixture in the coarse particle dominant region ($f_c < f_{c1}$) is different from for a mixture in the fine particle dominant region ($f_c > f_{c2}$). They are termed as ω_a and ω_b, respectively. Thus Eq. (6.5a) becomes

$$e = (e_1 y_1 + e_2 y_2) - \omega_a (1 + e_2) y_2 \quad \text{for } f_c < f_{c1} \tag{6.6a}$$

$$e = (e_1 y_1 + e_2 y_2) - \omega_b e_1 y_1 \quad \text{for } f_c > f_{c2} \tag{6.6b}$$

If ω_a and ω_b are two constants, Eqs. (6.6a) and (6.6b) represent two linear lines. Therefore, if we approximate the data by a bilinear line as shown in Fig. 6.7a, then in the range of $f_c < f_{c1}$, ω_a is a constant, and in the range of $f_c > f_{c2}$, ω_b is another constant as shown in Fig. 6.7b. In the range of $f_{c2} > f > f_{c1}$, ω is a transition value from ω_a to ω_b.

The ω calculated directly from experimental data reported by Lade et al. (1998) is shown as the symbol of circles in Fig. 6.7b. The ω calculated from the bilinear line, is shown as the solid curve in Fig. 6.7b. In the coarse particle dominant region, ω_a is a constant of 0.39. In the fine particle dominant region, ω_b is a different constant of 0.65. In the transition zone, ω varies from 0.39 to 0.65.

It is noted that Eq. (6.6a) and Eq. (6.6b) have the similar form as the linear particle packing density models (LPDM) (Chang et al., 2015; De Larrard, 1999; Dewar, 1999; Goltermann et al., 1997; Stovall, de Larrard, et al., 1986; Yu et al., 1996). These models consider interaction parameters (i.e. the loosening parameter a and wall parameter b), which always predicts a bilinear packing void ratio curve for a binary mixture as shown in Fig. 6.7a. Compared with these linear packing models, the packing potential parameter ω_a corresponds to the loosening parameter, and parameter ω_b corresponds to the wall

parameter. Precisely, the packing potential parameters can be related to the particle interaction parameters by: $\omega_a = 1 - a$, and $\omega_b = 1 - b$.

These two parameters, as shown in the test results on glass beads and steel shots (see Fig. 6.2a), are significantly dependent on the particle size ratio *r* (i.e., ratio of fine to coarse particle sizes), which can be obtained by regression analysis of the packing density experimental results for different mixtures.

The interaction functions derived by Yu et al. (1996) for their two interaction parameters:

$$a = 1 - (1 - r)^{3.3} - 2.8r(1 - r)^{2.7} \tag{6.7a}$$

$$b = 1 - (1 - r)^{2} - 0.4r(1 - r)^{3.7} \tag{6.7b}$$

The interaction functions derived by De Larrard (1999) for the interaction parameters in CPM:

$$a = \sqrt{1 - (1 - r)^{1.02}} \tag{6.8a}$$

$$b = 1 - (1 - r)^{1.5} \tag{6.8b}$$

6.4.2 Nonlinear Particle Packing Model

Models that considering the loosening parameter *a* and wall parameter *b* can be collectively classified as a 2-parameter model, which includes most of the linear particle packing density models (LPDM) (Chang et al., 2015; De Larrard, 1999; Dewar, 1999; Goltermann et al., 1997; Stovall, de Larrard, et al., 1986; Yu et al., 1996). As shown in Fig. 7a, the bilinear curve does not fit well the data in the range of f_c between 25 – 40%. To correct this situation, three methods have been developed.

One of the three methods, proposed by Chang and Deng (2017), can be linked to the concept of packing potential. Chang and Deng (2017; 2018) believed that the predicted

bilinear line is caused by the oversimplified assumption adopted in the LPDM. In LPDM, a packing of binary mixture is assumed to be built by one of the following two mechanisms: for lower content (coarse particle dominant region), fine particles are filled into the pores between coarse particles; for higher fines content (fine particle dominant region), the coarse particles are embedded into the fine particle matrix. In either case, only one type of mechanism (either filling or embedment) can occur for the binary mixture (see Eqs. 6.6a and 6.6b).

Opposite to the assumption adopted by LPDM, Chang and Deng (2017) assumed that both mechanisms can occur simultaneously in a packing of mixture. Thus, the potential parameter ω is divided into two parts: the filling potential parameter ω_1 and the embedment potential parameter ω_2. Consequently, the term $\omega(e^U - e^L)$ in Eq. (6.5a) can be viewed as a combination of two parts: $\omega_1(1 + e_2)y_2$ due to fine particles filled into the packing mixture, and $\omega_2 e_1 y_1$ due to coarse particles embedded into the packing mixture, thus

$$\omega(e^U - e^L) = \omega_1(1 + e_2)y_2 + \omega_2 e_1 y_1 \tag{6.9a}$$

Using Eq. (6.9a) and Eq. (6.1), Eq. (6.5a) becomes

$$e = (e_1 y_1 + e_2 y_2) - \omega_1(1 + e_2)y_2 - \omega_2 e_1 y_1 \tag{6.9b}$$

Eq. (6.9b) is in the same form as that proposed by Chang and Deng (2018), except ω_1 and ω_2 were expressed in symbols *a* and *b*. To facilitate the notion of combined mechanism, they introduced a state parameter *x*, and both the filling potential parameter ω_1 and the embedment potential parameter ω_2 are functions of the state parameter *x*. Thus, the void ratio of mixture is a function of the state parameter *x*:

$$e(x) = (e_1 y_1 + e_2 y_2) - \omega_1(x)(1 + e_2)y_2 - \omega_2(x) e_1 y_1 \tag{6.10a}$$

The state parameter x can be regarded as the controlling size of the packing ($d_1 \geq x \geq d_2$), which governs the magnitudes of packing potential parameters ω_1 and ω_2. Chang and Deng (2017) showed that these two parameters are functions of two size-ratios (between particle sizes and packing controlling size x), given by

$$\omega_1(x) = (1 - d_2/x)^p \tag{6.10b}$$

$$\omega_2(x) = (1 - x/d_1)^s \tag{6.10c}$$

The size ratio d_2/x governs the packing potential due to filling mechanism and the size ratio x/d_1 governs the packing potential due to embedment mechanism. The exponents p and s are two parameters corresponding to ω_1 and ω_2, respectively.

The state parameter x does not need to be known priori. According to the second law of thermodynamics, for a system reaches equilibrium at constant temperature and pressure, there is a natural tendency to achieve a minimum of the Gibbs free energy (i.e., the thermodynamic potential). Gibbs energy is proportional to the specific volume (related to void ratio by $(1 + e)/\rho_s$, ρ_s is density of solid), which is an important parameter for describing the system's thermodynamic equilibrium state. By varying x, the specific volume alternates. The system reaches equilibrium when the following equation is satisfied.

$$\frac{de(x)}{dx} = 0 \tag{6.11}$$

Thus, the solution of $e(x)$ can be solved from the set of governing Eqs. (6.10) and (6.11). This model requires only two parameters, p and s, which can be calibrated from experimental results (Chang & Deng, 2017).

The second method proposed by Kwan et al. (2013) introduced an additional parameter (i.e. wedging effect parameter c). The wedging effect becomes significant when

fine particles are enough to fill voids among coarse particles (e.g. f_c = 25 – 40%). The wedge effect is assumed to be related to the wedge parameter and proportional to the square of fines content (i.e., cf_c^2). This assumption allows the predicted relationship between e and f_c to be nonlinear so that the model is capable of modelling the nonlinear nature of data points as observed in Fig. 7a.

The interaction functions introduced by Kwan et al. (2013) for the 3-parameter packing model are as follows:

$$a = 1 - (1 - r)^{3.3} - 2.6r(1 - r)^{3.6} \quad (6.12a)$$

$$b = 1 - (1 - r)^{1.9} - 2r(1 - r)^{6} \quad (6.12b)$$

$$c = 0.322 \tanh(11.9r) \quad (6.12c)$$

where *a*, *b*, and *c* refer to the loosening, wall, and wedging effects, respectively.

The third method was proposed by de Larrard (1999) who considered that if a specimen is perfect compacted, a bilinear line would be achieved, and the measured curved line is due to insufficient compaction. To this end, he introduced a parameter (i.e., compaction index *K*). As the value of *K* approaches to infinity, the mixture is considered as a virtual packing being perfectly compacted. However, in real situations, the value of *K* usually ranges in 4.5 – 15. He proposed a method of converting from the density of a virtual packing to the density of a real packing. Thus, the real packing void ratios converted from the bilinear line through the variable K would give a curved shape. The model is called the Compressible Packing Model (CPM). Recently, Roquier (2016) introduced a 4th parameter (i.e., critical cavity size) within the framework of CPM.

Among the three methods for modelling the nonlinear nature of data points proposed by Chang and Deng (2017), Kwan et al. (2013) and de Larrard (1999), both

methods by Kwan et al. (2013) and de Larrard (1999) introduced a third parameter (i.e. the compaction index or the wedging effect parameter) in addition to the loosening parameter and the wall parameter. The physical meaning of the two added parameters are not related to the physical meaning of packing potential. Thus, these two methods cannot be linked to the concept of packing potential. It is noted that the method proposed by Chang and Deng (2017) utilized the concept of packing potential to model the nonlinear nature, thus it remains to be a 2-parameter model, without the need to introduce a third parameter.

As an example, the nonlinear model by Chang and Deng (2017) (i.e., Eqs. (6.10-6.11)) is now applied to model the experimental results by Lade (Lade et al., 1998), $e_1 = 0.58, e_2 = 0.72$, $d_1 = 0.5\ mm, d_2 = 0.7\ mm.$ The two parameters p and s were determined using the method described in the reference (Chang & Deng, 2017) (p = 3.3, and s = 2.3). The value of x computed for the data in Fig. 6.8a is a function of fines content as shown in Fig. 6.8b. The predicted curve of void ratio is shown by the solid curve in Fig. 6.8a, which is nonlinear with respect to fines content.

Note that the packing potential parameters ω_1 to ω_2 are independent of packing procedure as described in a previous section. And these two parameters are directly related to the parameters p and s as shown in Eqs. (6.10b) and (6.10c). Thus, we expect that the parameters p and s, like the packing potential parameters, are independent of packing procedure.

6.5 The Independence of Packing Procedure on the Parameters *p* and *s*

To verify this hypothesis that the parameters, p and s, are independent of packing procedure, the 24 sets of sand-silt mixtures listed in Table 6.1 were used. The two

parameters p and s, determined from experimental results under both packing procedures of achieving minimum void ratio and maximum void ratios, are compared in Fig. 6.9 for the 24 sets of sand-silt mixtures. For the 45-degree line, the coefficient of determination R^2 is 0.97, which indicates that the parameters are nearly independent of the packing procedure.

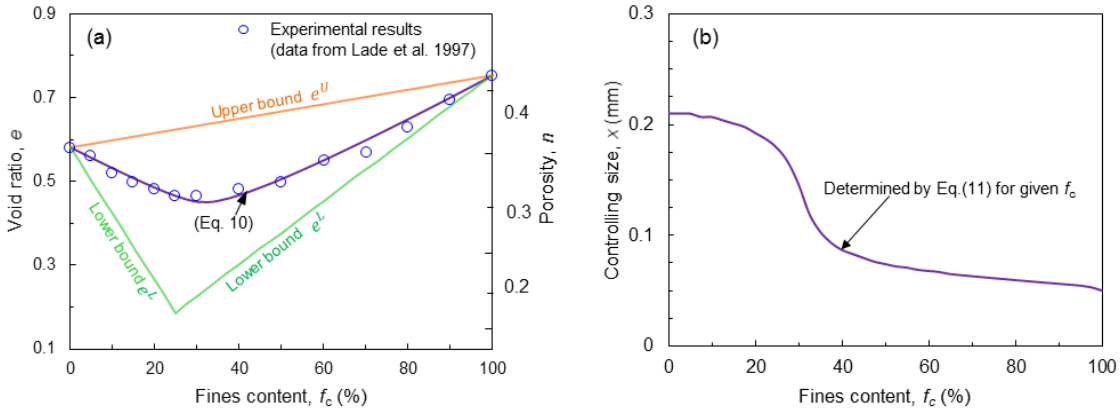

Figure 6.8 (a) The predicted void ratios for mixtures with different fines content, and (b) the calculated value of state parameter *x*

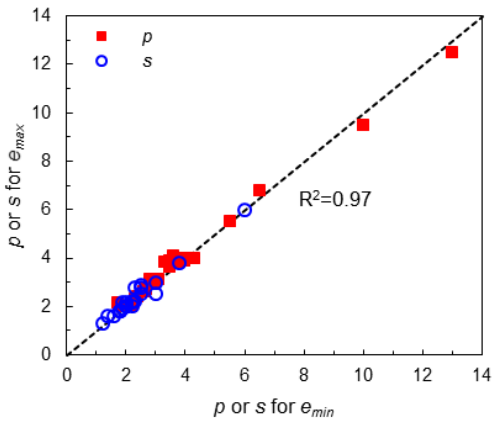

Figure 6.9 Comparison of the parameters *p* and *s* obtained from "minimum void ratio" packing procedure and from "maximum void ratio" packing procedure

Since the parameters p and s obtained for the "minimum void ratio" packing procedure are nearly the same as those obtained from the "maximum void ratio" packing

procedure, only the value of p and s obtained for the "minimum void ratio" packing procedure are listed in Table 6.1.

The values of p and s obtained from the "minimum void ratio" packing procedure are used for the prediction of both minimum and maximum void ratios using Eqs. (6.10) and (6.11). The predicted results are plotted in Fig. 6.10 for the 24 sets of sand-silt mixtures. Due to the good correlation of p and s shown in Fig. 6.9, it is not surprised to see the good agreement between the predicted and measured results for both minimum and maximum void ratios as shown in Fig. 6.10.

6.6 Values of Parameters *p* and *s* for Sand-silt Mixtures

The values of p and s depend on complex factors of particle morphology such as particle shapes and surface textures. To study the range of values of p and s due to the effect of particle shapes, the 13 sets of spherical particle mixtures and the 24 sets of sand-silt mixtures listed in Table 6.1 are classified into 3 groups of compound particle shapes: (1) R/R, (2) A/A or SA/SA, and (3) R/A or R/SA. (R-round, A-angular, SA- subangular). For the first two groups, coarse particles and fine particles have similar shapes. For the third group, coarse particles and fine particles have different shapes.

The box and whiskers plot was utilized to compare the values of p and s for the three groups of compound particle shapes as shown in Fig. 6.11. A box and whiskers plot is composed of a box and a set of whiskers. The upper whisker of the plot is the maximum of the data set and the lower whisker of the plot is the minimum of the data set. The box is drawn from the first quartile to third quartile with a horizontal line drawn in the box to denote the median. For the first two groups (R/R, A/A or SA/SA), the value range of p and

s are small compared to that of the third group (R/A, R/SA). For all three groups of compound particle shapes, the range of *p* is greater than the range of *s*. The length of box also shows the same trend. The median value of *p* is smallest for R/R, larger for A/A or SA/SA, and largest for R/A or R/SA. The median value of *s* has the same trend.

From an engineering point of view, when experimental results are not available for calibration, the values of *p* and *s* can be approximately estimated from Fig. 6.11 based on the rough descriptions of particle shapes of sand and silt. To assess the accuracy for this type of estimation, we classify the values of *p* and *s* into three groups. In each group, the median values are:

(1) R/R: p =2.8 and s =1.75 ;

(2) A/A or SA/SA: p =2.9 and s =2.0 ; and

(3) R/A or R/SA: p = 4.65 and s = 3.0.

The three sets of value are used for the prediction of the 24 sets of tests on sand-silt mixtures (Table 6.1), plus the two sets of tests on glass beads and steel shots mixtures (Fig. 6.3). The comparisons of meausred and predicted results are shown in Fig. 6.12a for mixtures with R/R particles shapes (glass beads and steel shots mixtures), shown in Fig. 6.12b for sand-silt mixtures with A/A or SA/SA particles shapes, and shown in Fig. 6.12c for sand-ssilt mixtures with R/A or R/SA particles shapes.

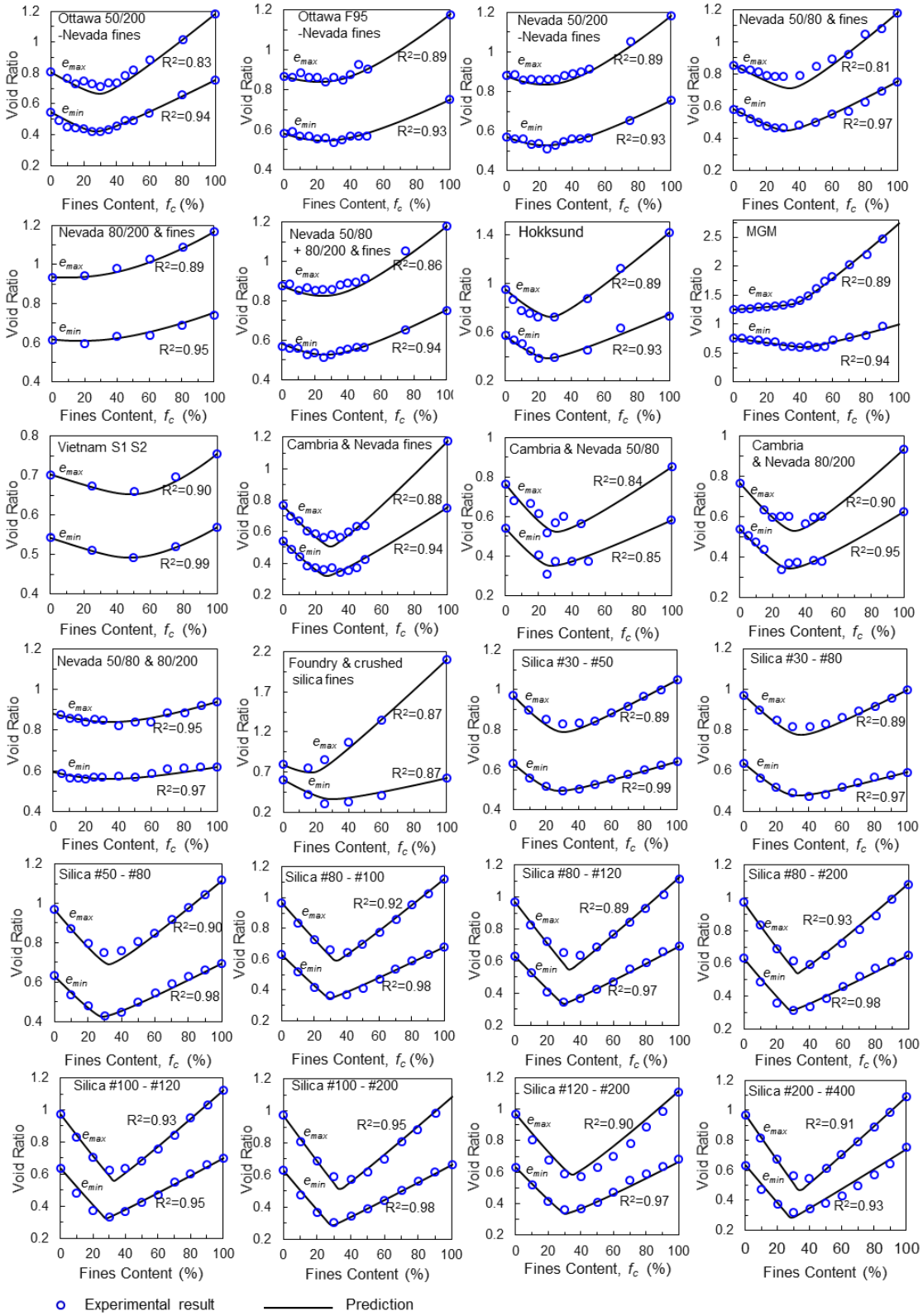

Figure 6.10 Comparison of the measured and predicted maximum void ratios using the values *p* and *s* obtained from the "minimum void ratio" packing procedure

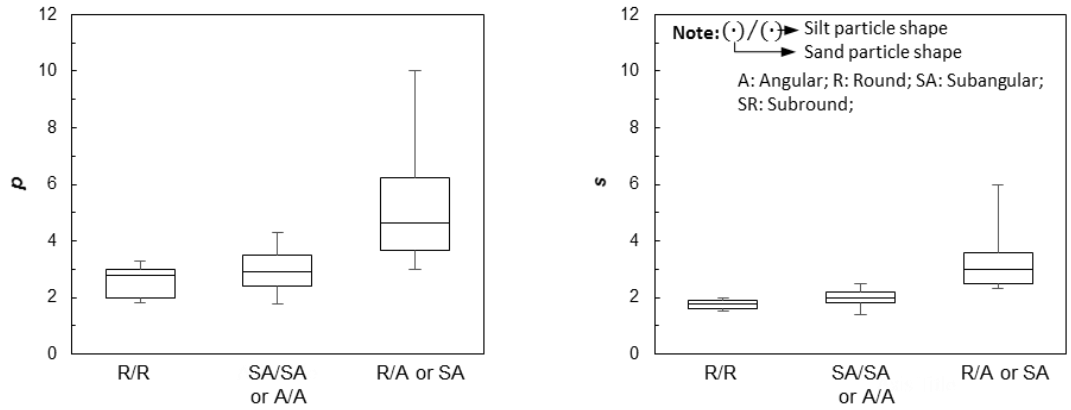

Figure 6.11 Variation of parameters *p* and *s* for 24 soil mixtures listed in Table 6.1 and for spherical particle mixtures used to produce Fig. 6.2

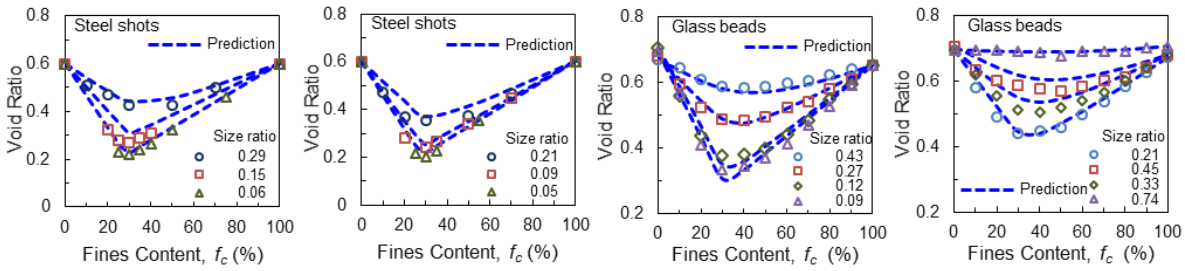

Figure 6.12 (a) Comparison of predicted results (with *p* = 2.8, *s* = 1.75) and measured results of mixtures with R/R compound particle shapes; (b) Comparison of predicted results (with *p* = 2.9, *s* = 2.0) and measured results of mixtures with A/A or SA/SA compound particle shapes; (c) Comparison of predicted results (with *p* = 4.65, *s* = 3.0) and measured results of mixtures with R/A or R/SA compound particle shapes

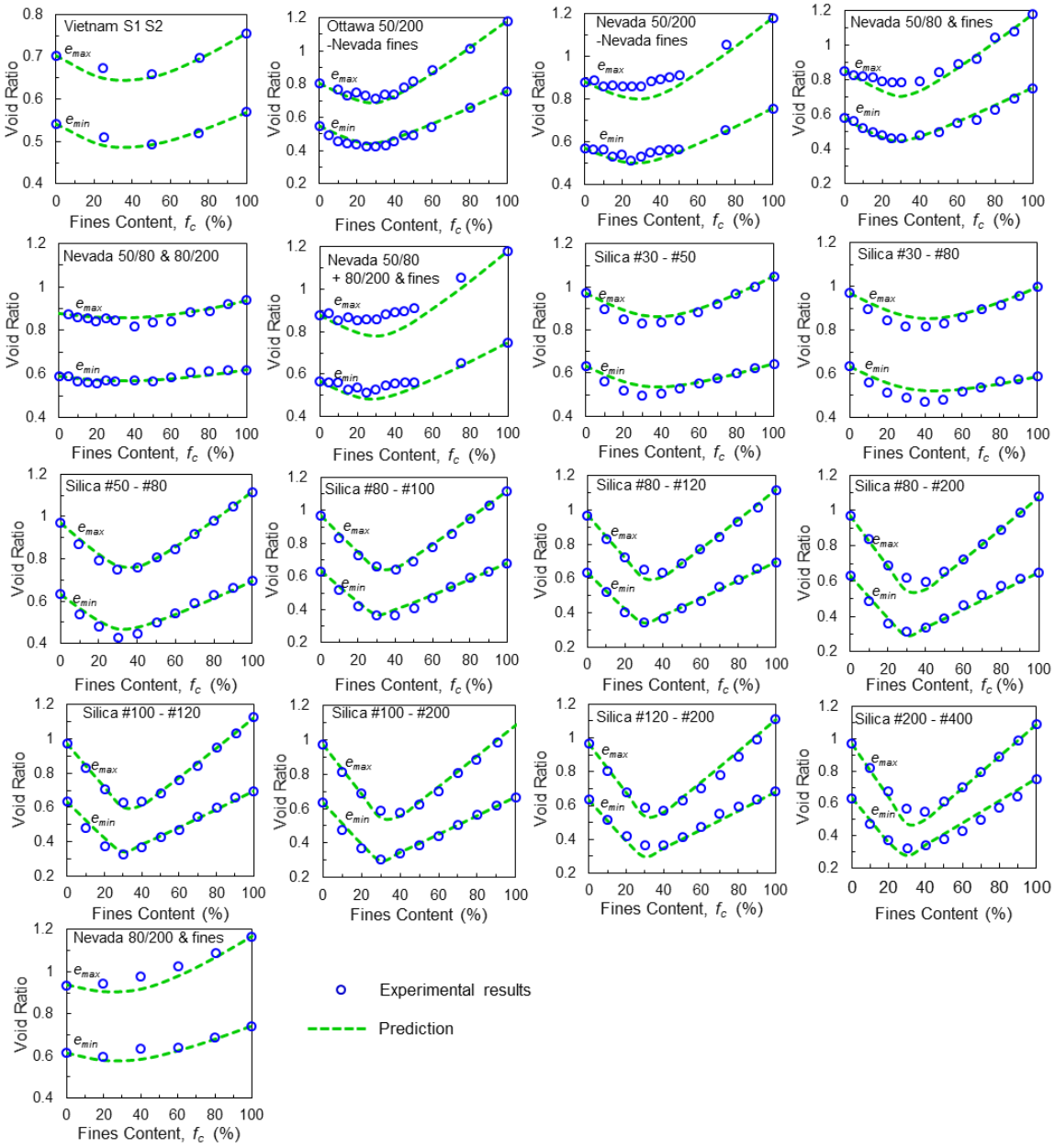

Figure 6.12 (*continued*)

The comparisons of measured and predicted results are plotted on Fig. 6.13a to show the degree of accuracy of the predicted values compared to the measured results. Fig. 6.13b show the distribution of Δe (predicted e – measured e). The one-standar deviation is 0.02 for mixtures with R/R particle shapes, is 0.03 for mixtures with A/A or SA/SA particle shapes, and is 0.054 for mixtures with R/A or R/SA particle shapes. This can be interpreted

that, at least 68% of probability, the predicted error is within ± 0.02 for mixture with R/R paticle shapes, within ± 0.03 for mixture with A/A or SA/SA paticle shapes, and within ± 0.054 for mixture with R/A or R/SA paticle shapes. In Fig. 6.13b, the shaded zone is the one-standard diviation band for all 3 cases.

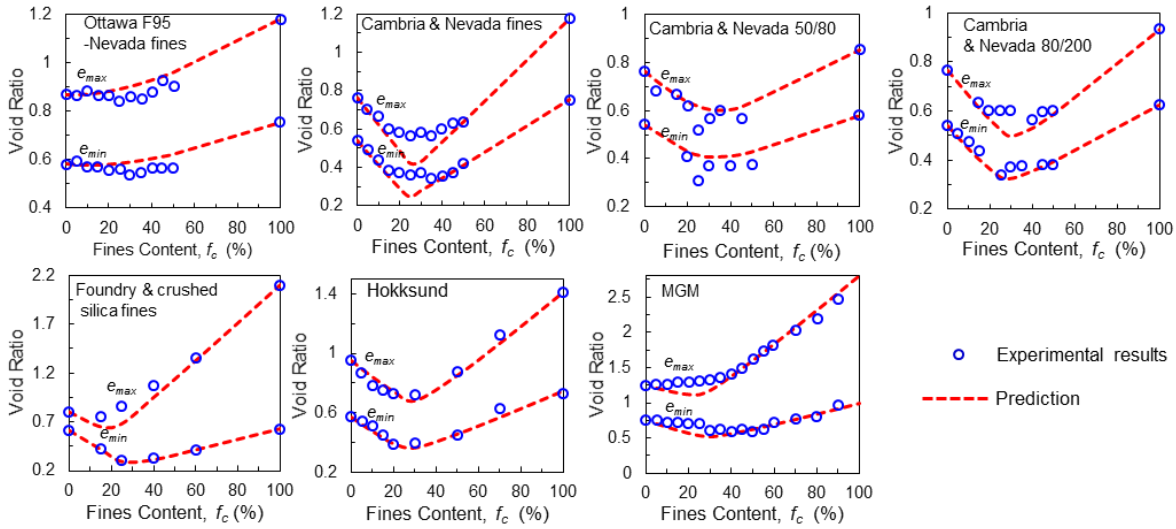

Figure 6.12 (*continued*)

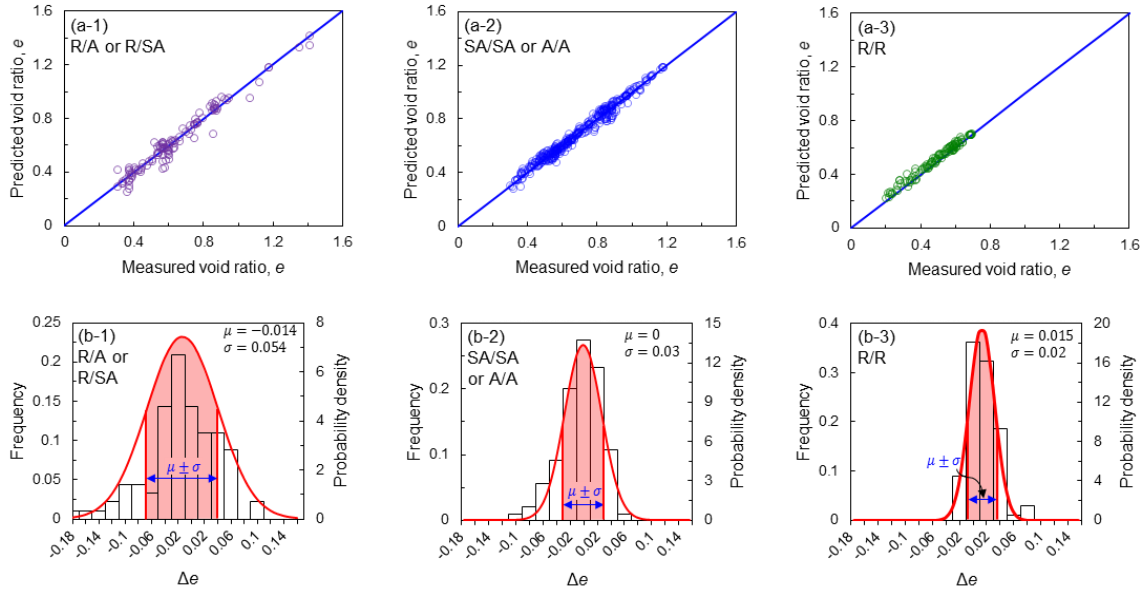

Figure 6.13 (a) The comparison of the predicted and measured results, and (b) the probability distribution of the difference between predicted and measured void ratios for 3 groups of compound particle shapes

6.7 Conclusions

In this chapter, we aim to study the packing procedure effect on density of mixtures. We have defined a packing potential index, which is a measure of volume reduction potential due to mixing of two components of a binary mixtures under a packing procedure. Based on 24 sets of experiments on sand-silt mixtures collected from the literature, we found that the packing potential index is significantly influenced by particle size ratio (d_2/d_1) and the particle morphology of the mixture, such as particle shape, particle surface texture. However, the packing potential index is nearly independent of packing procedure. Thus, packing potential index can be treated as a material characterization parameter of the mixture system.

The packing potential for a mixture of given f_c can be mathematically linked to the particle interaction parameters, which are used in the particle packing models to calculate the void ratio of a binary mixture based on the upper and lower bound void ratios. Thus, we found the parameters p and s, similar to the packing potential index, are also independent of packing procedure, from the analyses of 24 sets of tests results on sand-silt mixtures.

The particle packing model approach is a two-step process: (1) develop upper and lower bounds based on the given monodisperse void ratios e_1 and e_2, for packings of coarse and fine particles, and (2) determine the e of the mixture based on the bounds, using the particle interaction function.

The two-step process approach has two advantages. The first advantage is to account the complex factors of particle morphology (surface roughness, texture, sphericity), and the grain size distribution of silt or sand by using the values of e_1 and e_2 as input data,

which are obtained directly from experiments, and the complex factors of particle morphology and packing procedure are manifested in these two values. Thus, the model can at least capture some influence of these complex factors, which are usually not quantitatively measured, and no analytical method can include these factors in a satisfactory manner.

The second advantage is to use the particle interaction parameters, which are largely dependent only on the system of mixtures but independent of the packing procedure. This characteristic is useful for the packing density model, because the same parameters and the same modelling methodology can be conveniently applied to predict void ratios of mixtures under different packing procedures (e.g. the maximum and minimum void ratios produced by two different processes).

For predicting void ratio of sand-silt mixtures, we proposed a set values for the particle interaction parameters, p and s, (to be used in the nonlinear packing density model proposed by Chang and Deng (2017)). The values are suggested for mixtures with three types of compound particle shapes: R/R, A/A (or SA/SA), and R/A (or R/SA). The comparisons between measured and predicted results show that: the error of predicted values have a standard deviation of 0.02-0.03 for mixtures with compound particle shapes R/R and A/A (or SA/SA), whereas, the error of predicted values have a standard deviation of 0.054 for mixtures with compound particle shapes R/A (or R/SA). Thus, it is more difficult to achieve accurate predicted results for the binary mixtures composed of two components with different particle shapes.

CHAPTER 7

REVISITING THE CONCEPT OF INTER-GRANULAR VOID RATIO IN VIEW OF PARTICLE PACKING THEORY[6]

The equivalent intergranular void ratio appears to be a pertinent density variable in analyzing the mechanical response of silty sand. Using this density variable, the critical state locus in the void ratio vs mean effective stress plane (CSL) for soil mixtures with various fines contents can be normalized into a narrow band to give a single CSL. The equivalent intergranular void ratio is defined as a function of fines content and a parameter *b*. However, the parameter *b* is vaguely defined as the fraction of active fines, which is considered to be a constant by some researchers and considered as a function of fines content by other researchers. Until now, there are no conclusive ways of determining parameter *b*. In this respect, a new formula of the equivalent intergranular void ratio is derived from the perspective of a recently proposed particle packing model. The new formula also shows that the parameter *b* is a function of specific volumes of coarse particles and fine particles. The two specific volumes in general are different for coarse particles and fine particles. If the two specific volumes are same, the new formula is reduced to the same form of the classic formula. This new formula is then verified by several datasets of various sand-silt mixtures.

List of Notation

The following symbols are used in this chapter:

[6] This chapter has been published as a standalone paper: Chang, C. S., & Deng, Y. (2019). Revisiting the concept of inter-granular void ratio in view of particle packing theory. *Géotechnique Letters, 9*(2), 121–129.

b	Active fraction of fines in force structure
CSL	Critical state locus in the void ratio vs mean effective stress plane
C_u	Uniformity coefficient
d_{50}	Mean particle size of pure silt
D_{10}	Particle size of pure sand at 10% finer
D_{50}	Mean particle size of pure sand
e, e_c, e_f	Void ratio, void ratio of pure sand, and void ratio of pure silt
e_{min}, e_{cr}	Minimum void ratio, critical state void ratio
e_g^*, e_c^*	Intergranular void ratio, equivalent intergranular void ratio
f_c, f_{thre}	Fines content, threshold (or transitional) fines content
m, n	Slope
p'	Mean effective stress
PPM	Particle packing model
α, β	Filling parameter, embedding parameter
r, χ	Particle size ratios, $r = d_{50}/D_{10}$, $\chi = D_{10}/d_{50}$
RMSE	Root mean square error
s	Filling exponent
v_c, v_f	Specific volume of pure sand and pure silt, respectively

7.1 Introduction

For silty sand, besides void ratio, the fines content has a significant influence on its mechanical behavior. In order to account for the effect of fines content, Thevanayagam et al. (2002) proposed a density variable: equivalent intergranular void ratio (e_c^*), which is a function of void ratio, fines content, and a parameter *b* representing the fraction of active fines. Many investigators have reported that e_c^* has strong correlations with many aspects of mechanical behavior of silty sand (Mohammadi & Qadimi, 2015; Murthy, Loukidis, Carraro, Prezzi, & Salgado, 2007; Naeini & Baziar, 2004; Ni, Tan, Dasari, & Hight, 2004; Papadopoulou & Tika, 2008; Rahman, Lo, & Gnanendran, 2008; Stamatopoulos, 2010; Thevanayagam et al., 2002; Yang, Sandven, & L.Grande, 2006).

There are several methods suggested for determining the value of *b*. Some researchers consider that *b* is a constant, which can be determined by back-analysis from the experimental data (Thevanayagam et al., 2002; Ni et al., 2004; Yang et al., 2006). On the other hand, other researchers consider that *b* is dependent on fines content (Rahman et al., 2008, Nguyen et al. 2017). Nevertheless, these methods are not satisfactory (A. Mohammadi & Qadimi, 2015). Until now, it still is a challenge of determining the value of *b* for a silty sand.

Recently, based on a more theoretical approach, a particle packing model (PPM) was proposed by Chang et al. (2015) which can predict very well the void ratio of sand-silt mixtures with any fines content. The model takes into account the filling of fine particles into the voids between coarse particles for low fines content and embedment of coarse particles into the matrix of fine particles for high fines content. Only one parameter was

introduced into the model to represent the degree of disturbance of packing structure of the coarse particles due to the filling. The model provides an opportunity to study equivalent intergranular void ratio for silty sand from the particle packing perspective.

The main purpose of this paper is to derive a formulation of e_c^* based on PPM, and hope it can provide a better insight into e_c^* and an alternative way to determine the value of parameter *b*.

7.2 Particle Packing Model

Chang et al. (2015) developed a particle packing model (PPM) for predicting the void ratio *e* of a sand-silt mixture with an arbitrary fines content, which is given by Eq. (7.1) and Eq. (7.2) respectively for two different conditions:

$$e = e_c(1 - f_c) + e_f f_c - \alpha(1 + e_f)f_c$$

for coarse-particle dominant condition (i.e. $f_c < f_{thre}$) (7.1)

$$e = e_c(1 - \beta)(1 - f_c) + e_f f_c$$

for fine-particle dominant condition (i.e. $f_c > f_{thre}$) (7.2)

where f_c is fines content, α and β are the filling parameter and the embedding parameter respectively. The void ratios of pure sand and pure silt are denoted as e_c and as e_f respectively. The void ratios e_c, e_f and e in the two equations are achieved under the same mechanical process and loading conditions (Chang, Wang, & Ge, 2016; Chang & Meidani, 2013), for example, the void ratios can be regarded as minimum or maximum void ratio, or critical state void ratio under the same mean effective stress. In this study, the void ratios (i.e., e_c, e_f and e) refer to the critical void ratios for pure sand, pure silt and sand-silt mixture.

Eq. (7.1) and Eq. (7.2) represent respectively line AD and line BD in Fig. 7.1. These two lines intersect at point D. The fines content corresponding to this point is termed threshold (or transitional) fines content f_{thre}. This value can be solved from Eq. (7.1) and Eq. (7.2), given by

$$f_{thre} = \frac{\beta e_c}{\alpha(1+e_f)+\beta e_c} \tag{7.3}$$

Both the ranges of α and β are from 0 to 1. Note that when $\alpha = \beta = 0$, both Eq. (7.1) and Eq. (7.2) represent line AB, which is the upper bound solution. And when $\alpha = \beta = 1$, Eq. (7.1) and Eq. (7.2) represent lines AC and CB, which are the lower bound solution. Both parameters (α and β) can be calibrated by the slopes of line AD and line BD (i.e. *m* and *n* in Fig. 7.1) obtained from experimental results, using the following equations:

$$\alpha = \frac{e_f - e_c - m}{1+e_f}, \text{ and } \beta = \frac{n - e_f + e_c}{e_c} \tag{7.4}$$

PPM accounts for two mixing mechanisms, i.e., filling and embedment mechanisms. When the coarse particles are dominant, the fine particles are filled into the voids between coarse particles. If the fine particles are not small enough, filling the fine particles would disturb the packing of the coarse particles. On the other hand, when the fine particles are dominant, the coarse particles are embedded into the matrix of fine particles. The embedment would disturb the packing structure of the fine particles adjacent to the embedded coarse particles. The parameters α and β represent respectively the degree of disturbance of the packing structure due to the filling and the embedment. Since this study is limited to the case of 'coarse-particle dominant' range, only parameter α and Eq. (7.1) is involved.

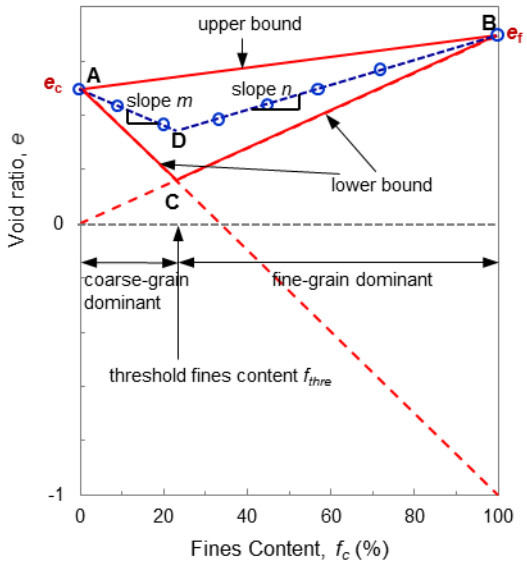

Figure 7.1 General characteristics of void ratio versus fines content for a sand-silt mixture

The parameter α was found to be a function of particle size ratio, d_{50}/D_{50} (Chang et al., 2015), given by:

$$\alpha = (1 - d_{50}/D_{50})^s \qquad (7.5)$$

The symbols d_{50} and D_{50} are mean particle size of pure silt and pure sand respectively. The range of α is 0~1 according to Eq. (7.5). The typical range of the filling exponent s is 2~8 as shown in Fig. 7.2 (Chang et al., 2015). Scatter of points is due to the different types of soil. The value of s is found to be influenced by the overall particle shape of the mixture, and by the contrast of particle shapes of coarse and fine particles. Generally, the value of α is calibrated by fitting Eq. (7.1) to the measured data on binary mixtures, and the value of s is determined by fitting Eq. (7.5) to the calibrated values of α (Chang et al., 2015). This model involves only one independent parameter s.

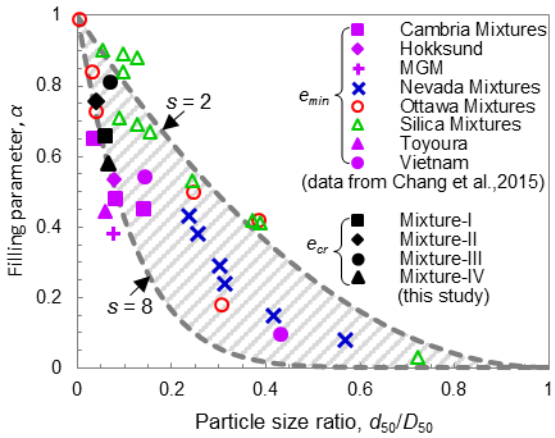

Figure 7.2 Filling parameter versus particle size ratio

7.3 Intergranular Void Ratio

A brief review is given here for the concept of intergranular void ratio. Intergranular void ratio (e_g^*) is also termed as skeleton void ratio by Mitchell (1976) and Vaid (1994). It is assumed that all fines are located in the voids formed by coarse particles of a sand-silt mixture, thus are inactive for carrying load. e_g^* is defined as the void ratio of a sand-silt mixture by removing the solid volume of all fines and calculated as follows:

$$e_g^* = \frac{e+f_c}{1-f_c};\ \ f_c < f_{thre} \qquad (7.6)$$

In a general case, not all fines are inactive. A fraction of fines would be wedged between coarse particles, which actively bear load. For the general case, Thevanayagam et al. (2002) defined an "equivalent" intergranular void ratio e_c^* by modifying Eq. (7.6) to

$$e_c^* = \frac{e+(1-b)f_c}{1-(1-b)f_c};\quad f_c < f_{thre} \qquad (7.7a)$$

The variable e_c^* is a function of the void ratio e and the fines content f_c of silty sand. The parameter b was vaguely defined as the active fraction of fines varying between 0 and 1. The parameter $b = 0$ means that all fines are inactive; whereas $b = 1$ means that all

fines act as load bearing particles. However, it is not clear that how to determine the exact amount of active fraction of fines in a soil mixture. Thus, the variable e_c^* is hypothetical and cannot be measured directly from any physical ways. However, the value of e_c^* can be obtained from a hypothesis suggested by Thevanayagam et al. (2002).

This hypothesis was established from experimental results on CSL tests. Eq. (7.7a) was applied to study the critical state locus (CSL) in the $e - p'$plane for various fines contents of silty sands (e.g., Mohammadi & Qadimi, 2015; Rahman et al., 2008; Thevanayagam et al., 2002; Yang et al., 2006). The experimental results show that CSL is dependent on fines content. However, these CSLs for various f_c can be normalized into a very narrow band in the $e_c^* - p'$plane and it was hypothesized that: CSL in the $e_c^* - p'$plane is a unique curve irrespective of f_c (Thevanayagam et al., 2002). Thus, for a given mean effective stress, e_c^* is a unique number for various f_c ($f_c < f_{thre}$). Based on Eq. (7.7a), e_c^* must be equal to e_c of the pure sand (f_c= 0). Therefore, even though the hypothetical variable e_c^* is not a measurable quantity, it is conjectured that e_c^* has the same value as e_c of the pure sand.

7.4 Another Meaning of *b* in Eq. (7.7a)

The hypothesis of $e_c^* = e_c$ is applied in this section to interpret the meaning of parameter *b*. First, Eq. (7.7a) is rearranged to a general form

$$F(e_c^*, e, f_c) = e - e_c^*(1 - f_c + bf_c) - (1 - b)f_c = 0; \quad f_c < f_{thre} \qquad (7.7b)$$

Then, using the notion of $e_c^* = e_c$ (for a given mean effective stress), Eq. (7.7b) can be converted to the following equation

$$F(e_c, e, f_c) = e - e_c\,(1 - f_c + bf_c) - (1 - b)f_c = 0; \quad f_c < f_{thre} \qquad (7.8a)$$

This equation can be rearranged into a special form

$$e = e_c\left(1 - f_c + bf_c\right) - (1-b)f_c; \quad f_c < f_{thre} \tag{7.8b}$$

Eq. (7.8b) represents a particle packing relationship between e vs f_c. Here, the dependency of b is examined with respect to (1) fines content, (2) particle size ratio and (3) effective mean stress.

(1) *Fines content*: Fig. 7.3a shows the experimental data on Foundry sand with various fines contents for two different mean effective stresses (Thevanayagam et al., 2002). Fig. 7.3b shows the experimental data on binary mixtures of steel shots for four particle size ratios and various fines contents (McGeary, 1961). It is noted that if the e vs f_c in Eq. (7.8b) is a linear line, then b is independent of f_c. According to Fig. 7.3a, the two linear lines adequately fit the data for $f_c < f_{thre}$. In Fig. 7.3b, the four linear lines also adequately fit the data for $f_c < f_{thre}$. These observations are in agreement with the assumption in PPM that the e vs f_c is a linear relationship. Thus, in Eq. (7.8b), b is independent of fines content.

However, for mixtures with larger particle size ratios, the e vs f_c deviates from a linear relationship for f_c near f_{thre} as shown in Fig. 7.3b. In this case, b is dependent on f_c. However, this is a secondary effect. In this study, the linear condition of Eq. (7.8b) is assumed.

Considering b to be independent of f_c, taking the derivative of e in Eq. (7.8b) with respect to f_c, the slope (m) of the line on the plot of e vs f_c can be obtained, i.e., $m = -(1-b)(1+e_c)$. Then:

$$b = \frac{-m+1+e_c}{1+e_c} \tag{7.9}$$

Hence, in addition to the fraction of active fines, another meaning of b is connected to the slope of $e - f_c$ line, which can be measured directly from experimental results.

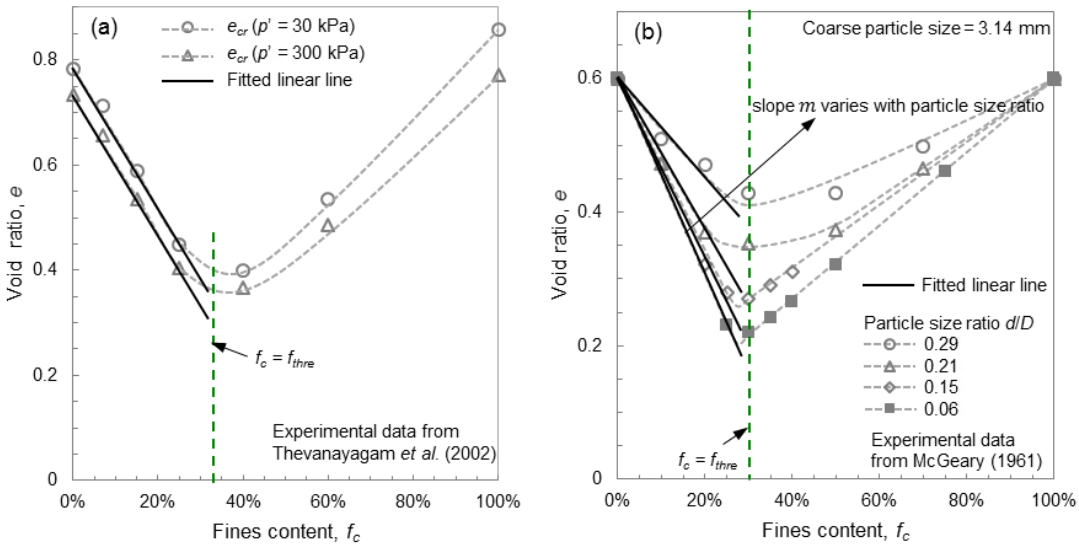

Figure 7.3 Void ratio vs fines content: (a) Foundry sand with various fines contents (the data of e_{cr} was interpolated from the experimental data reported by Thevanayagam et al. (2002)); (b) binary mixtures with various particle size ratios

(2) *Particle size ratio*: As shown in Fig. 7.3b, the linear lines adequately fit the data reported by McGeary (1961). Their slopes are obviously different for various particle size ratios. In PPM, the slope is treated as a function of particle size ratio. Consequently, b should be a function of particle size ratio.

(3) *Effective stress*: In Fig. 7.3a, e_c = 0.783 for 30 kPa and e_c = 0.733 for 300 kPa. By fitting linear lines to the data, and using Eq. (7.9), the calculated values of b = 0.27 for 30 kPa and b = 0.25 for 300 kPa. The parameter b is a function of e_c in Eq. (7.9) and e_c is known to be dependent on p'. Therefore, in this study, b is considered to be dependent on p'.

7.5 Formulation of e_c^* and b Based on Equation Derived from PPM

It is noted that, by replacing e_c^* with e_c, $F(e_c^*, e, f_c)$ in Eq. (7.7b) can be converted to $F(e_c, e, f_c)$ in Eq. (7.8a), which can be regarded as particle packing relationship for a sand-silt mixture. On the other hand, using the reverse process by replacing e_c with e_c^*, Eq. (7.8a) can be converted back to Eq. (7.7b). Due to the reciprocal relation between the two equations, Eq. (7.8a) can be regarded as the conjugate equation of Eq. (7.7b).

Besides Eq. (7.8b), there exist other particle packing relationships for a binary mixture. In an earlier section, a relationship of e vs f_c (see Eq. (7.1)) was derived from the perspective of particle packing theory. Eq. (7.1) can be rearranged into a general form

$$G(e_c, e_f, e, f_c) = e - e_c(1 - f_c) + e_f f_c - \alpha(1 + e_f) f_c = 0 \; ; \;\; f_c < f_{thre} \quad (7.10a)$$

It is noted that in this particle packing equation, unlike Eq. (7.8b), the void ratio of the binary mixture is not only associated with e_c but also with e_f, even in the range of $f_c < f_{thre}$. Whereas, in Eq. (7.8b), in this range of fines content, the void ratio of the binary mixture is assumed to be only associated with e_c.

By replacing e_c with e_c^* in Eq. (7.10a), the conjugate equation of Eq. (7.10a) can be obtained. After rearrangement, it becomes

$$e_c^* = \frac{e - e_f f_c + \alpha(1 + e_f) f_c}{1 - f_c} \quad (7.10b)$$

Eq. (7.10b) is a new formula of equivalent inter-granular void ratio. This formula indicates that e_c^* is related to the property of fine particles e_f, which differs from the classic formulation in Eq. (7.7a). Discussions about the influence of e_f will be given in a later section.

The e vs f_c relationship described in Eq. (7.1) contains a parameter α. Whereas, the relationship described in Eq. (7.8b) contains a parameter b. By considering that Eq. (7.8b) is equivalent to Eq. (7.1), the value of b can be related to α by

$$b = \frac{(1+e_f)}{(1+e_c)}(1-\alpha) = \frac{v_f}{v_c}(1-\alpha) \qquad (7.11)$$

It is noted that the same relationship between b and α can also be obtained by considering that Eq. (7.7a) is equivalent to Eq. (7.10b).

In Eq. (7.11), v_c and v_f are respectively the specific volumes of pure sand and pure silt at critical state, ($v_c = 1 + e_c$ and $v_f = 1 + e_f$). Specific volume represents the space-filling property, which describes the amount of solid mass required to fill a unit volume of space. The space-filling properties are generally different for sand and silt ($i.e., v_f \neq v_c$) due to their difference in particle shape .

Using the expression of α in Eq. (7.5), Eq. (7.11) becomes

$$b = \frac{v_f}{v_c}(1-(1-d_{50}/D_{50})^s) \qquad (7.12)$$

In Eq. (7.12), the range of particle size ratio is between 0 and 1. Thus, the range of b is between 0 and v_f/v_c. To show the variation of b with particle size ratio for various values of v_f/v_c, Eq. (7.12) is plotted in Fig. 7.4a for s = 2, 4 and 8, and for v_f/v_c = 0.8, 1.0 and 1.2. For comparison, the data points of b, obtained from the back-analysis (Thevanayagam et al., 2002) for ten types of silty sand, were also plotted in the Fig. 4a. The data are covered in the range of prediction by Eq. (7.12). A detailed evaluation of Eq. (7.12) is given in next section.

In what follows, two cases of Eq. (7.12) are discussed: (1) $v_f = v_c$ and (2) $v_f \neq v_c$.

(1) $v_f = v_c$: The specific volume of coarse particle is equal to the specific volume of fine particles. For an example of a binary mixture of glass beads, the coarse and fine particles are of the same shape and material. Therefore, it is expected that $v_f = v_c$ (i.e. $e_f = e_c$). In this case, Eq. (7.11) shows that $\alpha = 1 - b$ and Eq. (7.10b) is reduced to the same form of the classic equation (Eq. (7.7a)). Also, Eq. (7.12) can be expressed as

$$b = 1 - (1 - d_{50}/D_{50})^s \qquad (7.13)$$

This equation is shown by solid line (v_f/v_c=1) in Fig. 7.4a for *s* = 2, 4 and 8.

(2) $v_f \neq v_c$: When the coarse particles and the fine particles are of different particle shapes and different minerals, it is expected that $v_f \neq v_c$. For example, $v_f > v_c$ for the mixtures of and Hokksund sand and Chengbei silt (Yang, 2004), and $v_f < v_c$ for the Toyoura sand-silt mixtures (Zlatovic & Ishihara, 1995). It is noted that, according to Eq. (7.12), the maximum value of *b* can go beyond one as shown in Fig. 7.4a (v_f/v_c= 1.2), and the maximum value of *b* can be less than one as shown in Fig. 7.4a (v_f/v_c= 0.8).

Apart from Eq. (7.12), there are equations proposed by other investigators to predict the evolution of *b* with particle size ratio. Fig.7. 4b shows the evolution of *b* with particle size ratio (d_{50}/D_{10}) for various fines contents proposed by Rahman et al. (2011). Fig. 7.4a and 7.4b show very different patterns of *b* versus particle size ratio.

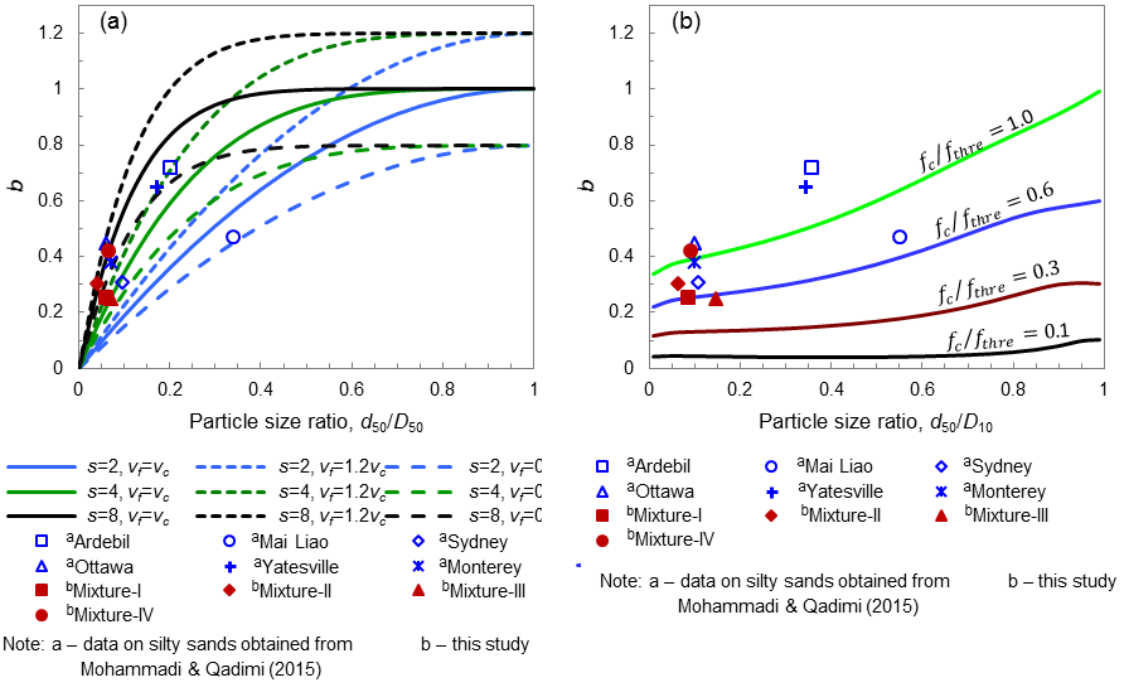

Figure 7.4 Variation of b with respect to particle size ratio computed from: (a) Eq. (7.12) for different values of v_f/v_c and (b) the equation for different f_c/f_{thre} proposed by Rahman *et al.* (2011)

It is of interest to compare the performance of the two approaches using a special case of a binary mixture of glass beads with a given fines content. In this special case, the particle size ratio of the binary mixture is very close to 1. Thus, the binary mixture with any fines content can be regarded as a mono-sized packing and the void ratio of this binary mixture (e) should be close to the pure coarse particle packing (e_c). Based on the classic definition of b (Eq. (7.7a)), since f_c is not zero, the value of b must be close to 1. This is consistent with the prediction of Eq. (7.13). In Eq. (7.13), under the condition of $v_f = v_c$ and $d_{50}/D_{50} = 1$, b is close to 1 and independent of fines content.

However, according to the predictions using the equation proposed by Rahman et al. (2011) as shown in Fig. 7.4b, under the condition of the particle size ratio being close

to 1, b is not close to 1 for all $f_c < f_{thre}$. For most level of f_c, the values of b are very small.

7.6 Comparison of 4 Methods of Determination of *b*

In the literature, there are several methods of determining b of Eq. (7.7a). Table 7.1 lists these available methods, including Eq. (7.12) and Eq. (7.13) derived in this study. Among these methods, 4 methods (see Method A, B, C D in Table 7.1) were chosen in this study for comparing their applicability.

Although the data related to the behavior of silty sand in the literature is quite abundant, they are not suitable for the evaluation of Eq. (7.12), because, in most of experimental datasets, the required information of CSL for silt is not available. For this purpose, four datasets of sand-silt mixtures published in the literature were selected. The material properties for these four mixtures are listed in Table 7.2. The CSL for these four mixtures with various fines contents are shown in Fig. 7.5.

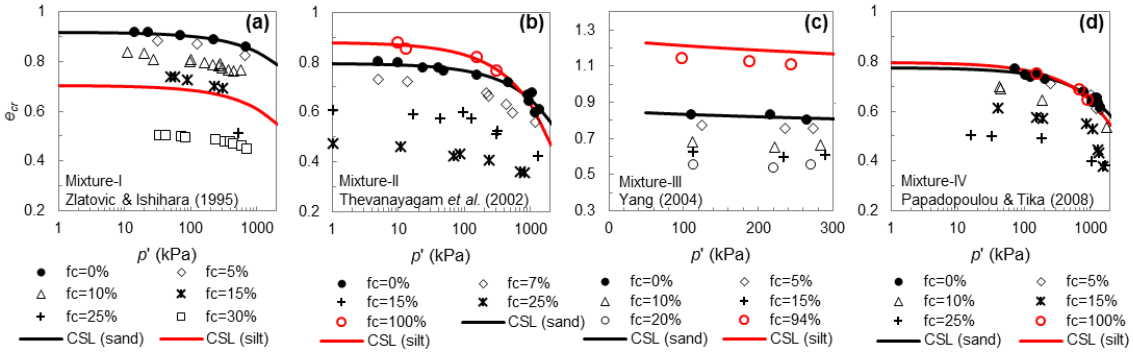

Figure 7.5 CSL for 4 mixtures with various fines contents: (a) Mixture-I, (b) Mixture-II, (c) Mixture-III and (d) Mixture-IV

In Method A, the value of b is determined from Eq. (7.12). The required value of e_c and e_f in Eq. (7.12) are computed from the measured CSL for pure sand and pure silt, shown in Fig. 7.5 for each mixture by

$$e_c = e_{ref,c} - \lambda_c \left(p'/p_a\right)^{0.7} \tag{7.14}$$

$$e_f = e_{ref,f} - \lambda_f \left(p'/p_a\right)^{0.7} \tag{7.15}$$

where the atmospheric pressure $p_a = 101.3$ kPa and $e_{ref,c}$, λ_c, and $e_{ref,f}$, λ_f are fitting parameters for pure sand and pure silt respectively, which were listed in Table 7.1.

Using Eq. (7.10b) and Eq. (7.5), e_c^* is dependent on the single parameter s. The value of s is determined so that the calculated e_c^* are the best-fit to the measured CSL of sand e_c. The determined value of s is also used in Method C.

Fig. 7.6 shows the computed e_c^* from 4 methods in the e_c^* -logp' plane. By using e_c^*, the data fall into a narrow band. The degrees of scatter of points e_c^* are different for the 4 methods, which reflect accuracy of the methods. Root mean square error (RMSE) for each mixture was computed to quantify the degree of scatter and is shown in Fig. 6 for each method.

In Fig. 7.6, the RMSEs are nearly the same for Method A and Method B. Method A is a best-fit process by varying s whereas Method B is a best-fit process by varying b. Both methods best-fit to one equation by varying one variable. Thus, the degrees of scatter of the two results are comparable.

Table 7.1 Summary of methods of determining *b* value

Ref.	Function	Formula	Used in this study
Thevanayagam et al. (2002)	b = constant	Back analysis	Method B
Rahman et al. (2011)	$b = F(f_c, r)$	$b = \left\{1 - \exp\left[-0.30\frac{(f_c / f_{thre})}{k}\right]\right\} \times \left(r\frac{f_c}{f_{thre}}\right)^r$ $r = d_{50} / D_{10}$; $k = 1 - r^{0.25}$ $f_{thre} = 0.4\left(\frac{1}{1+e^{0.5-0.13\chi}} + \frac{1}{\chi}\right)$ $\chi = 1/r$	Method D
Mohammadi & Qadimi (2015)	$b = F(\chi)$	$b = 0.26 + 1.22/\chi$	-
Nguyen et al. (2017)	$b = F(f_c, e, \chi)$	$b = 1.3 - \left[1 + exp\left(0.85 - 0.63\frac{e\chi + f_c\chi}{1 - f_c + 2f_c\chi}\right)\right]$	-
Eq. (7.12) (This study)	$b = F(\frac{v_f}{v_c}, \frac{d_{50}}{D_{50}})$	$b = \frac{v_f}{v_c}(1 - (1 - d_{50}/D_{50})^s)$	Method A
Eq. (7.13) (This study)	$b = F(d_{50}/D_{50})$	$b = 1 - (1 - d_{50}/D_{50})^s$	Method C

The scatter of Method C is slightly larger than that of Method A, because of the assumption: $e_f = e_c$. The actual values of e_f and e_c for these four mixtures are shown in Fig. 7.5. Viewing the actual values, the $e_f = e_c$ assumption is satisfied for Mixture-IV as shown in Fig. 7.5d, thus the RMSE (0.0251) are identical for Methods A and C in Fig. 7.6d. The assumption is reasonably acceptable for Mixture-II as shown in Fig. 7.5b, thus RMSEs are very close (0.0181 vs. 0.017) in Fig. 7.6b. The assumption is obviously not acceptable

for Mixture-I and Mixture-III as shown in Fig. 7.5a & 7.5c. The RMSEs are 0.0310 vs. 0.0301 (Fig. 7.6a) and 0.0167 vs. 0.0128 (Fig. 7.6c).

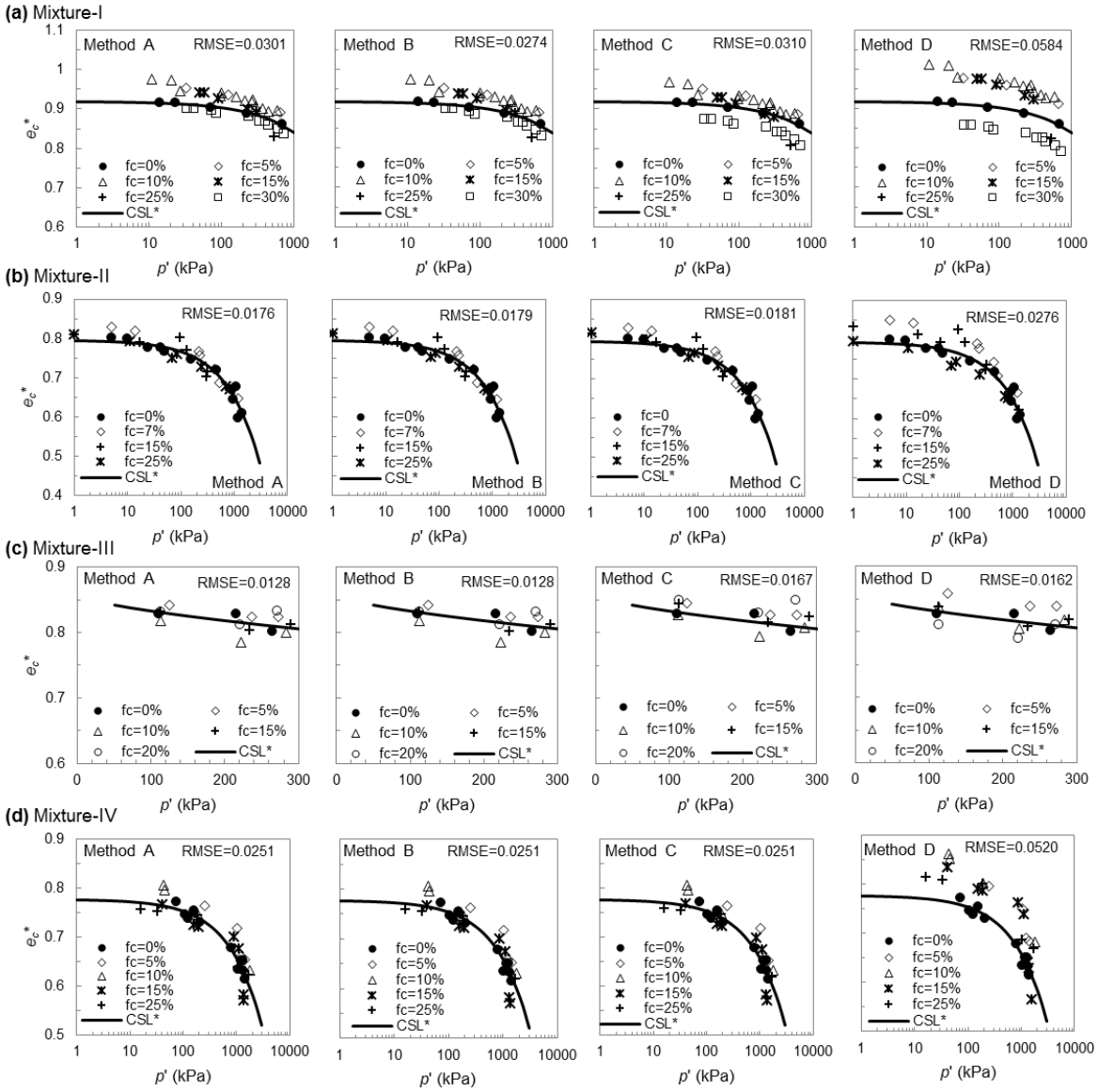

Figure 7.6 Comparison of computed e_c^* from 4 different methods for 4 mixtures: (a) Mixture-I (raw data extracted from Zlatovic and Ishihara (1995)), (b) Mixture-II (raw data extracted from Thevanayagam et al. (2002), (c) Mixture-III (raw data extracted from Yang (2004)) and (d) Mixture-IV (raw data extracted from Papadopoulou and Tika (2008))

Table 7.2 Selected four sand–silt mixtures from literature used in this study

Mixture #	Sand/silt	Sand				Silt			CSL (sand)		CSL (silt)		s	Method	
														B	C
		D_{10}	D_{50}	C_u	e_{min}	d_{50}	C_u	e_{min}	$e_{ref,c}$	λ_c	$e_{ref,f}$	λ_f		b	b
I	Toyoura/ Milled Toyoura (R1)	0.116	0.17	1.61	0.59	0.01	6.08	0.616	0.919	0.016	0.706	0.019	6.86	0.305	0.340
II	Foundry/ Crushed silica (R2)	0.16	0.25	1.69	0.608	0.01	7.5	0.627	0.796	0.029	0.880	0.051	6.89	0.252	0.245
III	Hokksund/Chengbei (R3)	0.218	0.45	2.25	0.572	0.032	2.32	0.731	0.856	0.024	1.250	0.038	2.85	0.248	0.206
IV	Quartz/ Quartz (R4)	0.22	0.3	1.3	0.585	0.02	7.5	0.652	0.777	0.024	0.796	0.031	7.88	0.419	0.419

R1: Zlatovic and Ishihara (1995); R2: Thevanayagam et al. (2002); R3: Yang (2004); R4: Papadopoulou and Tika (2008)

Comparing the results of Method C with that of Method D (Rahman et al. 2008), the scatter of Method C is generally smaller than that of Method D. However, note that Method C involves a best-fit process from data, which is not required in Method D. In Method D, the results are directly calculated from Rahman's formula. Thus, the smaller scatter of Method C is expected.

Based on the limited data sets, it cannot be concluded that the proposed equation has a better fit than that of the existing equations. However, these comparisons show that the new formulation of parameter *b*, derived from the viewpoint of particle packing theory, is adequate for determining CSL in the e_c^* -logp' plane. This new approach is also useful for investigating the various influence factors of parameter *b*.

The values of *b* used in the four methods are examined in Fig. 7.7. For method A, the value of *b* is a function of e_c and e_f, which in turn are functions of p' (see Eq. (7.14) and Eq. (7.15)). Thus, for convenience, the value of *b* for Method A is plotted against p' in Fig. 7.7a. Fig. 7.7a shows that the effect of p' for Method A is not significant for these four mixtures, in which the test ranges are p' < 1000 kPa and $f_c < 20\%$. In most of experiments for silty sand published in the literature, mean effective stress is less than 1000 kPa.

The values of *b*, for Method B and for Method C, are independent of p', and are marked in Fig. 7.7a in parenthesis for each mixture. The differences of *b* among Method A, Method B and Method C are not significant. The value of *b* for method D varies with f_c as shown in Fig. 7.7b. The variation of *b* with f_c is not considered in Method A.

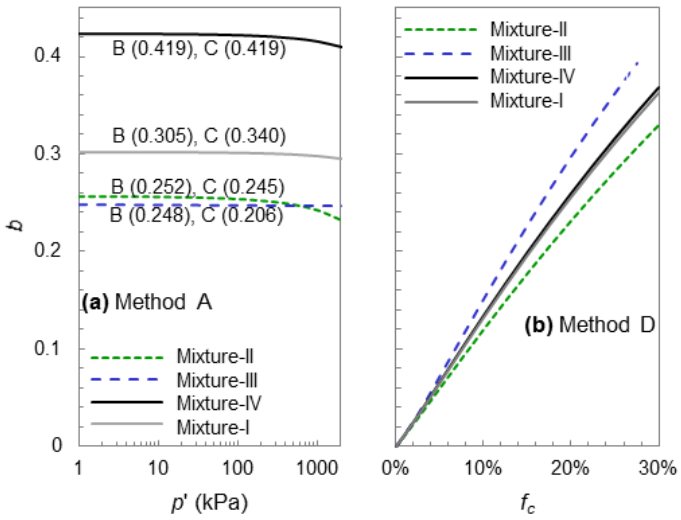

Figure 7.7 (a) The values of b versus mean effective stress p' for silt-sand mixtures in Method A (the b values in Methods B and C are marked in parentheses); (b) The values of b versus fines content fc for silt-sand mixtures for Method D

It is of interest to know, for Method B, whether the best-fitted b values determined from the data of e_{min} (denoted as b_{min}) are same as those determined from the data of e_{cr} (denoted as b_{cr}). Fig. 7.8a shows that, b_{min} are nearly the same as b_{cr} for two mixtures (II and IV). However, b_{min} are very different from b_{cr} for the other two mixtures (I and III). On the other hand, Fig. 7.8b shows the comparison of the best-fitted s_{min} and s_{cr} from method A. For all four mixtures, s_{min} are nearly the same as s_{cr}.

Therefore, s seems to be an intrinsic material parameter which is in agreement with that proposed in PPM. Thus, the value of s used in Eq. (7.12) for e_{cr} can be determined from the data of e_{min}. According to Eq. (7.12), the deviation between b_{min} and b_{cr} in Fig. 7.8a is caused by the differences in specific volume ratios, i.e. $(v_f/v_c)_{min} \neq (v_f/v_c)_{cr}$. Table 7.3 shows the values of specific volume ratios for the four mixtures. It is interesting

to note that for mixtures II and IV, the specific volume ratios are nearly the same. Whereas the specific volume ratios are very different for mixtures I and III.

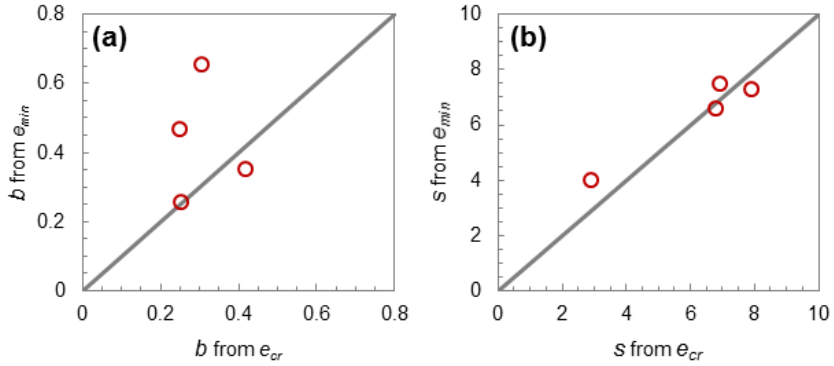

Figure 7.8 (a) The fitted values of *b* for 4 mixtures obtained from data of e_{min} vs. those obtained from data of e_{cr}; (b) The fitted values of *s* for 4 mixtures obtained from data of e_{min} vs. those obtained from data of e_{cr}

Table 7.3 Comparison of the specific volume ratio v_f/v_c between critical state and densest state for the selected four sand–silt mixtures

Mixture #	Densest state	Critical state		
	v_f/v_c	p' range (kPa)	v_f/v_c range	Average v_f/v_c
Mixture-I	1.016	10 - 1000	0.888 - 0.876	0.882
Mixture-II	1.012	1 - 1000	0.985 - 1.046	1.015
Mixture-III	1.101	100 - 300	1.207 - 1.202	1.205
Mixture-IV	1.042	10 - 1000	0.990 - 1.010	1.000

7.7 Conclusions

Based on particle packing theory, a new formula for e_c^* is proposed. The new formula shows that e_c^* of a sand-silt mixture is not only a function of e and f_c, but also a function of e_f. Thus, e_c^* is dependent on the property of fine particles. However, in the classic formula, e_c^* is only a function of e and f_c. The void ratio of fine particles e_f is generally not same as that of coarse particles e_c. However, under the condition of $e_f = e_c$, the form of the new formula is reduced to that of the classic formula.

Parameter b was defined as the fraction of fines that contributes to the active inter-grain contacts (Thevanayagam et al., 2002) or to the force structure (Rahman et al., 2008). According to this definition, the value of b is very difficult to be determined because the active fines are not measurable from experimental tests. In this study, from the perspective of particle packing theory, the value of b has a new interpretation related to the slope of the line on the plot of e vs f_c. Thus, the value can be easily determined from experimental tests.

Based on the new formula of e_c^* derived from particle packing theory, a new formula is also derived for parameter b which is a function of the ratio of specific volumes v_f/v_c for fine and coarse particles. This new formula of parameter b is verified by comparisons between predicted and measured results for four datasets of various sand-silt mixtures. The range of specific volume ratios for the four mixtures is 0.8 – 1.2. The results clearly show the influence of v_f/v_c on the predicted e_c^*, and indicate that the effect of v_f/v_c is not insignificant.

This study shows that the type of fine particles plays an important role in the intergranular void ratio. However, most experimental work in the literature of intergranular void ratio do not include the information of CSL for fine particles. Future experimental studies are needed for a better understanding of the influence of fines on the critical state behavior of sand-silt mixtures.

CHAPTER 8

MODELING FOR CRITICAL STATE LINE OF GRANULAR SOIL WITH EVOLUTION OF GRAIN SIZE DISTRIBUTION DUE TO PARTICLE BREAKAGE[7]

Determination of the critical state line (CSL) is important to characterize engineering properties of granular soils. Grain size distribution (GSD) has a significant influence on the location of CSL. The influence of particle breakage on the CSL is mainly attributed to the change in GSD due to particle breakage. However, GSD has not been properly considered in modeling the CSL with influence of particle breakage. This study aims to propose a quantitative model to determine the CSL considering the effect of GSD. We hypothesize that the change of critical state void ratio with respect to GSD is caused by the same mechanism that influences of the change of minimum void ratio with respect to GSD. Consequently, the particle packing model for minimum void ratio proposed by Chang et al. (2017) is extended to predict critical state void ratio. The developed model is validated by experimental results of CSL lines for several types of granular materials. Then the evolution of GSD due to particle breakage is incorporated into the model. The model is further evaluated using the experimental results on rockfill material, which illustrates the applicability of the model in predicting CSL for granular material with particle breakage.

[7] This chapter has been published as a standalone paper: Chang, C. S., & Deng, Y. (2020). Modeling for critical state line of granular soil with evolution of grain size distribution due to particle breakage. *Geoscience Frontiers, 11*(2), 473–486.

8.1 Introduction

Critical state is defined as the state at which the soil continues to deform in shear at constant stress and constant void ratio (Roscoe, Schofield, & Wroth, 1958). At this state, a unique relationship between the critical state void ratio (e_{cs}) and the mean effective stress (p') can be expressed by a critical state line (CSL) in the $e - \log p'$ plane, which is independent of stress path including intermediate stress. (Been, Jefferies, & Hachey, 1991; Riemer & Seed, 1997; Roscoe et al., 1958; Schofield & Wroth, 1968; Zhou, Liu, Ma, & Chang, 2017). The CSL is a fundamental property, which has been widely used to characterize strength, deformation, and liquefaction behavior of granular soil (Been & Jefferies, 1985; Imam et al., 2005; Jefferies & Been, 2006; Schofield & Wroth, 1968).

Many investigators found that the location of a CSL in the $e - \log p'$ plane is significantly influenced by particle breakage when granular soils undergo high stress. This observation has been found in experiments (Bandini & Coop, 2011; Biarez & Hicher, 1994; Carraro, Prezzi, & Salgado, 2009b; Hardin, 1985; Hyodo, Nakata, Yoshimoto, Kato, & Okabayashi, 2001; Verdugo & Ishihara, 1996; Yu, 2017) and in discrete element simulations (Ciantia, Arroyo, O'Sullivan, Gens, & Liu, 2019; Muir Wood & Maeda, 2008; Sadrekarimi & Olson, 2011; Zhou et al., 2017).

Traditionally, a three-segment linear CSL in the $e - \log p'$ plane (as the solid line shown in Fig. 8.1) has been adopted for the full range of p' (Been et al., 1991; Konrad, 1998; Russell & Khalili, 2004).

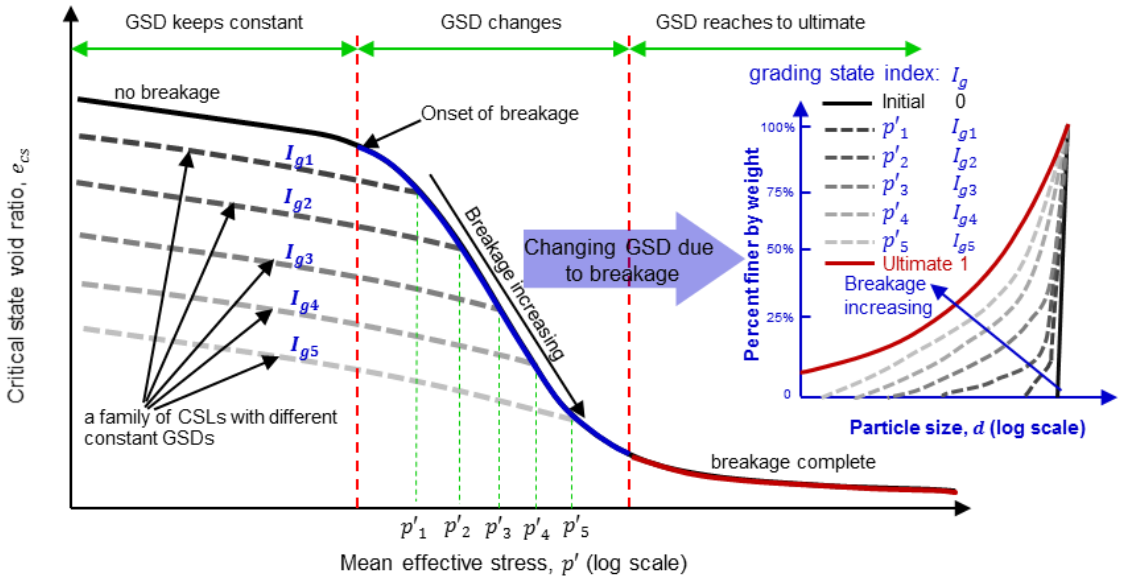

Figure 8.1 Three-segment Critical State Line

At the first segment, the stress level is very low where breakage is negligible, thus the grain size distribution (GSD) of the specimen keeps constant. At the second segment, the stress level is elevated where breakage becomes pronounced. Due to particle breakage, the CSL becomes steeper and the GSD at critical state changes with mean effective stress. At the third segment, the stress level is very high, but there is no further breakage because an ultimate GSD has been reached. Thus, the CSL becomes flatter.

The influence of particle breakage on CSL is mainly attributed to the change of GSD. Based on this viewpoint, Daouadji et al. (2001) first suggested that, instead of three-segment line, the CSL is related to a family of parallel lines (as the dashed lines shown in Fig. 8.1) where each line corresponds to a constant GSD. The second segment of the solid CSL was interpreted as a locus of end points of this family of dashed CSLs. Each point on the locus is at successively higher stresses and has more breakages. The changing GSD caused by the breakage leads to a steeper curve of the CSL. This family of parallel lines provide an alternative picture to the three-segment line. The dashed CSL moves downward

with increasing particle breakage or increasing coefficient of uniformity of gradation. This observation has also been found in experiments (Hu, Yin, Dano, & Hicher, 2011; Li et al., 2015; Xiao, Liu, Ding, et al., 2016; Yu & Su, 2016). The role of GSD on the location of dashed CSL has been raised as a key question in mechanics of sands (Bandini & Coop, 2011).

Muir Wood and Maeda (2008) developed this idea further by suggesting a "grading state index", a parameter between 0 and 1 which was used to characterize the changed GSD due to particle breakage. The set of parallel dashed CSLs in Fig. 8.1 correspond to different grading state indices I_g. As breakage occurs, the grading state index increases, and the dashed CSL moves downward. The relationship between the dashed CSL and grading state index was used to account for the effect of breakage.

Other than the grading state index, various types of breakage indices were used to characterize the change of GSD due to particle breakage (Einav, 2007; Hardin, 1985; Lade, Yamamuro, & Bopp, 1996; Marsal, 1963; Xiao & Liu, 2017). Attempts were also made to link the relationship between the dashed CSL with breakage index (Einav, 2007; Tengattini, Das, & Einav, 2016; Xiao & Liu, 2017).

However, this type of empirical relationship is obtained from fitting the experimental results, which is only applicable to the specific soil and the conditions used in the experiments. Furthermore, because this type of empirical relationship only uses grading/breakage index, which does not directly account for the influence of GSD. In this paper, we aim to develop an analytical model to predict the CSL with influence of particle breakage by directly considering GSD.

Herein, the particle packing model for minimum void ratio proposed by Chang et al. (2017) is extended to predict the CSL for granular soil considering the effect of GSD. In what follows, in order to make the model extension more logical, we begin with the correlation analysis between minimum and critical state void ratios. Then the particle packing model is extended to predict the CSL considering the effect of GSD. Two cases are considered: for material with particle breakage and for material without particle breakage. For the case without particle breakage, the proposed model is verified by experimental results for four types of granular materials at small stress range. For the case with particle breakage, the proposed model is verified by a rockfill material with considerable particle breakage.

8.2 Rationale Using Particle Packing Model for e_{cs}

The minimum void ratio (e_{min}), achieved through the method specified by American Society for Testing and Materials (ASTM), is found to be highly influenced by GSD of the granular soil (Lade et al., 1998; Thevanayagam et al., 2002; Yilmaz, 2009; Youd, 1973). An analytical particle packing model has been developed and verified by comparing the measured and predicted minimum void ratios for sand-silt mixtures with various fines content (Chang et al., 2015) and for multi-sized granular soils with various GSD (Chang et al., 2017).

It is interesting to note that the model for minimum void ratio was extended to predict the maximum void ratio (e_{max}) with great accuracy (Chang et al., 2016). The good performance was expected because a very strong correlation was noted between e_{max} and e_{min} (Cubrinovski & Ishihara, 2002, Chang et al., 2016). Thus, it was hypothesized that the

change of maximum void ratio with respect to GSD is caused by the same particle mixing mechanism that influences of the change of minimum void ratio with respect to GSD.

Along this line of reasoning, we exam the correlation between the critical state void ratio e_{cs} and the minimum void ratio e_{min}. Fig. 8.2a shows a strong correlation between e_{cs} and e_{min} for quartz silty-sand at three different stress levels $p' = 33{\sim}45, 185{\sim}250, 1380{\sim}1700\ kPa$. Fig. 8.2b shows a strong correlation between e_{cs} and e_{min} for glass beads at three different stress levels $p' = 120{\sim}145, 250{\sim}275, 498{\sim}578\ kPa$. The strong correlation between minimum void ratio and the critical state void ratio for granular material is also supported by the work in Chang and Meidani (2013), and Torres-Cruz et al. (2017). Thus, we hypothesize that the change of critical state void ratio with respect to GSD is caused by the same particle mix mechanism that influences of the change of minimum void ratio with respect to GSD.

In this chapter, based on this hypothesis, we aim to extend the particle packing model for minimum void ratios (Chang et al., 2017) to a new model for the prediction of critical state void ratios.

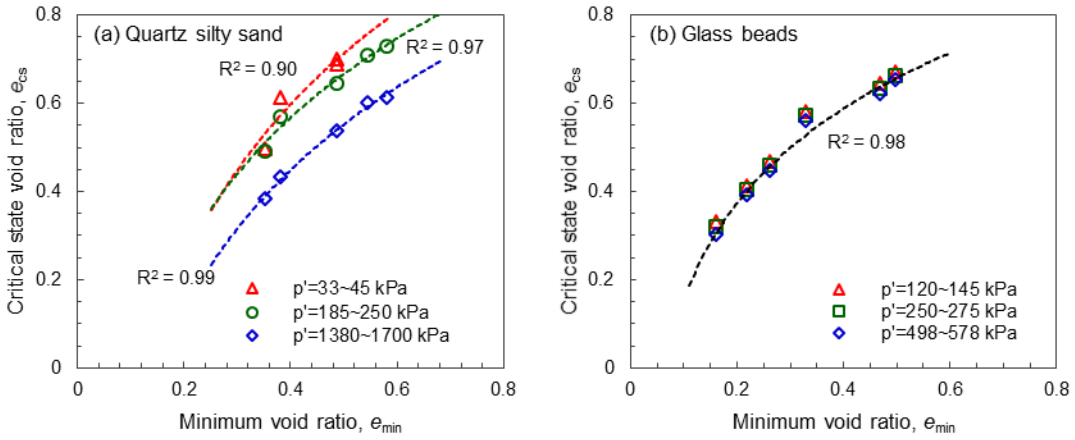

Figure 8.2 The correlation between minimum void ratio and critical state void ratio: (a) quartz silty sand (data from Papadopoulou & Tika (2008)) and (b) glass beads (data from Li (2013))

8.3 Development of a Model for e_{cs}

8.3.1 A Simplified Particle Packing Model for e_{min}

A simplified version of the particle packing model for predicting minimum void ratio considering the effect of GSD (Chang et al., 2017) is briefly summarized in Appendix A and Appendix B. The simplified model can be represented by a function:

$$e_{min} = F(\bar{e}_{min}, \Psi, s, t) \tag{8.1}$$

On the right-hand side of Eq. (8.1), $\bar{e}_{min}$ is the minimum void ratio for a mono-sized packing, which is assumed to be a constant, independent of particle size; parameters s and t are material properties of the granular soil, independent of the GSD. On the left-hand side of Eq. (8.1), e_{min} is the minimum void ratio of a packing of granular soil with any GSD (denoted as Ψ), which can be obtained from the following input variables: $\bar{e}_{min}$, the parameters s and t, and the GSD (Ψ) of a granular soil. The value of $\bar{e}_{min}$ can be directly obtained from the measured e_{min} data on uniformly graded samples. The model parameters, s and t, can be experimentally calibrated from the data for e_{min} of two samples with two

different GSDs. The procedure of determining these two parameters is illustrated in Chang et al. (2017).

Experimental tests on quartz silty sand (Papadopoulou & Tika, 2008) and glass beads (Li, 2013; Li et al., 2015) were used to validate the simplified model for e_{min}. Their grain size distributions are shown by gradation curves in Figs. 8.3a and 8.3b. The mono-sized packing $\bar{e}_{min}$ and the calibrated two parameters *s* and *t* for glass beads and quartz silty sand are listed in Table 8.1.

The predictions using the model are given in Fig. 8.4. Comparison of the predicted and measured results shows good agreement.

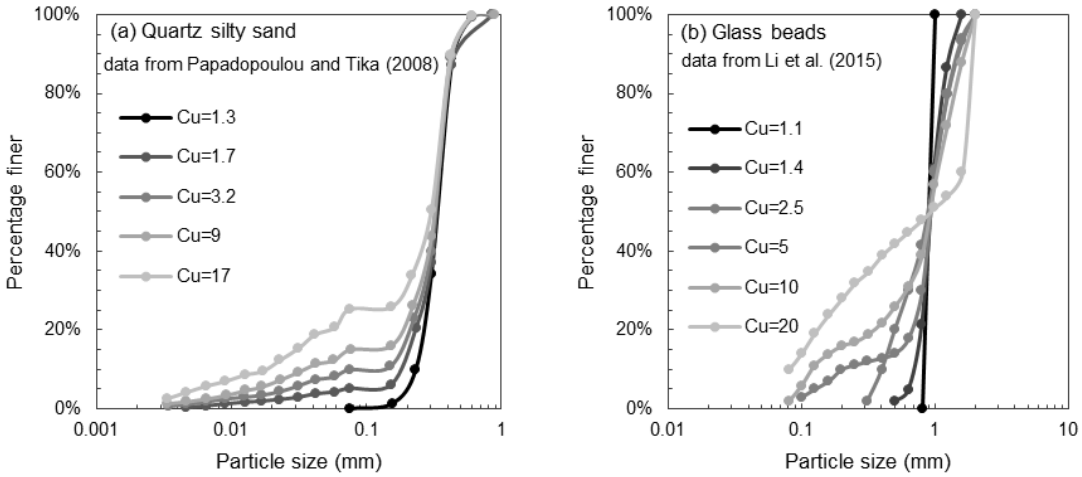

Figure 8.3 The gradation of (a) quartz silty sand, and (b) glass beads

Table 8.1 Input parameters for glass beads and quartz silty sand

Soil type	Ref.	$\bar{e}_{min}$	*s*	*t*
Glass beads	Li (2013)	0.445	2.3	2.2
Quartz silty sand	Papadopoulou and Tika (2008)	0.585	5.0	4.0

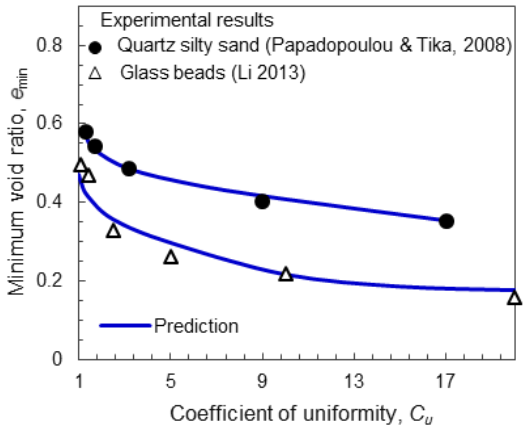

Figure 8.4 The comparison between predicted and measured minimum void ratios for quartz silty sand and glass beads

8.3.2 Extension of the Particle Packing Model to e_{cs}

The particle packing model for minimum void ratio in the previous section can be extended to critical state void ratio by replacing minimum void ratio e_{min} with critical state void ratio $e_{cs}(p')$ under a specified mean effective stress p'. Thus, the function of Eq. (8.1) can be written as,

$$e_{cs}(p') = F(\bar{e}_{cs}(p'), \Psi(p'), s, t) \tag{8.2}$$

On the right-hand side of Eq. (8.2), $\Psi(p')$ is the GSD of the granular soil at critical state under the mean effective stress p', $\bar{e}_{cs}(p')$ is the critical state void ratio of a mono-sized particle packing under the mean effective stress p'. We used the same assumption in the model described in last section that $\bar{e}_{cs}(p')$ is independent of particle size. Parameters *s* and *t* are material properties of the granular soil, independent of the GSD.

It is noted that $e_{cs}(p')$ and $\bar{e}_{cs}(p')$ represent the CSL of a multi-sized particle packing and a mono-sized particle packing respectively. Thus, Eq. (8.2) shows that the

CSL of a multi-sized granular material can be predicted from the CSL of a mono-sized packing. Regarding the variable $\Psi(p')$, two cases are considered in this study:

(1) Case I: no particle breakage occurs at critical states in the range of p'. Thus, the GSDs of the material at critical state under various p' maintain same and are independent of p' (i.e. $\Psi(p') = \Psi$). In this case, Eq. (8.2) can be reduced to the following equation.

$$e_{cs}(p') = F(\bar{e}_{cs}(p'), \Psi, s, t) \tag{8.3}$$

(2) Case II: particle breakage occurs at critical states in the range of p'. In this case, GSD is function of p' (i.e. $\Psi(p')$).

In the following two sections, the proposed model for predicting CSL will be verified for these two cases.

8.4 Model Application to CSL with Constant GSD (No Breakage)

In this section, four sets of experimental results obtained from the literature were used to validate the proposed model. These four sets of triaxial test results were reported by: Papadopoulou and Tika (2008) on quartz silty sand, Nguyen et al. (2017) on Camargue silty sand, and Li et al. (2015) on glass beads and on DEM simulation.

These four sets of experimental results satisfy the condition of Case I (constant GSD). For quartz silty sand and glass beads, Papadopoulou and Tika (2008) and Li et al. (2015) indicated that no particle breakage occurred in their triaxial tests and stated that the same GSD are maintained before and after tests. For DEM simulation, particle breakage was not considered (Li et al., 2015). For Camargue silty sand, although Nguyen et al. (2017) did not specifically mention about particle breakage, we assume that particle breakage is negligible because the maximum p' in the tests was 700 kPa, while particle breakage does

not occur for quartz uniform sand until p' is greater than 1 MPa, according to the study by Been et al. (1991).

8.4.1 Measured CSL for Four Materials without Effect of Particle Breakage

The gradation curves of specimens are presented in Fig. 8.3 for quartz silty sand and glass beads, and in Fig. 8.5 for DEM simulation and Camargue silty sand. Experimental data on CSL are presented in Fig. 8.6a for quartz silty sand, in Fig. 8.6b for Camargue silty sand, in Fig. 6c for glass beads and in Fig. 8.6d for DEM simulation. Each CSL corresponds to a gradation curve shown in Fig. 8.3 or Fig. 8.5. The measured e_{cs} on quartz silty sand and Camargue silty sand were obtained under both undrained and drained conditions under a range of confining pressure. The measured e_{cs} on glass beads and DEM simulation were obtained under the drained condition under several different confining pressures. Thus, there are many stress-level points in Fig. 8.6a and Fig. 8.6b while there are only a few stress-level points in Fig. 8.6c and Fig. 8.6d.

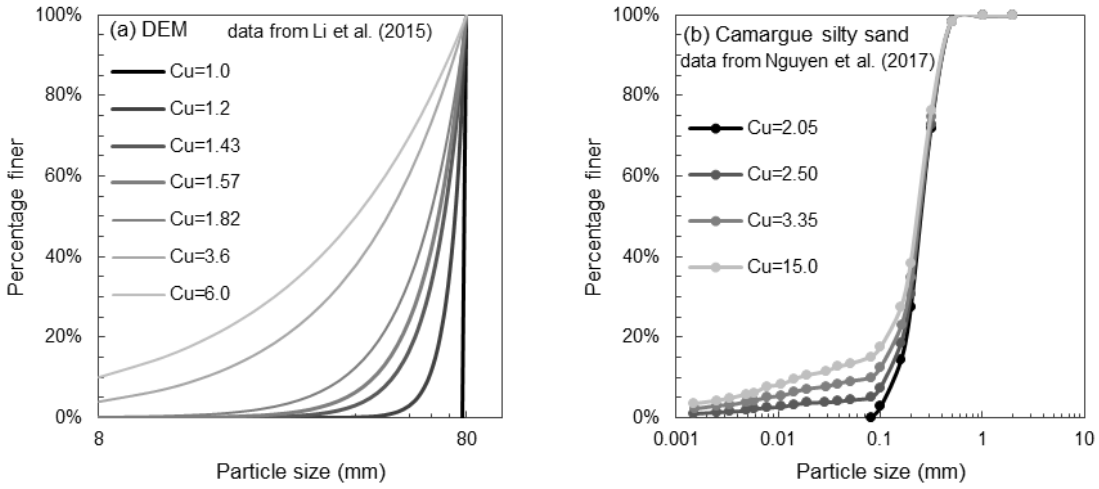

Figure 8.5 The gradation of (a) DEM simulation, and (b) Camargue silty sand

8.4.2 Model Prediction of CSL

The model (Eq. (8.3)) requires three types of input data, i.e., the mono-sized CSL ($\bar{e}_{cs}(p')$), parameters *s* and *t*, and GSD (Ψ).

(1) Grain size distribution

GSD is usually expressed in terms of gradation curve. The gradation curves for these four materials (in Fig. 8.3 and Fig. 8.5) can be converted to GSD in the way illustrated in Appendix B.

(2) Determination of $\bar{e}_{cs}(p')$, *s* and *t*

The function $\bar{e}_{cs}(p')$ is the CSL for a mono-sized packing, which can be obtained from triaxial tests on uniformly graded granular material. An empirical expression for CSL proposed by Li and Wang (1998) was used to fit the mono-sized CSL:

$$\bar{e}_{cs}(p') = \bar{e}_{ref} - \bar{\lambda}\left(\frac{p'}{p_{atm}}\right)^{\bar{\xi}} \tag{8.4}$$

where $\bar{e}_{ref}$ is the intercept of CSL on *e*-axis corresponding to a mean effective stress $p' = 0$; $\bar{\lambda}$ and $\bar{\xi}$ are two parameters controls the curve shape of CSL in the $e - \log p'$ plane; $p_{atm} = 101.3\ kPa$. To differentiate mono-sized packing from multi-sized packing, the overbar "$-$" is used for the parameters associated to mono-sized packing.

It is noted that two other types of formulas can also be used for the expression of mono-sized CSL (see Appendix A (Eq. 8.17 and Eq. 8.19). Herein, Eq. (8.4) is used.

For each material, the critical state parameters ($\bar{e}_{ref}, \bar{\lambda}, \bar{\xi}$) for mono-sized CSL were obtained by fitting Eq. (8.4) to the experimental CSL data from four uniformly graded

granular material in Fig. 8.3 and Fig. 8.5 (i.e., coefficient of uniformity C_u = 1.3, 2.05, 1.1 and 1.0 were used for quartz silty sand, Camargue silty sand, glass beads and DEM simulation, respectively). These fitted mono-sized critical state parameters for each material are listed in Table 8.2.

The two model parameters *s* and *t* were then calibrated from the data for critical state void ratios of samples with two different GSDs using the same procedure described by Chang et al. (2017). The two model parameters *s* and *t* for these four materials are listed in Table 8.2.

Table 8.2 Input parameters for four granular materials

Material type	Ref.	$\bar{e}_{min}$	Eq. (8.4)			*s*	*t*
			$\bar{e}_{ref}$	$\bar{\lambda}$	$\bar{\xi}$		
Glass beads	Li (2013), Li et al. (2015)	0.445	0.695	0.01	0.9	2.3	2.2
DEM	Li et al. (2015)	-	0.778	0.0012	0.9	1.8	1.8
Quartz silty sand	Papadopoulou and Tika (2008)	0.585	0.79	0.024	0.7	5.0	4.0
Camargue silty sand	Nguyen et al. (2017)	-	0.99	0.04	0.7	7.0	3.5

Note that the values of parameters *s*, *t* obtained from test data of critical state void ratios for glass beads and quartz silty-sand listed in Table 8.2 are identical to the values of parameters *s* and *t* obtained from test data of minimum void ratio listed in Table 8.1.

(3) Predicted CSL for various GSD

For each material, using the parameters listed in Table 8.2, the CSL for each GSD can be predicted by using Eq. (8.3). The predicted CSL in the $e_{cs} - \log p'$ plane for each GSD is presented in Fig. 8.6a for quartz silty sand, in Fig. 8.6b for Camargue silty sand, in Fig. 8.6c for glass beads, and in Fig. 8.6d for DEM simulation. The CSL moves downward

with increasing coefficient of uniformity (C_u). The comparison between the predicted and measured results on these four materials shows a good agreement.

Fig. 8.7 shows the critical state void ratios at three stress levels for various C_u. The data points were interpreted from experimental results in Fig. 8.6a for quartz silty sand and in Fig.8. 6c for glass beads. The minimum void ratios are also plotted in Fig. 8.7a for quartz silty sand and Fig. 8.7b for glass beads to show the influence of C_u on the minimum void ratio and the critical state void ratio. The predicted results are in a good agreement with the test results from experiments. The comparison also demonstrates the validity of the proposed model.

Observed from Fig. 8.7, the influence of C_u on the critical void ratio is in the same manner as that on the minimum void ratio. Note that the critical state void ratios were predicted using the same values of parameters s and t for minimum void ratio. This indicates that critical state void ratio is influenced by GSD with the same mechanisms that influence minimum void ratios.

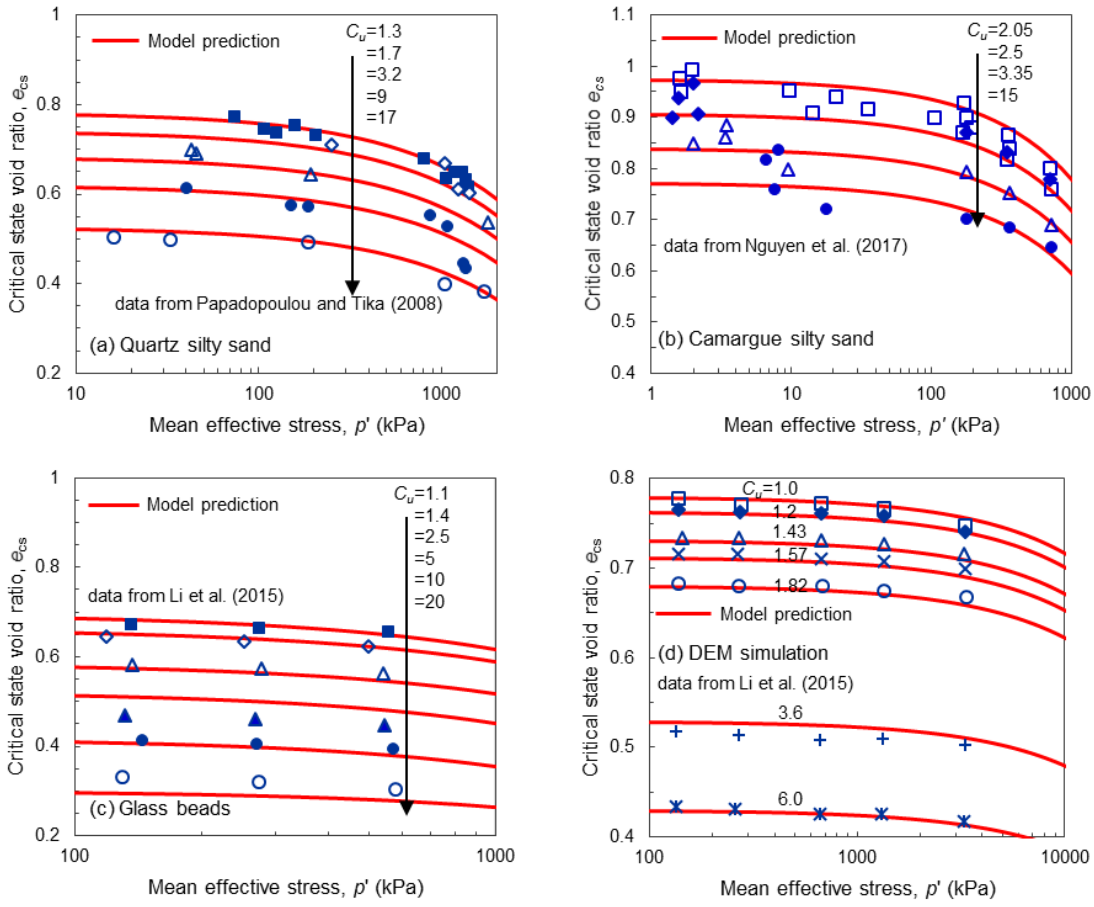

Figure 8.6 Comparison between predicted and measured CSLs: (a) quartz silty sand, and (b) glass beads

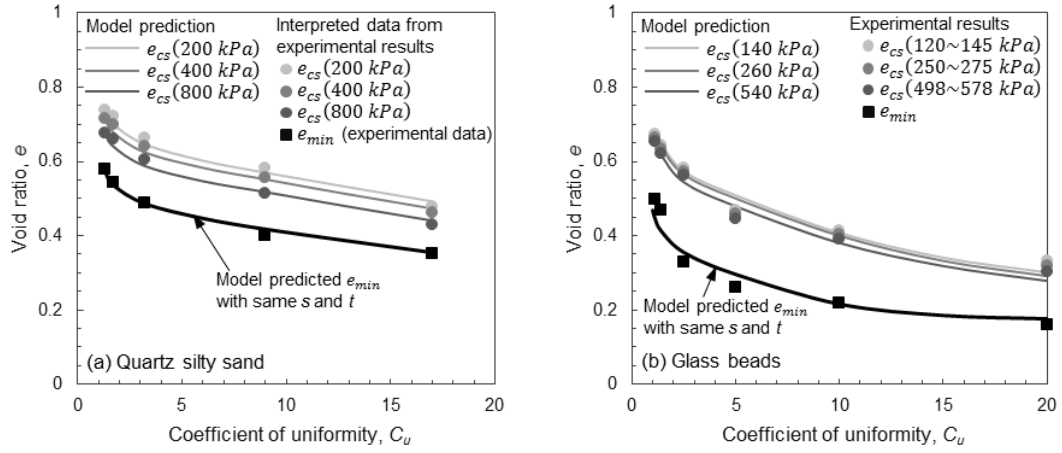

Figure 8.7 The predicted results and interpreted data points from experimental results for both critical state void ratio and minimum void ratio with respect to coefficient of uniformity C_u: (a) quartz silty sand, and (b) glass beads

8.4.3 Discussion

It is noted that the form of Eq. (8.4), with critical state parameters, e_{ref}, λ *and* ξ, is also used for multi-sized packing. According to the derivation in Appendix A, the value of λ is dependent on GSD, thus is not same for all CSLs obtained from a type of soils with different gradation. Therefore, theoretically, the CSLs are not parallel, which opposes the commonly used assumptions (e.g. Konrad, 1998; Verdugo and Ishihara, 1996). We plot the predicted λ versus C_u in Fig. 8.8a and e_{ref} versus C_u in Fig. 8.8b. These two figures show that both e_{ref} and λ decrease with an increase of C_u. The same trend were found by Bandini and Coop (2011), Li et al. (2015), and Xiao et al. (2015).

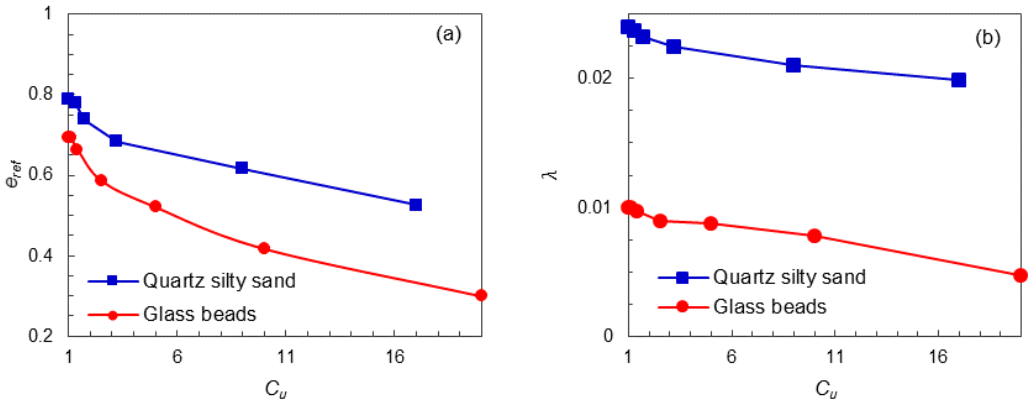

Figure 8.8 Relationships between (a) e_{ref} and C_u, and (b) λ and C_u

Here, we intend to show that the proposed model is capable to predict CSLs based on the GSD, independent of the expressions used for the CSL of a mono-sized particle packing. The predictions of CSL for these four sets of experimental tests were repeated in Appendix C, using the logarithmic formula in Eq. (8.17) and the sigmoid formula in Eq. (8.19) respectively. The comparison between the predicted results and the test results from experiments shows good agreement.

8.5 Model Application to CSL with GSD Changing Due to Particle Breakage

In this section, the applicability of this proposed model under the condition of Case II in section 8.3.2 is to be validated. Thus, it is required to use a set of experimental results of CSL with particle breakage, and with measured evolution of GSD with respect to p'. For this purpose, the set of experimental results reported on Tacheng rockfill material by Xiao et al. (2016b) was selected to verify the model on the condition of Case II.

8.5.1 Measured CSL for the Rockfill Material with Effect of Particle Breakage

The rockfill material is classified as well-graded gravel according to ASTM and its initial gradation is shown in Fig. 8.9a. The specimens were prepared by compacting into four different initial void ratios ($e_0 = 0.189, 0.244, 0.285, 0.317$). The specimens were then sheared to critical state under drained triaxial conditions at four different confining stresses (p_0= 0.2, 0.4, 0.8, 1.6 MPa). The measured CSLs of the rockfill material for the four different initial void ratios are plotted in the $e - \log p'$ plane as shown in Fig. 8.9b. Corresponding to each data point in Fig. 8.9b, the gradation curves were measured.

Xiao et al. (2016b) used Talbot equation to express the gradation of a specimen for the rockfill material as follows:

$$F(d) = \left(\frac{d}{d_M}\right)^{3-\alpha} \tag{8.5}$$

where d_M is the maximum particle diameter and α is a fractal dimension. For this rockfill material, d_M is 60 mm. The fractal dimension is denoted as α_0 for the initial gradation, α_c for the gradation at critical state and α_u for the ultimate gradation. The initial gradations for all specimens were same as shown in Fig. 8.9a ($\alpha_0 = 0.21$). The ultimate fractal dimension $\alpha_u = 2.69$ for the rockfill material (Yang Xiao, Liu, Ding, et al., 2016). The

gradation at critical state (at end of shearing) α_c for various tests are listed in Table 8.3. For a given initial void ratio (e.g., e_0= 0.244), the critical state fractal dimension α_c increases with the increasing of confining pressure as shown in Fig. 8.9a.

It is noted that the gradations of samples are different for the four initial void ratios due to particle breakage resulting from compaction during the sample preparation. Thus, the CSLs are different for each initial void ratio.

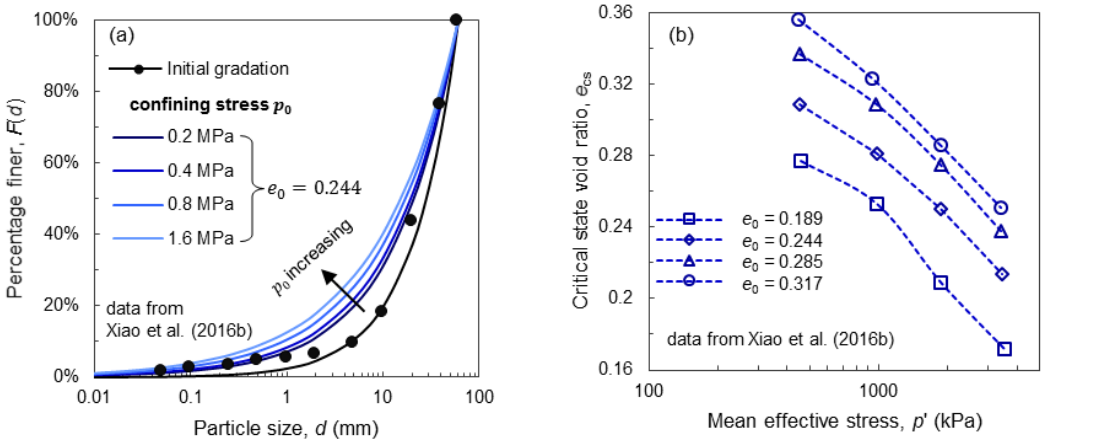

Figure 8.9 (a) Gradation curves and (b) the measured CSLs of the rockfill material at various initial void ratios and confining stresses

Table 8.3 lists the test results of gradations at critical state for all specimens. The experimental results in Table 8.3 show that, under the same p_0, smaller e_0 has more breakage (i.e. larger α_c).

Xiao et al. (2016b) interpreted five CSLs with five constant GSDs from their systematic experimental results on Tacheng rockfill material. The interpreted five CSLs were obtained by connecting the critical state points with same GSD (i.e. with same α_c). These five CSLs (with same α_c) are plotted in solid line as shown in Fig. 8.10a. The five GSDs corresponding to these five CSLs are shown in Fig. 8.10b in terms of gradation curve.

Table 8.3 Test results of large-Scale triaxial compression on the rockfill material (data obtained from Xiao *et al*. (2016b))

e_0	p_0 (MPa)	p' (MPa)	e_{cs}	α_c
0.189	0.2	0.46	0.277	2.41
	0.4	0.983	0.253	2.453
	0.8	1.863	0.209	2.514
	1.6	3.503	0.172	2.557
0.244	0.2	0.453	0.309	2.35
	0.4	0.98	0.281	2.39
	0.8	1.86	0.25	2.45
	1.6	3.453	0.214	2.496
0.285	0.2	0.45	0.337	2.29
	0.4	0.973	0.309	2.35
	0.8	1.857	0.275	2.4
	1.6	3.41	0.238	2.452
0.317	0.2	0.447	0.356	2.245
	0.4	0.94	0.323	2.33
	0.8	1.853	0.286	2.35
	1.6	3.407	0.251	2.403

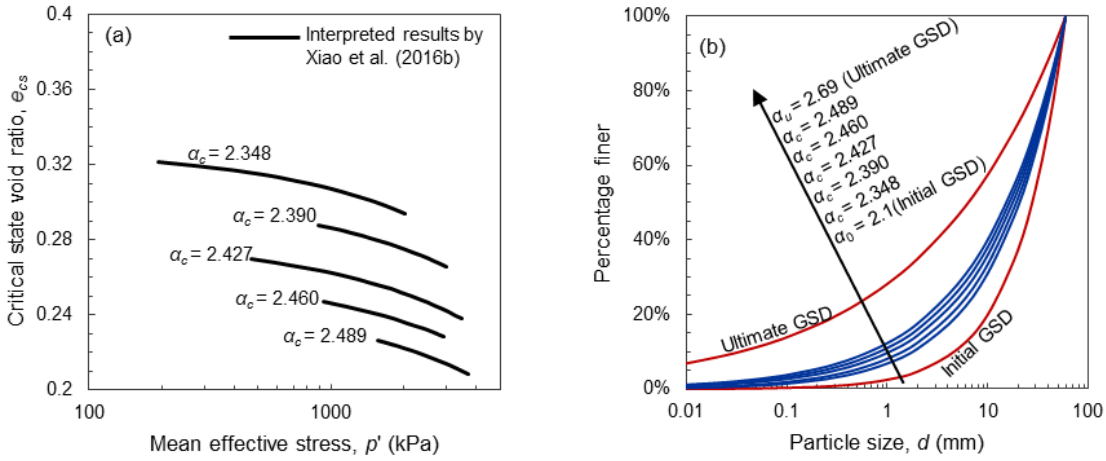

Figure 8.10 (a) Five CSLs for constant GSD and (b) the corresponding five gradation curves

8.5.2 Model Parameters and GSD Evolution

(1) Determination of $\bar{e}_{ref}, \bar{\lambda}, \bar{\xi}$, s and t

The model requires the following parameters: the mono-sized critical state parameters ($\bar{e}_{ref}, \bar{\lambda}, \bar{\xi}$) and the two model parameters (s and t). The mono-sized critical state parameters ($\bar{e}_{ref}, \bar{\lambda}, \bar{\xi}$) are usually obtained directly from the experimental results on CSL of uniformly graded sample without particle breakage. However, for Tacheng rockfill material, this type of experimental data is not available. Therefore, using Eq. (8.3), the mono-sized critical state parameters ($\bar{e}_{ref}, \bar{\lambda}, \bar{\xi}$) and the two model parameters (s and t) are obtained by back-fitting the five CSLs for constant GSDs available for Tacheng rockfill material as shown in Fig. 8.10a. (The back-fitting process required at least 2 CSLs for constant GSDs). The back fitted mono-sized critical state parameters and two model parameters (s and t) are listed in Table 8.4. The back fitted mono-sized CSL of Tacheng rockfill material is plotted in Fig. 8.11.

Using the input parameters in Table 8.4, the predictions for the five CSLs are shown in Fig. 8.11 in blue dashed lines. The predicted results are in good agreement with the interpreted results from experimental data.

(2) The change GSD – p'at critical state $\Psi(p')$

In order to predict the CSL using Eq. (8.2) considering the change of GSD due to particle breakage, the model requires the function $\Psi(p')$, i.e., the change of GSD with respect to p' at critical state. The function $\Psi(p')$ measured from experiments is used as an input in the following analysis.

Table 8.4 Input parameters for Tacheng rockfill material

$\bar{e}_{ref}$	$\bar{\lambda}$	$\bar{\xi}$	s	t	M
0.549	0.0048	0.7	7	2.5	1.64

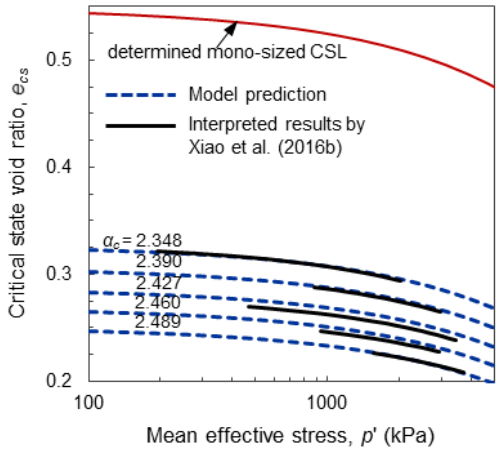

Figure 8.11 The determined mono-sized CSL of Tacheng rockfill material and predicted CSLs for constant GSD

Since the GSD for the rockfill material is represented by Talbot equation (Eq. (8.5)), $\Psi(p')$ can be obtained by $\alpha_c(p')$. Xiao et al. (2016b) suggested a form of the fractal dimension α_c of gradation at critical state as a function of initial void ratio e_0 and confining stress p_0, i.e. $\alpha_c(p_0, e_0)$, given by:

$$\alpha_c = \alpha_{eo} - \chi_a e_0 + \kappa_a log \frac{p_0}{p_{atm}} \tag{8.6}$$

where, α_{eo}, χ_a and κ_a are parameters. Xiao et al. (2016b) determined these parameters by fitting the experimental data: α_{eo} = 2.57, χ_a = 1.16, κ_a = 0.173.

Since the tests performed by Xiao et al. (2016b) were drained triaxial tests. Thus, the mean effective stress p' can be determined by the confining stress p_0 as following:

$$p' = \left[\left(\frac{3+2M}{3-M}\right) + 2\right] \cdot \frac{p_0}{3} \tag{8.7}$$

where M is the stress ratio at critical state. Xiao et al. (2016b) found that M = 1.64 for Tacheng rockfill material under all test conditions.

By substituting Eq. (8.7) into Eq. (8.6), the function $\alpha_c(p')$ for Tacheng rockfill material can be obtained, given by

$$\alpha_c = 2.57 - 1.16e_{0+}0.173log\frac{p'}{2.206p_{atm}} \tag{8.8}$$

Eq. (8.8) is plotted in Fig. 8.12. Fig. 8.12 shows that Eq. (8.8) is in good agreement with the measured results from Xiao et al. (2016b). With Eq. (8.8), $\Psi(p')$ can be obtained by substituting α_c into Eq. (8.5).

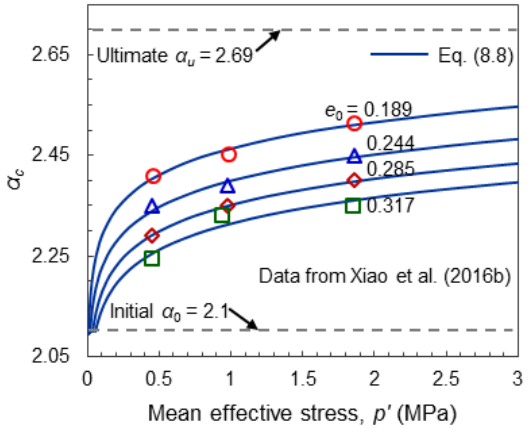

Figure 8.12 The fractal dimension αc of gradation at critical state for Tacheng rockfill material under various mean effective stresses

It is noted that for loading conditions different from the conventional triaxial condition, Ψ may not be only a function of mean stress p'. For example, Ψ may be dependent on factors of repeated loading conditions or intermediate principle stress ratio (Yang Xiao, Liu, Desai, Sun, & Liu, 2016). In order to model the CSL due to particle breakage, the GSDs at critical state under the specific types of loading conditions, such as repeated loading, need to be measured, which will be the required input into the model. In

this paper, only conventional triaxial conditions are considered, thus Ψ is considered to be only a function of mean stress p'.

8.5.3 Model Prediction of CSL for the Rockfill Material with Effect of Particle Breakage

Inputting the parameters in Table 8.4 and $\Psi(p')$ into the model (Eq. (8.2)), the CSL for Tacheng rockfill material with effect of particle breakage was predicted and plotted in Fig. 8.13. It is noted that $\Psi(p')$ are different for the specimens with different initial void ratios, the CSL is different for each initial void ratio. It is also noted that the predicted CSLs in Fig. 8.13 represent only the second segment of the CSL in Fig. 8.1. The model predicted results are in good agreement with the experimental results.

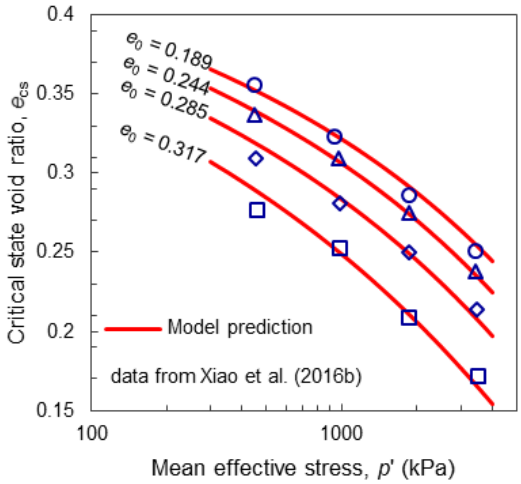

Figure 8.13 The CSL as GSD evolution due to particle breakage

8.6 Conclusions

Experimental results show that grain size distribution (GSD) has a significant influence on CSL. However, there are no analytical models available for determining CSL by directly considering GSD. This paper presents an analytical model for determining the

CSL of granular materials with influence of GSD based on the particle packing model. The following conclusions can be drawn from this study.

(1) The particle packing model for minimum void ratio proposed by Chang et al. (2017) was extended to predict critical state void ratio directly from GSD based on the hypothesis that the variation of critical state void ratio with respect to GSD is caused by the same particle mixing mechanism that influences of the variation of minimum void ratio. The experimental and predicted results indicated that this hypothesis is plausible.

(2) The proposed model can predict the CSL of a multi-sized particle packing based on the CSL of a mono-sized packing. The CSL of a mono-sized packing can be characterized by 2 or 3 critical state parameters shown in Eq. (8.4). The mono-sized critical state parameters can be obtained by fitting the critical state data on a uniformly graded granular material using Eq. (8.4).

(3) The proposed model requires two material parameters (s and t) and mono-sized critical state parameters. It was found that the same material parameters (s and t) can be used for predicting both minimum and critical state void ratios of granular materials with various gradations. Thus, these two material parameters (s and t) can be calibrated from the data for minimum or critical state void ratios of samples.

(4) The model was evaluated by experimental data on 4 types of granular materials. The comparisons between predicted and measured results have demonstrated that the proposed model is capable of predicting the CSL of a multi-sized packing from the CSL of a mono-sized packing.

(5) In this study, it is derived in Appendix A that both e_{ref} and λ in Eq. (8.16) or Eq. (8.17) depend on GSD of material. The model mathematically shows that both e_{ref} and λ decrease with an increase of C_u, which agrees with experimental observations (Bandini & Coop, 2011; Gang Li et al., 2015; Yang Xiao, Liu, Ding, et al., 2016).

(6) The particle breakage influence on CSL is caused mainly by the change of GSD. In this study, the relation the changed of GSD in relation to p'at critical state is known in advance. By incorporating the known relation $\Psi(p')$, CSL was predicted with influence of particle breakage. The proposed model is evaluated by the experimental results on Tacheng rockfill material to illustrate the applicability of the model in determining CSL for granular material with particle breakage. The predicted CSLs show a good agreement with the experimental results. Note that the function $\Psi(p')$ used in the prediction is exclusive for Tacheng rockfill material. For other granular material, this relation needs to be studied.

This proposed model has potential applicability in the analysis of liquefaction for silty sand. The model is also useful in the study for the degradation of strength and settlement for granular materials due to particle breakage in a high earth dam.

Appendix A: A Simple Particle Packing Model

Grain size distribution (GSD) of soil is usually represented by a gradation curve. A continuous gradation curve can be discretized into *n* size-classes of particles (shown in Appendix B), and the GSD of a multi-sized packing can be characterized by: solid fraction y_i for each size-class of particles with particle size d_i, i.e. $\{d_i, y_i, i = 1, n\}$. Note that the

particle size is sorted by $d_1 > d_2 > \cdots > d_n$. The detailed process of discretization is given in Appendix B.

In the particle packing model proposed by Chang et al. (2017), the minimum void ratio of a multi-sized packing can be expressed as:

$$e_i^M = \sum_{j=1}^{n} \left(e_j - a_{ij} \left(1 + e_j \right) - b_{ij} e_j \right) y_j \tag{8.9}$$

where e_i^M is the minimum void ratio of the multi-sized packing assuming the *i*-th size-class of particles is dominant; the subscript i is the dominant size-class of particles for the mixture; e_j is the minimum void ratio of a packing that contains only the *j*-th size-class of particles d_j; y_j is the solid volume fraction of the *j*-th size-class of particles; the filling-mechanism coefficient a_{ij} and the embedment-mechanism coefficient b_{ij} are determined by the following function:

$$a_{ij} = \begin{cases} \left(1 - \dfrac{d_j}{d_i} \right)^s & for\ d_i > d_j \\ 0 & for\ d_i \le d_j \end{cases} \tag{8.10}$$

$$b_{ij} = \begin{cases} \left(1 - \dfrac{d_i}{d_j} \right)^t & for\ d_i < d_j \\ 0 & for\ d_i \ge d_j \end{cases} \tag{8.11}$$

where, parameters s and t are material properties of the granular soil, independent of the GSD.

This model was developed based on the mix mechanism. In consideration of the mix mechanism, a dominant particle size d_i is selected. The packing containing particles of single size d_i is regarded as the base packing, which is used for building up the multi-sized

particle packing. The particles with sizes smaller than the dominant particle size (i.e., d_i) are regarded as fillers into the voids of the base packing, whereas the particles with sizes greater than the dominant particle size are regarded as inclusions embedded in the base packing.

Observed from the study of geological fault gouges, Sammis et al. (1987) found that the shapes of fractured smaller particles are similar in a fractal manner to the shapes of unfractured large particles. This conclusion is supported by the experiments on crushed Basalt by Youd (1973) and by the experiments on Huston sand by Li et al. (2015). Thus, for breakage material, the particle shape is independent of particle size. Consequently, we may assume that the minimum void ratio for a mono-sized packing (i.e. the coefficient of uniformity $C_u = 1$) is a constant for any particle size i.e. $e_j = \bar{e}$ ($j = 1, n$).

Based on this assumption, a simplified particle packing model is derived for breakage material. Eq. (8.9) becomes:

$$e_i^M = \alpha_i \bar{e} - \beta_i \tag{8.12}$$

where

$$\alpha_i = 1 - \sum_{j=1}^{n} \left(b_{ij} + a_{ij} \right) y_j; \quad \beta_i = \sum_{j=1}^{n} a_{ij} y_j \tag{8.13}$$

The dominant class of particles is not known in priori. Since the dominant class of particles is one of the size-classes of particles, there are n possible trial values for the dominant size, and n trial values of e_i^M can be computed by Eqs. (8.12 and 8.13). The true minimum void ratio of the multi-sized packing can be determined by the following equation:

$$e^M = \max\{e_i^M, i = 1, \ldots . n\} \tag{8.14}$$

The particle packing model described above is for the prediction of minimum void ratio. However, it can be extended for the prediction of critical state void ratio by treating the variable *e* as critical state void ratio. Thus, e_i^M is the critical state void ratio of the multi-sized packing assuming the *i*-th size-class of particles is dominant; $\bar{e}$ is the critical state void ratio of a mono-size packing; e^M is the true critical state void ratio of the multi-sized packing. The model can be summarized by Eqs. (8.12), (8.13) and (8.14). The required input data are $\bar{e}_{cs}$, GSD, *s*, *t*. Thus, we need to know the equation of CSL of the mono-sized packing in order to determine the value of $\bar{e}_{cs}$ for a given mean effective stress.

After the equation of CSL of the mono-sized packing is known, the equation of CSL of a packing with any constant GSD can be derived from this model. Considering the expression of CSL by three different formulas:

(1) power formula proposed by Li and Wang (1998)

The equation of CSL for a mono-size packing and for a packing with any constant GSD are given below:

$$e_{cs} = e_{ref} - \lambda\left(\frac{p'}{p_{atm}}\right)^{\xi}; \quad \bar{e}_{cs} = \bar{e}_{ref} - \bar{\lambda}\left(\frac{p'}{p_{atm}}\right)^{\bar{\xi}} \tag{8.15}$$

where e_{ref} is the intercept of CSL on *e*-axis corresponding to a mean effective stress $p' = 0$; λ and ξ are two parameters controls the curve shape of CSL in the $e - \log p'$ plane; $p_{atm} = 101.3\ kPa$. $\bar{e}_{ref}, \bar{\lambda}, \bar{\xi}$ are mono-sized critical state parameters. For distinguish from multi-sized packing, the overbar "−" refers to the parameter for mono-sized packing.

Substitute Eq. (8.15) into Eq. (8.12), it leads to:

$$e_{ref} = \alpha_i \bar{e}_{ref} - \beta_i; \quad \lambda = \alpha_i \bar{\lambda}; \quad \xi = \bar{\xi} \tag{8.16}$$

(2) logarithmic formula

The equation of CSL for a mono-size packing and for a packing with any constant GSD are given below:

$$e_{cs} = e_{ref} - \lambda log\left(\frac{p'}{p_{atm}}\right); \qquad \bar{e}_{cs} = \bar{e}_{ref} - \bar{\lambda} log\left(\frac{p'}{p_{atm}}\right) \tag{8.17}$$

where e_{ref} is a reference void ratio corresponding to a mean effective stress $p' = p_{atm} = 101.3\ kPa$, λ is the slope of the CSL in the $e - \log p'$ plane.

Substitute Eq. (8.17) into Eq. (8.12), it leads to:

$$e_{ref} = \alpha_i \bar{e}_{ref} - \beta_i; \qquad \lambda = \alpha_i \bar{\lambda} \tag{8.18}$$

(3) Sigmoid formula proposed by Gudehus (1997)

The equation of CSL for a mono-size packing and for a packing with any constant GSD are given below:

$$e_{cs} = e_{cu} + (e_{cmax} - e_{cu}) exp\left[-\left(\frac{p'}{m p_{atm}}\right)^{\xi}\right]; \quad \text{and}$$

$$\bar{e}_{cs} = \bar{e}_{cu} + (\bar{e}_{cmax} - \bar{e}_{cu}) exp\left[-\left(\frac{p'}{\bar{m} p_{atm}}\right)^{\bar{\xi}}\right] \tag{8.19}$$

where e_{cu} is critical void ratio when p' = infinity; e_{cmax} is critical void ratio when $p' = 0$; m and ξ are two parameters controls the curve shape of CSL in the e - log p' plane.

Substitute Eq. (8.19) into Eq. (8.12), it leads to:

$$e_{cu} = \alpha_i \bar{e}_{cu} - \beta_i; \ e_{c\,max} = \alpha_i \bar{e}_{c\,max} - \beta_i; \ m = \bar{m}; \ \xi = \bar{\xi} \tag{8.20}$$

Appendix B: Discretization of a Continuous Gradation

In this Appendix, a discretization process is described for a continuous gradation curve. As an example, the gradation curve is shown in Fig. 8.14. The vertical axis is percent

finer and the horizontal axis is particle size. The continuous gradation curve is to be discretized into *n* size-classes of particles; particles of each class are considered to be equal size. The solid fraction y_i for each size-class of particles with particle size d_i can be determined by the following process.

Note that the particle size is sorted by $d_1 > d_2 > \cdots > d_n$ for a soil mixture. Divided the gradation curve into n divisions, there are $n+1$ ticks: $\hat{d}_1, \ldots \hat{d}_n, \hat{d}_{n+1}$ (subscript order is from large size to small size). The *i*-th division has a size range from $\hat{d}_{i+1}$ to $\hat{d}_i$. Using a geometric series for the values of the tick marks, so that for all divisions, the ratios of $\hat{d}_i / \hat{d}_{i+1}$ are constant. This ratio can be determined from the total range $\hat{d}_1, \hat{d}_{n+1}$ and the number of divisions *n*, given by

$$\frac{\hat{d}_i}{\hat{d}_{i+1}} = \left(\frac{\hat{d}_1}{\hat{d}_{n+1}} \right)^{1/n} \qquad (i = 1,2,\ldots n+1) \tag{8.21}$$

Thus, the *i*-th tick mark $\hat{d}_i$ is related to $\hat{d}_1, \hat{d}_{n+1}$ and *n* by

$$\hat{d}_i = \hat{d}_1 \left(\frac{\hat{d}_{n+1}}{\hat{d}_1} \right)^{(i-1)/n} \qquad (i = 1,2,\ldots n+1) \tag{8.22}$$

The particle size d_i for the *i*-th division is the geometric average of its particle size range.

$$d_i = \sqrt{\hat{d}_i \hat{d}_{i+1}} \tag{8.23}$$

In order to minimize the errors induced by discretization, the number of division *n* should be large enough to assure that $d_i/d_{i-1} < 1.1$ suggested by Chang et al. (2017). The soil can thus be considered as a mixture consisting of n-component particles with particle

size d_i ($i = 1, 2, \ldots, n$). Each component is represented by a division of the gradation curve. The solid volume fraction y_i for each component in the mixture can be calculated from the gradation curve as shown in Fig. 8.14:

$$y_i = F_i - F_{i+1} \tag{8.24}$$

where F_i is the value on the vertical axis of the gradation curve (in percentage) corresponding to size $\hat{d}_i$ on the horizontal axis.

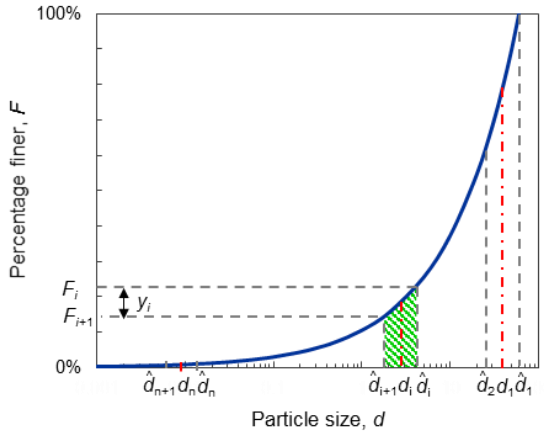

Figure 8.14 Discretization for a gradation curve

Appendix C: Other CSL Formulations

In the following, using the logarithmic formula in Eq. (8.17) and the sigmoid formula in Eq. (8.19) respectively, the CSLs for various GSDs were predicted by the proposed model for Quartz silty sand (Papadopoulou & Tika, 2008), Camargue silty sand (Nguyen et al., 2017), DEM (Gang Li et al., 2015) and glass beads (Li et al., 2015). The parameters for CSL of mono-sized packing and the parameters s and t are listed in Table 8.5. Note that the parameters s and t in the model for each material are same as the that used in Table 8.2.

Table 8.5 Input parameters for each material

Soil type	Ref.	Eq. (8.17)		Eq. (8.19)				*s*	*t*
		$\bar{e}_{ref}$	$\bar{\lambda}$	$\bar{e}_{cu}$	$\bar{e}_{cmax}$	$\bar{m}$	$\bar{\xi}$		
Glass beads	Li et al. (2015)	0.772	0.019	0.40	1.05	13	0.085	2.3	2.2
DEM	Li et al. (2015)	0.823	0.008	0.60	1.04	16	0.042	1.8	1.8
Quartz silty sand	Papadopoulou & Tika (2008)	0.981	0.047	0.45	0.85	35	0.380	5.0	4.0
Camargue silty sand	Nguyen et al. (2017)	1.025	0.025	0.48	1.00	83	0.425	7.0	3.5

The predicted CSLs for each material in the form of logarithmic formula in Eq. (8.17) are plotted in Fig. 8.15. The CSLs for each material become a series of straight lines in the $e - \log p'$ plane. Fig. 8.15 shows that there is a good agreement between predicted and experimental results.

The predicted CSLs for each material in the form of sigmoid formula in Eq. (8.19) are plotted in Fig. 8.16. The CSLs for quartz silty sand and Camargue silty sand are a series of curved lines in the $e - \log p'$ plane. Fig. 8.16 shows that there is a good agreement between predicted and experimental results. Note that, in contrast to these two silty sands, the CSLs for glass beads and DEM are flat in the $e - \log p'$ plane, which is captured by the low values of ξ for glass beads and DEM. Thus, the sigmoid formula provides a better fit for curved CSL lines.

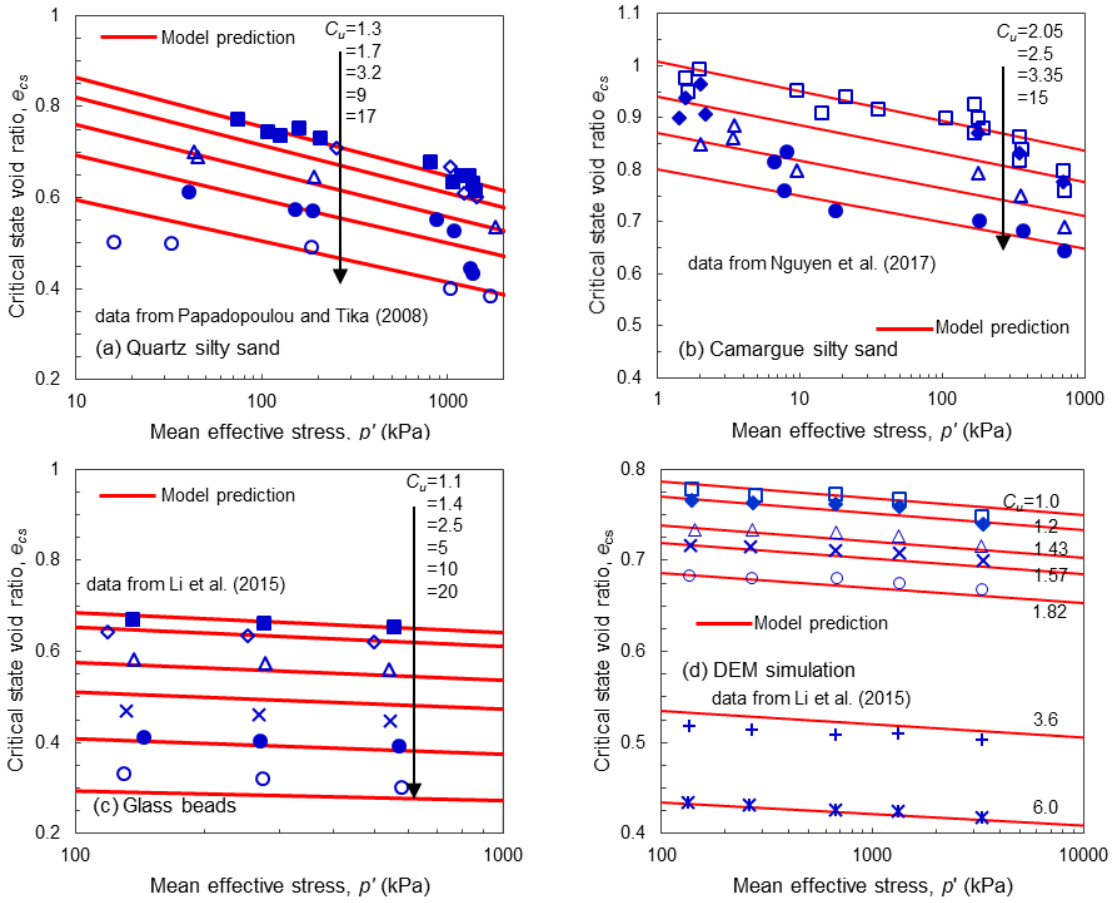

Figure 8.15 Comparison of predicted and measured CSLs using the logarithmic formula in Eq. (8.17)

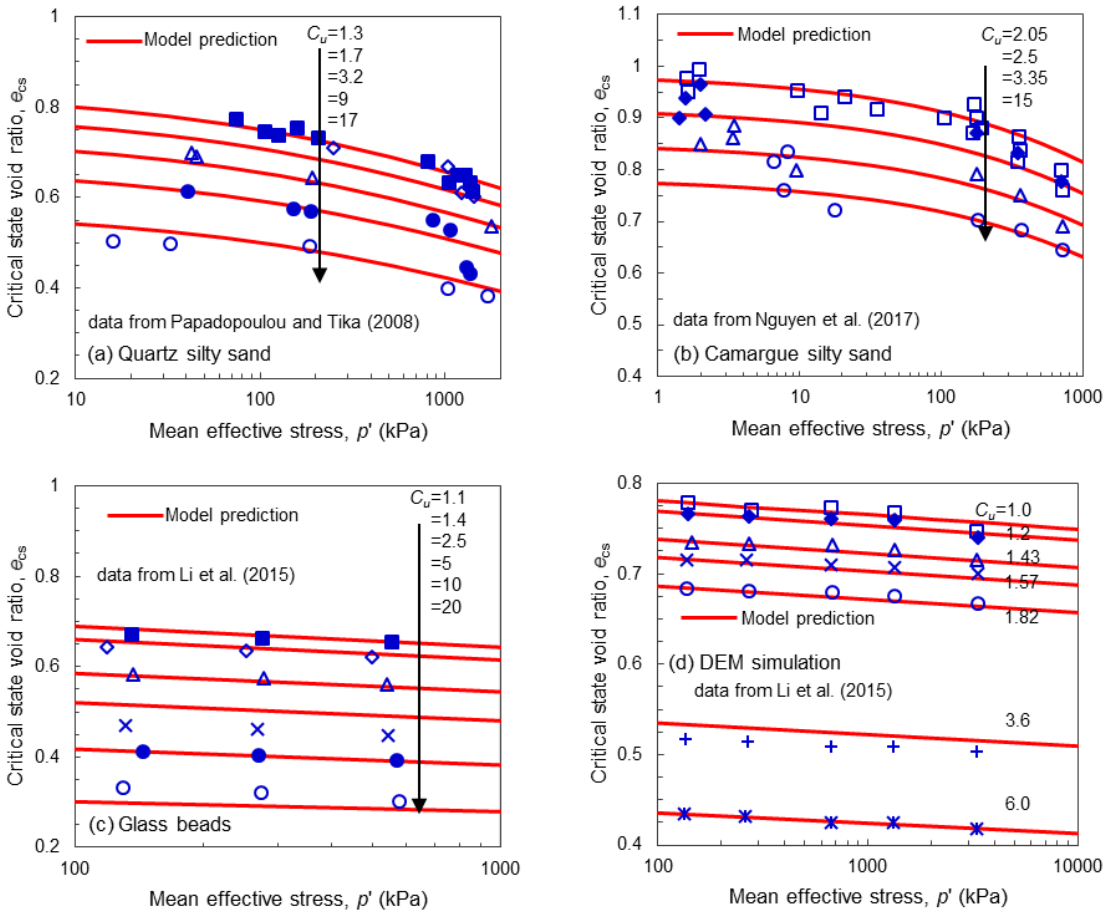

Figure 8.16 Comparison of predicted and measured CSLs using the sigmoid formula in Eq. (8.19)

CHAPTER 9

STRENGTH-DILATANCY AND CRITICAL STATE BEHAVIORS OF BINARY MIXTURES OF GRADED SANDS INFLUENCED BY PARTICLE SIZE RATIO AND FINES CONTENT[8]

Binary granular soil mixtures, as common heterogeneous soils, are ubiquitous in nature and man-made deposits. Fines content and particle size ratio are two important gradation parameters for a binary mixture, which have potential influences on mechanical behaviors. However, experimental studies on drained shear behavior considering the whole range of fines content and different particle size ratios are scarce in the literature. For this purpose, we performed a series of drained triaxial compression tests on dense binary silica sand mixtures with 4 different particle size ratios to systematically investigate the effects of fines content and particle size ratio on the drained shear behaviors. Based on these tests, the strength-dilation behavior and critical state behavior were examined. It was observed that both fines content and particle size ratio have significant influence on the stress-strain response, the critical state void ratio, the critical state friction angle, the maximum dilatancy angle, the peak friction angle, and the strength–dilatancy relation. The underlying mechanism for the effects of fines content and particle size ratio was discussed from the perspective of the kinematic movements at particle level.

[8] This chapter was submitted to Géotechnique as a standalone paper: Y. Yilmaz, Yibing Deng, Ching S. Chang, & A. Gokce (2020). Strength-dilatancy and critical state behaviors of binary mixtures of graded sands influenced by particle size ratio and fines content. *Géotechnique,* under review.

List of Notation

The following symbols are used in this chapter:

b	dilatancy parameter
CS	critical state
D	dilatancy or ratio of volumetric strain rate to deviator strain rate
$e_{\min}$, $e_{\max}$	minimum and maximum void ratios
e_0, e_{cs}	initial void ratio, critical state void ratio, void ratio at end of test
e_c, e_f, e_p, e_{end}	void ratios after consolidation, at onset of dilatancy, at peak stress, at end of test
ε_a, ε_v, ε_q	axial, volumetric, and deviator strains
$\varepsilon_q^{peak}, \varepsilon_q^{cs}$	deviator strain at peak state and critical state
ε_v^{peak}	volumetric at peak state
f_c, f_{th}	fines content, transitional fines content
M	stress ratio at critical state
N	volumetric coupling coefficient
p', p'_{cs}	mean effective stress, mean effective stress at critical state
q	deviatoric stress
Ratio	particle size ratio which is the ratio of the large particle size to the small particle size in a binary mixture
R_W	particle roundness
SS	sum of squared errors
η, η^{peak}	stress ratio, stress ratio at peak state

σ_1', σ_3' major and minor principal effective stresses

Ω packing potential index

ϕ_p, ϕ_{cv} peak and critical state friction angles

ψ_p maximum dilation angle

9.1 Introduction

Heterogeneous soils are ubiquitous in nature and man-made deposits. These soils are generally composed of a binary mixture of large particles and small particles, such as gravel-sand mixtures and sand-silt mixtures, which are commonly encountered in dams, fills, fault zones, and landslides. The mechanical behavior of binary soil mixtures have been found very different from that of uniform soil (Carraro, Prezzi, & Salgado, 2009a; Chang & Phantachang, 2016; Derkaoui, Missoum, Bendani, & Belhouari, 2016; Jehring & Bareither, 2016; Salgado, Bandini, & Karim, 2000).

Fines content and particle size ratio are two important gradation parameters for a binary mixture, which distinguished mixtures from uniform soils. Thus, it is important to understand the effects of fines content and particle size ratio on the mechanical behavior of a binary soil mixture.

Many efforts have been made to study the behavior of binary soil mixtures. The effect of fines content on critical void ratio have been studied using the experimental results by many investigators (e.g., Carrera et al., 2011; Dash & Sitharam, 2011; Kwa & Airey, 2016; Naeini & Baziar, 2004; Papadopoulou & Tika, 2008; Thevanayagam et al., 2002; Yang, 2004; Zlatović & Ishihara, 1995). All these results show important effects of fines content on critical state void ratio, which decreases as fine content increases from zero to

about 30%. Then, as the fines content continues to increase, the void ratio increases. This trend is very useful for the evaluation of engineering properties of silty sands using the critical state soil mechanics framework.

The effect of fines content on dilatancy for silty sands is usually studied by drained triaxial tests. However, there were limited studies in this area (Carraro et al., 2009; Salgado et al., 2000; Xiao et al., 2017; Patil et al., 2018). Also, in these studies, the fines contents were less than 30%. Among these studies some investigators stated that the Bolton's dilatancy equation proposed for clean sand could still be used for silty sands (Xiao et al., 2017) with the same parameter b: $b = (\phi_p - \phi_{cv})/\psi_p$, where ϕ_p, ϕ_{cv}, and ψ_p are the peak friction angle, critical state friction angle and maximum dilation angle, respectively. b is a dilatancy parameter of 0.436 for Fujian sand with non-plastic fines. This statement needs to be verified for the case of higher fines content (i.e., greater than 30%).

The effect of fines content on the critical state friction angle have been studied by both drained and undrained triaxial tests. Some investigator found that the critical state friction angle varies with fines content (Murthy et al., 2007; Salgado et al., 2000; Xiao et al., 2017), while others found the critical state friction angle is independent of fines content (Bouckovalas, Andrianopoulos, & Papadimitriou, 2003; Ni et al., 2004; Rahman, Lo, & Dafalias, 2014).

Besides fines content, the particle size ratio is also an important factor for a binary mixture. However, until now, very few studies are available in the literature addressing the effect of particle size ratio on critical state behavior and stress-dilatancy behavior. Although there are abundant drained triaxial test results on silty sands in the literature, these test results cannot be used to evaluate the effect of particle size ratio because the particle size

ratio cannot be isolated from other factors. As far as the authors are aware, there have been only a few studies on particle size ratio using discrete element simulations (Ueda et al., 2011; Zhou, Xu, Ma, Yang, & Chang, 2016; Zhu et al., 2020). But, in the literature, there is no attempts have been made in real soil mixtures or glass beads mixtures to study the effect of particle size ratio on critical state behavior and stress-dilatancy behavior.

The main objective of this work is to investigate the effects of fines content and particle size ratio on critical state behavior and shear-dilatancy behavior of binary granular soil mixtures. For this purpose, a series of drained triaxial compression tests at a constant confining stress (200 kPa) were conducted on dense binary silica sand mixtures. These binary mixtures were made up of 5 size classes of sand particles with various fines contents so that the factor of particle size ratio can be isolated. This paper is organized as follows. The testing program and test results are firstly presented. Then the test results are analyzed to observe the effects of fines content and particle size ratio on the critical state and the strength-dilatancy characteristics of the mixed graded material. The observed patterns are discussed and the underlying mechanism for the influences of fines content and particle size ratio on drained shear behavior is discussed.

9.2 Testing Program

The drained triaxial compression tests on dense binary silica sand mixtures with 4 different particle size ratios were performed by our collaborators, Dr. Yilmaz and Dr. Gokce, at Gazi University, Ankara, Turkey.

9.2.1 Testing Material

Pasabahce silica sand (herein referred to as silica sand) were selected to use in this experimental study. The silica sand is formed as a result of disintegration of magmatic metamorphic rocks being rich in quartz. The fluvial transportation brought it to actual deposit in Istanbul, Turkey. By sieving the silica sand, five graded uniform silica sands were obtained and used in this experimental study, i.e., #16-#18, #30-#50, #50-#80, #100-#120, and #120-#200, each of which is the upper sieve number and the lower sieve number. The particle size and specific gravity of the samples (obtained by ASTM D854-14) are listed in Table 9.1. A qualitative look at the shape and surface texture of the individual sand grains were determined using the method of 2-D microscopy. Fig. 9.1 shows a series of micrographs of some grains from the silica sands used in this study. The sand grains are mostly sub-angular. Based on these micrographs, Roundness (R_W) for each uniform sand was calculated using its definition proposed by Wadell (1935) and listed in Table 9.1. The minimum void ratio e_{min} (maximum index density) and the maximum void ratio e_{max} (minimum index density) of each uniform silica sand were determined according to Method 2A of ASTM D4253 (ASTM D4253-00, 2006) and Method B of ASTM D4254 (ASTM D4254-00, 2006), respectively. The minimum and the maximum void ratios of samples are tabulated in Table 9.1.

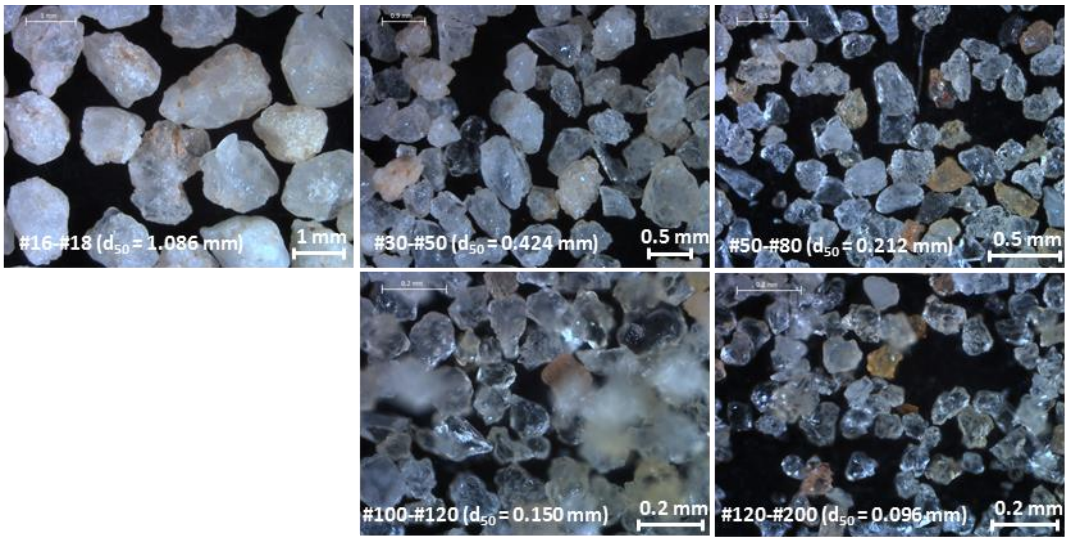

Figure 9.1 Micrographs of uniform silica sands of five different particle sizes

Table 9.1 Properties of the uniform silica sands of five different particle sizes

Uniform sand[1]	Notes[2]	d_{50} (mm)	Roundness	G_s	e_{max}	e_{min}
#16 – #18	Medium sand	1.086	0.36	2.624	0.901	0.632
#30 – #50	Medium/Fine sand	0.424	0.26	2.640	0.999	0.698
#50 – #80	Fine sand	0.232	0.17	2.646	1.102	0.786
#100 – #120	Fine sand	0.137	0.18	2.652	1.108	0.778
#120 – #200	Fine sand	0.096	0.23	2.654	1.099	0.717

Note: [1]No.# - No.# are the upper sieve number and the lower sieve number respectively for a uniform sand. [2]the classification is according to ASTM D422-63 (2007).

To study the effects of fines content and particle size ratio, four series of binary mixtures with four different particle size ratios were prepared by mixing #16-#18 uniform sand with one of the other four uniform sands. Herein, the #16-#18 sand is referred to as "coarse" particles and the other four smaller size sand are referred to as "fine" particle. For each particle size ratio, the series of binary mixture were prepared with fines content f_c = 0.1, 0.2, 0.3, 0.5, 0.7. We define fines content as the ratio of the mass of the small particle sand to the total mass of a binary mixture in this study. Particle size ratio is the ratio of the large particle size to the small particle size in a binary mixture. The particle size

distributions of binary mixtures with four different particle size ratios are presented in Fig. 9.2. The minimum void ratio and the maximum void ratio of four series of binary mixtures were determined according to Method 2A of ASTM D4253 (2006) and Method B of ASTM D4254 (2006), respectively. The minimum and the maximum void ratios of these binary mixture samples are tabulated in Table 9.2.

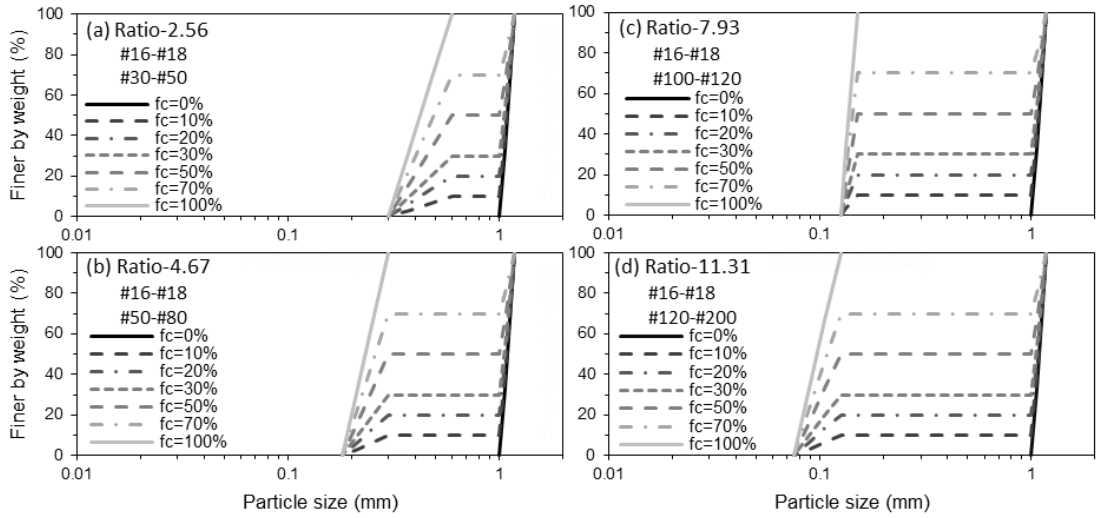

Figure 9.2 The grain size distributions of binary mixtures with four different particle size ratios: (a) Ratio-2.56, (b) Ratio- 4.67, (c) Ratio-7.93, and (d) Ratio-11.31

9.2.2 Drained Triaxial Compression Testing

A conventional triaxial device was used to study the drained shear behavior of binary silica sand mixtures. All tests were performed on cylindrical specimens (50 mm in diameter and 100 mm in height) under the confining stress of 200 kPa. A total number of 25 triaxial tests were performed. All specimens were prepared by the moist tamping method with the under-compaction technique introduced by Ladd (1978). The moist soil with a moisture content of 5% was placed in the split mold and then compacted to a specified density in five layers. A 3% under-compaction ratio, defined as the difference in density

between successive layers, was used in the sample preparation to improve the uniformity within specimens. The moist tamping method is able to minimize particle segregation because of capillarity. Because of the advantage in creating uniform samples and avoiding particle segregation, the moist tamping method using under-compaction is preferred in the sample preparation for sand-silt mixtures (e.g., Huang et al., 2004; Wei & Yang, 2019; Yang et al., 2006).

Table 9.2 List of index properties of tested binary mixtures

Symbol	Mixture series	Size ratio[1] $\frac{d_{50\_coarse}}{d_{50\_fine}}$	f_c (%)	e_{max}	e_{min}
Ratio-2.56	#16-#18 #30-#50	2.56	10	0.874	0.603
			20	0.828	0.566
			30	0.8	0.54
			50	0.802	0.548
			70	0.873	0.620
Ratio-4.67	#16-#18 #50-#80	4.67	10	0.830	0.571
			20	0.734	0.508
			30	0.703	0.491
			50	0.725	0.501
			70	0.858	0.592
Ratio-7.93	#16-#18 #100-#120	7.93	10	0.795	0.547
			20	0.679	0.452
			30	0.635	0.393
			50	0.648	0.463
			70	0.821	0.585
Ratio-11.31	#16-#18 #120-#200	11.31	10	0.797	0.523
			20	0.659	0.408
			30	0.583	0.335
			50	0.600	0.415
			70	0.776	0.517

Note: [1] d_{50_coarse} is the large particle mean size and d_{50_fine} is the small particle mean size.

Note that the minimum and the maximum void ratios of the samples were obtained by using dry sand (according to ASTM D4253-00 (2006) and ASTM D4254-00 (2006)). The void ratios e_0 of all samples after preparation using wet compaction were plotted in Fig. 9.3, compared with the measured values of e_{min} and e_{max}. As shown in Fig. 9.3, the

value of e_0 for all samples is nearly the same as that of e_{min}, which indicates that all samples have same initial relative density of around 97%.

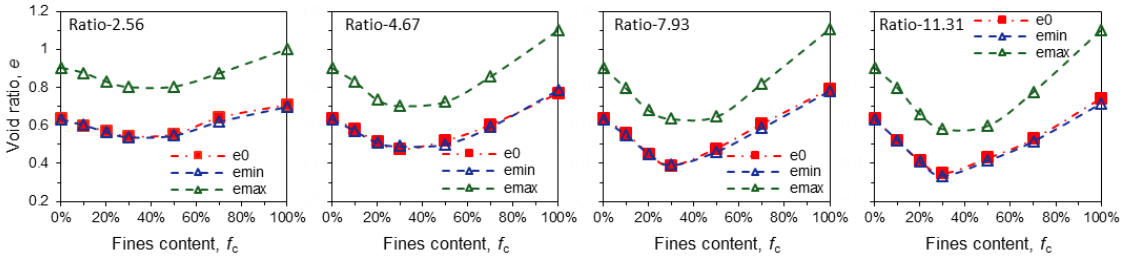

Figure 9.3 The initial void ratios e_0 of all samples

After the sample preparation and installation into the triaxial cell, the specimen was saturated by flushing with carbon dioxide gas and then flushing with deaired water, followed by backpressure saturation to achieve a value of Skempton's B parameter of greater than 0.96. Then the specimen was isotropically consolidated under the desired effective confining stress. After consolidation, the specimen was sheared until failure by compressing the specimen at a constant vertical displacement rate of 0.2 mm/min under the confining stress. All samples were under a drained condition during the course of shearing. Particle breakage was not observed in any test. The results of the triaxial tests are summarized in Table 9.3.

Major and minor principal effective stresses are denoted by σ_1' and σ_3'. Axial and volumetric strains are denoted by ε_a and ε_v. Contractive strains are considered positive and dilative strains are considered negative.

Table 9.3 Summary results of drained triaxial compression tests on the specimens of binary silica sand mixtures of various fines contents for four different particle size ratios

Samples	Fines content	Void ratio					Shearing				
		Initial	Consoli-dation	Onset of dilatancy	Peak stress	Critical State (CS)	Strain at peak stress		Peak friction angle	Max. dilatancy angle	CS friction angle
							Axia	Vol.			
	f_c (%)	e_0	e_c	e_f	e_p	e_{cs}	ε_a	ε_v (%)	ϕ_p (◦)	ψ_p (◦)	ϕ_{cv} (◦)
#16-#18	-	0.637	0.621	0.617	0.663	0.727	9.5	-2.6	38.0	11.0	32.8
#16-#18 #30-#50 (Ratio-2.56)	10	0.599	0.583	0.579	0.619	0.692	10.9	-2.5	36.9	9.3	31.6
	20	0.573	0.558	0.553	0.584	0.643	10.3	-1.7	36.0	7.7	31.5
	30	0.544	0.531	0.527	0.561	0.611	8.2	-1.5	37.6	9.0	33.6
	50	0.555	0.544	0.541	0.575	0.631	8.3	-2.0	38.1	9.9	33.6
	70	0.643	0.631	0.626	0.655	0.713	9.0	-1.6	37.0	8.3	33.1
	100	0.711	0.700	0.696	0.746	0.805	9.4	-2.7	39.0	11.7	33.6
#16-#18 #50-#80 (Ratio-4.67)	10	0.580	0.562	0.558	0.603	0.665	12.2	-2.5	36.2	8.5	31.7
	20	0.513	0.499	0.494	0.517	0.569	9.0	-1.3	36.4	7.1	31.9
	30	0.475	0.461	0.456	0.471	0.503	8.95	-0.7	36.6	5.2	32.8
	50	0.521	0.512	0.508	0.528	0.559	8.7	-0.9	36.8	6.6	33.7
	70	0.604	0.595	0.591	0.625	0.690	8.9	-2.1	39.2	9.6	34.5
	100	0.767	0.756	0.752	0.812	0.894	9.2	-3.2	40.0	12.3	35.0
#16-#18 #100-#120 (Ratio-7.93)	10	0.558	0.542	0.535	0.561	0.601	11.8	-1.5	35.2	8.0	31.8
	20	0.449	0.435	0.428	0.464	0.500	14.4	-1.8	34.9	6.7	32.1
	30	0.386	0.376	0.370	0.375	0.408	6.5	-0.03	35.9	4.6	31.3
	50	0.479	0.470	0.465	0.484	0.525	7.9	-1.2	38.4	8.2	34.8
	70	0.608	0.598	0.593	0.617	0.677	7.3	-1.2	38.1	10.1	33.3
	100	0.794	0.784	0.780	0.829	0.903	7.8	-2.0	39.9	12.6	35.2
#16-#18 #120-#200 (Ratio-11.31)	10	0.521	0.505	0.502	0.550	0.597	11.0	-3.0	38.1	11.0	33.0
	20	0.414	0.404	0.402	0.433	0.484	9.5	-1.7	36.9	7.1	31.9
	30	0.349	0.339	0.333	0.339	0.356	7.8	-0.03	36.8	4.0	31.7
	50	0.430	0.422	0.420	0.435	0.459	5.65	-0.9	38.4	9.2	33.1
	70	0.530	0.523	0.519	0.544	0.621	5.72	-1.32	40.1	12.0	35.2
	100	0.744	0.734	0.730	0.770	0.865	7.0	-2.1	41.1	13.3	35.1

9.3 Test Results

9.3.1 Stress-strain and Volume Change Responses

Fig. 9.4 shows deviatoric stress q ($q = \sigma_1' - \sigma_3'$) and volumetric strain (ε_v) versus axial strain (ε_a) relationships for these four series of binary mixtures, respectively. As shown in Fig. 9.4, all specimens exhibited a softening behavior in the plot of stress versus strain and a dilative behavior in the plot of volumetric strain versus axial strain. Following the initial slight contraction at a small axial strain, dilation then commences. After the onset of dilation, it continues during shearing until the deviatoric stress mobilizes to the peak value. After the peak deviatoric stress, the stress decreases and appears to approach a stable value indicating that a critical state will be reached at larger strains.

Fig. 9.4 shows that fines content affects peak shear strength and volumetric response. There is a general trend of the effect of f_c on peak shear strength: at low f_c, the peak strength is reduced with an increase of f_c until a particular f_c termed transitional fines content f_{th} is reached; After that a further increase in f_c results in an increase of the peak strength. Herein, the transitional fines content f_{th} is defined as the point at which the trend reverses.

Considering volumetric response, it was observed that the curve of ε_v vs. ε_a moves upwards with increase of f_c until reaching a transitional f_{th}, after that the curve tends to move downwards with further increasing f_c. For example, for Ratio-4.67 mixtures, the curve moves upwards from the curve of f_c = 0 to the top one (f_c = 30%) with increase of f_c. Then, with further increasing f_c, the curve moves downwards from the top one to the lowest

one (f_c = 100%). This observation implies that increasing f_c could suppress dilation when $f_c < f_{th}$, on the other hand, increasing f_c could promote dilation when $f_c > f_{th}$.

Fig. 9.4 shows particle size ratio has significant influence on the characteristics of the stress-strain curve for high f_c samples (i.e. $f_c \geq 50\%$). However, particle size ratio has little influence on that for low f_c samples ($f_c < 30\%$).

It was observed that for high f_c samples, increasing particle size ratio intensifies the post peak softening of the stress-strain curves (i.e., brittle characteristic). It can be found that for the samples of Ratio-11.31 at high f_c, the strain softening is so intense that it exhibits a collapse behavior of the stress-strain curves. Correspondingly, visible shear bands were observed in these tests. For low f_c samples, however, increasing particle size ratio has little influence on the degree of post peak softening of the stress-strain curve.

The reason could be that, for low f_c, large particle network dominates the behavior. The large particles are of same size in the mixtures of four different particle size ratios. On the other hand, for high f_c, small particle matrix dominates the behavior. And the sizes of small particles are dramatically different in the mixtures of four size ratios.

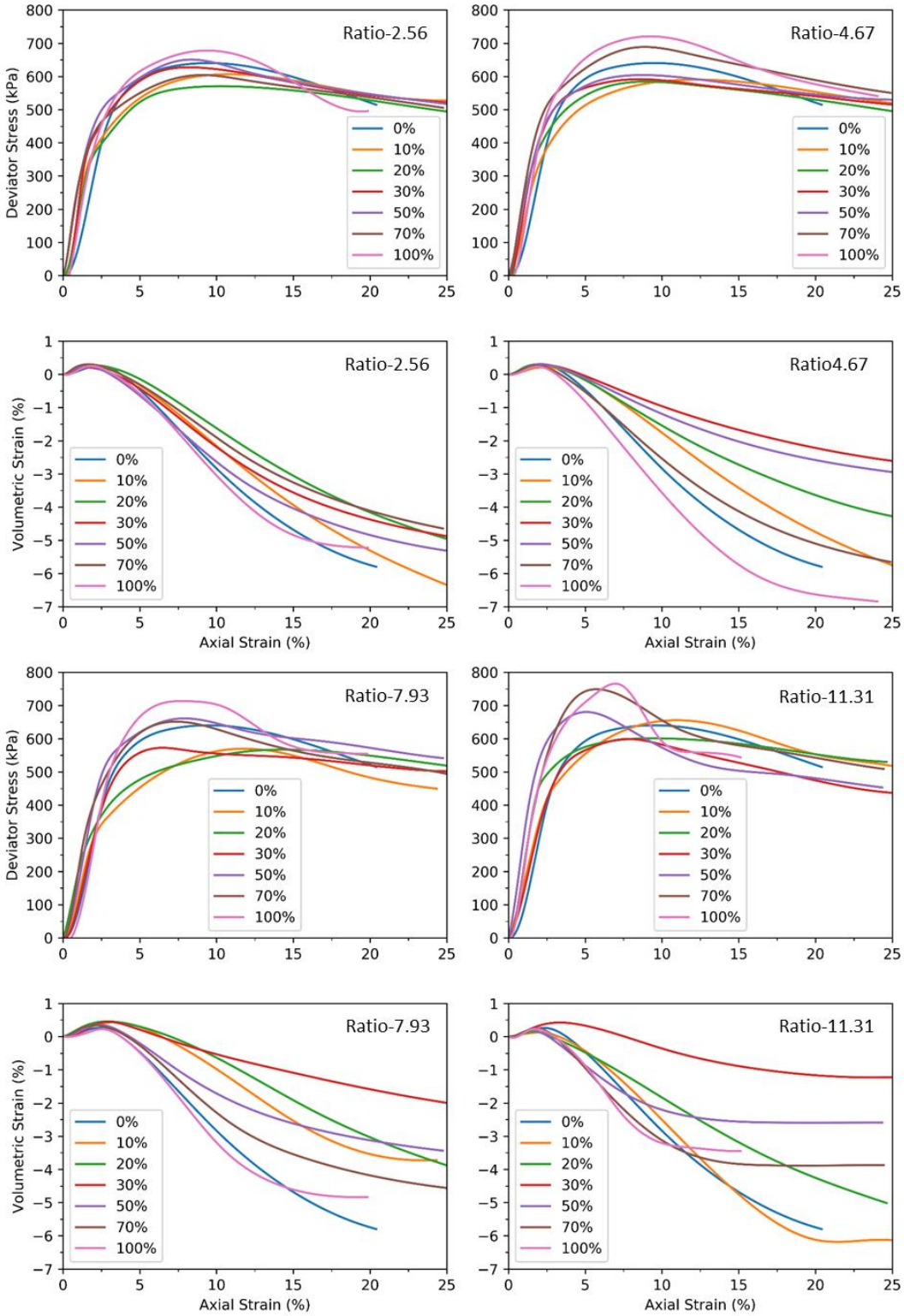

Figure 9.4 Experimental results of the drained triaxial compression tests on binary mixtures of various fines contents and particle size ratios

9.3.2 Stress-dilatancy Plot

The stress- dilatancy evolution of mixtures is presented in Fig. 9.5 for each particle size ratio. For clarity, the data for $f_c \leq f_{th}$ and $f_c \geq f_{th}$ are separately shown in Fig. 9.5.

All stress-dilatancy plots show that there is an initial nonlinear part of the curve before the stress ratio η ($\eta = q/p'$) has reached around $\eta = 0.8$. Then, a consistent increase of dilatancy D ($D = -d\varepsilon_v/d\varepsilon_q$) with an increase in the stress ratio $\eta = q/p'$, prior to the maximum dilatancy. Here, p' is mean effective stress ($p' = (\sigma_1' + 2\sigma_3')/3$) and ε_q is deviator strain ($\varepsilon_q = \varepsilon_a - \varepsilon_v/3$).

Once D reaches a peak (D_{max}), the curves go backwards, yielding a "hook" in the curve as it approaches to the critical state. This behavior is in agreement with that of Erksak sand (Been & Jefferies, 2004). Li and Dafalias (2000) proposed a model to capture this behavior.

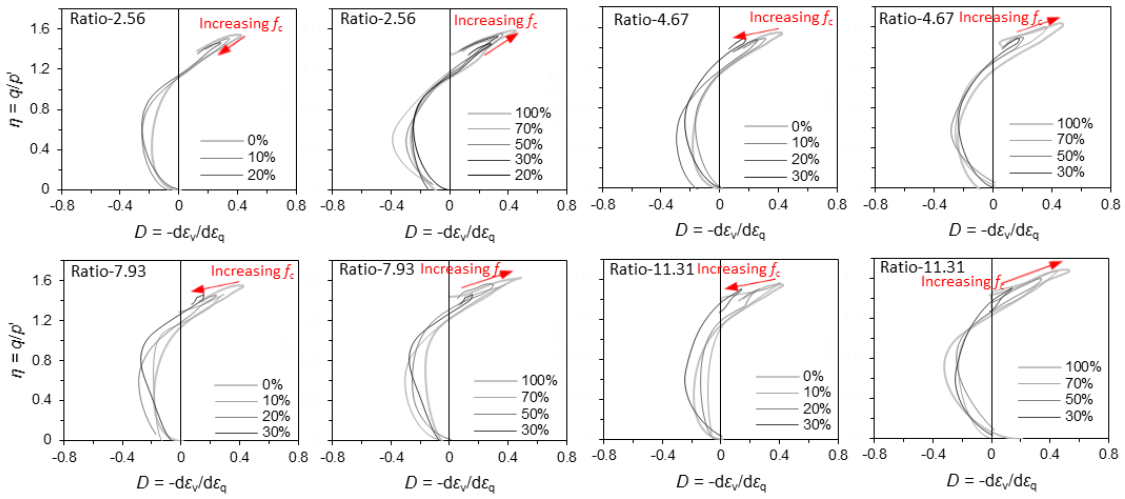

Figure 9.5 The stress-dilatancy plots for binary mixtures of various fines contents and particle size ratios

As shown in Fig. 9.5, D_{max} and the corresponding peak stress ratio η_{max} on the stress-dilatancy plot vary with different f_c. For $f_c \leq f_{th}$, addition of fine particle reduces the values of D_{max} and the corresponding η_{max}. For $f_c \geq f_{th}$, further increasing f_c rises the values of D_{max} and the corresponding η_{max}. This behavior agrees with the effect of fines content on peak shear strength and volumetric response mentioned previously. The measured values of D_{max} and the corresponding η_{max} will be used to calculate the maximum dilation angle ψ_p and the peak friction angle ϕ_p, respectively, which will be discussed in the later section.

9.4 Analyses of Test Results

Based on the test results, the critical state void ratio, the critical state friction angle, the maximum dilatancy angle, and the peak friction angle can be obtained. In this section, we will discuss the effects of fines content and particle size ratio on the critical state void ratio, the critical state friction angle, the maximum dilatancy angle, the peak friction angle, and the strength–dilatancy relation.

9.4.1 Determination of Critical State Void Ratio and Critical State Friction Angle

Critical state (CS) is defined as the state at which the soil continues to deform in shear at constant stress (effective mean stress and shear stress) and constant void ratio (Roscoe et al., 1958). In this study, the triaxial tests were performed up to the maximum axial strain in the apparatus (25%). At this strain, however, the samples have not yet reached the critical state. As suggested by Murthy et al. (2007) and Carrera et al. (2011), it is necessary to extrapolate the stress–strain data to reach the critical state. An extrapolation

method, used by Indraratna et al. (2014) and Xiao et al. (2016), was applied to determine the critical state for our tests. Typical examples for extrapolating the data to critical state are given in Appendix. The extrapolation is more reliable if localization has not yet occurred at 25% strain. However, the extrapolation is not reliable if the occurrence of localization is before 25% axial strain and accompanied with large nonhomogeneous deformation. In our tests, localization was observed in some samples (9 out of 25), especially the samples with large particle size ratios at very high or very low fines contents. In the other 16 samples (mostly in the transitional region of fines content) localization was not observed.

For these samples with localization, the abovementioned method is no longer applicable due to the nonhomogeneous deformation. For these cases with localization, we have adopted another method suggested by investigators (Harehdasht et al., 2017; Nova, 1982). This method requires multiple test results from the same sample under different confining stresses, instead of a single test, to determine the critical state. Examples using the multiple tests method are given in Appendix.

9.4.2 Critical State Void Ratio

(1) *Background*

The effects of fines content and particle size ratio on random close packing density (corresponding to minimum void ratio) have been studies by McGeary (1961) for steel shots and by Kwan et al. (2013) for glass beads as shown in Fig. 9.6. Fig. 9.6 shows that the minimum void ratio of a binary packing depends on fines content f_c and particle size ratio. It was found that the void ratio of binary mixtures decreases with increasing particle

size ratio, for any given fines content. Similar results have been found in soil mixtures (Yilmaz, 2009). The relationship between void ratio and f_c has two features: (1) it is a V-shape curve. The lowest void ratio corresponds to a transitional or threshold fines content. (2) the curve has two regions separated by the transitional fines content. The region is coarse-particle dominate region for lower f_c, and fine-particle dominant region for higher f_c.

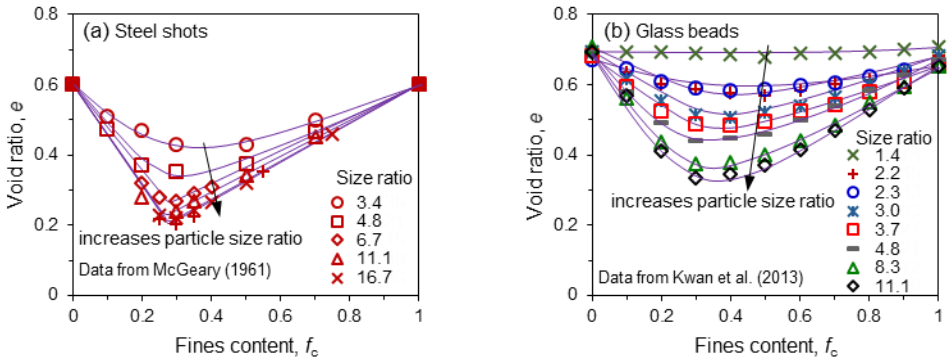

Figure 9.6 The minimum void ratios of binary granular mixtures with various particle size ratios: (a) steel shots and (b) glass beads

The question raised now is whether the special features for minimum void ratio versus f_c are also applicable to critical state void ratio. There have been a lot of experimental data shown that the relationship between e_{cs} and f_c has V-shape characteristic (e.g., Carrera et al., 2011; Dash & Sitharam, 2011; Kwa & Airey, 2016; Naeini & Baziar, 2004; Papadopoulou & Tika, 2008; Thevanayagam et al., 2002; Yang, 2004; Zlatović & Ishihara, 1995). For example, Fig. 9.7 shows the critical void ratios for five different types of sand-silt mixtures. The V-shape characteristics exhibit in the relationship between critical void ratio and fines content.

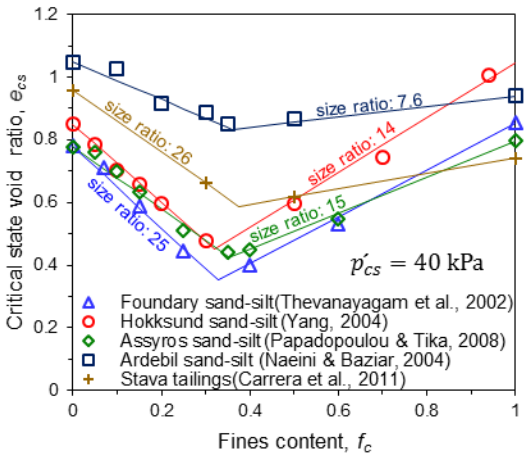

Figure 9.7 The critical state void ratios of five different types of sand-silt mixtures with various fines contents

The plots of critical void ratios under the mean effective stress p'_{cs} of 40 kPa in Fig. 9.7 were from five types of binary mixtures with different particle size ratios (ranges from 7.6 – 26) (Carrera et al., 2011; Naeini & Baziar, 2004; Papadopoulou & Tika, 2008; Thevanayagam et al., 2002; Yang, 2004). The particle size ratio is 26 for Stava tailings mixtures (Carrera et al., 2011), 25 for Foundry sand-silt mixture (Thevanayagam et al., 2002), 15 for Assyros sand-silt mixtures (Papadopoulou & Tika, 2008), 14 for Hokksund sand-silt (Yang, 2004), and 7.6 for Ardebil sand-silt (Naeini & Baziar, 2004). Fig. 9.7 shows that there is no trend of the particle size ratio effect on the critical state void ratios of these mixtures, because each mixture has a different material type.

Thus, in order to study the particle size ratio effect, it is necessary to have test results on mixtures of the same material type so that the effect of particle size ratio can be isolated. However, there are no experimental data available in the literature. Therefore, a series of drained compression triaxial tests on binary silica sand mixture of the same material type are conducted for this purpose.

(2) *The results of e_{cs}*

The results of critical state void ratios e_{cs} in this study were plotted in Fig. 9.8a. The void ratios of samples at the end of testing e_{end} were also plotted in this figure for comparison. The values of e_{cs} and e_{end} for each test are very close. It is observed that the critical state void ratio is dependent on fines content and particle size ratio.

Considering the effect of fines content, the relationship between e_{cs} and fines content is a V-shape character. On the left side, increasing f_c results in decreasing e_{cs} of the binary mixture. On the right side, increasing f_c results in increasing e_{cs} of the binary mixture. This V-shape pattern of fines content influence was also observed in many experiment investigations on silt-sand mixtures (e.g., Carrera et al., 2011; Dash & Sitharam, 2011; Kwa & Airey, 2016; Naeini & Baziar, 2004; Papadopoulou & Tika, 2008; Thevanayagam et al., 2002; Yang, 2004; Zlatović & Ishihara, 1995).

Considering the effect of particle size ratio, as shown Fig. 9.8a, the curve of e_{cs} vs. f_c moves downwards with increasing particle size ratio. The minimum and maximum void ratios of these mixtures used in this study (in Table 9.1) are plotted in Fig. 9.8b and 9.8c. Comparing the three void ratios in Fig. 9.8a, 9.8b, and 9.8c, it is observed that the influences of fines content and particle size ratio on e_{cs} are similar to these on e_{max} and e_{min}, even though, the three density states: e_{cs}, e_{max} and e_{min} are achieved by three different mechanical processes. The similarity between the changes of e_{cs} and of e_{min} due to fines content has also been found by other investigators (Chang & Yin, 2011; Chang & Meidani, 2013; Yin et al., 2014).

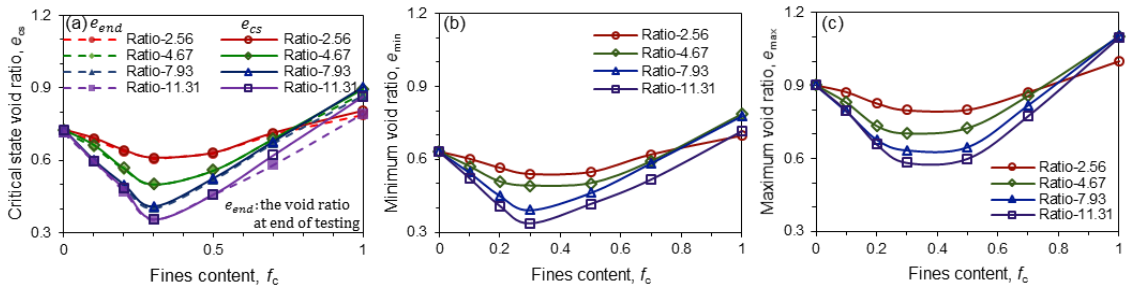

Figure 9.8 The effects of fines content and particle size ratio on (a) critical state void ratio, (b) minimum void ratio, and (c) maximum void ratio

We further investigate the packing potential indices of the three density states. For a system of mixtures (i.e., mixtures with the same two components of various combinations), the upper and the lower bounds can be defined by particle packing theory (Chang & Deng, 2020; De Larrard, 1999; Furnas, 1931; Westman & Hugill, 1930). The void ratios of the binary mixtures with various f_c are between the upper and the lower bounds as the curve ADB shown in Fig. 9.9a. The packing potential index Ω is defined as the ratio of area ADB to area ACB, which is a material descriptor for a system of mixtures (Chang & Deng, 2020). This index is a measure of volume reduction potential due to mixing of two components of a binary mixture system under a packing procedure, which is a simple scalar and can be directly obtained from experimental data. The value of packing potential index Ω is between 0 and 1. The higher value of Ω indicates a higher potential of volume reduction of the mixtures.

The packing potential indices of the three density states (e_{cs}, e_{max} and e_{min}) for the four particle size ratios are plotted in Fig. 9.9b. It is interesting to observe that, for each size ratio, the values of these packing potential indices (Ω_{cs}, Ω_{max}, and Ω_{min}) are nearly identical for the three density states (e_{cs}, e_{max}, and e_{min}). The value of Ω seems to be affected mainly by the composition of a mixture but affected marginally by the mechanical

procedures that leads to the three density states. It implies that fines content plays the same role in the reduction of void ratio of a binary mixture for these three density states. This particular feature is useful for predicting the critical void ratios as a function of particle size ratio and fines content.

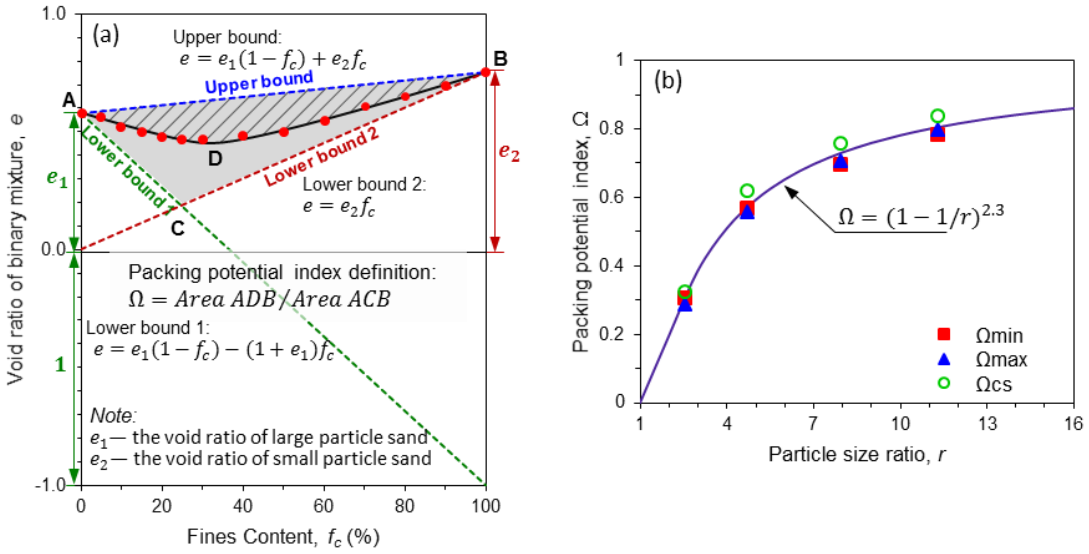

Figure 9.9 (a) The definition of packing potential index and (b) packing potential indices for the void ratios of a system of mixtures at three density states

9.4.3 Critical State Friction Angle

The influence of fines content on critical state friction angle ϕ_{cv} were presented in Fig. 9.10. There are three regions:

(a) For low fines content, ϕ_{cv} of binary mixtures keep close to that of the large particle sand and are almost independent on fines content. This could be because the resistance at critical state for these fines contents is dominated by the contacts between large particles while small particles located in the voids are inactive.

(b) For high fines content, ϕ_{cv} of binary mixtures keep close to that of the fine sand and are also almost independent on fines content. This could be because the resistance at

critical state for these fines contents is dominated by the contacts between small grains while large grains embedding in the matrix formed by small grains.

(c) The third region is a transition region. ϕ_{cv} of binary mixtures is a transition value from ϕ_{cv} of the large particle sand to ϕ_{cv} of the fine sand. In the transition region, with increasing fines content, the resistance of a binary mixture at critical state is initially dominated from large particle-to-large particle contacts, transition to large particle-to-small particle contacts, and finally to small particle-to-small particle contacts.

It is noted that in Fig. 9.8, the transitional fines content is defined as a point (reverse of behavior). Now, in Fig. 9.10, there is no abrupt change of behavior for critical state friction angle; instead, the behavior change is gradual. Thus, we define a transition region between the lower transitional fines content and the upper transitional fine content.

As shown in Fig. 9.10, the lower and upper transitional fines contents and the width of transition region vary with different particle size ratio. Particle size ratio might be a key factor controlling transition region, as suggested by Ueda et al. (2011).

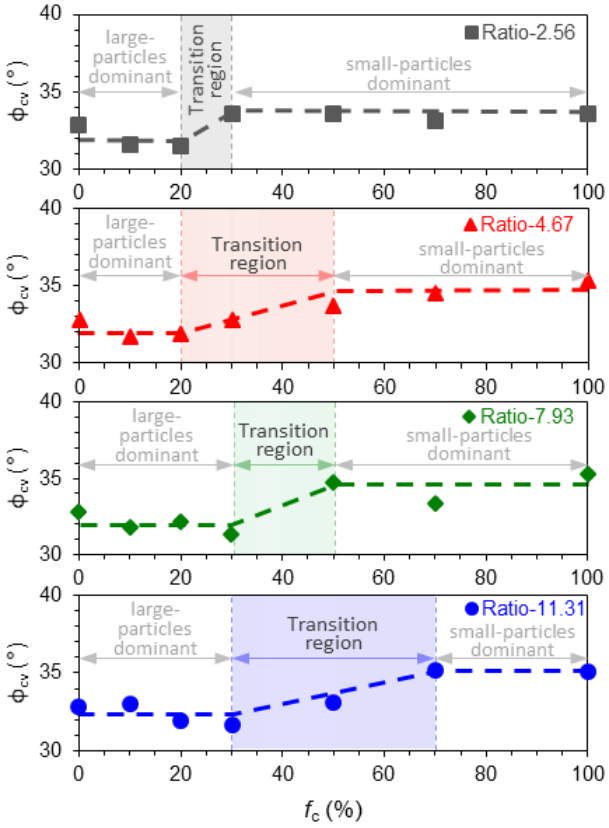

Figure 9.10 The influence of fines content on critical state friction angles of binary mixtures with four different particle size ratios

As shown in Fig. 9.10, the transition occurs at lower fines contents with smaller particle size ratios. The reason might be that at smaller particle size ratios the fine particles are too large to fit in the voids between large particles, consequently the network of large particles is altered by the filled fine particles. Thus, the resistance of the binary mixture begin to be dominated by the contacts between large particle-to-small particle at lower fines contents, as suggested by Shire et al. (2014). Therefore, the transition occurs at lower fines contents. At larger particle size ratios, on the contrary, the fines fit well in the voids between large particles, consequently the network of large particles is not altered until the

voids are fully filled up. Therefore, the transition occurs at higher fines content for the large particle size ratios compared to that for the small particle size ratios.

This transitional behavior of critical state friction angle varying with fines content is consistent with the influence of fines content on residual friction angle in experimental investigations (Polito & Sibley, 2020; Vallejo, 2001) and in DEM simulation (Ueda et al., 2011) for simple and direct shear tests.

However, it was observed from other discrete element simulations that the critical state friction angle is roughly independent of fines content and particle size ratio (Zhu et al., 2020) and independent of the particle size distribution (Azéma, Linero, Estrada, & Lizcano, 2017; Yan & Dong, 2011). The experimental investigation on glass beads also showed the grading independence (Harehdasht et al., 2017).

The independence of fine content on ϕ_{cv} could be caused by the fact that the two particle components in a system of mixtures have the same critical state friction angle. In DEM simulation, the particles normally have identical shape, stiffness, and inter-particle coefficient of friction. These identical properties for the two components cause the ϕ_{cv} to be independent of fines content. But, in the DEM simulation by Ueda et al., (2011), the inter-particle coefficients of friction are assigned to be different for the two components, which cause the friction angle to be dependent of fines content. In our tests, the two particle components in a system of mixtures have different critical state friction angles due to the difference in particle angularity. The finer component is a bit more angular than the coarser component and therefore the ϕ_{cv} is higher for pure fines than pure coarse particles. Hence, the value of ϕ_{cv} is dependent on fines content in our test results.

9.4.4 Maximum Dilation Angle and Peak Friction Angle

The dilation angle (ψ) was calculated using the following relationship proposed by Vermeer and de Borst (1984):

$$\sin\psi = \frac{-(d\varepsilon_v/d\varepsilon_a)}{2-(d\varepsilon_v/d\varepsilon_a)} \quad (9.1)$$

The results of maximum dilation angle ψ_p were presented in Fig. 9.11a. It was observed that fines content has significant influence on ψ_p, especially for the larger particle size ratios, i.e., Ratio-4.67, Ratio-7.93, and Ratio-11.31. For these three particle size ratios, the relationship between ψ_p and fines content has an obvious change around f_c = 30%: ψ_p decreases with an increase in fines content for f_c < 30%, while ψ_p increases with an increase in fines content for f_c > 30%. The smallest ψ_p occurred at the fines content of 30%. For the Ratio-2.56 results, the relationship between ψ_p and fines content is different from those of other three ratios. ψ_p decreases with an increase in fines content for f_c < 20%. The smallest ψ_p occurred at the fines content of 20%. For f_c > 20%, ψ_p increases with an increase in fines content in general except for f_c = 70%.

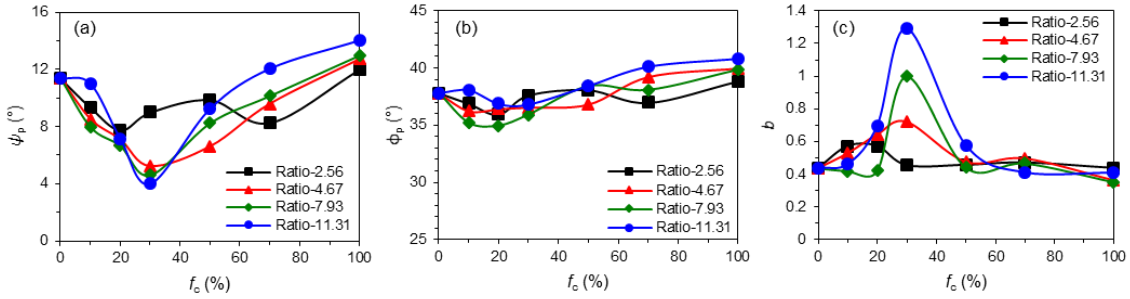

Figure 9.11The influence of fines content on: (a) the maximum dilation angle ψ_p, (b) the peak friction angle ϕ_p, and (c) the dilatancy parameter b in Bolton's stress-dilatancy relation, for binary mixtures with four different particle size ratios

No obvious trend was observed for the particle size ratio effect on ψ_p for f_c < 30%. However, some trends were observed for $f_c \geq$ 30%. At f_c = 30%, ψ_p decreases with an

increase in particle size ratio. The trend evolves and becomes opposite when f_c is above 50%, in which, ψ_p increases with an increase in particle size ratio.

The mechanism of the abovementioned behavior will be discussed in the later section.

The results of peak friction angle ϕ_p were presented in Fig. 9.11b. For all particle size ratios, at low fines content, ϕ_p decreases slightly with increasing fines content. With further increasing fines content, ϕ_p is in transition to approach the ϕ_p of the small particle size sand. But the trend for the effect of particle size ratio on the value of ϕ_p was not found.

Bolton (1986) has proposed an empirical formulation to describe the stress-dilatancy relation given by:

$$\phi_p = \phi_{cv} + b\psi_p \tag{9.2}$$

where parameter b is dilatancy parameter which implies the contribution of dilatancy to the peak strength. The values of b were calculated using the above equation and presented in Fig. 9.11c. There is little variation in the values of b at low or high fines content, which is consistent with the statement made by Xiao et al. (2017) that the effect of f_c on the value of b is negligible. However, Xiao et al. (2017) observed only on their data of Fujian sand mixtures for $f_c \leq 20\%$. Fig. 11c clearly shows that in the transitional fines content region (around 30%), values of b are much greater than that in low and high fines content regions, and increase with increasing particle size ratio. The large values of b show that the contribution of dilatancy to the peak strength is different between the transitional f_c region and the other two f_c regions. The different contribution of dilatancy to the peak strength indicated that the mechnisms of dilatancy must be different between the transitional f_c region and the other two f_c regions, which will be discussed in the following section.

9.5 Discussion on the Mechanism for the Influences of Fines Content and Particle Size Ratio on Drained Shear Behavior

A dense uniform sand sample shearing to critical state successively experiences hardening process and softening process, in which a shear band is usually occurred. The mechanism ending up with the formation of shear bands is the buildup of particle columns during the hardening process and its collapse during the softening process (Iwashita & Oda, 2000).

According to Iwashita and Oda (2000), in the hardening process up to failure, particles are rearranged in chains to form particle columns aligned in the direction of the major principal stress axis, and the applied load is mainly transmitted through them in the form of force chains. As shown in Fig 9.12a, during the loading process, the pre-existing contacts are lost in the minor principal stress direction, but new contacts are formed in the major principal stress direction. Consequently, an elongated void is generated between two neighboring columns. This is the mechanism causing dilatancy before failure. Due to the forming of particle columns and the elongated void parallel to the major principal stress direction, the packing structure becomes highly anisotropic. Such anisotropic structure becomes gradually unstable because of the loss of surrounding contact points. Finally, the particle columns are collapsed via buckling, as shown in Fig. 9.12b. The number of buckled columns increases during the loading process, which eventually leads to a peak stress failure. After peak stress, a new packing structure is re-constructed during the softening process. The main process now is the continuing buckling of particle columns gradually concentrated in a narrow shear band, which causes the growth of large voids between buckling columns and particle rotation. Finally, the structure reaches a dynamically stable

condition at the critical state. During critical state, buildup and collapse of particle columns keep equilibrium within persistent shear bands. The dilatancy is balanced with the contraction so that the overall volumetric strain remains unchanged, resulting in a constant void ratio.

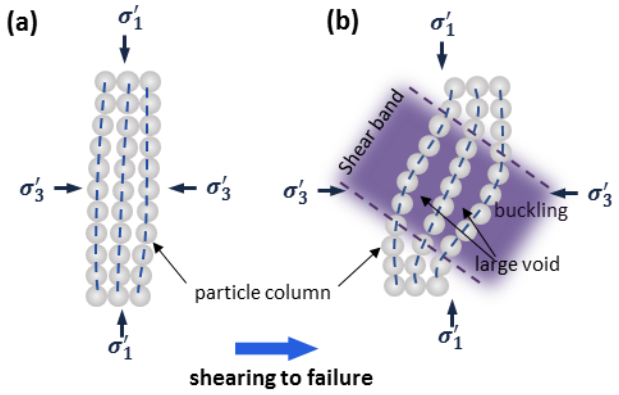

Figure 9.12 A schematic diagram illustrating the mechanism for dilatancy: (a) buildup of particle columns and (b) buckling particle columns

The mechanism for influences of fines content and particle size ratio could be explained from the perspective of particle column buckling, as illustrated in Fig. 9.13.

For large particle dominant binary mixtures (i.e. at low f_c), as illustrated in Fig 13a, the particle columns are mainly formed by large particles during the hardening process. Small particles are filled between two neighboring columns. Small particles laterally support the particle column to suppress buckling. Consequently, the generation of the elongated void between two neighboring columns is limited. As the elongated void leads to dilatancy before failure, therefore, the dilatancy in the binary mixture is smaller than that in the uniform large particle sand. Increasing fines content further suppress dilatancy, consequently results in a decrease of the maximum dilation angle as shown in Fig. 9.10a.

Although the lateral support provided by the small particles makes the columns more difficult to buckle, at large strain, the columns are still buckled and concentrated within a shear band, which exhibits a localized failure.

For the binary mixtures with a transitional fines content (i.e. f_c is around 30%), as illustrated in Fig 9.13b, there could be fewer contacts between large-particles owing to being surrounded by small-particles. On the other hand, small particles are not yet enough to form a matrix. As a result, both large and small particle columns cannot be built up during the hardening process. At this f_c, the dilatancy may mainly be caused by particle rearrangement and overriding each other during shearing process. As a result, a smaller level of dilatancy is expected comparing to that induced by column buckling. Since the dilatancy is caused by the overriding of particles, the level of dilatancy is influenced by the size of particles. Therefore, the smallest dilatancy in Ratio-11.31 test with f_c = 30% was observed, compared with the other three ratios with this f_c (see Fig. 9.11a). Because there are no buckling particle columns, shear band formation is not as visible during the softening process. As a result, we observe a diffuse-type failure is exhibited instead of a localized failure shown in Fig. 9.13b.

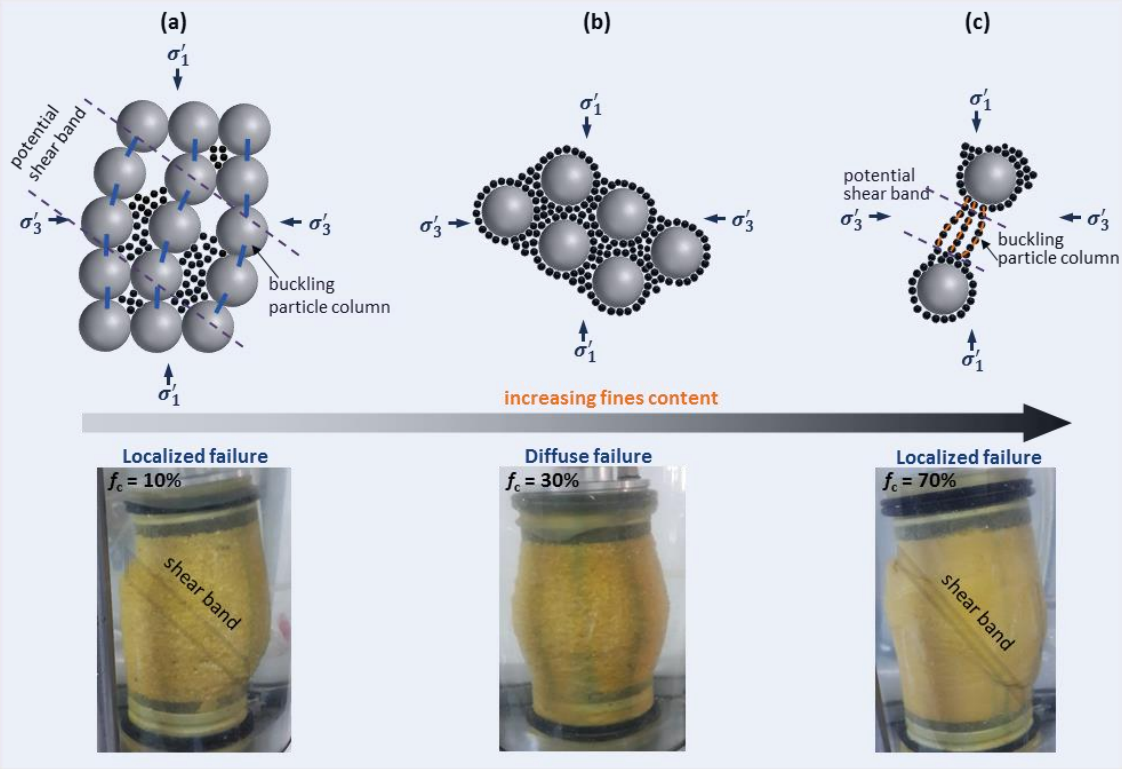

Figure 9.13 The mechanisms for dilatancy and failure of binary sand mixtures in: (a) low fines content region, (b) transitional fines content region, and (c) high fines content region

For small particle dominant binary mixtures (i.e. at high f_c), a matrix is formed by small particles and large particles are floated into it, as illustrated in Fig. 9.13c. During the hardening process, the particle columns are formed by small particles. Large elongated voids causing dilatancy gradually grow between two buckling small particle columns. The number of small particle columns increases with increasing f_c. Therefore, the dilatancy also increases with increasing f_c. Similar to large particle dominant binary mixtures, small particle dominant binary mixtures exhibit a localized failure because buckling particle columns are eventually concentrated within a shear band.

As shown in Fig. 9.11a, the uniform sand with smaller particle size has a higher maximum dilation angle, which was consistent with the observations on glass beads and

Peribonka sand reported by Harehdasht et al. (2017). Harehdasht et al. (2017) has attributed the increase of dilation angle to the particle size effect. In the silica sand used in this study, the particle roundness generally increases with particle size, thus the effect is caused by both factors of particle size and particle roundness.

At very high f_c, the packing structure for the binary sand mixture is nearly the same as that of uniform fine-sand. Therefore, in this case, higher maximum dilation angle was observed for a mixture with larger particle size ratio (i.e. smaller size particle is more angular in shape) (see Fig. 9.11a).

As discussed above, the mechanism for dilatancy in the transitional fines content region is different from that in the regions of low and high fines content. Dilatancy in the transitional fines content region is governed by particle rearrangement and overriding each other, while dilatancy in the regions of low and high fines content is governed by the buckling columns. Therefore, as shown in Fig. 9.11c, the values of b, implying the contribution of dilatancy to the peak strength, are clearly different between the transitional f_c region and the other f_c regions.

9.6 Conclusions

In this paper, the effects of fines content and particle size ratio on the drained shear behaviors were studied through a series of drained triaxial compression tests on dense binary silica sand mixtures with 4 different particle size ratios. The critical state and the strength-dilatancy behavior were analyzed. The mechanism for the effects of fines content and particle size ratio on drained shear behavior was illustrated. Based on this study the major conclusions can be drawn as follows.

(1) It was observed that when $f_c < f_{th}$, increasing f_c suppresses dilation, on the other hand, when $f_c > f_{th}$, increasing f_c promote dilation.

(2) It was observed that, for high f_c samples, increasing particle size ratio intensifies the post peak softening of the stress-strain curves (i.e., brittle characteristic). For low f_c samples, however, increasing particle size ratio has little influence on the degree of post peak softening of the stress-strain curve.

(3) Both fines content and particle size ratio have significant influence on critical state void ratio. It is interesting to note that the pattern of critical state void ratio is similar to that on minimum and maximum void ratios influenced by particle size ratio. The similar pattern might imply that fines content plays the same role in the reduction of void ratio of a binary mixture for these three density states.

(4) The value of ϕ_{cv} of a mixture is influenced by its fines content, which can be divided in 3 regions: (a) at low fines content region, the ϕ_{cv} values of binary mixtures are close to the ϕ_{cv} of large particles; (b) at high fines content region, the ϕ_{cv} values of binary mixtures are close to the ϕ_{cv} of fine particles; (c) in the transition region, the ϕ_{cv} values of binary mixtures are transition from the ϕ_{cv} of the large particle sand to the ϕ_{cv} of the fine sand.

(5) A general trend for the effect of fines content on ψ_p is observed. ψ_p decreases with an increase in fines content for $f_c < 30\%$. But, ψ_p increases with an increase in fines content for $f_c > 30\%$. The smallest ψ_p occurred at the fines content of 30%. No obvious trend was observed for the particle size ratio effect on ψ_p for $f_c < 30\%$. However, at $f_c = 30\%$, there is a clear trend that ψ_p decreases with an

increase in particle size ratio. The trend evolves and becomes opposite when f_c is above 50%, in which, ψ_p increases with an increase in particle size ratio.

(6) It was found that the parameter *b* in Bolton' stress-dilatancy relation has a little variation in low and high fines content regions. In the transitional fines content region, however, the parameter *b* is much greater than that in the other two regions and increase with increasing particle size ratio.

(7) The mechanism was proposed to illustrate the influences of fines content and particle size ratio on the drained shear behavior from the perspective of particle column buckling. Dilatancy in the transitional region of fines content is governed by the rearrangement of particle, which override each other. Whereas, dilatancy in the regions of low or high fines content is governed by the buckling of particle columns. The influences of fines content and particle size ratio on dilatancy and value of *b* in the Bolton's stress–dilatancy equation were explained by the proposed mechanism.

Appendix: Examples to Determine the Critical State

A.1 For Samples without Visualized Localization at Large Strain

For a sample without visualized deformation localization, we assume that localization is minute and the deformation is relatively uniform for the range of stress-strain curve between the peak stress and the end of test, which can be used to assess the critical state.

The critical state was determined by an extrapolating method described herein. The sample with Ratio-4.67 at 30% f_c was taken as an example shown in Fig. 9.14. The critical

state friction angle was firstly estimated with a stress-dilatancy analysis as shown in Fig. 9.14a. In this analysis, the Nova's stress-dilatancy relationship (Nova, 1982) was used to fit the stress-dilatancy data of post-peak stress,

$$\eta = M + (1 - N)D \tag{9.3}$$

where M is the stress ratio at critical state and N is a volumetric coupling coefficient. After the values of M and N were obtained from fitting the data, the critical state friction angle ϕ_{cv} was then obtained using the relationship $sin\phi_{cv} = 3M/(6 + M)$ and listed in Table 9.3.

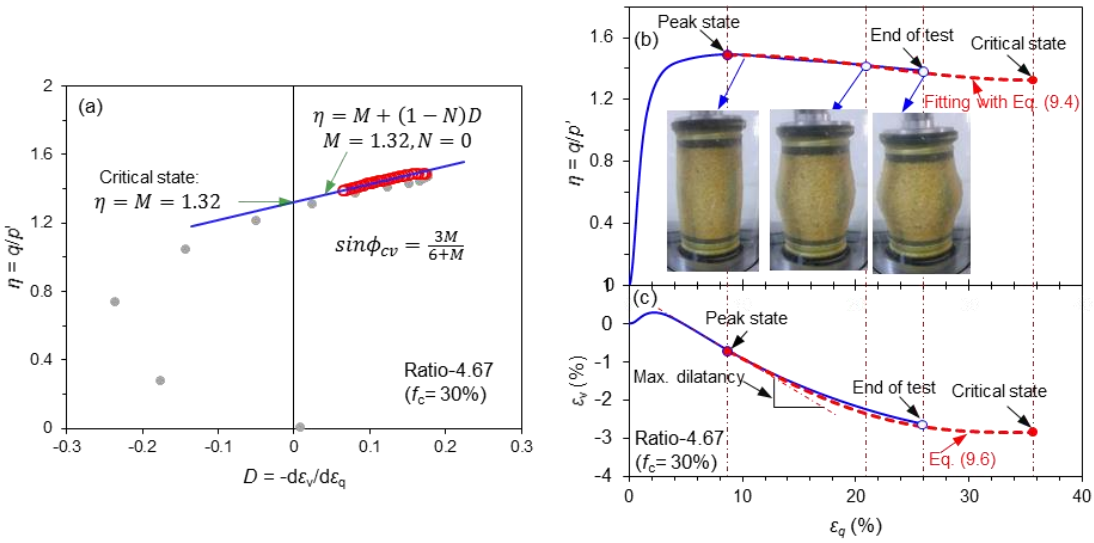

Figure 9.14 An example of extrapolating the data to determine the critical state for a sample without visualized localization: (a) stress-dilatancy analysis, (b) extrapolated stress-strain curve, and (c) extrapolated volumetric strain curve

For convenience, a cosine function was used to extrapolate the post-peak stress-strain curve.

$$\eta = \frac{\eta^{peak}+M}{2} + \frac{\eta^{peak}-M}{2} cos\left(\frac{\varepsilon_q-\varepsilon_q^{peak}}{\varepsilon_q^{cs}-\varepsilon_q^{peak}} \cdot \pi\right);\ \varepsilon_q \in [\varepsilon_q^{peak}, \varepsilon_q^{cs}] \tag{9.4}$$

where the superscripts 'peak' and 'cs' denote for peak state and critical state, respectively. Fig. 9.14b and Fig 9.15a show that this cosine function is satisfactory to express the post-peak stress-strain curves. The deviator strain ε_q^{cs}, where the critical state occurs, was estimated by a regression analysis performed on the stress-strain data from the peak stress to the end of the test. The regression analysis minimizes the sum of squared errors *SS*,

$$SS\left(\varepsilon_q^{cs}\right) = \sum_i \left[\eta^i - \eta\left(\varepsilon_q^i, \varepsilon_q^{cs}\right)\right]^2 \qquad (9.5)$$

where η^i and ε_q^i are the measured i^{th} point on the stress-strain curve. Substituting Eq. (9.4) into Eq. (9.3) and then integrating with respect to ε_q, the expression of volumetric strain ε_v as a function of ε_q between peak state and critical state was obtained as follows

$$\varepsilon_v = \frac{M-\eta^{peak}}{2(1-N)} \cdot \left[\left(\varepsilon_q - \varepsilon_q^{peak}\right) + \frac{\varepsilon_q^{cs}-\varepsilon_q^{peak}}{\pi} sin\left(\frac{\varepsilon_q-\varepsilon_q^{peak}}{\varepsilon_q^{cs}-\varepsilon_q^{peak}} \cdot \pi\right)\right] + \varepsilon_v^{peak} \qquad (9.6)$$

As shown in Fig. 9.14c and Fig 9.15b, Eq. (9.6) matches the measured results well and can be used to extrapolate the curve of volumetric change response. Using this extrapolation method, the critical state void ratios for the samples without visualized deformation localization were determined and listed in Table 9.3.

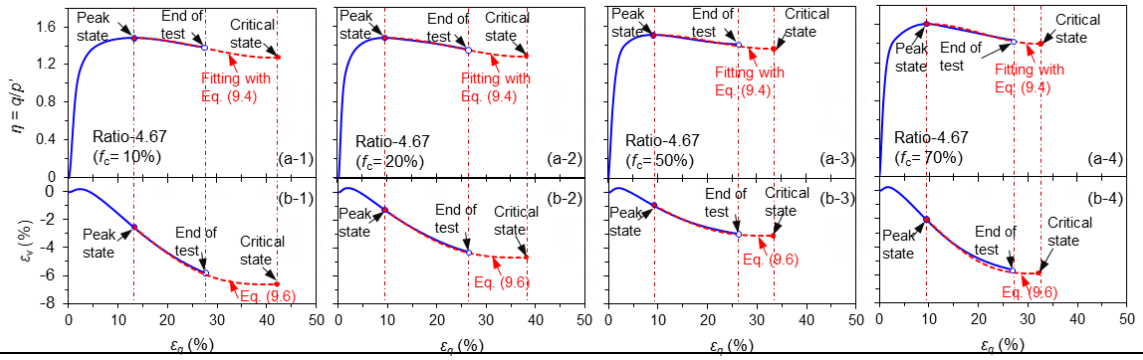

Figure 9.15 Examples of extrapolating the data to determine the critical state for four samples of binary mixtures without visualized localization: (a) extrapolated stress-strain curve and (b) extrapolated volumetric strain curve

A.2 For Samples with Visualized Localization at Large Strain

The sample deformation after the occurrence of localization is not representative of a uniformly deformed material thus cannot be used for extrapolation. Thus, for a sample with visualized localization, the critical state needs to be determined by using multiple test results (Harehdasht et al., 2017; Nova, 1982). In this study, we use test results from three different confining stresses (i.e., 100 kPa, 200 kPa, and 400 kPa). Assuming that the occurred localization is minute at peak stress state, the critical state stress ratio *M* was obtained by fitting the peak points of three stress-dilatancy curves using Eq. (9.3) as shown in Fig. 9.16a. After the stress-dilatancy relationship for each sample was obtained, the critical state friction angle ϕ_{cv} was then obtained using the relationship $sin\phi_{cv} = 3M/(6+M)$ and listed in Table 9.3.

The initiation of localization begins at peak stress state. The localization becomes prominent after a point of maximum curvature, at which the stress strain curve deviates from the smooth curve. After this point, a greater softening commences. The minute localization propagates into a visualized shear band with abrupt stress reduction (see Fig. 9.16b). We assume that localization is ineffective and the deformation is relatively uniform for the range of stress-strain curve between the peak stress and the point of maximum curvature. This portion of measured curve can be used to assess the critical state.

As discussed previously, the post-peak stress-strain curve without visualized localization can be expressed by a cosine function (Eq. 9.4). Hence, this cosine function was also used to extrapolate the stress-strain curve between the peak stress and the point of maximum curvature for the samples with visualized deformation localization. Using Eq. (9.4) with the determined *M* from three test results, the critical state deviator strain ε_q^{cs} was

estimated by a regression analysis performed on the stress-strain data from the peak stress to the point of maximum curvature. The examples of the extrapolating stress-strain curves are shown in Fig. 9.16b. The expression of volumetric strain ε_v as a function of ε_q between peak state and critical state was obtained based on the established stress-dilatancy relationship and the estimated ε_q^{cs}. The examples of the extrapolating volumetric strain curves are shown in Fig.9.16c. Using this extrapolation method, the critical state void ratios for the samples with visualized localization were determined and listed in Table 9.3.

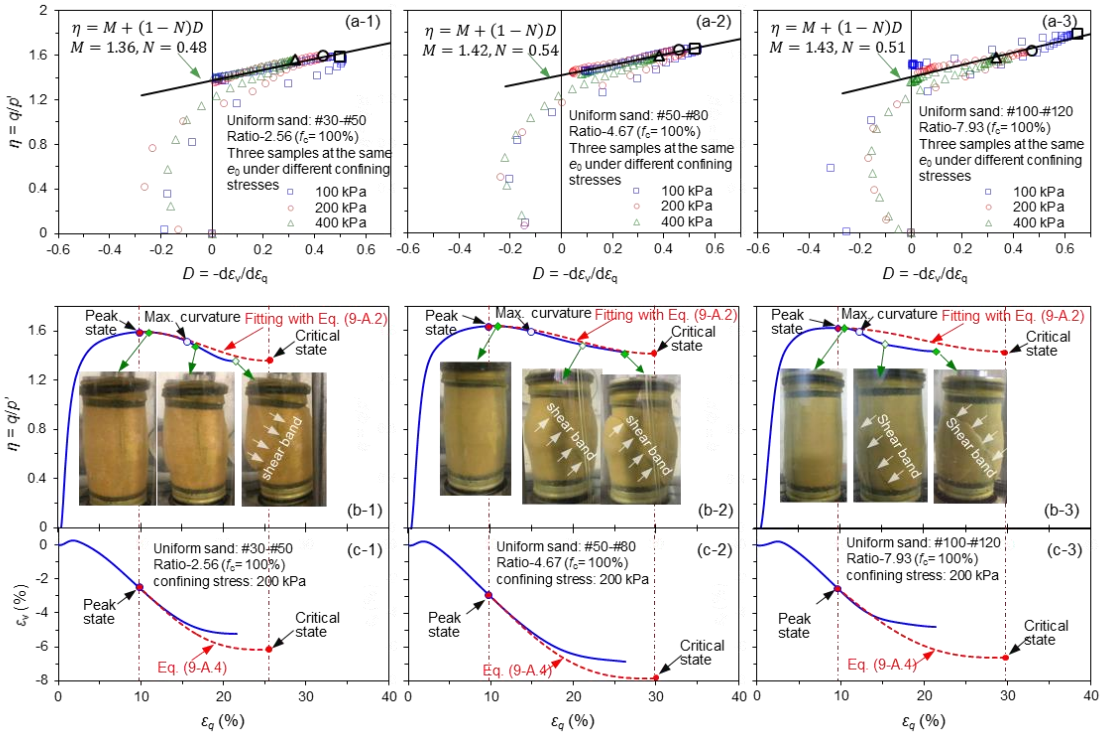

Figure 9.16 Examples of extrapolating the data to critical state for the samples with deformation localization: (a) stress-dilatancy analysis, (b) extrapolated stress-strain curve, and (c) extrapolated volumetric strain curve

CHAPTER 10

CONCLUSIONS AND RECOMMENDATIONS

10.1 Summary and Conclusions

The particle size distribution of soil is the main factor that affects its mechanical properties. However, in soil mechanics, the influence of particle size distribution on mechanical properties is only considered in an empirical manner. There are no analytical methods that can explicitly account for the effect of particle size distribution. In this research, the necessary knowledge was developed for modeling the effect of particle size distribution on density state of soil, which is the fundamental property relating to mechanical behavior of soil. The developed theory from this research is potentially useful for analyzing geotechnical engineering problems, such as liquefaction of silty sand, landslides of weathered soil, levee failure due to erosion of fine particles, and dam instability due to grain crushing. The method developed in this research can help reducing the future risks of failures, developing more robust design methodologies, and better targeted mitigation works.

The conclusions drawn from the present dissertation can be summarized as follows:

(1) A statistical model has been developed for predicting the minimum and the maximum void ratios of uniform sands based on their particle morphology (i.e. particle size and particle roundness). A new material parameter, morphology index, was proposed in this statistical model, which gives a bearing on the influence of particle morphology on the magnitudes of minimum and maximum void ratios of granular material.

(2) A linear particle packing theory has been developed for predicting the minimum and maximum void ratios of multi-sized soil mixtures, in which, sand-silt mixture is a special case. This theory is established by assuming a dominant particle size for the mixture. Using this concept, the mix mechanism of filling and embedment can be considered for each size class of the particle mixture. This allows the determination of the minimum and maximum void ratios for granular soil with an arbitrary particle size distribution.

(3) A nonlinear particle packing theory has been developed for predicting the minimum and maximum void ratios of multi-sized soil mixtures. This theory can fit better the experimental results than linear theory. In the linear packing model, the dominant size is assumed to be one of the size class of the particle mixture. In the nonlinear model, it was recognized that the dominant skeleton is composed of more than one class of particles. Thus, it is hypothesized that the dominant size is an effective size, which represents the dominant packing skeleton made up of various size classes of particles. Using this hypothesis, the nonlinear model overcomes the limitation of conventional linear packing model. The linear theory is a special case of the nonlinear theory.

(4) A packing potential index has been defined to study the void reduction due to mixing of binary packing. It is found that the packing potential index is nearly independent of the packing procedure of a mixture but significantly dependent on the compound particle shapes of the mixture. A set values for the particle interaction parameters were proposed for soil mixtures with three types of compound particle shapes for the proposed particle packing density model.

(5) A new formula of inter-granular void ratio of silty sand has been proposed based on the particle packing theory. The concept of inter-granular void ratio was revisited. Based

on the particle packing theory, the inter-granular void ratio should be a function of both specific volumes of coarse and fine particles. The new formula of inter-granular void ratio has shown to provide better results for predicting critical state void ratio for sand-silt mixtures.

(6) A framework of modeling the CSL of granular soils was established by explicitly considering their particle size distribution. It was found that there is a strong correlation between critical state void ratio and the minimum void ratio. Therefore, it is hypothesized that the change of critical state void ratio with respect to particle size distribution (PSD) is caused by the same mechanism that influences of the change of minimum void ratio with respect to PSD. Consequently, the particle packing model for minimum void ratio is extended to predict critical state void ratio. It was found that the influence of particle breakage on the CSL is mainly attributed to the change in PSD due to particle breakage. The model was further developed to predict the CSL of granular material with effect of particle breakage.

(7) A mechanism was proposed to illustrate the influences of fines content and particle size ratio on the drained shear behavior from the perspective of particle column buckling. It was found that both fines content and particle size ratio have significant influence on the drained shear behaviors of binary granular soil mixtures, i.e., critical state friction angle ϕ_{cv}, maximum dilation angle ψ_p, and the parameter b in Bolton' stress-dilatancy relation. Dilatancy in the transitional region of fines content is governed by the rearrangement of particle, which override each other. Whereas, dilatancy in the regions of low or high fines content is governed by the buckling of particle columns. The influences

of fines content and particle size ratio on dilatancy and value of *b* in the Bolton's stress–dilatancy equation can be explained by the proposed mechanism.

10.2 Recommendations for Future Research

Based on the findings from this investigation in the present dissertation, some recommendations for further research are suggested as follows:

(1) The density states of granular soils in this study belong to the scope of the jammed state of granular matter in physics field. From a fundamental theoretical point of view, it is important to understand the packing of granular soils from a statistical mechanics view (Baule, Morone, Herrmann, & Makse, 2018). The statistical mechanics framework might be applied in polydisperse granular soils to further study the role of particle size distribution in influencing their density states.

(2) The mechanism explaining the effects of fines content and particle size ratio on the strength and dilatancy of binary granular soil mixtures in present dissertation is only a conjecture, which cannot be verified by triaxial tests alone. It needs to be further verified by other analysis such as DEM simulation and X-ray computed tomography imaging analysis.

(3) The study of the strength-dilatancy and critical state behaviors of bidisperse granular soils has been carried out in present dissertation. This work needs to be extended to polydisperse granular soils in the future research.

(4) The strength-dilatancy relation for granular soils differs from monodisperse granular soils to polydisperse granular soils. It is important to understand the fundamental issues of the influence of particle size distribution on the dilatancy behavior from an energy

perspective. The current particle packing theory may be extended to model the dilatancy behavior.

BIBLIOGRAPHY

AASHTO. (1986). *Correction for coarse particles in the soil compaction test*. Washington, D.C.: AASHTO Designation: T224-86.

Aberg, B. (1992). Void ratio of noncohesive soils and similar materials. *Journal of Geotechnical Engineering*, *118*(9), 1315–1334. https://doi.org/10.1061/(ASCE)0733-9410(1992)118:9(1315)

Aïm, R. B., & Goff, P. L. (1968). Effet de paroi dans les empilements désordonnés de sphères et application à la porosité de mélanges binaires. *Powder Technology*, *1*(5), 281–290. https://doi.org/10.1016/0032-5910(68)80006-3

Allen, T. (1997). *Particle size measurement. Vol. 1 : Powder sampling and particle size measurment* (5th ed.). London: Chapman & Hall.

Alshibli, K. A., & Alsaleh, M. I. (2004). Characterizing Surface Roughness and Shape of Sands Using Digital Microscopy. *Journal of Computing in Civil Engineering*, *18*(1), 36–45. https://doi.org/10.1061/(ASCE)0887-3801(2004)18:1(36)

An, X. Z., Li, C. X., Yang, R. Y., Zou, R. P., & Yu, A. B. (2009). Experimental study of the packing of mono-sized spheres subjected to one-dimensional vibration. *Powder Technology*, *196*(1), 50–55. https://doi.org/10.1016/j.powtec.2009.06.016

An, Xi Zhong. (2013). Densification of the packing structure under vibrations. *International Journal of Minerals, Metallurgy and Materials*, *20*(5), 499–503. https://doi.org/10.1007/s12613-013-0757-9

Aste, T., & Weaire, D. (2008). *The Pursuit of Perfect Packing* (2nd ed). Hoboken, NJ: Taylor & Francis.

ASTM D422-63. (2007). Standard test method for particle-size analysis of soil. West Conshohocken, PA: ASTM International.

ASTM D4253-00. (2006). Standard test methods for maximum index density and unit weight of soils using a vibratory table. In *Annual Book of ASTM Standards* (Vol. 04.08, pp. 1–15). West Conshohocken, PA: ASTM International. https://doi.org/10.1520/D4253-00R06.

ASTM D4254-00. (2006). Standard Test Methods for Minimum Index Density and Unit Weight of Soils and Calculation of Relative Density. In *Annual Book of ASTM Standards* (Vol. I, pp. 1–9). West Conshohocken, PA: ASTM International. https://doi.org/10.1520/D4254-00R06E01.1.3

Atieg, A., & Watson, G. A. (2003). A class of methods for fitting a curve or surface to data by minimizing the sum of squares of orthogonal distances. *Journal of Computational and Applied Mathematics*, *158*(2), 277–296. https://doi.org/10.1016/S0377-0427(03)00448-5

Azéma, E., Linero, S., Estrada, N., & Lizcano, A. (2017). Shear strength and microstructure of polydisperse packings: The effect of size span and shape of particle size distribution. *Physical Review E*. https://doi.org/10.1103/PhysRevE.96.022902

Balazs, R. J., & Klein, G. D. (1972). Roundness-mineralogical relations of some intertidal sands. *Journal of Sedimentary Research*, *42*(2), 425–433. https://doi.org/10.1306/74D72577-2B21-11D7-8648000102C1865D

Bandini, P., & Sathiskumar, S. (2009). Effects of Silt Content and Void Ratio on the Saturated Hydraulic Conductivity and Compressibility of Sand-Silt Mixtures. *Journal of Geotechnical and Geoenvironmental Engineering*, *135*(12), 1976–1980. https://doi.org/10.1061/(ASCE)GT.1943-5606.0000177

Bandini, V., & Coop, M. R. (2011). The influence of particle breakage on the location of the critical state line of sands. *Soils and Foundations*, *51*(4), 591–600. https://doi.org/10.3208/sandf.51.591

Bareither, C. a., Edil, T. B., Benson, C. H., & Mickelson, D. M. (2008). Geological and Physical Factors Affecting the Friction Angle of Compacted Sands. *Journal of Geotechnical and Geoenvironmental Engineering*, *134*(10), 1476–1489. https://doi.org/10.1061/(ASCE)1090-0241(2008)134:10(1476)

Barrett, P. J. (1980). The shape of rock particles, a critical review. *Sedimentology*, *27*(3), 291–303. https://doi.org/10.1111/j.1365-3091.1980.tb01179.x

Baule, A., Morone, F., Herrmann, H. J., & Makse, H. A. (2018). Edwards statistical mechanics for jammed granular matter. *Reviews of Modern Physics*, *90*(1), 15006. https://doi.org/10.1103/RevModPhys.90.015006

Been, K., & Jefferies, M. G. (1985). A state parameter for sands. *Géotechnique*, *35*(2), 99–112.

Been, K., Jefferies, M. G., & Hachey, J. (1991). The critical state of sands. *Géotechnique*, *41*(3), 365–381. https://doi.org/10.1680/geot.1991.41.3.365

Been, Ken, & Jefferies, M. (2004). Stress-dilatancy in very loose sand. *Canadian Geotechnical Journal*, *41*, 972–989. https://doi.org/10.1139/t04-038

Belkhatir, M., Schanz, T., & Arab, A. (2013). Effect of fines content and void ratio on the saturated hydraulic conductivity and undrained shear strength of sand-silt mixtures. *Environmental Earth Sciences*, *70*(6), 2469–2479. https://doi.org/10.1007/s12665-013-2289-z

Biarez, J., & Hicher, P.-Y. (1994). *Elementary Mechanics of Soil Behaviour： Saturated Remoulded Soils*. Rotterdam: Balkema.

Blaker, Ø., Lunne, T., Vestgården, T., Krogh, L., Thomsen, N. V, Powell, J. J. M., & Wallace, C. F. (2015). Method dependency for determining maximum and minimum dry unit weights of sands. In Meyer， Vaughan (Ed.), *Frontiers in Offshore Geotechnics III* (pp. 1159–1166). London: Taylor & Francis Group. https://doi.org/DOI: 10.1201/b18442-174

Bobei, D. C., Lo, S. R., Wanatowski, D., Gnanendran, C. T., & Rahman, M. M. (2009). Modified state parameter for characterizing static liquefaction of sand with fines. *Canadian Geotechnical Journal*, *46*(3), 281–295. https://doi.org/10.1139/T08-122

Bolton, M. D. (1986). The strength and dilatancy of sands. *Géotechnique*, *36*(1), 65–78. https://doi.org/10.1680/geot.1986.36.1.65

Bouckovalas, G. D., Andrianopoulos, K. I., & Papadimitriou, A. G. (2003). A critical state interpretation for the cyclic liquefaction resistance of silty sands. *Soil Dynamics and Earthquake Engineering*, *23*(2), 115–125. https://doi.org/10.1016/S0267-7261(02)00156-2

Carraro, J. A. H., Prezzi, M., & Salgado, R. (2009a). Shear strength and stiffness of sands containing plastic or nonplastic fines. *Journal of Geotechnical and Geoenvironmental Engineering*, *135*(200), 1167–1178. https://doi.org/10.1061/(ASCE)1090-0241(2009)135

Carraro, J. A. H., Prezzi, M., & Salgado, R. (2009b). Shear Strength and Stiffness of Sands Containing Plastic or Nonplastic Fines. *Journal of Geotechnical and Geoenvironmental Engineering*, *135*(200), 1167–1178.

Carrera, A., Coop, M., & Lancellotta, R. (2011). Influence of grading on the mechanical behaviour of Stava tailings. *Géotechnique*, *61*(11), 935–946. https://doi.org/10.1680/geot.9.P.009

Chang, C.S., & Deng, Y. (2017). A particle packing model for sand–silt mixtures with the effect of dual-skeleton. *Granular Matter*, *19*(4). https://doi.org/10.1007/s10035-017-0762-1

Chang, C.S., & Deng, Y. (2018). A nonlinear packing model for multi-sized particle mixtures. *Powder Technology*, *336*. https://doi.org/10.1016/j.powtec.2018.06.008

Chang, C.S., Wang, J. Y., & Ge, L. (2016). Maximum and minimum void ratios for sand-silt mixtures. *Engineering Geology*, *211*, 7–18. https://doi.org/10.1016/j.enggeo.2016.06.022

Chang, Ching S., & Deng, Y. (2017). A particle packing model for sand–silt mixtures with the effect of dual-skeleton. *Granular Matter*, *19*(4), 80. https://doi.org/10.1007/s10035-017-0762-1

Chang, Ching S., & Deng, Y. (2020). Packing potential index for binary mixtures of granular soil. *Powder Technology*, *372*, 148–160. https://doi.org/10.1016/j.powtec.2020.06.005

Chang, Ching S., Deng, Y., & Meidani, M. (2018). A multi-variable equation for relationship between limiting void ratios of uniform sands and morphological characteristics of their particles. *Engineering Geology*, *237*(January), 21–31. https://doi.org/10.1016/j.enggeo.2018.02.003

Chang, Ching S., & Meidani, M. (2013). Dominant grains network and behavior of sand–silt mixtures: stress–strain modeling. *International Journal for Numerical and Analytical Methods in Geomechanics*, *37*, 2563–2589. https://doi.org/10.1002/nag.2152

Chang, Ching S., Meidani, M., & Deng, Y. (2017). A compression model for sand–silt mixtures based on the concept of active and inactive voids. *Acta Geotechnica*, *12*(6), 1301–1317. https://doi.org/10.1007/s11440-017-0598-1

Chang, Ching S., Wang, J.-Y., & Ge, L. (2015). Modeling of minimum void ratio for sand–silt mixtures. *Engineering Geology*, *196*, 293–304.

https://doi.org/10.1016/j.enggeo.2015.07.015

Chang, Ching S., & Yin, Z. Y. (2011). Micromechanical modeling for behavior of silty sand with influence of fine content. *International Journal of Solids and Structures*, *48*(19), 2655–2667. https://doi.org/10.1016/j.ijsolstr.2011.05.014

Chang, Ching S, Deng, Y., & Yang, Z. (2017). Modeling of Minimum Void Ratio for Granular Soil with Effect of Particle Size Distribution. *Journal of Engineering Mechanics*, *143*(9), 04017060. https://doi.org/10.1061/(ASCE)EM.1943-7889.0001270.

Chang, W., & Phantachang, T. (2016). Effects of gravel content on shear resistance of gravelly soils. *Engineering Geology*, *207*(May), 78–90. https://doi.org/10.1016/j.enggeo.2016.04.015

Chatterjee, S., Hadi, A. S., & Price, B. (2000). *Regression Analysis by Example* (3rd ed.). New York, USA: John Wiley and Sons.

Cho, G.-C., Dodds, J., & Santamarina, J. C. (2006). Particle Shape Effects on Packing Density, Stiffness, and Strength: Natural and Crushed Sands. *Journal of Geotechnical and Geoenvironmental Engineering*, *132*(5), 591–602. https://doi.org/10.1061/(ASCE)1090-0241(2006)132:5(591)

Cho, Y. T. (2014). *The study of GCTS triaxial apparatus function and mixing sand void ratio*. National Taiwan University, Taiwan.

Ciantia, M. O., Arroyo, M., O'Sullivan, C., Gens, A., & Liu, T. (2019). Grading evolution and critical state in a discrete numerical model of Fontainebleau sand. *Geotechnique*, *69*(1), 1–15. https://doi.org/10.1680/jgeot.17.P.023

Clayton, C. R. I., Abbireddy, C. O. R., & Schiebel, R. (2009). A method of estimating the form of coarse particulates. *Géotechnique*, *59*(6), 493–501. https://doi.org/10.1680/geot.2008.P.009

Cox, M. R., & Budhu, M. (2008). A practical approach to grain shape quantification. *Engineering Geology*, *96*(1–2), 1–16. https://doi.org/10.1016/j.enggeo.2007.05.005

Cubrinovski, M., & Ishihara, K. (2002). Maximum and Minimum Void Ratio Characteristics of Sands. *Soils and Foundations*, *42*(6), 65–78. https://doi.org/10.3208/sandf.42.6_65

Daouadji, A., Hicher, P. Y., & Rahma, A. (2001). An elastoplastic model for granular materials taking into account grain breakage. *European Journal of Mechanics-A/Solids*, *20*(1), 113–137.

Das, N. (2007). *Modeling Three-Dimensional Shape of Sand Grains Using Discrete Element Method*. PhD Thesis, University of South Florida.

Dash, H. K., & Sitharam, T. G. (2011). Undrained monotonic response of sand–silt mixtures: effect of nonplastic fines. *Geomechanics and Geoengineering*, *6*(1), 47–58. https://doi.org/10.1080/17486021003706796

De Larrard, F. (1999). *Concrete mixture proportioning: A scientifil approach* (Vol. 1). London: E & FN Spon. https://doi.org/10.1017/CBO9781107415324.004

Derkaoui, M., Missoum, H., Bendani, K., & Belhouari, F. (2016). Shear Behavior of Sand–Silt Mixtures: A Laboratory Investigation of Coastal Silty Sand Soils of Mostaganem. *Marine Georesources and Geotechnology*, *34*(7), 668–680. https://doi.org/10.1080/1064119X.2015.1070388

Desmond, K. W., & Weeks, E. R. (2014). Influence of particle size distribution on random close packing of spheres. *Physical Review E*, *90*, 022204. https://doi.org/10.1103/PhysRevE.90.022204

Dewar, J. D. (1999). *Computer modelling of concrete mixtures*. London: E & FN Spon.

Diepenbroek, M., Bartholomä, A., & Ibbeken, H. (1992). How round is round? A new approach to the topic "roundness" by Fourier grain shape analysis. *Sedimentology*, *39*(3), 411–422. https://doi.org/10.1111/j.1365-3091.1992.tb02125.x

Dodds, J. A. (1980). The porosity and contact points in multicomponent random sphere packings calculated by a simple statistical geometric model. *Journal of Colloid and Interface Science*, *77*(2), 317–327. https://doi.org/10.1016/0021-9797(80)90302-1

Dutt, M., & Elliott, J. A. (2014). Granular dynamics simulations of the effect of grain size dispersity on uniaxially compacted powder blends. *Granular Matter*, *16*(2), 243–248. https://doi.org/10.1007/s10035-013-0463-3

Edil, T. B., Krizek, R. J., & Zelasko, J. S. (1975). Effect of grain characteristics on packing of sands. In *Proceedings of Istanbul Conf on Soil Mech and Found Eng* (pp. 46–54). Istanbul, Turkey: Istanbul Technical University.

Einav, I. (2007). Breakage mechanics-Part I: Theory. *Journal of the Mechanics and Physics of Solids*, *55*(6), 1274–1297. https://doi.org/10.1016/j.jmps.2006.11.003

Fourie, A. B., & Papageorigou, G. (2001). Defining an appropriate steady state line for Merriespruit gold tailings. *Canadian Geotechnical Journal*, *38*, 695–706. https://doi.org/10.1139/cgj-38-4-695

Fragaszy, R. J., & Sneider, C. A. (1991). *Compaction control of granular soils*. Washington State Department of Transportation, Final Report WA-RD 230.1.

Fuggle, A. R., Roozbahani, M. M., & Frost, J. D. (2014). Size effects on the void ratio of loosely packed binary particle mixtures. In M. Abu-Farsakh, X. Yu, & L. R. Hoyos (Eds.), *Geo-Congress 2014 Technical Papers* (pp. 129–138). Atlanta,GA, USA: American Society of Civil Engineers. https://doi.org/10.1061/9780784413272.014

Furnas, C. C. (1931). Grading aggregates I: Mathematical relations for beds of broken solids of maximum density. *Industrial and Engineering Chemistry*, *23*(9), 1052–1058. https://doi.org/10.1021/ie50261a017

Goltermann, P., Johansen, V., & Palbøl, L. (1997). Packing of aggregates: an alternative tool to determine the optimal aggregate mix. *ACI Materials Journal*, *94*(5), 435–443.

Gudehus, G. (1997). Attractors, percolation thresholds and phase limits of granular soils. In R. P.

Behringer & J. T. Jenkins (Eds.), *Powders & Grains 97* (pp. 169–183). Rotterdam, Balkema.

Hardin, B. O. (1985). Crushing of Soil Particles. *Journal of Geotechnical Engineering*, *111*(10), 1177–1192. https://doi.org/10.1061/(ASCE)0733-9410(1985)111:10(1177)

Harehdasht, S. A., Karray, M., Hussien, M. N., & Chekired, M. (2017). Influence of Particle Size and Gradation on the Stress-Dilatancy Behavior of Granular Materials during Drained Triaxial Compression. *International Journal of Geomechanics*, *17*(9), 04017077. https://doi.org/10.1061/(ASCE)GM.1943-5622.0000951.

Hettiarachchi, C., & Mampearachchi, W. K. (2020). Effect of surface texture , size ratio and large particle volume fraction on packing density of binary spherical mixtures. *Granular Matter*, *8*(22), 1–13. https://doi.org/10.1007/s10035-019-0978-3

Holtz, R. D., Kovacs, W. D., & Sheahan, T. C. (2011). *An introduction to geotechnical engineering* (second). Upper Saddle River, NJ: Pearson.

Hu, W., Yin, Z., Dano, C., & Hicher, P. Y. (2011). A constitutive model for granular materials considering grain breakage. *Science China Technological Sciences*, *54*(8), 2188–2196. https://doi.org/10.1007/s11431-011-4491-0

Huang, Y.-T., Huang, A.-B., Kuo, Y.-C., & Tsai, M.-D. (2004). A laboratory study on the undrained strength of a silty sand from Central Western Taiwan. *Soil Dynamics and Earthquake Engineering*, *24*(9), 733–743. https://doi.org/10.1016/j.soildyn.2004.06.013

Humphres, H. W. (1957). *A method for controlling compaction of granular materials*. Highway Research Board Bulletin No. 159, 41-57.

Hyodo, M., Nakata, Y., Yoshimoto, N., Kato, Y., & Okabayashi, T. (2001). The role of fines in the shear and liquefaction of a volcanic soil 'Shirasu' as a reclamation material. In *Proc. 11th Int. Offshore and Polar Engineering Conf.* (pp. 501–507). Norway.

Hyslip, J. P., & Vallejo, L. E. (1997). Fractal analysis of the roughness and size distribution of granular materials. *Engineering Geology*, *48*(3–4), 231–244. https://doi.org/10.1016/S0013-7952(97)00046-X

Imam, S. R., Morgenstern, N. R., Robertson, P. K., & Chan, D. H. (2005). A critical-state constitutive model for liquefiable sand. *Canadian Geotechnical Journal*, *42*(3), 830–855. https://doi.org/10.1139/t05-014

Indraratna, B., Nimbalkar, S., Coop, M., & Sloan, S. W. (2014). A constitutive model for coal-fouled ballast capturing the effects of particle degradation. *Computers and Geotechnics*, *61*, 96–107. https://doi.org/10.1016/j.compgeo.2014.05.003

Inman, D. L. (1953). *Areal and seasonal variations in beach and nearshore sediments at La Jolla, California*. Memo 39. Beach Erosion Board, Corps of Engrs Tech, US Dept of the Army, Washington, DC, USA.

Inman, D. L., Ewing, G. C., & Corliss, J. B. (1966). Coastal Sand Dunes Of guerrero Negro, baja

Caolifornia, Mexico. *GSA Bulletin*, *77*(8), 787–802.

Itasca Consulting Group, I. (2014). PFC-Particle Flow Code,Ver. 5.0. Minneapolis: Itasca: Itasca Consulting Group, Inc.

Ivsic, T., & Ivsic, A. G. (2012). State equation of mineral sands. *Granular Matter*, *14*, 37–50. https://doi.org/10.1007/s10035-011-0301-4

Iwashita, K., & Oda, M. (2000). Micro-deformation mechanism of shear banding process based on modified distinct element method. *Powder Technology*, *109*, 192–205.

Jalali, P., & Li, M. (2007). Model for estimation of critical packing density in polydisperse hard-disk packings. *Physica A*, *381*, 230–238. https://doi.org/10.1016/j.physa.2007.03.024

Japanese Geotechnical Society. (2000). Test Method for Minimum and Maximum Densities of Sand. In *Soil Testing Standards (in Japanese)* (pp. 136–138).

Jefferies, M., & Been, K. (2006). *Soil Liquefaction: A Critical State Approach*. New York: Taylor & Francis.

Jehring, M. M., & Bareither, C. A. (2016). Tailings composition effects on shear strength behavior of co-mixed mine waste rock and tailings. *Acta Geotechnica*, *11*(5), 1147–1166. https://doi.org/10.1007/s11440-015-0429-1

Jones, M. R., Zheng, L., & Newlands, M. D. (2002). Comparison of particle packing models for proportioning concrete constituents for minimum voids ratio. *Materials and Structures*, *35*(5), 301–309.

Kelly, E. G., & Spottiswood, D. J. (1982). *Introduction to mineral processing*. New York: Wiley.

Kezdi, A. (1979). *Soil physics*. Amsterdam: Elsevier.

Kolbuszewski, J. J. (1948). An experimental study of the maximum and minimum properties of sands. In N. Nanninga, G. A. Oosterholt, E. C. W. A. Geuze, & A. W. Koppejan (Eds.), *Proceedings of the Second International Conference on Soil Mechanics and Foundation Engineering* (pp. 158–165). Rotterdam.

Konrad, J.-M. (1998). Sand state from cone penetrometer tests: a framework considering grain crushing stress. *Géotechnique*, *48*(2), 201–215. https://doi.org/10.1680/geot.1998.48.2.201

Krumbein, W. C. (1941). Measurement and geological significance of shape and roundness of sedimentary particles. *Journal of Sedimentary Petrology*, *11*(2), 64–72.

Kumar, N., Magnanimo, V., Ramaioli, M., & Luding, S. (2016). Tuning the bulk properties of bidisperse granular mixtures by small amount of fines. *Powder Technology*, *293*, 94–112. https://doi.org/10.1016/j.powtec.2015.11.042

Kwa, K. A., & Airey, D. W. (2016). Critical state interpretation of effects of fines in silty sands. *Géotechnique Letters*, *6*(1), 100–105. https://doi.org/10.1680/jgele.15.00176

Kwan, A. K. H., Chan, K. W., & Wong, V. (2013). A 3-parameter particle packing model incorporating the wedging effect. *Powder Technology*, *237*, 172–179. https://doi.org/10.1016/j.powtec.2013.01.043

Ladd, R. S. (1978). Preparing test specimens using undercompaction. *Geotechnical Testing Journal*, *1*(1), 16–23.

Lade, P. V., Liggio, C. D., & Yamamuro, J. A. (1998). Effects of non-plastic fines on minimum and maximum void ratios of sand. *Geotechnical Testing Journal*, *21*(4), 336–347. https://doi.org/10.1520/GTJ11373J

Lade, P. V., & Yamamuro, J. A. (1997). Effects of nonplastic fines on static liquefaction of sands. *Canadian Geotechnical Journal*, *34*(6), 918–928. https://doi.org/10.1139/t97-052

Lade, P. V., Yamamuro, J. A., & Bopp, P. A. (1996). Significance of particle crushing in granular materials. *Journal of Geotechnical and Geoenvironmental Engineering*, *122*(4), 309–316. https://doi.org/10.1061/(ASCE)0733-9410(1996)122:4(309)

Larrard, François de. (1999). *Concrete mixture proportioning : a scientific approach*. London: CRC Press.

Li, G. (2013). *Étude de l'influence de l'étalement granulometrique sur le comportement mecanique des materiaux granulaires*. Nantes, France: Ecole Central de Nantes.

Li, Gang, Liu, Y., Dano, C., & Hicher, P. (2015). Grading-dependent behavior of granular materials: from discrete to continuous modeling. *Journal of Engineering Mechanics*, *141*(6), 04014172. https://doi.org/10.1061/(ASCE)EM.1943-7889.0000866.

Li, X. S., & Dafalias, Y. F. (2000). Dilatancy for cohesionless soils. *Geotechnique*, *50*(4), 449–460. https://doi.org/10.1680/geot.2000.50.4.449

Li, X. S., & Wang, Y. (1998). Linear Representation of Steady-State Line for Sand. *Journal of Geotechnical and Geoenvironmental Engineering*, *124*(12), 1215–1217. https://doi.org/10.1061/(ASCE)1090-0241(1998)124:12(1215)

Luding, S. (2004). Micro-macro transition for anisotropic, frictional granular packings. *International Journal of Solids and Structures*, *41*(21), 5821–5836. https://doi.org/10.1016/j.ijsolstr.2004.05.048

Man, W., Donev, A., Stillinger, F. H., Sullivan, M. T., Russel, W. B., Heeger, D., … Chaikin, P. M. (2005). Experiments on random packings of ellipsoids. *Physical Review Letters*, *94*(19), 1–4. https://doi.org/10.1103/PhysRevLett.94.198001

Marsal, R. J. (1963). Large scale testing of rockfill materials. *Journal of Soil Mechanics and Foundations*, *93*(2), 27–43.

Martin, C. L., & Bouvard, D. (2004). Isostatic compaction of bimodal powder mixtures and composites. *International Journal of Mechanical Sciences*, *46*(6), 907–927. https://doi.org/10.1016/j.ijmecsci.2004.05.012

McGeary, R. K. (1961). Mechanical Packing of Spherical Particles. *Journal of the American Ceramic Society*, *44*(10), 513–522. https://doi.org/10.1111/j.1151-2916.1961.tb13716.x

Meidani, M., Chang, C. S., & Deng, Y. (2017). On active and inactive voids and a compression model for granular soils. *Engineering Geology*, *222*, 156–167. https://doi.org/10.1016/j.enggeo.2017.03.006

Minh, N. H., & Cheng, Y. P. (2013). A DEM investigation of the effect of particle-size distribution on one-dimensional compression. *Geotechnique*, *63*(1), 44–53. https://doi.org/10.1680/geot.10.P.058

Mitchell, J. K. (1976). *Fundamentals of soil behaviour*. New York, USA: John Wiley & Sons, Inc.

Miura, K., Maiida, K., Furukawa, M., & Toki, S. (1997). Physical Characteristics of Sands with Different Primary Properties. *Soils and Foundations*, *37*(3), 53–64.

Mohammadi, A., & Qadimi, A. (2015). A simple critical state approach to predicting the cyclic and monotonic response of sands with different fines contents using the equivalent intergranular void ratio. *Acta Geotechnica*, *10*(5), 587–606. https://doi.org/10.1007/s11440-014-0318-z

Mohammadi, Amirabbas, & Qadimi, A. (2015). A simple critical state approach to predicting the cyclic and monotonic response of sands with different fines contents using the equivalent intergranular void ratio. *Acta Geotechnica*, *10*(5), 587–606. https://doi.org/10.1007/s11440-014-0318-z

Muir Wood, D., & Maeda, K. (2008). Changing grading of soil: Effect on critical states. *Acta Geotechnica*, *3*(1), 3–14. https://doi.org/10.1007/s11440-007-0041-0

Mulilis, J. P., Arulanandan, K., Mitchell, J. K., Chan, C. K., & Seed, H. B. (1977). Effects of Sample Preparation on Sand Liquefaction. *Journal of the Geotechnical Engineering Division*, *103*(2), 91–108. https://doi.org/10.1016/0148-9062(77)90060-2

Murthy, T. G., Loukidis, D., Carraro, J. A. H., Prezzi, M., & Salgado, R. (2007). Undrained monotonic response of clean and silty sands. *Géotechnique*, *57*(3), 273–288. https://doi.org/10.1680/geot.2007.57.3.273

Muszynski, M. R. (2006). Determination of maximum and minimum densities of poorly graded sands using a simplified method. *Geotechnical Testing Journal*, *29*(3), 263–272. https://doi.org/10.1520/GTJ12591

Muzzio, F. J., Shinbrot, T., & Glasser, B. J. (2002). Powder technology in the pharmaceutical industry: the need to catch up fast. *Powder Technology*, *124*(1–2), 1–7. https://doi.org/10.1016/S0032-5910(01)00482-X

Naeini, S. A., & Baziar, M. H. (2004). Effect of fines content on steady-state strength of mixed and layered samples of a sand. *Soil Dynamics and Earthquake Engineering*, *24*(3), 181–187.

Nguyen, T., Benahmed, N., & Hicher, P. (2017). Determination of the equivalent intergranular

void ratio - Application to the instability and the critical state of silty sand. In F. Radjai, S. Nezamabadi, S. Luding, & J. Y. Delenne (Eds.), *Powders and Grains 2017 – 8th International Conference on Micromechanics on Granular Media* (Vol. 140, p. 02019). Montpellier, France: EDP Sciences. https://doi.org/10.1051/epjconf/201714002019

Ni, Q., Tan, T. S., Dasari, G. R., & Hight, D. W. (2004). Contribution of fines to the compressive strength of mixed soils. *Geotechnique*, *54*(9), 561–569.

Norris, G. M. (1977). *The drained shear strength of uniform quartz sand as related to particle size and natural variation in particle shape and surface roughness*. Ph.D. thesis, University of California, Berkeley.

Nova, R. (1982). A constitutive model under monotonic and cyclic loading. In G. Pande & O. C. Zienkiewicz (Eds.), *Soil mechanics — transient and cyclic loads* (pp. 343–373). New York, USA: John Wiley & Sons Ltd.

Ogarko, V., & Luding, S. (2013). Prediction of polydisperse hard-sphere mixture behavior using tridisperse systems. *Soft Matter*, *9*(40), 9530–9534. https://doi.org/10.1039/c3sm50964h

Okonta, F. N. (2015). Effect of grading category on the roundness of degraded and abraded railway quartzites. *Engineering Geology*, *193*, 231–242. https://doi.org/10.1016/j.enggeo.2015.03.018

Papadopoulou, A., & Tika, T. (2008). The effect of fines on critical state and liquefaction resistance characteristics of non-plastic silty sands. *Soils and Foundations*, *48*(5), 713–725. https://doi.org/10.3208/sandf.47.887

Patil, U. D., Hoyos, L. R., Puppala, A. J., & Bheemasetti, T. V. (2018). Modeling Stress – Dilatancy Behavior of Compacted Silty Sand Under Suction-Controlled Axisymmetric Shearing. *Geotechnical and Geological Engineering*, *36*(6), 3961–3977. https://doi.org/10.1007/s10706-018-0647-z

Patra, C. R., Sivakugan, N., Das, B. M., & Rout, S. K. (2010). Correlations for relative density of clean sand with median grain size and compaction energy. *International Journal of Geotechnical Engineering*, *4*(2), 195–203. https://doi.org/10.3328/IJGE.2010.04.02.195-203

Peters, J. F., & Berney, E. S. (2010). Percolation Threshold of Sand-Clay Binary Mixtures. *Journal of Geotechnical and Geoenvironmental Engineering*, *136*(2), 310–318. https://doi.org/10.1061/(ASCE)GT.1943-5606.0000211

Pettijohn, F.J. (1957). *Sedimentary rocks*. New York, USA: Harper.

Pettijohn, Francis John, & Lundahl, A. C. (1943). Shape and roundness of Lake Erie beach sands. *Journal of Sedimentary Petrology*, *13*(2), 69–78. https://doi.org/10.1306/D426919D-2B26-11D7-8648000102C1865D

Pitman, T. D., Robertson, P. K., & Sego, D. C. (1994). Influence of fines on the collapse of loose sands. *Canadian Geotechnical Journal*, *31*(5), 728–739. https://doi.org/10.1139/t94-084

Polito, C. P., & Martin, J. R. (2001). Effects of nonplastic fines on the liquefaction resistance of

sands. *Journal of Geotechnical and Geoenvironmental Engineering*, *127*(5), 408–415. https://doi.org/10.1061/(ASCE)1090-0241(2001)127:5(408)

Polito, C. P., & Sibley, E. L. D. (2020). Threshold fines content and behavior of sands with nonplastic silts. *Canadian Geotechnical Journal*, *57*(3), 462–465. https://doi.org/10.1139/cgj-2018-0698

Powers, M. C. (1953). A new roundness scale for sedimentary particles. *Journal of Sedimentary Petrology*, *23*(2), 117–119. https://doi.org/10.1306/d4269567-2b26-11d7-8648000102c1865d

Powers, T. C. (1968). *The properties of fresh concrete*. New York: John Wiley & Sons.

Rahman, M., Lo, S., & Gnanendran, C. (2008). On equivalent granular void ratio and steady state behaviour of loose sand with fines. *Can Geotech J*, *45*(10), 1439–1455. https://doi.org/10.1139/T08-064

Rahman, M.M., Lo, S.-C. R., & Dafalias, Y. F. (2014). Modelling the static liquefaction of sand with low-plasticity fines. *Ge´otechnique*, *64*(11), 881–894. https://doi.org/10.1680/geot.14.P.079

Rahman, Md Mizanur, Lo, S. R., & Baki, M. A. L. (2011). Equivalent granular state parameter and undrained behaviour of sand-fines mixtures. *Acta Geotechnica*, *6*(4), 183–194. https://doi.org/10.1007/s11440-011-0145-4

Ramez, M. R. H., & Mosalamy, F. H. (1969). The deformed nature of various size fractions in some clastic sands. *Journal of Sedimentary Petrology*, *39*(3), 1182–1187.

Reed, J. S. (1995). *Principles of ceramics processing* (2nd ed., Vol. 83). New York: John Wiley & Sons.

Rhodes, M. (2008). *Introduction to particle technology* (second). West Sussex: John Wiley & Sons.

Richard, A.-S. (1994). Model Comparisons and R2. *The American Statistician*, *48*(2), 113–117.

Riemer, M. F., & Seed, R. B. (1997). Factors affecting apparent position of steady-state line. *Journal of Geotechnical and Geoenvironmental Engineering*, *123*(3), 281–288.

Roquier, G. (2016). The 4-parameter Compressible Packing Model (CPM) including a new theory about wall effect and loosening effect for spheres. *Powder Technology*, *302*, 247–253. https://doi.org/10.1016/j.powtec.2016.08.031

Roscoe, K. H., Schofield, A. N., & Wroth, C. P. (1958). On the yielding of soils. *Geotechnique*, *1*(8), 22–53.

Rouse, P. C., Fannin, R. J., & Shuttle, D. A. (2008). Influence of roundness on the void ratio and strength of uniform sand. *Géotechnique*, *58*(3), 227–231. https://doi.org/10.1680/geot.2008.58.8.681

Rout, S. K. (2009). *Prediction of Relative Density of Sand with Particular Reference to Compaction Energy*. National Institute of Technology Rourkela, Odisha, India.

Russell, A. R., & Khalili, N. (2004). A bounding surface plasticity model for sands exhibiting particle crushing. *Canadian Geotechnical Journal*, *41*(6), 1179–1192. https://doi.org/10.1139/t04-065

Russell, R. D. (1937). Mineral composition of mississippi river sands. *Bulletin of the Geological Society of America*, *48*(9), 1307–1348.

Russell, R. D., & Taylor, R. E. (1937). Roundness and Shape of Mississippi River Sands. *The Journal of Geology*, *45*(3), 225–267.

Sadrekarimi, A., & Olson, S. M. (2011). Yield strength ratios, critical strength ratios, and brittleness of sandy soils from laboratory tests. *Canadian Geotechnical Journal*, *48*(3), 493–510. https://doi.org/10.1139/T10-078

Salgado, R., Bandini, P., & Karim, A. (2000). Shear Strength and Stiffness of Silty Sand. *Journal of Geotechnical and Geoenvironmental Engineering*, *126*(5), 451–462. https://doi.org/10.1061/(ASCE)1090-0241(2000)126:5(451)

Sammis, C., King, G., & Biegel, R. (1987). The kinematics of gouge deformation. *Pure and Applied Geophysics*, *125*(5), 777–812. https://doi.org/10.1007/BF00878033

Santamarina, J. C., & Cho, G. C. (2004). Soil behaviour: The role of particle shape. In R. J. Jardine, D. M. Potts, & K. G. Higgins (Eds.), *Advances in Geotechnical Engineering: Proceedings of the Skempton Conference* (pp. 604–617). Thomas Telford, London.

Schofield, A. N., & Wroth, C. P. (1968). *Critical state soil mechanics*. Maidenhead, England: McGraw-Hill.

Selig, E., & Ladd, R. (1973). Evaluation of Relative Density Measurements and Applications. In E. Selig & R. Ladd (Eds.), *Evaluation of Relative Density and its Role in Geotechnical Projects Involving Cohesionless Soils* (pp. 487–18). West Conshohocken, PA: ASTM International. https://doi.org/10.1520/STP37891S

Shaebani, M. R., Madadi, M., Luding, S., & Wolf, D. E. (2012). Influence of polydispersity on micromechanics of granular materials. *Physical Review E*, *85*(1), 011301. https://doi.org/10.1103/PhysRevE.85.011301

Shen, S., & Yu, H. (2011). Characterize packing of aggregate particles for paving materials: Particle size impact. *Construction and Building Materials*, *25*(3), 1362–1368. https://doi.org/10.1016/j.conbuildmat.2010.09.008

Shimobe, S., & Moroto, N. (1995). A new classification chart for sand liquefaction. In Ishihara (Ed.), *Proc. 1st Int. Conf. on Earthquake Geotechnical Engineering* (pp. 315–320). Tokyo.

Shire, T., O'Sullivan, C., Hanley, K. J., & Fannin, R. J. (2014). Fabric and effective stress distribution in internally unstable soils. *Journalof Geotechnicaland Geoenvironmental Engineering*, *140*(12), 04014072. https://doi.org/10.1061/(ASCE)GT.1943-5606.0001184

Skrinjar, O., & Larsson, P. (2004). On discrete element modelling of compaction of powders with size ratio. *Computational Materials Science*, *31*(1), 131–146. https://doi.org/10.1016/j.commatsci.2004.02.005

Smith, L. (2003). *A knowledge-based system for powder metallurgy technology*. John Wiley & Sons.

Stamatopoulos, C. A. (2010). An experimental study of the liquefaction strength of silty sands in terms of the state parameter. *Soil Dynamics and Earthquake Engineering*, *30*(8), 662–678. https://doi.org/10.1016/j.soildyn.2010.02.008

Stovall, T., de Larrard, F., & Buil, M. (1986). Linear packing density model of grain mixtures. *Powder Technology*, *48*(1), 1–12. https://doi.org/10.1016/0032-5910(86)80058-4

Stovall, T., De Larrard, F., & Buil, M. (1986). Linear packing density model of grain mixtures. *Powder Technology*, *48*(1), 1–12. https://doi.org/10.1016/0032-5910(86)80058-4

Tafesse, S., Fernlund, J. M. R., & Bergholm, F. (2012). Digital sieving-Matlab based 3-D image analysis. *Engineering Geology*, *137–138*, 74–84. https://doi.org/10.1016/j.enggeo.2012.04.001

Tavenas, F., Ladd, R., & La Rochelle, P. (1973). Accuracy of Relative Density Measurements: Results of a Comparative Test Program. In *Evaluation of Relative Density and its Role in Geotechnical Projects Involving Cohesionless Soils* (pp. 18–43). West Conshohocken, PA: ASTM International. https://doi.org/10.1520/STP37862S

Tengattini, A., Das, A., & Einav, I. (2016). A constitutive modelling framework predicting critical state in sand undergoing crushing and dilation. *Géotechnique*, *66*(9), 695–710. https://doi.org/10.1680/jgeot.14.P.164

Thevanayagam, S., Shenthan, T., Mohan, S., & Liang, J. (2002). Undrained fragility of clean sands, silty sands, and sandy silts. *Journal of Geotechnical and Geoenvironmental Engineering*, *128*(10), 849–859. https://doi.org/10.1061/(ASCE)1090-0241(2002)128:10(849)

Torres-Cruz, L. A., Geyer, S., & Mackechnie, P. R. (2017). Effect of the minimum void ratio on the vertical intercept of the steady state line of non-plastic soils. *Journal of the South African Institution of Civil Engineering*, *59*(2), 59–64. https://doi.org/10.17159/2309-8775/2017/v59n2a7

Toufar, W., Klose, E., & Born, M. (1977). Berechnung der packungsdichte von korngemischen. *Aufbereitung-Technik*, *11*, 603–608.

U.S. Navy. (1982). *Soil Mechanics, NAVFAC Design Manual 7.1*. Arlington, VA: Navy Facilities Engineering Command.

Uday, K. V., Padmakumar, G. P., & Singh, D. N. (2013). Some studies on morphology of the coarse-grained soils. *Engineering Geology*, *152*(1), 48–55. https://doi.org/10.1016/j.enggeo.2012.10.001

Ueda, T., Matsushima, T., & Yamada, Y. (2011). Effect of particle size ratio and volume fraction on shear strength of binary granular mixture. *Granular Matter*, *13*(6), 731–742. https://doi.org/10.1007/s10035-011-0292-1

Vaid, Y., & Negussey, D. (1988). Preparation of Reconstituted Sand Specimens. In R. T. Donaghe, R. C. Chaney, & M. L. Silver (Eds.), *American Society for Testing and Materials* (pp. 405–417). Philadelphia: ASTM International. https://doi.org/10.1520/STP29090S

Vaid, Y. P. (1994). Liquefaction of silty soils. In S. Prakash & P. Dakoulas (Eds.), *Proceedings of Ground failures under seismic conditions* (pp. 1–16). New York, USA: Geotechnical Special Publication 44, ASCE.

Vallejo, L. E. (2001). Interpretation of the limits in shear strength in binary granular mixtures. *Canadian Geotechnical Journal*, *38*(5), 1097–1104. https://doi.org/10.1139/t01-029

Verdugo, R., & Ishihara, K. (1996). The steady state of sandy soils. *Soils and Foundations*, *36*(2), 81–91. https://doi.org/10.1248/cpb.37.3229

Vermeer, P. A., & de Borst, R. (1984). Non-associated plasticity for soils, concrete and rock. *HERON*, *29*(3), 1–64.

Voigt, W. (1889). Ueber die Beziehung zwischen den beiden Elasticitätsconstanten isotroper Körper. *Annalen Der Physik*, *274*, 573–587. https://doi.org/10.1002/andp.18892741206

Voivret, C., Radjaï, J., Delenne, J.-Y., & Youssoufi, M. S. El. (2007). Space-filling properties of polydisperse granular media. *Physical Review E*, *76*(2), 021301. https://doi.org/10.1103/PhysRevE.76.021301

Wadell, H. (1933). Sphericity and Roundness of Rock Particles. *The Journal of Geology*, *41*(3), 310–331.

Wadell, H. (1935). Volume, Shape, and Roundness of Quartz Particles. *The Journal of Geology*, *43*(3), 250–280.

Wei, X., & Yang, J. (2019). Characterizing the effects of fines on the liquefaction resistance of silty sands. *Soils and Foundations*, *59*(6), 1800–1812. https://doi.org/10.1016/j.sandf.2019.08.010

Westman, A. E. R., & Hugill, H. R. (1930). The packing of particles. *Journal of the American Ceramic Society*, *13*(10), 767–779. https://doi.org/10.1111/j.1151-2916.1930.tb16222.x

Wiącek, J. (2016). Geometrical parameters of binary granular mixtures with size ratio and volume fraction : experiments and DEM simulations. *Granular Matter*, *18*(3), 42. https://doi.org/10.1007/s10035-016-0642-0

Wiącek, Joanna, & Molenda, M. (2014). Particuology Effect of particle polydispersity on micromechanical properties and energy dissipation in granular mixtures. *Particuology*, *16*, 91–99. https://doi.org/10.1016/j.partic.2013.11.006

Wichtmann, T., & Triantafyllidis, T. (2014). Stiffness and Damping of Clean Quartz Sand with

Various Grain-Size Distribution Curves. *Journal of Geotechnical and Geoenvironmental Engineering*, *140*(3), 06013003. https://doi.org/10.1061/(ASCE)GT.1943-5606.0000977

Xiao, Y., Xiang, J., Liu, H., & Ma, Q. (2017). Strength-dilatancy relation of sand containing non-plastic fines. *Géotechnique Letters*, *7*(2), 204–210. https://doi.org/10.1680/jgele.16.00144

Xiao, Yang, & Desai, C. (2016). General Stress – Dilatancy Relation for Granular Soils. *Journal of Geotechnical and Geoenvironmental Engineering*, *142*(4), 2816001. https://doi.org/10.1061/(ASCE)GT.1943-5606.0001473

Xiao, Yang, & Liu, H. (2017). Elastoplastic Constitutive Model for Rockfill Materials Considering Particle Breakage. *International Journal of Geomechanics*, *17*(1), 04016041. https://doi.org/10.1061/(ASCE)GM.1943-5622.0000681.

Xiao, Yang, Liu, H., Desai, C. S., Sun, Y., & Liu, H. (2016). Effect of Intermediate Principal-Stress Ratio on Particle Breakage of Rockfill Material. *Journal of Geotechnical and Geoenvironmental Engineering*, *142*(4), 06015017. https://doi.org/10.1061/(ASCE)GT.1943-5606.0001433.

Xiao, Yang, Liu, H., Ding, X., Chen, Y., Jiang, J., & Wengang Zhang. (2016). Influence of Particle Breakage on Critical State Line of Rockfill Material. *International Journal of Geomechanics*, *16*(1), 04015031. https://doi.org/10.1061/(ASCE)GM.1943-5622.0000538

Xiao, Yang, Sun, Y., & Hanif, K. F. (2015). A particle-breakage critical state model for rockfill material. *Science China Technological Sciences*, *58*(7), 1125–1136. https://doi.org/10.1007/s11431-015-5831-2

Yan, W., & Dong, J. (2011). Effect of particle grading on the response of an idealized granular assemblage. *International Journal of Geomechanics, ASCE*, *11*(4), 276–285. https://doi.org/10.1061/(ASCE)GM.1943-5622.0000085.

Yang, S. L. (2004). *Characterization of the properties of sand-silt mixtures*. Norwegian University of Science and Technology.

Yang, S. L., Sandven, R., & Grande, L. (2006). Instability of sand-silt mixtures. *Soil Dynamics and Earthquake Engineering*, *26*, 183–190. https://doi.org/10.1016/j.soildyn.2004.11.027

Yang, S. L., Sandven, R., & L.Grande. (2006). Steady- state lines of sand-silt mixtures. *Canadian Geotechnical Journal*, *43*(11), 1213–1219. https://doi.org/10.1139/t06-069

Yang, S., Lacasse, S., & Sandven, R. (2006). Determination of the transitional fines content of mixtures of sand and non-plastic fines. *Geotechnical Testing Journal*, *29*(2), 1–6. https://doi.org/10.1520/GTJ14010

Yi, L. Y., Dong, K. J., Zou, R. P., & Yu, A. B. (2012). Radical tessellation of the packing of ternary mixtures of spheres. *Powder Technology*, *224*, 129–137. https://doi.org/10.1016/j.powtec.2012.02.042

Yilmaz, Y. (2009). A study on the limit void ratio characteristics of medium to fine mixed graded sands. *Engineering Geology*, *104*(3–4), 290–294.

https://doi.org/10.1016/j.enggeo.2008.11.009

Yin, Z. Y., Zhao, J., & Hicher, P. Y. (2014). A micromechanics-based model for sand-silt mixtures. *International Journal of Solids and Structures*, *51*(6), 1350–1363. https://doi.org/10.1016/j.ijsolstr.2013.12.027

Youd, T. L. (1973). Factors Controlling Maximum and Minimum Densities of Sands. In *Evaluation of Relative Density and its Role in Geotechnical Projects Involving Cohesionless Soils,STP 523* (pp. 98–112). West Conshohocken, PA: ASTM International. https://doi.org/10.1520/STP37866S

Yu, A. B., & Standish, N. (1987). Porosity calculations of multi-component mixtures of spherical particles. *Powder Technology*, *52*(3), 233–241. https://doi.org/10.1016/0032-5910(87)80110-9

Yu, A. B., & Standish, N. (1988). An analytical-parametric theory of the random packing of particles. *Power Technology*, *55*(3), 171–186. https://doi.org/10.1016/0032-5910(88)80101-3

Yu, A. B., & Standish, N. (1991). Estimation of the Porosity of Particle Mixtures by a Linear-Mixture Packing Model. *Industrial & Engineering Chemistry Research*, *30*(6), 1372–1385. https://doi.org/10.1021/ie00054a045

Yu, A. B., Zou, R. P., & Standish, N. (1996). Modifying the linear packing model for predicting the porosity of nonspherical particle mixtures. *Industrial & Engineering Chemistry Research*, *35*(10), 3730–3741. https://doi.org/10.1021/ie950616a

Yu, F.-W., & Su, L.-J. (2016). Particle breakage and the mobilized drained shear strengths of sand. *Journal of Mountain Science*, *13*(8), 1481–1488. https://doi.org/10.1007/s11629-016-3870-1

Yu, F. W. (2017). Particle breakage and the critical state of sands. *Géotechnique*, *67*(8), 713–719. https://doi.org/10.1016/j.sandf.2014.04.016

Zhao, J., Li, S., Jin, W., & Zhou, X. (2012). Shape effects on the random-packing density of tetrahedral particles. *Physical Review E - Statistical, Nonlinear, and Soft Matter Physics*, *86*(3), 1–6. https://doi.org/10.1103/PhysRevE.86.031307

Zheng, J., & Hryciw, R. D. (2016a). Index Void Ratios of Sands from Their Intrinsic Properties. *Journal of Geotechnical and Geoenvironmental Engineering*, *142*(12), 06016019. https://doi.org/10.1061/(ASCE)GT.1943-5606.0001575

Zheng, J., & Hryciw, R. D. (2016b). Roundness and Sphericity of Soil Particles in Assemblies by Computational Geometry. *Journal of Computing in Civil Engineering*, *30*(6), 1–13. https://doi.org/10.1061/(ASCE)CP.1943-5487.0000578.

Zhou, W., Liu, J., Ma, G., & Chang, X. (2017). Three-dimensional DEM investigation of critical state and dilatancy behaviors of granular materials. *Acta Geotechnica*, *12*(3), 527–540. https://doi.org/10.1007/s11440-017-0530-8

Zhou, W., Xu, K., Ma, G., Yang, L., & Chang, X. (2016). Effects of particle size ratio on the macro- and microscopic behaviors of binary mixtures at the maximum packing efficiency state. *Granular Matter*, *18*(4), 1–13. https://doi.org/10.1007/s10035-016-0678-1

Zhu, Y., Nie, Z., Gong, J., Zou, J., Zhao, L., & Li, L. (2020). An analysis of the effects of the size ratio and fines content on the shear behaviors of binary mixtures using DEM. *Computers and Geotechnics*, *118*(2), 103353. https://doi.org/10.1016/j.compgeo.2019.103353

Zlatovic, S., & Ishihara, K. (1995). On the influence of nonplastic fines on residual strength. In K. Ishihara (Ed.), *Earthquake Geotechnical Engineering* (pp. 239–244). Balkema, Rotterdam.

Zou, R. P., & Yu, A. B. (1996). Evaluation of the packing characteristics of mono-sized non-spherical particles. *Powder Technology*, *88*(1), 71–79. https://doi.org/10.1016/0032-5910(96)03106-3